PERFORMANCE MODELLING AND SIMULATION OF A 100 KM HYBRID SOUNDING ROCKET

Fiona Kay Leverone

Submitted in fulfilment of the academic requirements for the degree of Master of Science in
Mechanical Engineering, College of Agriculture, Engineering and Science,
University of KwaZulu-Natal

Supervisor: Mr Michael Brooks

Co-Supervisor: Mr Jean-François Pitot de la Beaujardiere

Co-Supervisor: Prof Lance Roberts

December 2013

DECLARATION 1 - PLAGIARISM

I, Fiona Leverone, declare that

1. The research reported in this thesis, except where otherwise indicated, is my original research.
2. This thesis has not been submitted for any degree or examination at any other university.
3. This thesis does not contain other persons' data, pictures, graphs or other information, unless specifically acknowledged as being sourced from other persons.
4. This thesis does not contain other persons' writing, unless specifically acknowledged as being sourced from other researchers. Where other written sources have been quoted, then:
a. Their words have been re-written but the general information attributed to them has been referenced
b. Where their exact words have been used, then their writing has been placed inside quotation marks, and referenced.
5. This thesis does not contain text, graphics or tables copied and pasted from the Internet, unless specifically acknowledged, and the source being detailed in the thesis and in the References sections.

Signed _____ Date _____

Miss Fiona Leverone

As the candidate's supervisor I have approved this dissertation for submission.

Signed _____ Date _____

Mr. Michael Brooks

As the candidates co-supervisor I have approved this dissertation for submission.

Signed _____ Date _____

Mr. Jean-François Pitot de la Beaujardiere

As the candidates co-supervisor I have approved this dissertation for submission.

Signed _____ Date _____

Prof. Lance Roberts

DECLARATION 2 - PUBLICATIONS

Leverone, F. K., Pitot de la Beaujardiere, J. P., Brooks, M. J. and Roberts, L. W., 2011. Recent Advances in South Africa's Phoenix Hybrid Sounding Rocket Programme. *62nd International Astronautical Congress*, Cape Town, South Africa, 3-7 October.

Leverone, F. K., Veale, K. L., Brooks, B. J., Pitot de la Beaujardiere, J. P. and Roberts, L. W., 2013. Performance Modeling of the Phoenix-2A Hybrid Sounding Rocket using HYROPS Software. *49th AIAA/ASME/SAE/ASEE Joint Propulsion Conference & Exhibit*, San Jose, CA, United States of America, 14-17 July.

Signed _____ Date _____

Fiona Leverone

ACKNOWLEDGEMENTS

ABSTRACT

The University of KwaZulu-Natal (UKZN) Phoenix Hybrid Sounding Rocket Programme was established in 2010. The programme's main objective is to develop a sounding rocket launch capability for the African scientific community, which currently lacks the ability to fly research payloads to the upper atmosphere. In this dissertation, UKZN's in-house Hybrid Rocket Performance Simulator (HYROPS) software is used to improve the design of the Phoenix-2A vehicle, which is intended to deliver a 5 kg instrumentation payload to an apogee altitude of 100 km.

As a benchmarking exercise, HYROPS was first validated by modelling the performance of existing sub-orbital sounding rockets similar in apogee to Phoenix-2A. The software was found to approximate the performance of the published flight data within 10%. A generic methodology was then proposed for applying HYROPS to the design of hybrid propellant sounding rockets. An initial vehicle configuration was developed and formed the base design on which parametric trade studies were conducted. The performance sensitivity for varying propulsion and aerodynamic parameters was investigated. The selection of parameters was based on improving performance, minimising cost, safety and ease of manufacturability. The purpose of these simulations was to form a foundation for the development of the Phoenix-2A vehicle as well as other large-scale hybrid rockets.

Design chamber pressure, oxidiser-to-fuel ratio, nozzle design altitude, and fin geometry were some of the parameters investigated. The change in the rocket's propellant mass fraction was the parameter which was found to have the largest effect on performance. The fin and oxidiser tank geometries were designed to avoid fin flutter and buckling respectively. The oxidiser mass flux was kept below 650 kg/m^{2}s and the pressure drop across the injector relative to the chamber pressure was maintained above 15% to mitigate the presence of combustion instability.

The trade studies resulted in an improved design of the Phoenix-2A rocket. The propellant mass of the final vehicle was 30 kg less than the initial conceptual design and the overall mass was reduced by 25 kg. The Phoenix-2A vehicle was 12 m in length with a total mass of 1006 kg. The fuel grain length of Phoenix-2A was 1.27 m which is approximately 3 times that of Phoenix-1A. The benefit of aluminised paraffin wax as a fuel was also investigated. The results indicated that more inert mass can be delivered to the target apogee of 100 km when using a 40% aluminised paraffin wax.

Table of Contents

LIST OF FIGURES

CHAPTER 5

LIST OF TABLES

NOMENCLATURE

Symbols

A	Area
A_{ref}	Reference area
AR	Aspect panel ratio
a	Regression rate coefficient, Speed of sound
B	Blowing coefficient
b	Fin semichord
C_D	Drag coefficient, Injector discharge coefficient
C_F	Thrust coefficient
CG	Centre of gravity
CP	Centre of pressure
C_r	Fin root chord
C_t	Fin tip chord
c	Fin chord
c^*	Characteristic velocity
D	Outer diameter
d	Inner diameter
E	Joint efficiency, Young's Modulus
F	Thrust
F_{all}	Allowable failing load
F_{axial}	Axial compressive load
F_D	Drag Force
G	Mass flux, Gravitational constant
G_E	Shear modulus
g	Gravitational acceleration
h	Altitude
I_{sp}	Specific impulse
I_t	Total impulse
k	Specific heat ratio
L	Length
m	Mass
$\dot{m}$	Mass flow rate
N	Number of

O/F	Oxidiser-to-fuel ratio
P	Pressure
P_l	Pressure loss in feed system
R	Outer radius
R_{air}	Ideal gas constant for air
r	Inner radius
$\dot{r}$	Regression rate
$\dot{r}_{classical}$	Classical regression rate
S	Fin span
SF	Factor of safety
SM	Static margin
T	Temperature
t	Thickness
t_b	Burn time
V	Volume
v	Velocity
X	Nondimensional geometric parameter
x	Axial distance from the fuel grain's front leading edge
Δp_{inj}	Pressure drop across the injector
ΔV	Velocity increment
$\Delta \sigma_{c_{cr}}$	Change in the critical compressive stress
ε	Nozzle expansion ratio
ζ	Propellant mass fraction
η	Combustion efficiency
η_p	Plasticity correction factor
θ_{cn}	Conical nozzle half angle
λ	Nozzle correction factor, Fin taper ratio
μ	Combustion gas viscosity
ρ	Density
$\sigma_{c_{cr}}$	Critical compressive stress
σ_t	Longitudinal tensile stress
σ_{tot}	Total compressive stress
σ_y	Yield strength

Subscripts

atm	Atmospheric
c	Chamber
cyl	Cylinder
d	Design
e	Nozzle exit
ear	Earth
ent	Entrainment
f	Fuel
fl	Flutter
$hemi$	Hemisphere
inj	Injector orifice
n	Nose cone
noz	Nozzle
ox	Oxidiser
p	Port
$prop$	Propellant
T	Tank
t	Nozzle throat
tot	Total
ull	Ullage volume
v	Evaporation
0	Standard sea level

Abbreviations

ASReG	Aerospace Systems Research Group
ATLO	Assembly Test and Launch Operations
CaNoRock	Canadian and Norwegian Student Sounding Rocket
CDR	Critical Design Review
CEA	Chemical Equilibrium with Applications
CFD	Computational Fluid Dynamics
DARE	Delft Aerospace Rocket Engineering
DATCOM	Data Compendium
DOF	Degree-of-Freedom
EOM	End of Mission
ESA	European Space Agency
FRR	Flight Readiness Review
GIRD	Gruppa Izucheniya Reaktivnogo Dvizheniya (Groups for study of jet propulsions)
GUI	Graphical User Interface
HRPC	Hybrid Rocket Performance Code
HTPB	Hydroxyl-Terminated Polybutadiene
HYROPS	Hybrid Rocket Performance Simulator
HYSR	Hybrid Sounding Rocket
ISRO	Indian Space Research Organisation
ITAR	International Traffic in Arms Regulation
KARI	Korea Aerospace Research Institute
MaCH-SR1	Multi-disciplinary University of Colorado Hybrid Student Rocket
MOS	Mission Operations
NASA	National Aeronautics and Space Administration
ONERA	Office National d'Études et de Recherches Aérospatiales
ODE	Ordinary Differential Equations
OTR	Overberg Test Range
PDR	Preliminary Design Review
RASAero	Rocket Aerodynamic Analysis and Flight Simulation Software
RK4	Fourth Order Runge-Kutta
SPaSE	Stanford Propulsion and Space Exploration
SPG	Space Propulsion Group
UKZN	University of KwaZulu-Natal

CHAPTER 1

Introduction

Rockets are used to deliver payloads to specific altitudes, orbits and beyond. These payloads vary from scientific instrumentation to planetary exploration rovers. Rocket propulsion is based on the principle of Newton's 3rd law whereby propellants are accelerated through a nozzle to generate thrust. This allows a rocket to be propelled in both atmospheric and vacuum conditions. Although solid propellant rockets have been around for over 800 years, rockets were not considered feasible until breakthroughs in the twentieth century that saw the development of mathematical models and liquid propulsion systems (Sutton and Biblarz, 2001).

The atmospheric region, which cannot be reached by weather balloons or satellites, has been well documented using sounding rockets for the past 60 years. The mission of a sounding rocket is to deliver a scientific payload to a desired altitude to conduct upper atmospheric research (Seibert, 2006). This research includes performing meteorology, microgravity and astronomy experiments. The payload is housed within a fairing generally situated near the fore end of the rocket. Atmospheric research conducted with sounding rockets has led to valuable scientific and engineering advancements.

Sounding rockets are technically simpler and less expensive than orbital spacecraft and have the flexibility of being launched from almost anywhere. They follow a parabolic flight trajectory profile to reach the required altitudes. To reach higher apogees, a sounding rocket can have multiple propulsion stages and/or an aerodynamically designed section at the fore end referred to as a dart. This consists of a nose cone and a non-propulsive cylindrical section that houses the payload. At motor burnout, the dart separates from the booster and travels higher than the booster, in atmospheric flight, due to the improved aerodynamic design.

The United States of America (USA), Britain, France, Germany, Russia, Sweden, South Korea, and developing nations such as China, Brazil, and India, are among many countries that are pursuing scientific research through sounding rocket programmes. The USA's space agency, the National Aeronautics and Space Administration (NASA), has a well-established sounding rocket programme. Figure 1.1 indicates the performance characteristics of various NASA sounding rockets. The inverse exponential relationship between payload weight and apogee is shown in this figure.
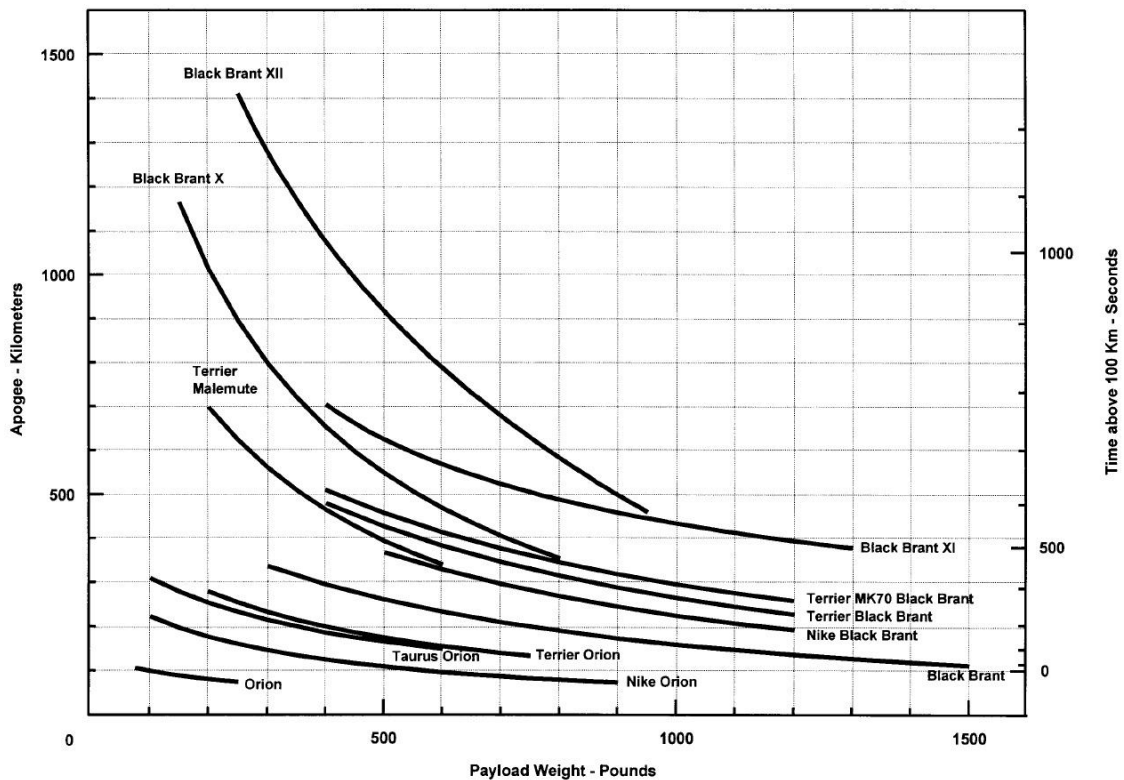
Figure 1.1: Graph illustrating the performance versus payload weight of NASA sounding rockets (NASA, 1999).

Chemical propulsion is the most common type of rocket propulsion method used. A chemical rocket generates thrust by accelerating hot combustion gases through a nozzle. Combustion occurs in an engine chamber through an exothermic chemical reaction between the fuel and oxidiser, and an external source of energy is generally required to initiate the combustion process.

Chemical propulsion can be divided into three categories based on the propellant form. These are: solid, liquid, and hybrid propulsion, shown in Figure 1.2. A solid rocket consists of a premixed fuel and oxidiser which form a heterogeneous or homogeneous solid grain structure dependant on the types of propellants used. This grain is stored in the combustion chamber. In a liquid rocket the fuel and oxidiser are stored in separate tanks, in their liquid states, prior to ignition. These propellants are often cryogenic liquids and are only mixed together in the combustion chamber. In a hybrid rocket the fuel and oxidiser are separated from each other, similar to a liquid rocket, however in different phases (Sutton and Biblarz, 2001).

Both solid and liquid propulsion systems are currently used for commercial sounding rockets, although the solid version dominates. This dissertation investigates the use of hybrid propulsion for a sounding rocket application.

2
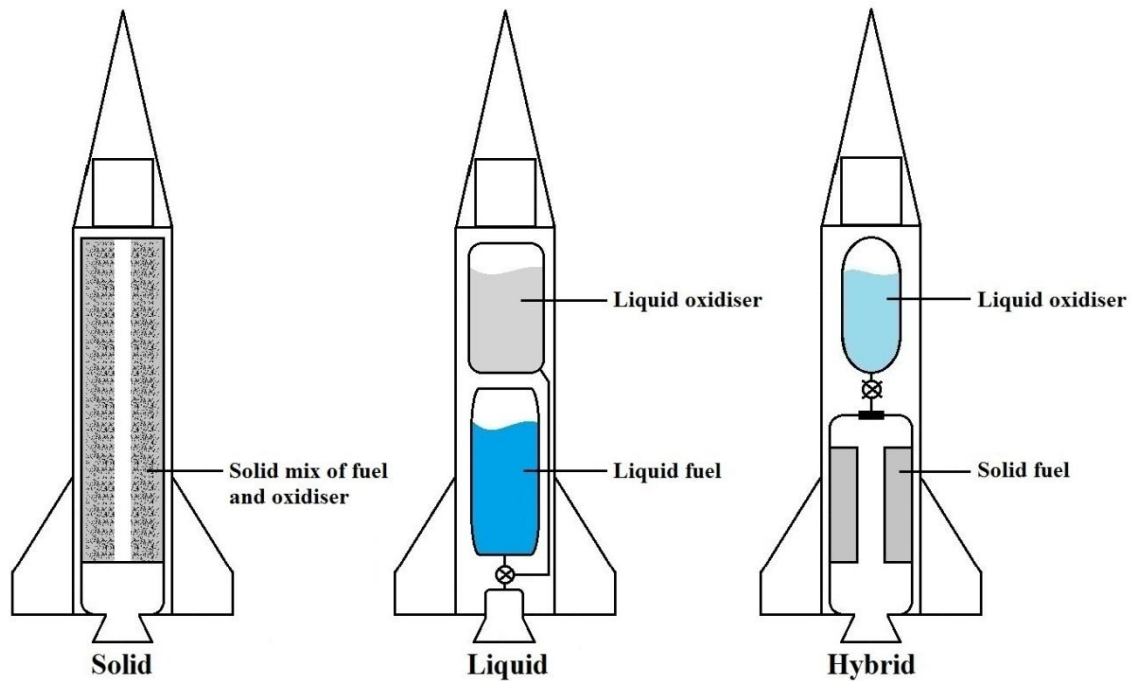
Figure 1.2: Chemical rocket propulsion systems.

There are various hybrid rocket configurations, such as classical, reverse, and tribrid. The classical hybrid configuration is the most common and has a liquid or gaseous oxidiser and a solid fuel grain. The oxidiser is stored in a tank and the combustion chamber houses the fuel grain. The reverse hybrid configuration has a solid oxidiser and a liquid fuel. This configuration however is impractical due to the difficulty in manufacturing solid oxidisers. To mould the oxidiser grains, an inert filler or a small amount of fuel needs to be added. This decreases the performance and raises the risk of explosion. The tribrid configuration has a liquid oxidiser and liquid fuel that mix together with a solid fuel in the combustion chamber. This gives the highest specific impulse and combustion temperatures but is more complex than the other configurations (Chiaverini and Kuo, 2007).

When comparing hybrid propulsion systems to conventional solid and liquid systems, the hybrid version is deemed safer. This is because the fuel and oxidiser are stored separately and in different phases, making the system less explosive. Hybrid rocket fuel is inert which means it can be easily stored, transported, and handled. Solid rocket propellants are hazardous because the oxidiser and fuel are mixed together to form an explosive grain cartridge. Hybrid propulsion systems are relatively inexpensive due to lower manufacturing and operational costs associated with simpler propellant storage, transportation, and handling (Sutton and Biblarz, 2001). They can be easily throttled or shut-down by adjusting the oxidiser flow rate, with less plumbing required than for a liquid system. They are also more reliable than liquid systems since they have less plumbing and are less complex. A solid rocket has no plumbing and therefore cannot

be throttled, restarted, or shut-down. In an emergency the hybrid rocket can be shut-down immediately while a solid rocket motor would have to be damaged or destroyed to terminate its flight.

A further advantage of hybrid systems is propellant versatility; a greater range of fuel-to-oxidiser combinations can be used. Metal additives can be mixed into the solid fuel grain to increase performance. Small fuel grain cracks do not have as disastrous effects in hybrid systems, as they do in solid systems. This is because the burning of the fuel only occurs in the port where the oxidiser flow meets the grain, meaning that grain robustness is not as important (Chiaverini and Kuo, 2007). Certain hybrid rocket propellant combinations produce combustion gases that are more environmentally friendly than liquid and solid propellant gases.

The main disadvantage of a hybrid propulsion system is its low fuel regression rate. This requires a larger fuel grain surface area in order to produce the desired thrust and is normally achieved by using a multiport grain design. Figure 1.3 illustrates a 6 port fuel grain configuration on the right and a single port fuel grain configuration on the left. Other multiport fuel grain configurations include double-D, double row, and wagon wheel profiles (Humble et al., 1995). Multiport fuel grain designs often result in large amounts of unburnt fuel, uneven burning in the fuel ports, complex grain fabrication methods, and structural integrity issues (Karabeyoglu et al., 2001).
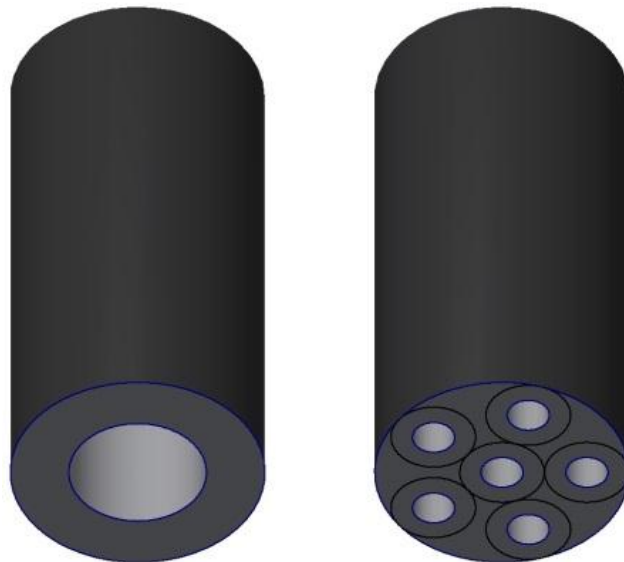
Figure 1.3: Single port fuel grain (left) and multi-port fuel grain (right) configurations.

Another disadvantage of a hybrid system is the shift in oxidiser-to-fuel ratio (O/F) that occurs throughout the burn time of the motor, as the fuel grain port diameter increases. This results in a

lower theoretical performance (Van Pelt et al., 2004). Hybrid rockets also have slow ignition and thrust throttling transients. Certain hybrid rocket propellant combinations have low density impulses. Density impulse refers to the impulse of the vehicle per unit of volume of propellant and therefore a lower density impulse requires a larger propellant volume. This results in bulkier propellant tanks and larger overall vehicle configurations. Lower combustion efficiencies are expected in hybrid rockets when compared to solid or liquid rockets since there is imperfect oxidiser and fuel mixing. This is because of the large diffusion flame above the fuel grain surface (Chiaverini and Kuo, 2007).

The advantages of hybrid rockets as well as the recent discovery of high regression rate fuels (discussed in detail in Chapter 2) have led to a global increase in hybrid propulsion research for sounding rocket applications. South Africa presently has no local sounding rocket programme even though the country is involved in space-related projects such as SunSat, SumbandilaSat, the Square Kilometre Array project and CubeSat production. South Africa relies on international space agencies for the provision of launch services to carry their payloads leading to logistical problems and high costs that limit the growth of indigenous research in this area.

In 2010, the Aerospace Systems Research Group (ASReG) of the Discipline of Mechanical Engineering, based at the University of KwaZulu-Natal (UKZN), formed the Phoenix Hybrid Sounding Rocket Programme in order to fill the void in local sounding rocket capabilities (Brooks et al., 2010). The programme's objectives are to develop a number of low-cost commercially available sub-orbital hybrid sounding rockets for use by the African scientific community, to increase the domestic research capacity in aerospace technology and to develop human capital in propulsion engineering. Hybrid technology was selected by the programme mainly due to safety considerations and lower cost than solid and liquid rockets. The first phase of the programme included the development of Phoenix-1A, a hybrid rocket demonstrator capable of delivering a 1 kg payload to an altitude of 10 km. Phoenix-2A is part of the second phase of the programme and is a hybrid sounding rocket capable of reaching 100 km with a 5 kg payload. Previous accomplishments in the UKZN Phoenix Hybrid Sounding Rocket Programme include:

1. The design, development, and testing of two laboratory-scale (lab-scale) motors
2. The design, development, and testing of a portable lab-scale test stand
3. Development of the HYROPS software
4. Design and development of Phoenix-1A
5. Cold-flow and hot-fire testing of the Phoenix-1A flight motor
6. Design and development of a mobile launch platform for Phoenix-1A

The aim of this dissertation is to conduct various parametric trade studies (or trade-off studies) to improve the design of a large-scale hybrid sounding rocket. The Phoenix-2A vehicle must have a target apogee of 100 km and a payload of 5 kg, be safe, be reusable, and be feasible in terms of South African manufacture. Performance modelling on the propulsion and aerodynamic systems is investigated to determine the best parameter range for designing large-scale hybrid rockets. Modelling is performed using the in-house Hybrid Rocket Performance Simulator (HYROPS) software developed by Geneviève (2013) and Chowdhury (2012).

This study contributes to a better understanding of hybrid rocket technology and airframe design. Building on the work of Geneviève (2013) and Chowdhury (2012), it acts as a foundation for the development of large-scale sounding rockets and sub-orbital launch vehicles in South Africa. The research also aims to increase expertise in the local space industry and remove technological obstacles to the development of an indigenous sounding rocket launch service (Pitot de la Beaujardiere et al., 2010).

Chapter 2 gives an overview of the history of sounding rockets and hybrid rocket propulsion. Existing hybrid programmes are discussed in terms of worldwide research. A classification of hybrid combustion theory is provided, followed by an outline of the possible combustion instabilities that can occur in hybrid rocket motors. Finally, current available rocket flight simulation software packages are evaluated, including the UKZN-developed HYROPS software.

Chapter 3 focuses on the development of a design methodology for the Phoenix-2A rocket which incorporates the use of the HYROPS software; a decision based on an investigation of existing methods. This is followed by an in-depth review of the HYROPS software and its sub-models. The chapter concludes with validation simulations of commercially available sub-orbital sounding rockets to verify the use of HYROPS for the design of Phoenix-2A.

Chapter 4 provides the concept generation of the Phoenix-2A rocket resulting in the selection of the rocket's configuration and propellants. The design assumptions used to develop the initial concept of Phoenix-2A are detailed. Propellant mass fraction and combustion efficiency trade studies are investigated in this chapter, illustrating their effect on performance.

Chapter 5 details the trade studies of the hybrid rocket propulsion system and aerodynamic geometries. The methodology used to analyse each parameter is discussed and this is followed by the simulation results obtained from HYROPS. The propulsion variables investigated are design chamber pressure, O/F ratio, nozzle design altitude, ullage volume, fuel grain geometry

and thrust. The aerodynamic parameters investigated are the nose cone, fin and fuselage geometry. Results from these trade studies are used to develop the final Phoenix-2A design. The chapter concludes with a comparison of the final vehicle using pure paraffin wax to a design utilising an aluminised paraffin wax fuel grain.

Chapter 6 summarises the dissertation with concluding remarks and identifies potential areas of future work with regard to the design and manufacture of Phoenix-2A.

CHAPTER 2

Literature Review

2.1 Development of Sounding Rockets

The first rockets were propelled by gunpowder and launched in China in the 13th century (Sutton and Biblarz, 2001) where they were used as fireworks and as weapons in battle. It was not until the late 19th century that they were used for scientific research. The replacement of warheads on military rockets such as the German liquid propelled V2 led to the development of sounding rockets. The Russian mathematician Konstantin Tsiolkowski and the German physicist Hermann Oberth, proved that leaving the earth was feasible and promoted the idea of sounding rockets (Seibert, 2006).

Robert Goddard, an American physicist, carried out the earliest recorded successful liquid propelled rocket experiment in 1926. Liquid propellant rockets gained popularity due to their stop and restart functions which are not possible in solid rockets. National space societies were formed in France, Germany, the USA, the Union of Soviet Socialist Republics (USSR), and the United Kingdom (UK), where experimental testing was performed (Seibert, 2006). The WAC Corporal was designed to be the first rocket built primarily for scientific atmospheric research and was successfully launched in 1945 with an 11 kg payload to an altitude of 64 km (Corliss, 1971).

2.1.1   Sounding Rocket Review

There are a number of space agencies worldwide which have research divisions dedicated to sounding rocket programmes such as NASA, the Korea Aerospace Research Institute (KARI), and the European Space Agency (ESA). Table 2.1 illustrates a number of well-known sounding rockets that have been developed around the world and provides key features such as geometry, mass, and apogee. The American Aerobee and Viking rockets shown in Table 2.1 were used after the V2 rockets became unavailable.

Table 2.1: Sounding rockets from around the world (Wade, 2013).

Country	Rocket	Propulsion System	Stages	Apogee (km)	Payload Mass (kg)	Geometry	
						Length (m)	Diameter (m)
America	Aerobee 150A	Solid & liquid	2	188	90.7	9.30	0.38
	Arcas	Solid	1	52	4.5	2.30	0.11
	Viking	Liquid	1	200	230.0	14.90	0.81
Canada	Black Brant I	Solid	1	225	68.0	7.41	0.26
	Black Brant VIII	Solid	2	430	136.0	11.90	0.44
	Black Brant XII	Solid	4	1500	136.0	17.00	0.76
France	Belier II	Solid	1	130	30.0	5.90	0.31
	Centaure	Solid	2	140	60.0	6.02	0.28
	Dragon 1	Solid	2	475	60.0	7.10	0.56
Korea	KSR-I	Solid	1	75	150.0	6.70	0.42
	KSR-II	Solid	2	160	1500	11.04	0.42
	KSR-III	Liquid	1	80	150.0	9.60	1.00

Many private and academic institutions have formed sounding rocket programmes to develop human capital in their respective countries and to promote careers in aerospace. CaNoRock is a Canadian and Norwegian student sounding rocket programme which educates students in the field of atmospheric research, flight dynamics, and propulsion (Miles, 2012). The Physics and Astronomy Department at Johns Hopkins University initiated a sounding rocket programme in 1961 which has successfully launched numerous payloads on the Aerobee and Terrier-Black Brant rockets (Johns Hopkins University, 2004).

Engineering students from the Vellore Institute of Technology in India developed the Rohini-200 sounding rocket with the assistance of the Indian Space Research Organisation (ISRO) in 2010. This project demonstrates the importance of collaboration between universities and space agencies for the transfer of knowledge to younger generations (The Hindu, 2010). Sounding rockets that are commercially available are either liquid or solid propelled, creating a niche for hybrid sounding rockets where their advantages may be exploited.

2.1.2   Hybrid Rocket Review

Hybrid propulsion has not seen the same advancement over the last century that solid and liquid rockets have but has the potential to be used for various applications. These include strap-on and large launch boosters, sounding rockets, and space engine propulsion systems that require throttling and propellant flexibility (Chiaverini and Kuo, 2007).

The earliest report of a hybrid rocket was made in 1933 by Sergei Korolev and Mikhail Tikhonravov (Altman, 1991) who reported a flight of the GIRD-09 rocket which achieved an apogee of 1.5 km. The earliest documented use of hybrid propulsion in sounding rockets was made in the 1960s by the Office National d'Études et de Recherches Aérospatiales (ONERA) in France, and Volvo-Flygmotor in Sweden. The French rockets used a mixture of solid amine fuel and liquid nitric acid and the Swedish rockets used Tagaform and liquid nitric acid.

Many companies in the 1980s to 1990s were involved in developing and testing large-scale liquid oxygen (LOX) and hydroxyl-terminated polybutadiene (HTPB) hybrid rocket motors. These companies include AMROC, NASA, Lockheed Martin and Thiokol. The motors had thrusts of up to 1100 kN but flight testing was generally unsuccessful due to the liquid oxygen freezing the oxidiser valve. Lockheed Martin and NASA collaborated in 1999 to form the Hybrid Sounding Rocket (HYSR) Project resulting in the successful launch of a multiport LOX/HTPB hybrid sounding rocket in 2002. The target apogee was to 100 km with a design thrust value of 267 kN, however the rocket only reached 70 km as a result of the low regression rate and failure of the grain structure (Arves et al., 2003).

The development of liquefying fuels such as paraffin wax was made in the 1990s by Karabeyoglu, Altman, Cantwell, and Zilliac (Karabeyoglu et al., 2002). These fuels have regression rates three to four times higher than that of conventional solid fuels. This discovery has led to a recent increase in hybrid research. Past failures related to inefficient or complex grain configurations, and low regression rates, can now be reduced or eliminated (Dyer et al., 2007).

Stanford University formed the Stanford Propulsion and Space Exploration (SPaSE) Group which has conducted various experimental investigations on hybrid rocket motors and launched numerous small-scale hybrid rockets. A collaboration between Stanford University, NASA Ames Research Centre, the Space Propulsion Group (SPG) and NASA Wallops led to the formation of the Peregrine Sounding Rocket Program in 2006 (Dyer et al., 2007). The goal was to design, develop, test, and launch a 100 km nitrous oxide (N_2O) and SP1x01 paraffin wax

hybrid sounding rocket to show the feasibility of hybrid technology in a large-scale application with liquefying fuels.

University research into hybrid rockets in South Africa began in 2010 with the formation of the Phoenix Hybrid Sounding Rocket Programme under ASReG at UKZN (Brooks et al., 2010). As of 2010 the programme has successfully hot fire tested two lab-scale motors of approximately 500 N as well as the Phoenix-1A flight motor. The programme has also developed a multi-purpose trailer that can be used as a portable test stand and launch platform for vehicles similar in size to Phoenix-1A.

Stratos II is a project run by students at the Delft University of Technology under the Delft Aerospace Rocket Engineering (DARE) programme. It is a hybrid vehicle capable of reaching an apogee of 50 km using nitrous oxide as the oxidiser and a sorbitol paraffin wax mixture with aluminium additives as the fuel (Knop et al., 2013). Many other universities world-wide are researching hybrid rocket propulsion. The Pennsylvania State University focuses on regression rate and combustion studies. Purdue University is conducting research into hybrid rockets that can reach altitudes of over 100 km (Tsohas et al., 2009) and the University of Colorado has formed a multi-disciplinary programme (MaCH-SR1) with the goal of developing sub-orbital hybrid rockets (Kanner et al., 2007).

Hybrid propulsion is playing a central role in the development of sub-orbital vehicles for the growing space tourism sector in the United States. It is emerging as a popular choice for manned spacecraft due to its safety and throttling capability. The 2004 Ansari X Prize winner, SpaceShipOne has a N_2O/HTPB hybrid rocket motor and has successfully flown humans to 100 km. Built by Scaled Composites, the vehicle is designed to safely carry a pilot and two passengers to and from space (Calabro, 2011). Virgin Galactic's SpaceShipTwo is an air launched sub-orbital space plane designed to carry up to six passengers and two pilots to an apogee of 110 km using a larger N_2O/HTPB hybrid rocket motor (Virgin Galactic, 2013).

The Sierra Nevada Corporation (2013) is developing the DreamChaser which is designed to fly crew members and cargo to orbital and sub-orbital altitudes, as well as transport astronauts back and forth to the International Space Station. The vehicle is designed to use two N_2O/HTPB hybrid rocket motors to provide on-orbit propulsion capable of producing approximately 445 kN of thrust. Copenhagen Suborbitals is another example of a private organisation intending to use hybrid rockets to transport humans to space (Copenhagen Suborbitals, 2013).

2.2 Hybrid Rocket Propulsion Theory

The functionality of a standard hybrid rocket motor and its associated combustion process are key aspects to understanding hybrid propulsion theory. Grain regression rate theory can be classified as either classical or non-classical, and is detailed in this chapter. Hybrid rockets are also susceptible to combustion instabilities that may affect the performance of the motor. These must be identified so that necessary prevention methods can be incorporated into the design process.

2.2.1   Classical Hybrid Rocket Configuration

A hybrid rocket generally consists of a nose cone, a payload, a recovery system, a pressurant system, an oxidiser tank, a combustion chamber, the fuselage, a feed system, an injector, a nozzle, and fins. The design is inherently safe as propellants are kept separately and in different phases, meaning that the risk of unintended ignition is reduced. The system operates by injecting oxidiser from an oxidiser tank into the combustion chamber via the feed system and injector. The oxidiser can be fed through the plumbing system either by its own self-pressurising properties, a pump assembly, or a pressurant tank system as indicated in Figure 2.1.
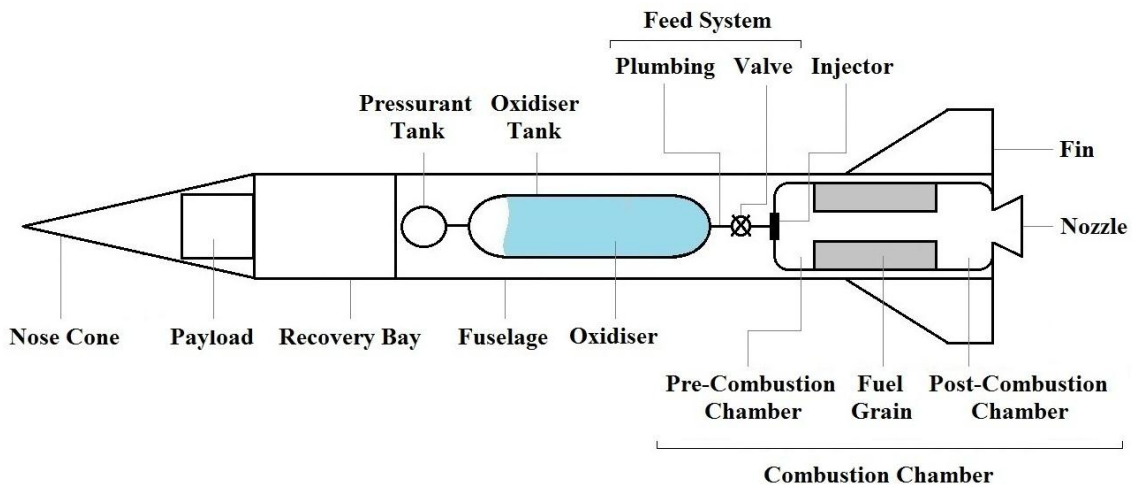
Figure 2.1: A classical hybrid rocket configuration.

Self-pressurising oxidisers, of which nitrous oxide is an example, are commonly used in hybrid systems and maintain the working pressure of the supply tank above that of the combustion chamber. An inert pressurant gas such as helium or nitrogen can be added to further increase the working pressure of the tank. This process is called supercharging. Using a self-pressurising oxidiser is simple, cost-effective, and can be referred to as a blowdown system. A turbine-

driven pump assembly can also be used in the feed system between the combustion chamber and oxidiser tank. This is a complex system used mainly in large-scale rockets to assist in minimising the mass of oxidiser tanks with low working pressure. A third possibility is the use of a separate tank for a pressurant gas which is connected to the oxidiser tank.

With all hybrid propulsion systems the mass flow of the oxidiser can be controlled in the feed system by the use of a valve allowing throttling and stop-restart capabilities. The motor may include a pre- and post-combustion chamber in the fore and aft end respectively for improved atomisation and gas mixing during combustion.

2.2.2   Combustion Process

The combustion process of a hybrid rocket starts with the firing of the igniters. Heat begins to melt the surface layer of the exposed solid fuel after which a valve is opened to admit oxidiser through the injector and into the combustion chamber. The heat from the igniters also decomposes the injected oxidiser. The propellants burn together creating a turbulent boundary layer on the surface of the fuel grain, as shown in Figure 2.2.
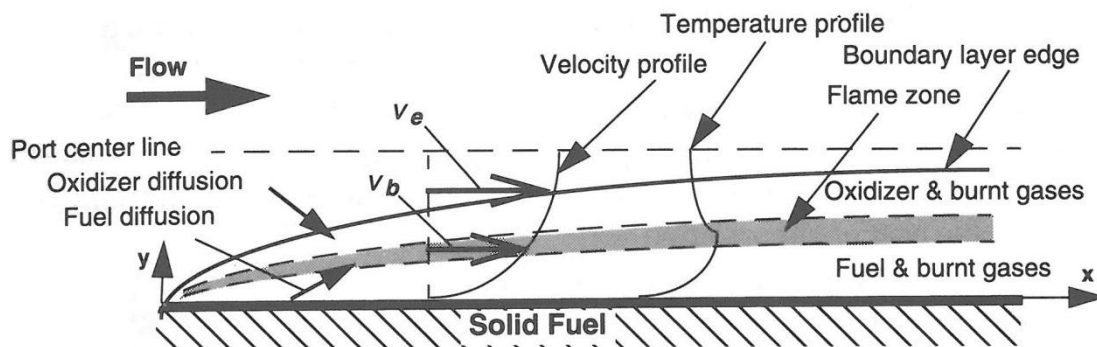
Figure 2.2: Combustion process above the fuel grain surface of a hybrid rocket (Humble et al., 1995).

The flame zone is the area inside the boundary layer that contains both vapourised fuel and oxidiser. Its thickness depends on the rate at which oxidisation occurs. Fuel-rich and oxidiser-rich zones appear below and above the flame zone respectively. The vapourised fuel travels up to the flame zone via convection and the oxidiser is supplied to the flame zone by flow turbulence and diffusion. After ignition the combustion process is self-sustaining until either the fuel or oxidiser is finished. This is due to the oxidiser and fuel continuously reacting with each other in the diffusion flame zone within the boundary layer - referred to as the classical diffusion flame theory (Humble et al., 1995).

Classical Fuel Theory

A hybrid motor's regression rate limiting mechanisms are either the heat transfer (convection and radiation) from the diffusion-limited flame or the interaction of gas and solid phase reactions (Marxman et al., 1964). Generally, a classical non-metallised hybrid rocket motor is based on the classical diffusion theory and operates within the region where convective heat transfer dominates. In this region the regression rate is only dependent on the total mass flux and is not affected by changes in chamber pressure as in solid rocket motors. The combustion process is dominated by the chemical reaction kinetics if the oxidiser mass flux becomes significantly high (metallised fuels) or by radiation superseding convection when the oxidiser mass flux is low. These regions are sensitive to changes in chamber pressure. Figure 2.3 illustrates this phenomenon (Humble et al., 1995).
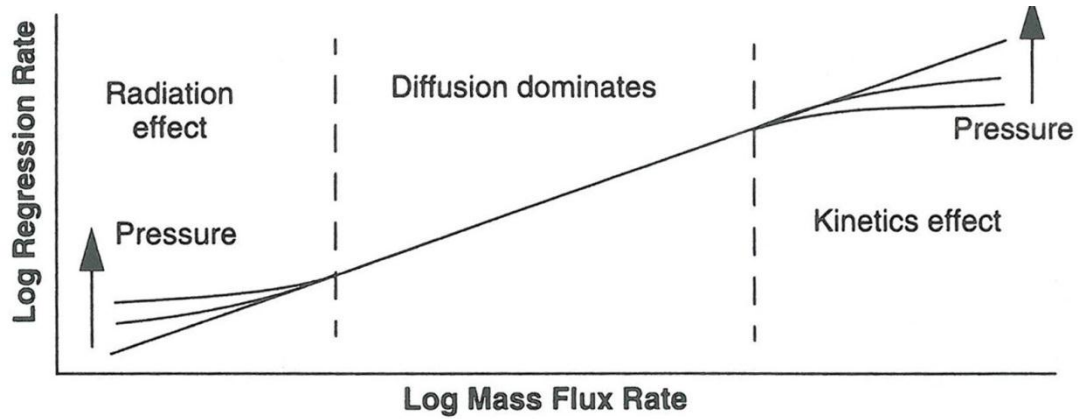
Figure 2.3: Graph illustrating the effects of chamber pressure on the regression rate
(Humble et al., 1995).

The instantaneous regression rate, $\dot{r}$, shown in Equation 2.1, can be empirically derived by investigating the energy balance at the surface of the fuel grain based on the classical diffusion-limited theory (Sutton and Biblarz, 2001):

$$\dot{r}_{classical} = 0.036\left(G^{0.8}/\rho_f\right)(\mu/x)^{0.2}B^{0.23} \qquad (2.1)$$

where G is the total mass flux ($G = G_{ox}+G_f$), ρ_f is the solid fuel density, μ is the combustion gas viscosity, x is the axial distance from the fuel grain's front edge, and B is the blowing coefficient (non-dimensional fuel mass flux). The blowing parameter is inversely proportional to the amount of energy required to change the fuel into gas (Karabeyoglu, 1998). This equation shows that the regression rate for a hybrid rocket limited by diffusion is not affected by chamber pressure but is primarily dependant on the total mass flux.

14

Equation 2.1 can be simplified by incorporating the fuel density, combustion gas viscosity, and blowing coefficient into a ballistic coefficient term, a. The regression rate exponents, n and m, are found empirically and dependant on the fluid dynamics. Equation 2.2 is a reasonably accurate semi-empirical formula for the regression rate of a general hybrid rocket motor:

$$\dot{r} = aG^n x^m \tag{2.2}$$

The above equation can be further simplified into Equation 2.3 which is more commonly used:

$$\dot{r} = aG_{ox}^n \tag{2.3}$$

The oxidiser mass flux, G_{ox}, can be explicitly determined because the mass flow rate and port area of the grain are known inputs ($G_{ox} = \dot{m}_{ox}/A_p$). The total mass flux is replaced with the oxidiser mass flux because it is relatively larger than the fuel mass flux and the above equation approximates the regression rate with reasonable accuracy (Humble et al., 1995). The fuel mass flux is not an input design parameter and can be found implicitly. The ballistic coefficient, m, is generally disregarded since the regression rate with respect to the length of the fuel grain can be considered constant.

The regression rate with respect to length is taken as constant due to conflicting effects relative to the axial position. Some effects cause the boundary layer thickness to increase along the length of the grain, which results in a decrease in regression rate, while an increase in total mass flux causes an increase in the regression rate with respect to length (Sutton and Biblarz, 2001). The ballistic coefficient, a, in Equation 2.3 includes the axial distance, x. Both a, and n, are determined experimentally for a specific oxidiser and fuel combination for a particular hybrid rocket motor configuration.

Non-classical Fuel Theory

Karabeyoglu et al. (2002) developed the non-classical regression rate theory from the classical theory. The non-classical approach applies to hybrid fuels that create a liquid layer at the combustion surface of the grain. These include paraffin wax and cryogenic fuels such as solid pentane and methane. During combustion the fuel burns and liquefies, producing a thin liquid layer that has a low viscosity and surface tension. This layer is unstable and causes the liquid surface to break up into droplets. The degree of instability is dependent on the viscosity and surface tension of the fuel. The droplets are transferred from the melt layer into the core flow by convection due to the high velocity stream of gas inside the port. This significantly increases the

fuel mass transfer rate and is known as droplet entrainment, as shown in Figure 2.4 (Chiaverini and Kuo, 2007).
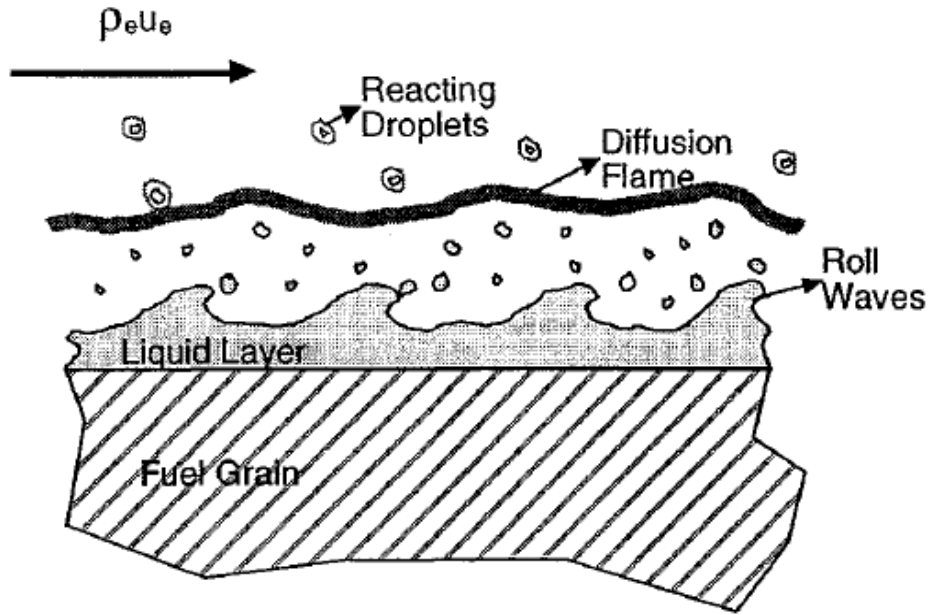
Figure 2.4: Entrainment process of a hybrid rocket fuel grain (Chiaverini and Kuo, 2007).

The non-classical hybrid fuel theory therefore allows a mass transfer mechanism that incorporates both droplet entrainment and the classical theory gasification process. This predicts that the non-classical fuels will have considerably higher regression rates than the classical hybrid fuels. The non-classical regression rate can be defined as the sum of the entrainment regression rate, $\dot{r}_{ent}$, and evaporation regression rate, $\dot{r}_v$, due to droplet entrainment and the classical gasification mass transfer mechanisms respectively:

$$\dot{r} = \dot{r}_{ent} + \dot{r}_v \qquad (2.4)$$

A few adjustments need to be made to the classical hybrid theory (Equation 2.1) due to liquid layer instabilities and entrainment of liquid droplets as defined by Karabeyoglu (1998) and Karabeyoglu et al. (2005). These adjustments are:

1. The entrainment process results in a reduction of energy required for the classical vapourisation process.
2. The blowing coefficient is only dependant on the vapourisation mass transfer mechanism and it is assumed that the liquid droplets are evaporated above the flame zone.

16

3. During entrainment, the waves formed in the liquid layer improve the surface roughness, and therefore the heat transfer from the flame zone to the surface fuel grain.

History has shown that conventional hybrid fuels are typically impractical for large-scale motors due to their low regression rate and complex geometries. Paraffin based wax has been chosen as the fuel for the Phoenix-2A rocket project because it is a liquefying fuel that has a higher regression rate than conventional hybrid fuels. A detailed propellant selection study was conducted and is discussed in Chapter 4. Carbon black is blended into the paraffin wax (discussed in section 4.2.2) and a pre-and post-combustion chamber are used to reduce the amount of unburnt fuel being ejected through the nozzle.

2.2.3 Combustion Instabilities

Hybrid rockets, like solid and liquid rockets, are prone to combustion instabilities due to the transient phases that occur during the operation of the motors. Instabilities arise when the pressure in the motor fluctuates by more than 5% of the expected chamber pressure and there are two types: low frequency (non-acoustic) and high frequency (acoustic) (Chiaverini and Kuo, 2007). These chamber pressure oscillations can be reduced to approximately 2% to 3% of the mean value for a well-designed hybrid motor (Sutton and Biblarz, 2001). Instabilities in hybrid motors are not often severe but it is important to reduce the pressure oscillation amplitude because it causes thrust oscillations that affect the structural integrity of the rocket and payload.

Low frequency instabilities are the most common type in hybrid systems and are categorised according to their driving mechanisms. These may be caused by the coupling between the feed system and combustion chamber, or the breaking off of melted fuel at low regression rates (chuffing), or the source may be unknown. Current theories (Karabeyoglu, 1998) that may explain the unknown driving mechanism unique to hybrid systems are:

1. Lags in atomisation or vapourisation of the liquid oxidiser
2. Mass flux coupling (the regression rate of a hybrid system is generally dependant on the mass flux)
3. Chuffing
4. Chamber pressure coupling when the motor operates at low and high flux conditions
5. Vortex shedding
6. DC shift theory (an abrupt increase in the chamber pressure)
7. Characteristic length (L*) theory

The typical range for low frequency instability is 0-60 Hz. A possible solution for mitigating feed system coupling instability, is to stiffen the feed system by increasing the pressure drop across the injector to prevent backflow from the motor. Liquid rocket motors have a 15% to 20% pressure drop across the injector relative to the chamber pressure, to ensure stability of the motor (Casiano et al., 2009). This general rule was applied in the design of Phoenix-2A.

High frequency or flame holding instabilities display acoustic behaviour and occur in the longitudinal mode only. They are due to the presence of an unstable flame in the boundary layer of the fuel grain. The instability can be alleviated by improving the stability of the combustion in the boundary layer. This can be achieved by introducing a combustible fluid into the fore end of the motor to allow for adequate pre-heating of the oxidiser or by using an axial flow injector configuration. The axial injector creates a recirculation zone of hot gases in the fore end of the motor which preheats the oxidiser, reducing high frequency instability (Boardman et al., 1995). For the design of Phoenix-2A, an axial injector will be employed in preference to a conical injector because it is more efficient at producing the hot gas recirculation zone as shown in Figure 2.5 and therefore exhibits better stability (Sutton and Biblarz, 2001).
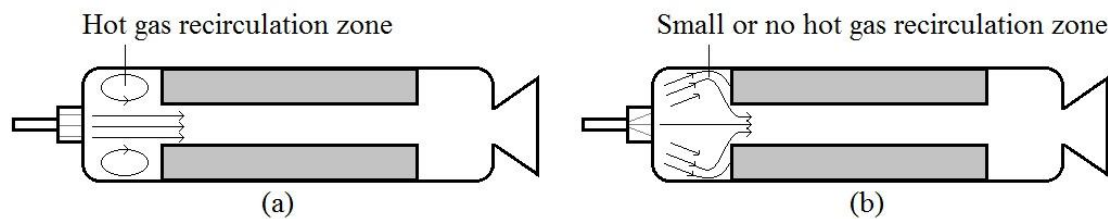
Figure 2.5: (a) Axial injection of oxidiser and (b) Conical injection of oxidiser.

Recent hot-fire tests by Zilliac et al. (2012) on the Peregrine motor have demonstrated flame holding instabilities at the beginning of the burn due to high oxidiser mass flux. Although there is no known mass flux limit for combustion stability, it was found that the motors become unstable for mass fluxes above $650 \, \text{kg/m}^2\text{s}$. The Peregrine motor exhibited chamber pressure oscillations due to the first longitudinal acoustic mode being excited. It is important to dampen these oscillations to prevent excessive fluctuation in chamber pressure. The use of a conical injector can also lead to severe motor failure due to a collection of unreacted nitrous oxide and fuel vapour in the fore end of the motor. When the mixture comes into contact with the flame because of inadequate flame holding, it can cause the motor to explode due to the decomposition of nitrous oxide. This occurred and resulted in a structural failure of the combustion chamber during one of the Peregrine hot-fire tests.

2.3 Rocket Simulation Software Review

The growing interest in model rocketry has led to increased availability of rocket simulation software such as RocketSim, RASAero, and OpenRocket. More advanced rocket modelling software such as Missile DATCOM is used by the military and private rocket companies but public access is restricted.

RocketSim is freeware software for both Windows and Macintosh systems. It allows the user to model a rocket trajectory with a 3 DOF, flat earth model, to altitudes of up to 86 km with a maximum Mach number of 2. A simple wind model can be implemented as well as a dual parachute recovery system. RocketSim uses a simple graphic user interface (GUI) and can model various geometries including clipped delta and free form shaped fins. The upgrade from RocketSim is RocketSim Pro or RS-Pro. The pro version is a commercial product available for sale to US citizens only. It is a multi-platform sub-orbital 6 DOF flight dynamics simulator with a rotating elliptical earth model. It can model the splash-down pattern of a rocket for various uncertainties. Other functions include modelling a dual parachute recovery system, and various launch and wind parameters. The user can export the trajectory data into Google Earth. RocketSim Pro can analyse rocket trajectories up to 632 km above sea level with a maximum Mach number of 10. The fins may have various cant angles to induce spin on the rocket (Apogee Rockets, 2013).

The freeware software RASAero (Rocket Aerodynamic Analysis and Flight Simulation Software) analyses the flight trajectory and aerodynamic characteristics of a rocket. The flight simulation can either be a 1, 2, or 3 DOF trajectory with parachute recovery and wind modelling. The aerodynamic analysis provides aerodynamic coefficients for various Mach numbers and angles of attack (Rogers and Cooper, 2008).

OpenRocket is an open-source multi-platform 6 DOF simulator that has an optimised and multi-stage design function. It has a GUI that displays the trajectory with respect to time throughout the flight and has the ability to model recovery systems, wind and canted fin (Niskanen, 2009).

The South African company MARCOM Aeronautics and Space (Pty) Ltd. has developed an in-house programme called LaunchSIM. This 6 DOF flight dynamics software can simulate a multi-stage vehicle and models wind, turbulence, and gravity (Marcom, 2012). Other available programmes include the 1 DOF Rocket Altitude Simulation Programme for Windows (wRASP), SpaceCAD, JSBSim, and WinRoc.

Missile DATCOM is an ITAR restricted software and therefore user-limited. It can be used to predict the aerodynamic characteristics of the preliminary design of a missile with Mach numbers below 20, and up to 9 fin sets (Blake, 2011).

The Research and Technology Division of the American Air Force Flight Dynamics Laboratory has developed the Six Degree-of-Freedom Flight-Path Generalized Computer Program (Brown et al., 1964). This uses a non-spherical rotating earth and atmospheric model and allows the user to select between 2 DOF and 6 DOF. It can model the effects of wind and vehicle spin as well as a vehicle with thrust vector control and autopilot. It has the ability to analyse uncertainties such as thrust misalignment, and a trajectory obtained from flight testing can be used to determine the corresponding aerodynamic characteristics. The software uses generalised equations of motion to allow for modelling of a wide variety of vehicles.

This brief survey of rocket simulation software illustrates that there are readily available and cost-effective choices but that they are limited in apogee, Mach number, DOF, and simulation parameters. ASReG has developed a programme called HYROPS (Chowdhury, 2012; Geneviève, 2013) which consists of a Hybrid Rocket Performance Code (HRPC) and a 6 DOF Flight Dynamics Simulator.

The MATLAB-based HRPC is integrated with NASA CEA and used to design a hybrid rocket motor and determine its performance. It outputs time-dependent motor variables such as regression rate, chamber pressure and thrust.

The Microsoft Visual C++ coded 6 DOF Flight Dynamics Simulator is able to model the trajectory of a rocket with up to four stages under various input launch parameters. These parameters include initial altitude and velocity, launch angle, rail length, and azimuth. It can model a 3D wind profile with turbulence and jet streams. The Monte Carlo function analyses various uncertainties for a number of generated runs, and has a built-in optimisation feature based on algebraic equations. This optimisation feature can only be used with the aerodynamic tool within the programme. This simulator has no restriction on apogee and the Mach number is limited to 5 but can be increased to a maximum of 10.

The optimisation feature of the Flight Dynamics Simulator was not used in this dissertation. This was because the HRPC has not yet been integrated with the software, and the aerodynamic modelling within the programme is inadequate to determine the location of the centre of pressure and transonic aerodynamic coefficients (Chowdhury, 2012). In this study, HYROPS and RASAero are used for modelling the Phoenix-2A rocket. These programmes require no

financial outlay, and meet the simulation requirements of Phoenix-2A such as a 100 km apogee and supersonic Mach numbers. At the time of writing, the author was not aware of any commercially available hybrid rocket motor performance software, thus the HRPC was selected for performance modelling and design of the Phoenix-2A motor.

CHAPTER 3

Design Approach

An overview of existing methods used in the aerospace industry was undertaken and used to formulate a design procedure for Phoenix-2A, based on the UKZN HYROPS software. A detailed review of the Hybrid Rocket Performance Code (HRPC) and Flight Dynamics Simulator is provided. The HYROPS software is validated against existing literature to ensure that it can be used with confidence in the present work. The software is, at the time of writing, still awaiting flight validation from a planned Phoenix-1A launch.

3.1 Review of Existing Design Methods

Sutton and Biblarz (2001) state that 'although there are some common elements in the design of all solid propellant rocket motors, there is no, single, well-defined procedure'. The same can be said for a hybrid rocket. The chosen method depends on the rocket's mission, and available background information and resources such as rocket modelling software. Existing data from similar missions can be used to shorten the lead time of the vehicle. Existing processes that were used to develop the hybrid design methodology in this study are discussed in the following paragraphs.

3.1.1   Rocket Life cycle Method

Brown (2002) describes the life cycle of a space vehicle, based on NASA practice. The cycle is divided into five phases, A to E, as shown in Figure 3.1. Phase A and B involve analysing the mission requirements, formulating concepts, and performing trade studies to lead to a Preliminary Design Review (PDR). A detailed design of the vehicle with full production drawings is completed in Phase C. The components undergo computational analysis and are modified until a satisfactory design is reached. Phase D overlaps Phase C as manufacturing and testing of certain sub-system components are necessary to ensure that the required performance is achieved. Design changes are expected to occur during the testing phase; flexibility is therefore allowed for all of the life cycle phases, enabling the vehicle to be continuously developed and improved. Manufacture, assembly, and testing of components occurs in Phase D. The vehicle is reviewed for flight and modified until it has passed the Flight Readiness Review (FRR). Launch operations are then set up and the vehicle is prepared for launch. Phase E

22

involves the operation of the vehicle after launch, and data capturing until end of mission (EOM).
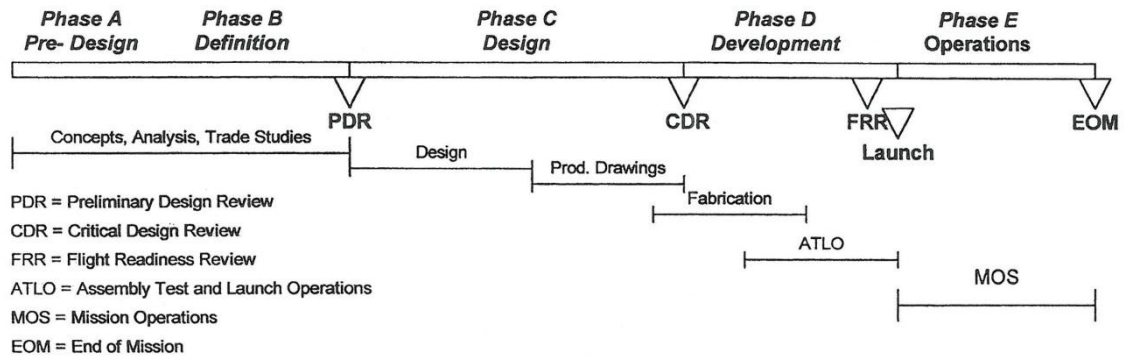
Figure 3.1: The life cycle of a vehicle for space application (Brown, 2002).

Figure 3.2 illustrates the key aspects and iterative loops in a rocket design process. The initial step is to use the mission statement in the concept selection to determine the requirements and constraints. The requirements and constraints are used to develop conceptual ideas which, along with trade studies, are used to obtain a successful initial preliminary design. This demonstrates flexibility which is essential due to the iterative nature of the preliminary design block. The trade studies are used to optimise the initial design and quantify the effect of each parameter on performance, as well as to reduce design time and cost.
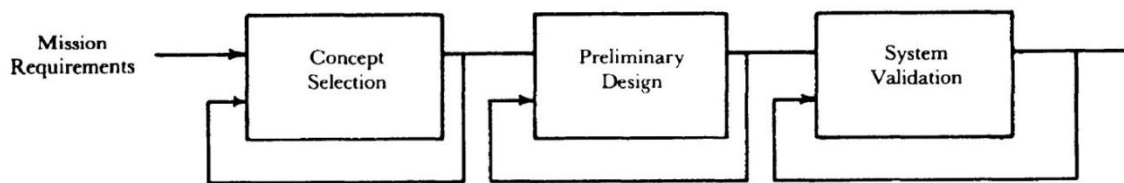
Figure 3.2: Simplified design process of a rocket (US Army Missile Command, 1990).

Developed models and manufactured prototypes of components, systems, and sub-systems, as well as hardware developments, are tested in the system validation process. This process verifies that they are able to provide the desired performance and pass physical inspection and testing. Scale models and prototypes are used to reduce the costs of conducting experiments on components. The iterative loop allows for changes in the design until each component, system, and sub-system has met the desired requirements. CAD drawings along with the design specifications are used in the development of the full-scale rocket that undergoes extensive system validation. System integration is maintained throughout the entire design phase as it is important to ensure that the components are compatible.

3.1.2   Preliminary Design Method

Humble et al. (1995) proposes that the preliminary vehicle design phase feeds from the conceptual phase along with trade studies until a final baseline design is achieved (Figures 3.3 and 3.4). Existing data on the preliminary design methods of solid and liquid propelled rockets were examined and adapted to develop the hybrid rocket procedure used in this dissertation.
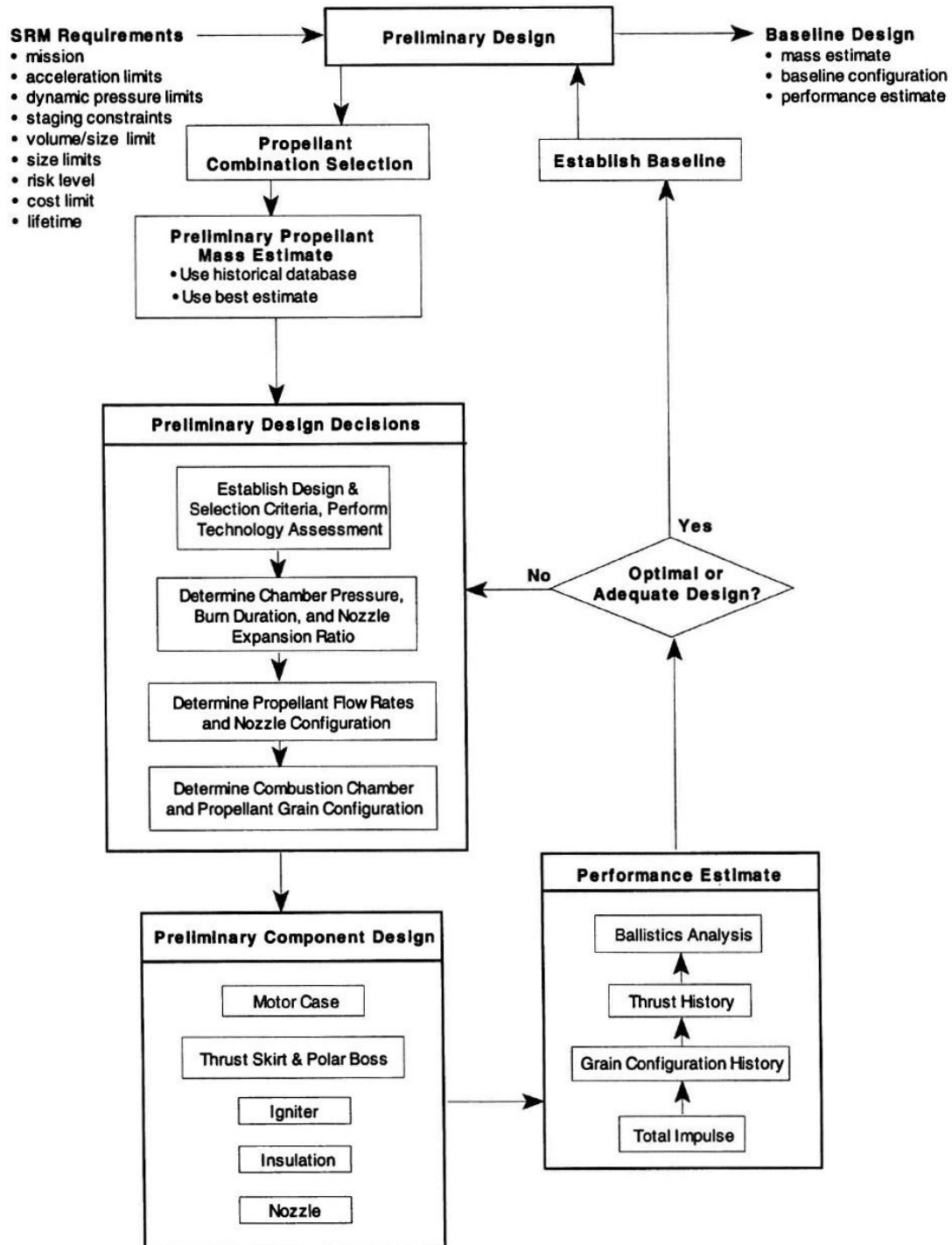
Figure 3.3: Flow chart of a solid rocket preliminary design process (Humble et al., 1995).

The flow sequence for solid and liquid rockets dictates that the mission requirements and constraints are used to develop a preliminary design, which is modified until a satisfactory baseline design is developed. The iterative loop starts with determining the propulsion design conditions. These conditions are used to design and size the major components of the rocket such as the nozzle, motor or tank. The performance of the rocket can then be modelled, and if the vehicle achieves the mission's requirements the baseline design is formulated. If not, the iterative process is repeated.
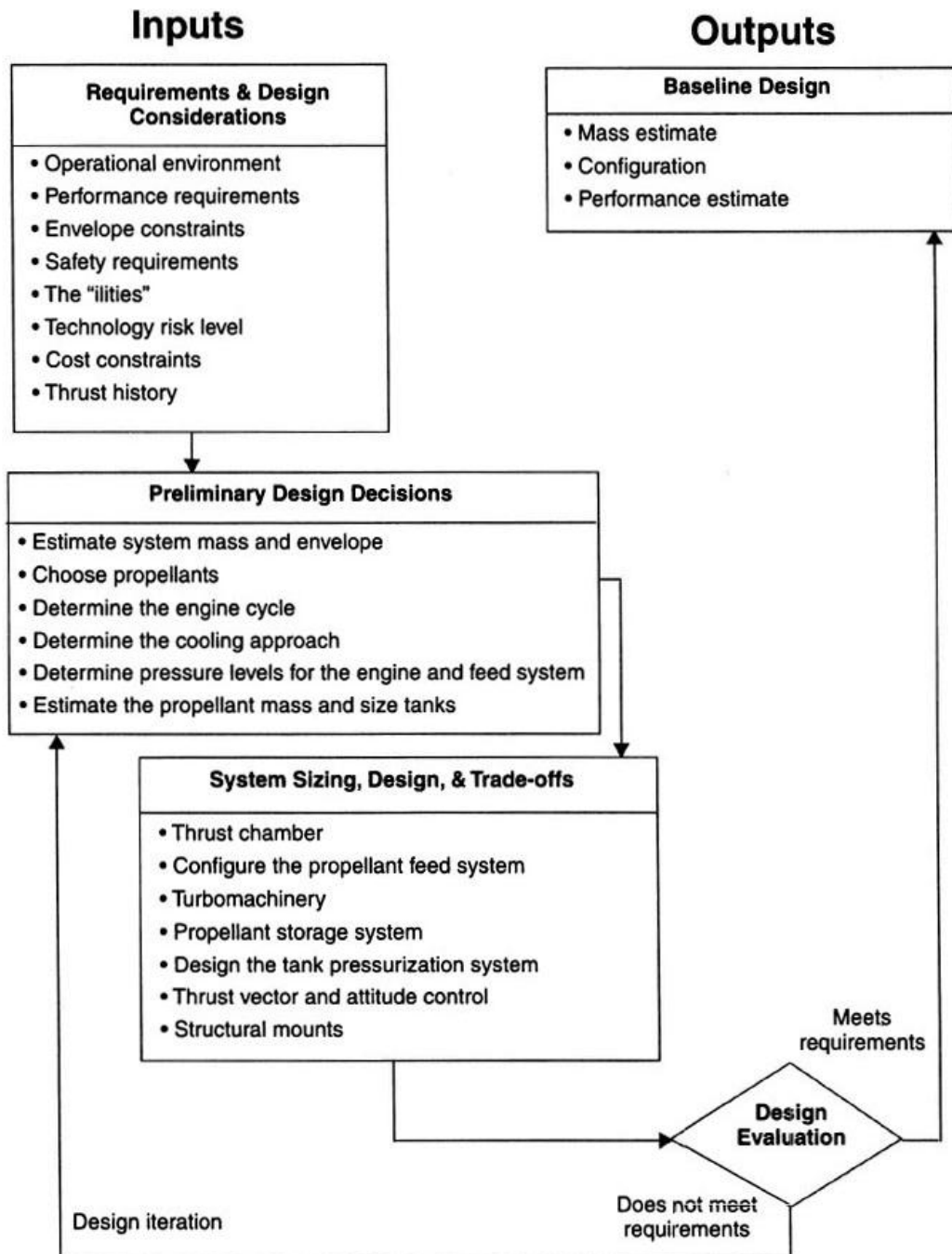
Figure 3.4: Flow chart of a liquid rocket preliminary design process (Humble et al., 1995).

3.1.3   Structural Design Method

Comprehensive structural design is vital to obtain a safe and reliable vehicle. Figure 3.5 shows the structural analysis of an unguided rocket, indicating key design aspects such as material selection, structural layout, mass allocation, as well as the stress, dynamic, and thermal analyses that must be considered. During the preliminary phase the major components are sized according to simplified structural analyses that undergo further computational investigation. Finite Element Analysis (FEA) and Computational Fluid Dynamics (CFD) are necessary before the components are manufactured. This ensures the structural integrity of the components using predicated loads from available flight software. If the design is found to be unacceptable it is modified and re-analysed until the design requirements are met and complete production CAD drawings can be made.
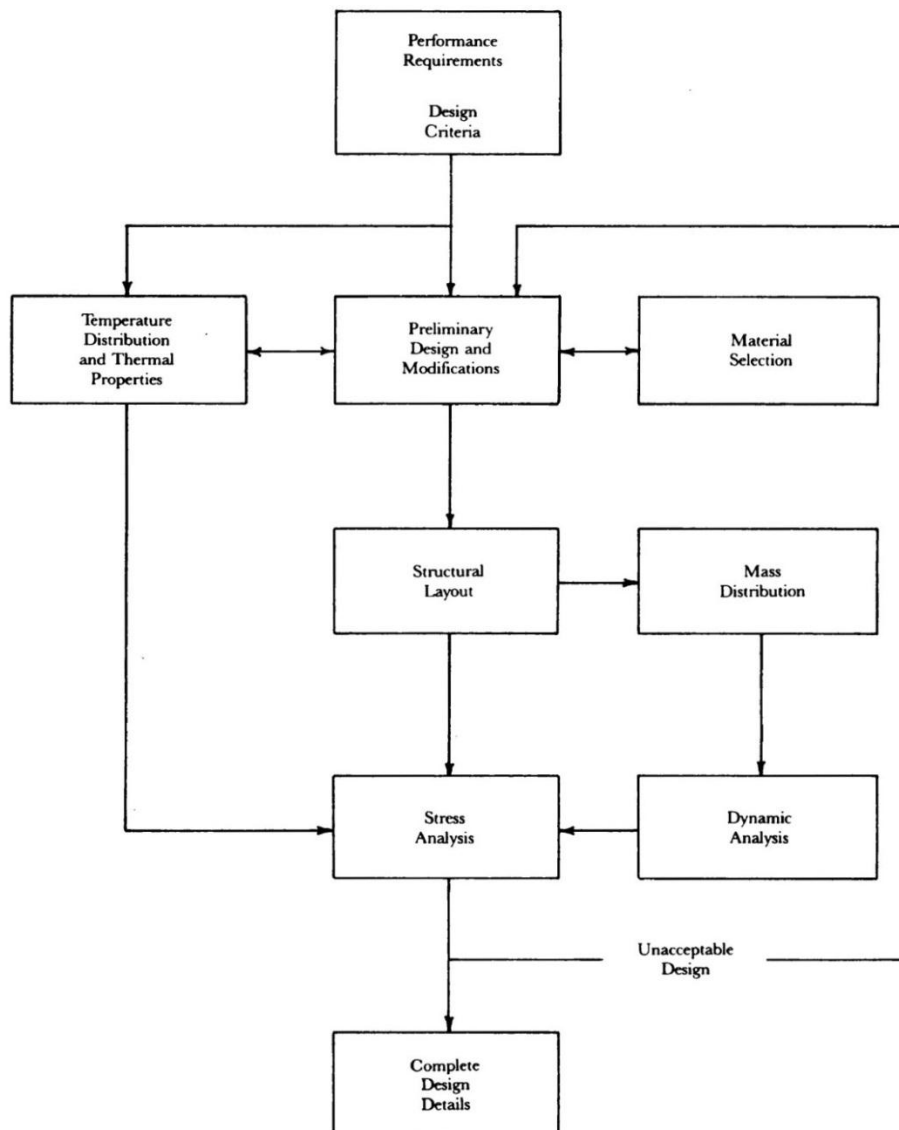
Figure 3.5: Structural design method of an unguided rocket (US Army Missile Command, 1990).

3.2 Hybrid Rocket Performance Simulator

UKZN's in-house HYROPS programme was selected for the design process of Phoenix-2A, as it is readily available and open source, allowing for modification and improvements. A brief overview of the software and its role in the design process of a hybrid sounding rocket are discussed. HYROPS can be divided into sub-sections as illustrated in Figure 3.6. The dash lines indicate the manual coupling required in HYROPS.
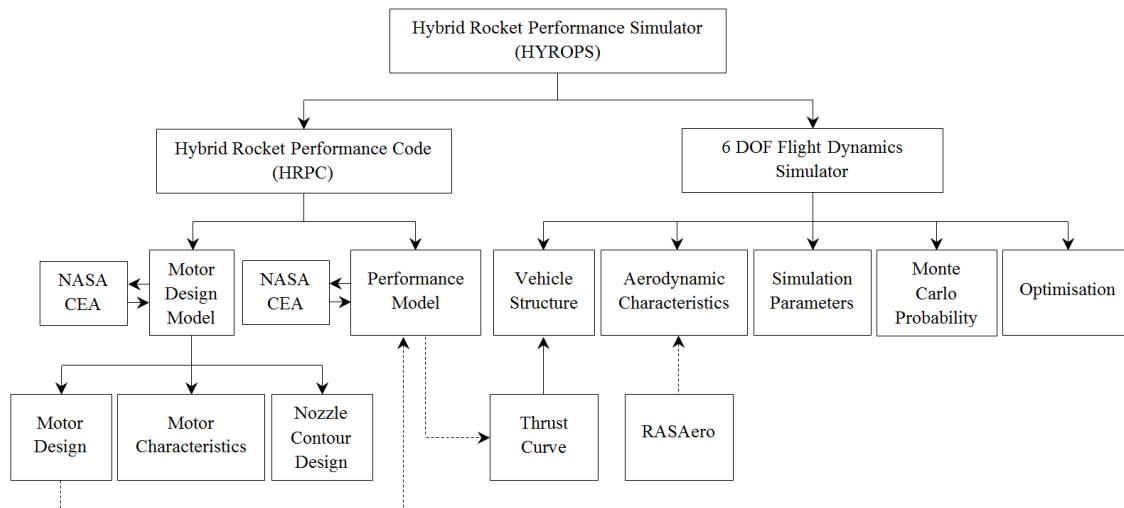
Figure 3.6: Simplified hierarchy model of HYROPS.

3.2.1   Hybrid Rocket Performance Code

The HRPC is split into a Motor Design Model and a Performance Model. Both models incorporate the NASA CEA (Gordon and McBride, 1994) equilibrium chemistry code to determine the theoretical rocket performance parameters required. The inputs for NASA CEA are as follows:

1. Propellant properties
2. Flow composition (frozen or equilibrium)
3. O/F ratio
4. Chamber pressure
5. Nozzle expansion ratio or inverse pressure ratio

HRPC-Motor Design Model

The HRPC-Motor Design Model has three sub-sections that can be selected:

1. Designing the motor including the fuel grain and nozzle
2. Analysing the motor characteristics
3. Designing the nozzle contour

Motor design

The fuel grain and nozzle geometry are determined under steady-state conditions. The model can analyse up to 10 port geometries and either conical- or bell-shaped nozzles. The characteristic velocity, c^*, optimal expansion ratio, ε, thrust coefficient, C_F, and the critical pressure ratios of the nozzle, are obtained from NASA CEA. The nozzle throat area, A_t, can be determined using the HRPC-Motor Design Model inputs, design thrust, F_d, and design chamber pressure, P_{c_d} (Equation 3.1). The motor's nozzle, fuel, and oxidiser mass flow rates, $\dot{m}_{noz}$, $\dot{m}_f$, and $\dot{m}_{ox}$ can then be found using Equations 3.2 to 3.4, as well as the oxidiser mass flux, G_{ox}, (Equation 3.5). The regression rate, $\dot{r}$, is calculated using Equation 2.3 and used to determine the fuel grain length, L_f. The fuel grain density, ρ_f, port diameter, D_p, and number of ports, N_p, are also inputs to the grain length calculation shown in Equation 3.6.

$$A_t = F_d/\left(C_F P_{c_d}\right) \tag{3.1}$$

$$\dot{m}_{noz} = \left(P_{c_d} A_t\right)/c^* \tag{3.2}$$

$$\dot{m}_f = \dot{m}_{noz}/(O/F + 1) \tag{3.3}$$

$$\dot{m}_{ox} = \dot{m}_{noz} - \dot{m}_f \tag{3.4}$$

$$G_{ox} = 4\dot{m}_{ox}/\left(\pi D_p{}^2\right) \tag{3.5}$$

$$L_f = \dot{m}_f/\left(\pi N_p D_p \rho_f \dot{r}\right) \tag{3.6}$$

The outer diameter of the fuel grain, D_f, is calculated using Equation 3.7, assuming the mass of fuel, m_f, for the theoretical burn time, t_b, where $m_f = \dot{m}_f t_b$.

$$D_f = \sqrt{[(4m_f)/(\pi\rho_f L_f)] + D_p{}^2}$$

$$(3.7)$$

Motor characteristic

The motor characteristic model is useful to compare motors to each other over a wide range of inputs that have been defined by the user. The model provides graphical visualisation for a specific impulse, thrust coefficient, characteristic velocity, nozzle exit velocity, optimum expansion ratio, and combustion temperature for various chamber pressures and O/F ratios. NASA CEA is required to determine these motor characteristics. Figure 3.7 illustrates one of the results obtained from this model. It shows the graphical representation of specific impulse for varying chamber pressure and O/F ratio of a hybrid motor operating at sea level.
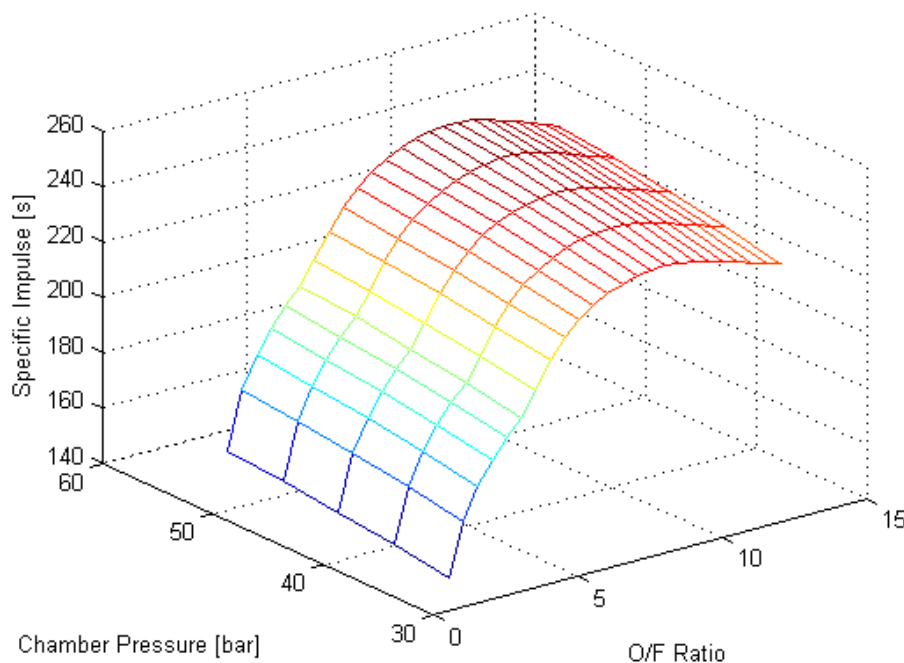
Figure 3.7: HRPC-Motor Design Model output of specific impulse for varying O/F ratio and chamber pressure.

Nozzle contour design

The nozzle contour design model can create either a conical- or bell-shaped nozzle. The model outputs the points of the internal nozzle geometry to an Excel document that can be imported into a CAD programme. The design of the contour of the converging section of the conical- and bell-shaped nozzles is the same because it does not significantly affect the motor's performance. The diverging section for a conical-shaped nozzle is linear whereas the bell-shaped nozzle has a gradual curve that shapes the flow axially before leaving the nozzle, therefore reducing the flow losses.

29

HRPC-Performance Model

The HRPC-Performance Model employs either an explicit Euler or 4th-order Runge-Kutta (RK4) numerical method to solve the ordinary differential equations (ODE). The RK4 method is used for all simulations performed in this dissertation because it is more accurate. The model is used to determine the motor's time-dependent performance throughout the burn or until the model executes a stop command. NASA CEA lookup tables are required before the model can be run. The tables include theoretical rocket performance parameters such as specific impulse for a specific oxidiser and fuel combination, and nozzle flow composition and expansion ratios for a range of O/F ratios and chamber pressures. The O/F ratio and chamber pressure values are selected to cover the expected conditions of the motor.

The HRPC-Performance model requires inputs for the type of oxidiser flow selected. Five different oxidiser flow processes can be modelled:

1. The oxidiser mass flow rate, $\dot{m}_{ox}$, is constant for the entire burn, representing the use of a turbine driven pump.
2. Constant oxidiser mass flow rate, $\dot{m}_{ox}$, with timed throttling.
3. The oxidiser is delivered to the combustion chamber by a blowdown process (only nitrous oxide can be modelled with this flow process).
4. The oxidiser tank pressure, P_T, is constant for the entire burn, representing the use of a pressurised system above the oxidiser tank.
5. The oxidiser tank pressure is equal to a time dependent polynomial equation.

The oxidiser flow rate, $\dot{m}_{ox}$, is calculated using Equation 3.8 when the flow process selected is not constant:

$$\dot{m}_{ox} = C_D A_{inj} N_{inj} \sqrt{2\rho_{ox}(P_T - P_l - P_c)} \tag{3.8}$$

where C_D is the discharge coefficient of the injector, A_{inj} is the cross-sectional area and N_{inj} is the number of holes of the injector. The density of the oxidiser is denoted as ρ_{ox} and P_T is the tank pressure. P_l is the pressure loss in the feed system and P_c is the chamber pressure.

The HRPC requires the fuel grain design parameters. These include the grain's length, density, inner and outer diameter, as well as the number of ports and regression rate ballistic coefficients. Other inputs required for the code include the nozzle geometry, injector geometry, performance correction factors, and critical nozzle pressure ratios (Geneviève, 2013).

3.2.2   Six Degree-of-Freedom Flight Dynamics Simulator

The Flight Dynamics Simulator is able to predict and display the trajectory of a sub-orbital sounding rocket. It uses generic kinematics and Newtonian equations of motion that are broad enough to analyse orbital trajectories. A rotating spherical geodetic model and a standard atmospheric model form the foundation for the flight performance analysis. RK4 is used to numerically solve the differential equations necessary for the flight trajectory.

The start window of the GUI of the Flight Dynamics Simulator is shown in Figure 3.8. The individual tabs of the separate sub-sections are placed on the right-hand side of the screen, for example Edit Airframe and Edit Vehicle. This GUI will be the interface for the final integrated version of HYROPS which includes the HYROPS and Edit Motor tab for all the input requirements necessary for the HRPC.
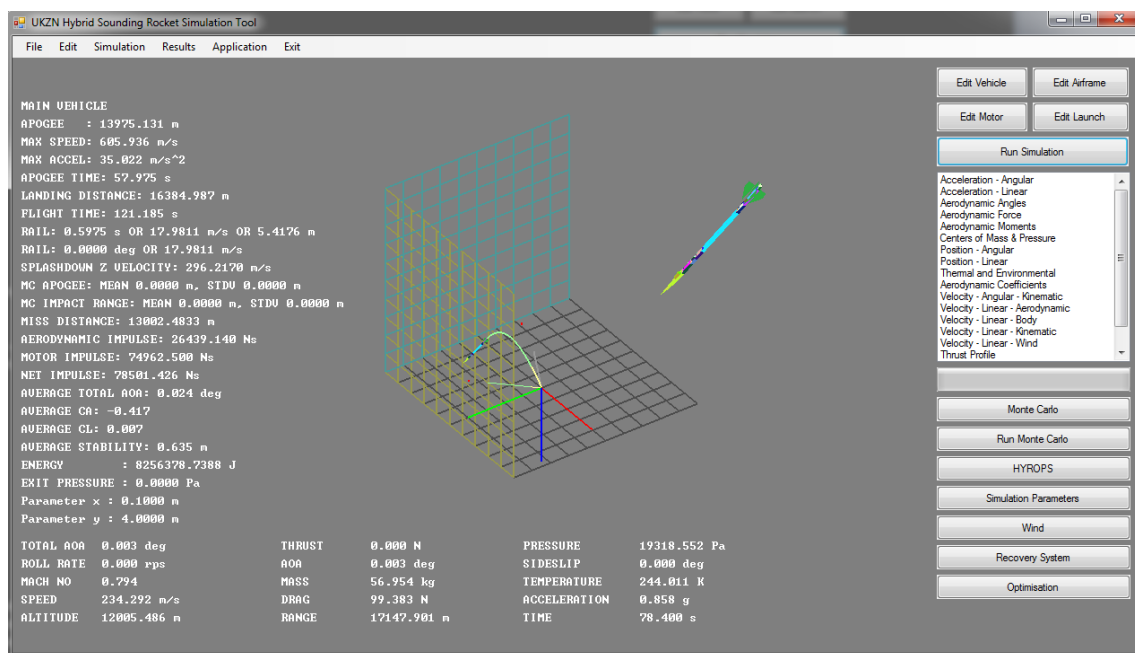
Figure 3.8: HYROPS graphical user interface showing the default Phoenix-1A rocket.

The Edit Airframe tab is where the user defines the aerodynamic structure for aerodynamic modelling within the programme. Aerodynamic characteristics can be found by using an external programme such as RASAero, from which the aerodynamic tables are input into the Flight Dynamics Simulator. The launch parameters are found in the Edit Launch tab and include rail length, initial velocity, and launch angle. The programme models the rocket vehicle as a rigid body made up of simple geometric components such as cylinders, cones, ogives, and annuli that have constant density, and are defined in the Edit Vehicle tab. The simulator is

capable of modelling a dual stage parachute recovery system. The smaller drogue parachute is deployed after a specified time delay once apogee is achieved and the main chute is deployed at a specified altitude above sea level. The thrust of the vehicle can be modelled by a ramp function or a time varying thrust curve.

The Wind tab of the Flight Dynamics Simulator allows the user to model 3D winds and has options for turbulence and jet streams. Wind turbulence is random localised wind gusts, and jet streams are regions of fast moving air at high altitudes. The Optimisation tab provides an optimised function that uses generic algorithms and the Monte Carlo tab allows the user to analyses a number of uncertainties that may occur during the rocket's flight path. These include separation failure in a multistage rocket, parachute deployment failure, or thrust misalignment (Chowdhury, 2012).

3.2.3 Design Methodology

The life cycle of a hybrid sounding rocket based on existing design methods and incorporating the HYROPS tool is shown in Figure 3.9. The processes that use HYROPS are indicated by blue boxes and the red lines show the iterative paths. HYROPS is used in the design process to simulate motor performance and to perform the flight trajectories of each of the designed vehicles. Rocket design methods begin with analysing the mission to determine constraints and requirements. These include feasibility, manufacturability, transportability, reliability, and storability of the proposed vehicle, as well as the environmental impact and flight environment (Humble et al., 1995).

The conceptual process is used to create a base design on which to conduct propulsion and aerodynamic parametric trade studies. Modifications to the preliminary design are made using knowledge gained from the trade studies to optimise the design. This dissertation includes the initial concept of Phoenix-2A, presented in Chapter 4 and the parametric trade studies, in Chapter 5. These studies provide a technology base for the Phoenix programme on which further research into hybrid rocket technology can be built, especially for large-scale vehicle development.

A Preliminary Design Review ensures the vehicle achieves its requirements, validating it to become the baseline design. Detailed design specifications are produced based on selected materials. The components are computationally analysed under static and dynamic loading conditions to ensure structural integrity and thermal protection during transportation, handling, launch, and flight conditions. The loading conditions are obtained from HYROPS and can be

used in FEA and CFD analyses. Components are manufactured and tested to ensure that design performance is achieved and to provide system validation. After the Critical Design Review, the final design and production drawings are completed and all components are manufactured, assembled, and tested and if necessary, modifications are made to allow the vehicle to pass the Flight Readiness Review. For the purpose of a successful vehicle, the design is continuously evaluated and modified. The vehicle is then ready to be launched and to complete its mission. Figure 3.10 illustrates the modelling process of a rocket utilising the HYROPS software. The concept selection process follows from the definition of mission requirements.

Figure 3.9: Life cycle of a hybrid sounding rocket based on HYROPS.

Apogee trade studies

Scaling

Existing similar mission rocket database

Parametric trade study objective

Start

Mission statement:
Gives constraints, requirements and environment

Concept selection

Inputs:
Propellant properties
Flow composition
Oxidiser flow method
Design thrust
Design chamber pressure
Design atmospheric pressure point
Design O/F
Port diameter

HRPC Motor Design Model

Outputs:
Grain dimensions
Mass flow rates
Nozzle geometry
1st, 2nd and 3rd critical pressure ratios
Characteristic velocity
Thrust coefficient
Optimal expansion ratio

Material properties

Material:
Selection
Sizing (analytically)
Availability
Weight

Design of propulsion system:
Combustion chamber geometry
Oxidiser tank geometry
Injector design
Nozzle design

NASA CEA:
Generate theoretical rocket performance parameter look-up table using optimal expansion ratio and nozzle flow composition

Inputs:
Oxidiser flow method
Flow composition through nozzle
Oxidiser tank design
N_2O properties
Fuel grain specifications
Nozzle and motor geometry
Injector and feed system design
Atmospheric properties
Critical pressure ratios

Outputs with respect to time:
Burn time
Regression rate
Thrust - at vacuum and sea-level
Temperature - tank and chamber
Pressure - tank, chamber and exit
Mass flow rates - oxidiser, fuel, nozzle and total

HRPC Performance Model

Outputs:
Burn time
Vacuum thrust
Exit pressure

External modelling:
- RASAero
- Wind tunnel data

Internal modelling:
-HYROPS aerodynamic tool

Aerodynamics:
Nose cone
Fuselage dimension
Fin geometry
Surface finish
Boattail structure
Inter-tank connection

Flight Dynamics Simulator

Meet mission requirement

No

Yes

Vehicle design

Legend

Blue boxes - HYROPS based procedure
Black arrow - normal flow
Red arrow - iterative flow

Figure 3.10: Design model of a hybrid sounding rocket based on HYROPS.

34

The inputs for the HRPC-Motor Design Model are determined using the selected concepts, scaling techniques, knowledge from existing literature and/or apogee trade studies. The design process focuses on the motor as it is a key feature of the rocket.

The inputs for the HRPC-Motor Design Model such as thrust, chamber pressure, O/F ratio, expansion ratio, and propellant selection, are used to determine the grain, motor, and nozzle geometries. The propulsion system configuration then determines the HRPC-Performance Model inputs, which yield the motor performance.

The rocket structure is designed in the Flight Dynamics Simulator of HYROPS and the aerodynamic characteristics for the rocket can be modelled within the software, using a commercially available aerodynamic programme, or with wind tunnel data. The HRPC-Performance Model outputs time dependant momentum thrust and exit pressure curves which are used in the 6 DOF Flight Dynamics Simulator to simulate the thrust of the rocket throughout its burn time. The trajectory of the rocket is modelled to determine if it will achieve its objective satisfactorily. An iterative design process is implemented until a satisfactory vehicle has been achieved.

3.2.4   Validation of HYROPS

Validation of the HYROPS Fight Dynamics Simulator was performed by comparing its outputs with published data, both experimental and simulated. Malemute and Aerobee 150A sub-orbital sounding rocket trajectories were used because they have similar performance characteristics to those envisioned for Phoenix-2A. The key performance parameters used in this study were apogee, range, and flight time.

Aerobee 150A

The Aerobee 150A has a solid propellant first stage and a liquid propellant second stage, each of which has a fin set with four fins that are used to stabilise the vehicle. Typically the first stage motor burns for 2.5 s and the second stage ignites 0.3 s after the first stage and continues for 52 s. Russ and Randall (1961) illustrated the geometry of the Aerobee 150A, shown in Figure 3.11.

Two degree-of-freedom simulation comparison

As a test case, the Aerobee 150A trajectory was modelled using the HYROPS Flight Dynamics Simulator, and compared with simulated results from Russ and Randall (1961), who used a 2 DOF non-rotating earth model and a 1959 ARDC atmospheric model. The HYROPS results are

likely to differ because it uses a 6 DOF, rotating spherical earth, and international standard atmospheric model.

Figure 3.11: Aerobee 150A geometry (Russ and Randall, 1961).

RASAero was used to obtain the aerodynamic characteristics of the Aerobee 150A and the Phoenix-2A design. RASAero limits the aerodynamic characteristics to only one fin set which also contributed to the variation in the results. The fin set was modelled on the second stage to ensure stability during flight. The nominal thrust value was modelled as a ramp function due to the absence of motor performance data for the Aerobee 150A. Figure 3.12 demonstrates that HYROPS follows closely with the published results for various payload mass at an 88° launch angle (Leverone et al., 2013).

Figures 3.13 to 3.15 illustrate similar trends when varying the launch angle and payload mass. The HYROPS simulator underestimates apogee at higher launch angles and overestimates at low angles. The minimum and maximum percentage apogee differences were 0.7% and 25% for launch angles of 88° and 70° respectively in the simulation with a 136.0 kg payload mass. The maximum percentage range variation was found to be 16% for an 88° launch angle with a 43 kg

payload mass. The technique used to simulate the gravity turn for the 2 DOF (Russ and Randall) and 6 DOF (HYROPS) models may also contribute somewhat to the variation in results.
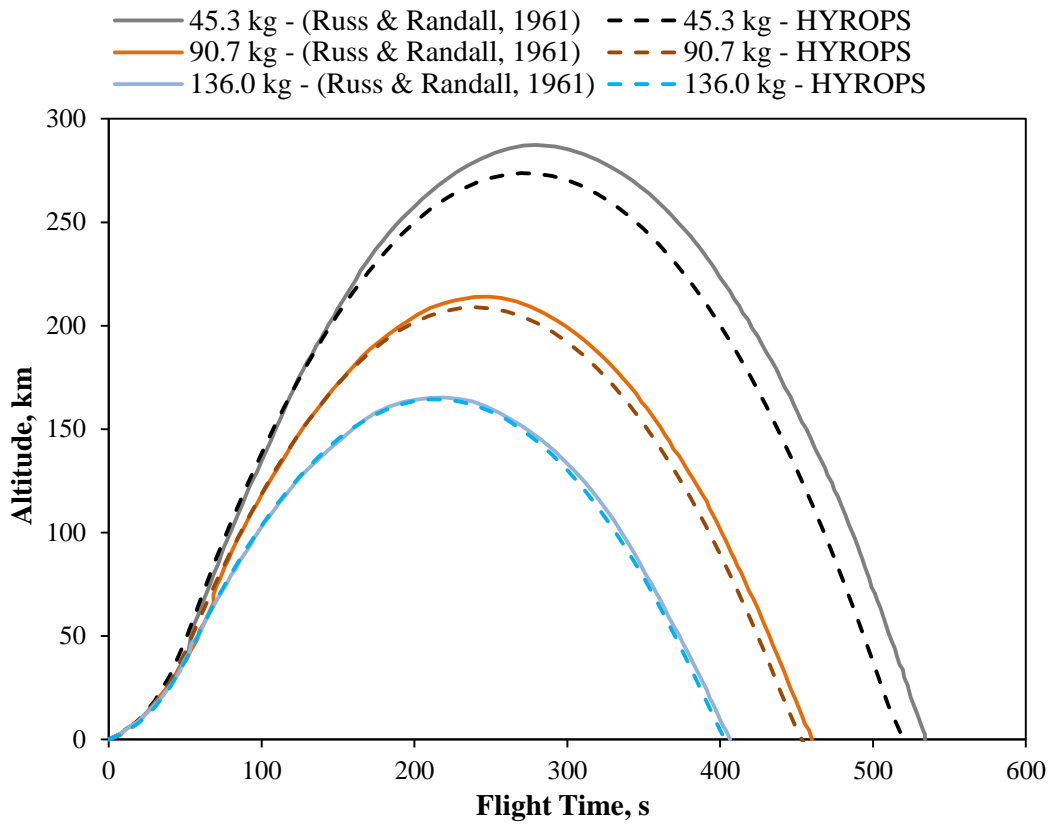
Figure 3.12: Validation simulation showing altitude versus time for the Aerobee 150A for various payload masses.
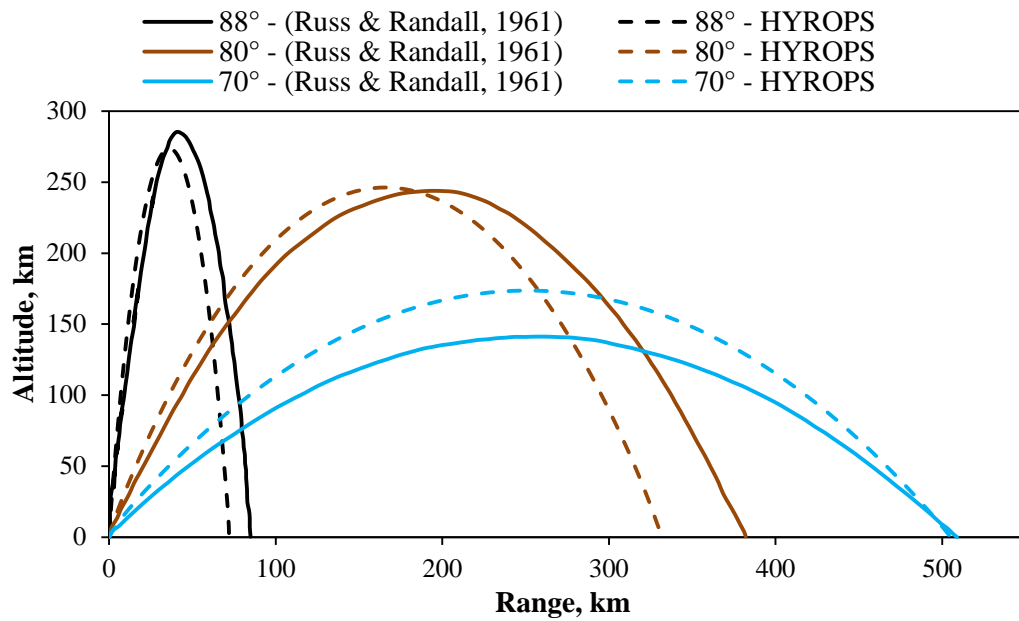
Figure 3.13: Trajectory profile of Aerobee 150A with a 45.3 kg payload.
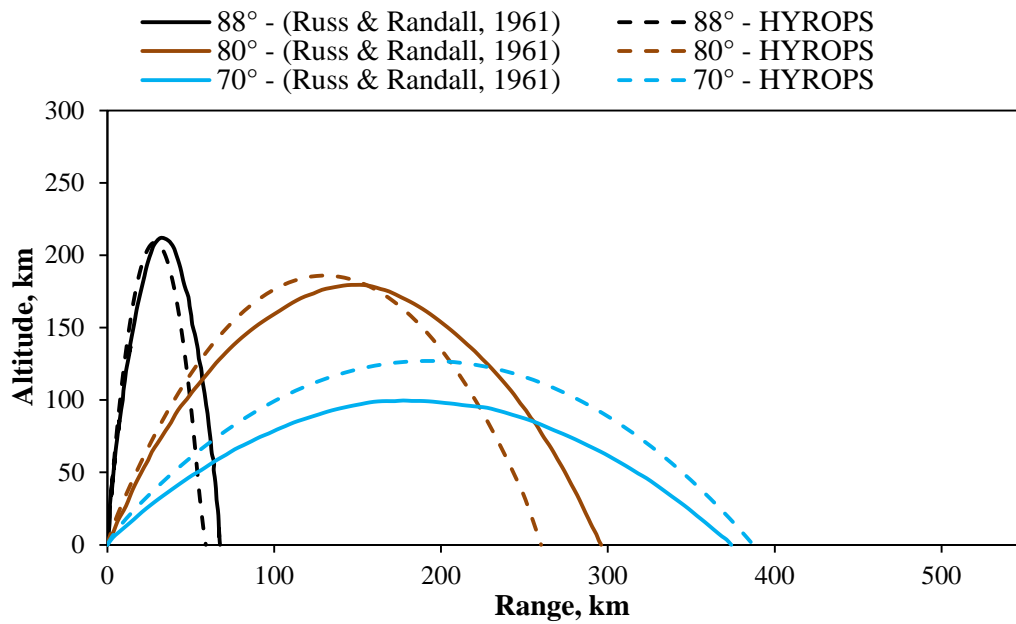
Figure 3.14: Trajectory profile of Aerobee 150A with a 90.7 kg payload.
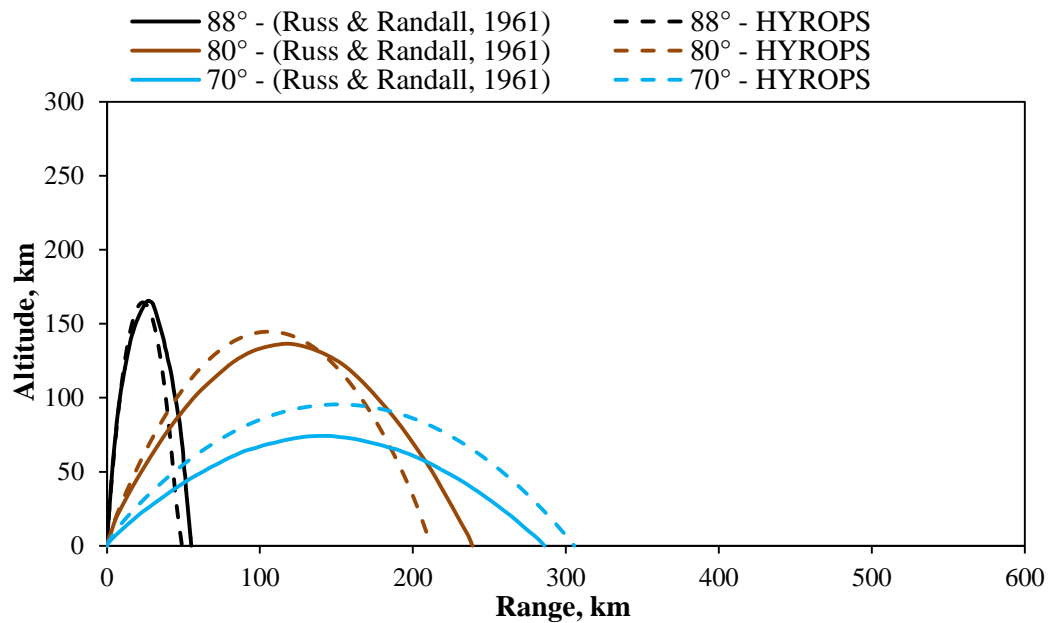
Figure 3.15: Trajectory profile of Aerobee 150A with a 136.0 kg payload

Flight data comparison

Data available from the flight of a NASA Aerobee 150A sounding rocket, launched 18 September 1964 from Wallops Island in Virginia and designated as 4.155 NA, was modelled in the HYROPS Flight Dynamics Simulator (Busse et al., 1967). For this flight a conical nose cone with a cylindrical extension was used to house the 108.9 kg payload. The HYROPS representation of the Aerobee 150A used for this flight is shown in Figure 3.16. The rocket was

38

launched from sea level at an angle of 87° and the results are given in Table 3.1, along with the HYROPS simulated outputs.

Figure 3.16: HYROPS representation of the Aerobee 150A rocket.

Table 3.1: HYROPS simulation validation against flight data for the Aerobee 150A rocket.

	Flight Data	HYROPS Data	Percentage Difference
Apogee (km)	168.02	145.66	14.26
Time to apogee (s)	222.10	206.99	7.04
Centre of gravity from the nose tip (calibre)	9.67	9.92	2.55
Centre of pressure from the nose tip (calibre)	12.72	15.21	17.83
Second stage - Burnout altitude (km)	34.75	32.98	5.23
Second stage - Burnout velocity (km/s)	1.62	1.49	8.36

For this flight, HYROPS used average thrust values for the entire burn of each stage as the detailed thrust curves were classified. Figure 3.17 illustrates how HYROPS underestimates the vehicle's acceleration. This explains the discrepancy between the flight and simulated apogee results as well as the lower second stage velocity obtained by the simulation. The centre of pressure used in HYROPS differed to the complete configuration of the rocket due to the inability of RASAero to model both fin sets.
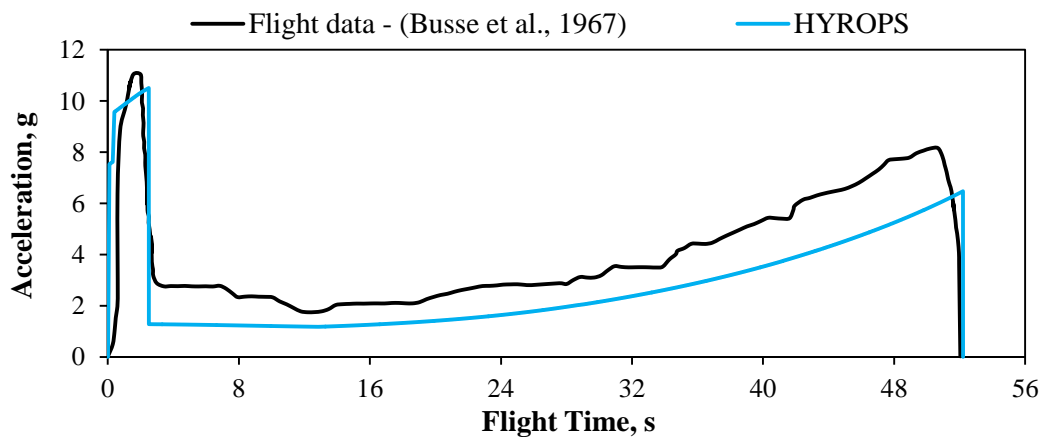
Figure 3.17: Acceleration versus time comparison for the Aerobee 150A sounding rocket.

Malemute

The Malemute rocket has a single stage solid propellant motor that is also used as the second stage in vehicles such as the Terrier Malemute, which achieve altitudes of up to 700 km.

Six degree-of-freedom simulation comparison

A comparison was performed between the HYROPS Flight Dynamics Simulator and the Six Degree-of-Freedom Flight-Path Generalized Computer Program simulation of the Malemute rocket (Millard et al., 1977). The simulation launch parameters were an 87° launch angle with a 130° azimuth and a 4.72 m launch rail. The rocket was launched from an altitude of 1.625 km. Figure 3.18 shows the Malemute flight configuration with dimensions in centimetres. Figure 3.19 illustrates the corresponding HYROPS simulator configuration.
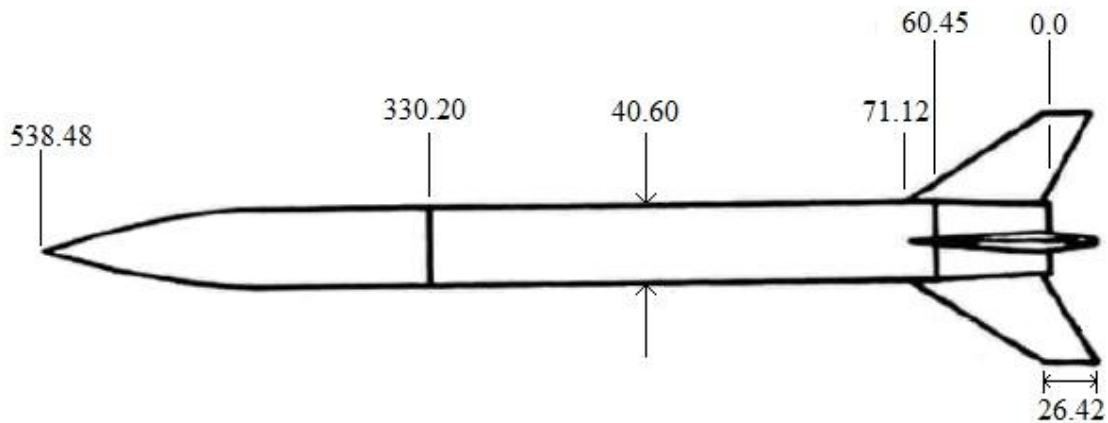
Figure 3.18: Malemute flight configuration (Millard et al., 1977).

Figure 3.19: HYROPS simulator representation of the Malemute rocket.

The results in Figure 3.20 indicate that HYROPS underestimates the flight time by 4.4%, the ground range by 7.7% and the apogee by 8.1%. Millard et al. (1977) provide the thrust curve for this motor which reduced the possible causes of error when compared to the 2 DOF Aerobee 150A simulations. The HYROPS velocity closely follows the velocity in literature during the burn phase because of the known thrust curve, shown in Figure 3.21. The HYROPS velocity

40

then falls lower during the coasting ascent phase. At the end of the burn, the altitudes from both simulations are similar, however the altitudes deviate during the coasting phase (Figure 3.20). This variation in velocity and thus altitude may be attributed to possible variations in the aerodynamic data as the aerodynamic characteristics obtained from literature were from wind tunnel testing (Millard et al., 1977).
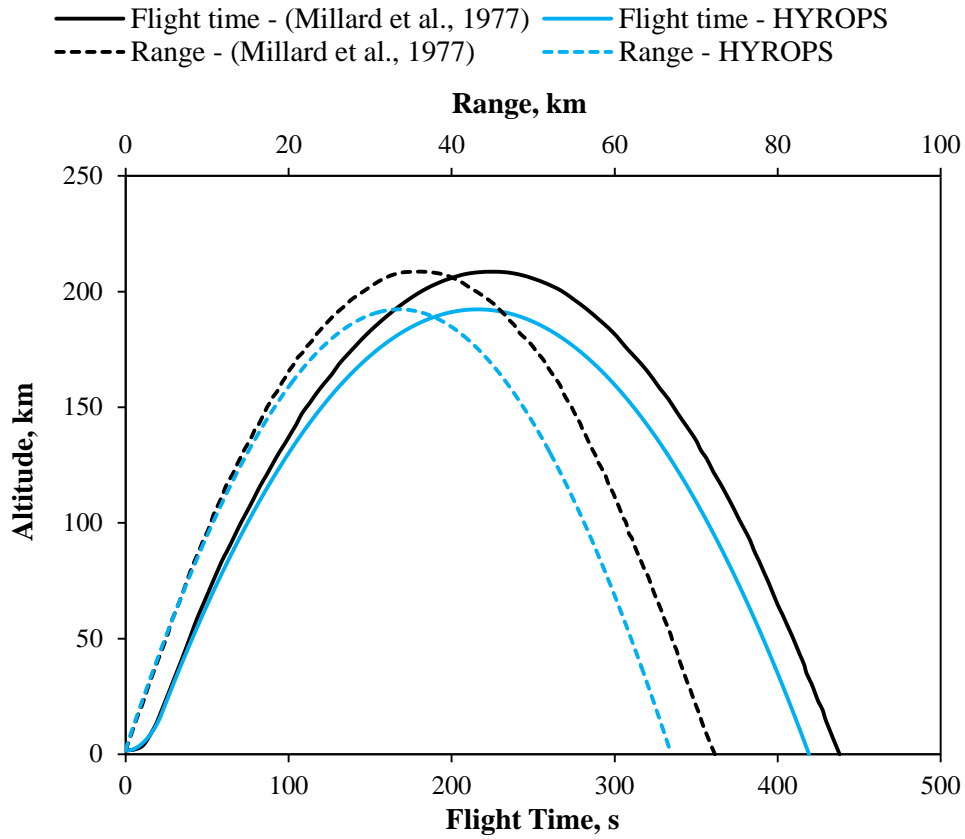
Figure 3.20: Simulated trajectory profiles of the Malemute rocket.
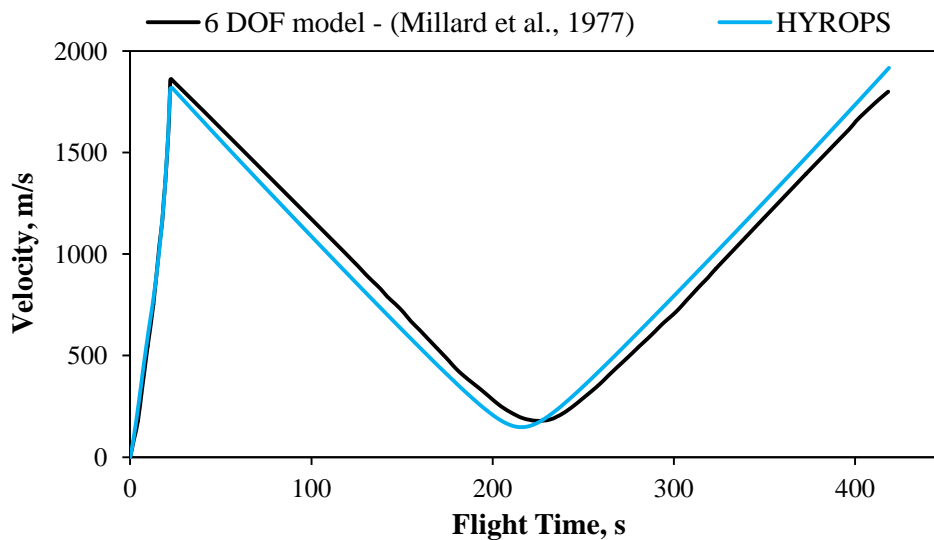
Figure 3.21: Simulated velocity profiles of the Malemute rocket.

Hybrid Rocket Performance Code Validation

At the time of writing, the author was not aware of any published commercial hybrid rocket thrust curve data that could be used to verify the HRPC for large-scale motors. During the testing phase of the Phoenix-2A motors, the results should be used to validate the software as part of future work in the Phoenix programme. To verify the HRPC on a small-scale, a thrust comparison from the work of Geneviève (2013) is provided. The investigated motor used nitrous oxide as the oxidiser and 40% aluminised paraffin wax as the fuel.

The results in Figure 3.22 illustrate that the HRPC thrust curve follows the curve from the work of Karabeyoglu et al. (2003) with reasonable accuracy. The liquid range of the nitrous oxide took 2.6 s longer to be consumed in the HRPC than in the literature. Geneviève (2013) ascribed the difference to an assumption of the nitrous oxide mass loaded into the tank, unknown fuel grain and nozzle dimensions, and the possibility of the literature simulation having a higher mass flow rate because of combustion chamber and tank pressure differences. The regression rate coefficient and exponent were assumed as these were not reported by Karabeyoglu et al. (2003). Another difference is that the simulation in the literature accounted for changes in atmospheric pressure related to altitude, whereas the HRPC models the hybrid rocket motor at a single atmospheric pressure.
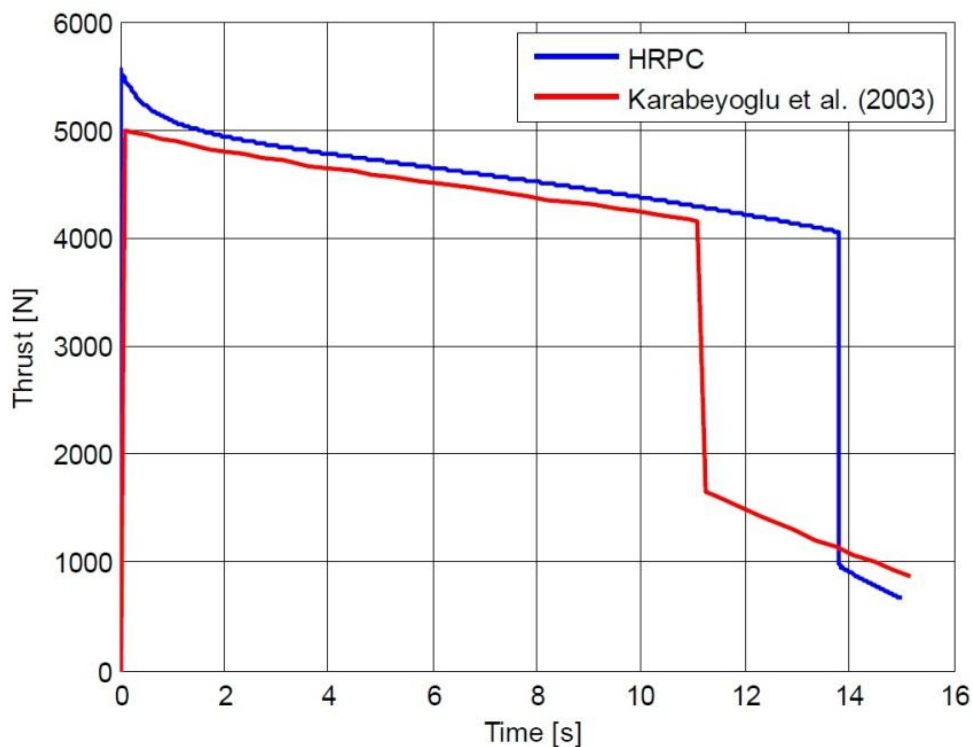
Figure 3.22: Thrust validation of the HRPC (Geneviève, 2013).

In summary, the work of Geneviève (2013) indicates that the HRPC has been adequately validated against lab-scale motor hot-fire tests in the Phoenix programme and, at the time of writing, was being validated against the recent Phoenix-1A hot-fire test results. The HYROPS Flight Dynamics Simulator also performs adequately compared to existing 2 DOF and 6 DOF simulations, as well as flight data. The Flight Dynamics Simulator was more accurate when the thrust curve was known and the maximum deviance of performance was within 8.1% for known thrust data. With this in mind, the HYROPS software is considered as an acceptable tool for implementing the Phoenix-2A design methodology adopted in this study.

CHAPTER 4

Phoenix-2A Concept Generation

The methodological process described in Chapter 3 is used to determine the initial conceptual design of the Phoenix-2A rocket. This follows from the mission statement which determines the requirements and constraints pertinent to the design of the rocket, while maintaining flexibility. Once the vehicle configuration, propellant selection, and oxidiser delivery method are determined, the HRPC is used to design the propulsion system of the initial conceptual design of Phoenix-2A, and to analyse its performance. The vehicle structure is determined from the propulsion system geometry and the aerodynamic characteristics found using RASAero. The Flight Dynamics Simulator enables the prediction of the flight trajectory to ensure that it meets the requirements of the mission statement. The concept design was initially based on a 95% combustion efficiency, but amended to 93% due to the findings from recent hot-fire tests in the USA.

4.1 Rocket Mission Statement

The aim of the Phoenix-2A project is to develop a stable hybrid sounding rocket capable of reaching an altitude of 100 km with a 5 kg payload as part of the Phoenix Hybrid Sounding Rocket Programme at UKZN. The vehicle must be safe, reusable, and feasible in terms of South African manufacturing capability. Generally the propulsion system is not constrained as this would limit the design flexibility. However Phoenix-2A is required to utilise hybrid propulsion because of the academic nature of the project where safety and cost reduction are essential. The safety of hybrid technology has been discussed in the previous chapters. For reusability and recoverability of the Phoenix-2A vehicle, a recovery bay was included to allocate space for parachutes.

There are no restrictions on the dimensional envelope of the rocket related to existing launch infrastructure because there are currently no launch facilities in South Africa (Brooks et al., 2010). The construction of a facility that can test motors up to 100 kN, as well as a launch platform should be investigated as part of future work in the Phoenix programme. The purpose of the test facility would be to perform experimental testing on large-scale motors to measure the actual parameters such as combustion efficiency. Phoenix-2A is designed to be aerodynamically stable throughout its flight path so that it does not require thrust vector control.

4.2 Concept Selection

4.2.1 Configuration

Vehicle Configuration

From the sounding rocket survey in Chapter 2, it was found that a single or two stage rocket can be used for apogees near 100 km. A multi-stage vehicle can be configured in series, partial, parallel, or piggy-back staging as shown in Figure 4.1. The series two stage rocket is most commonly used in sounding rocket applications.
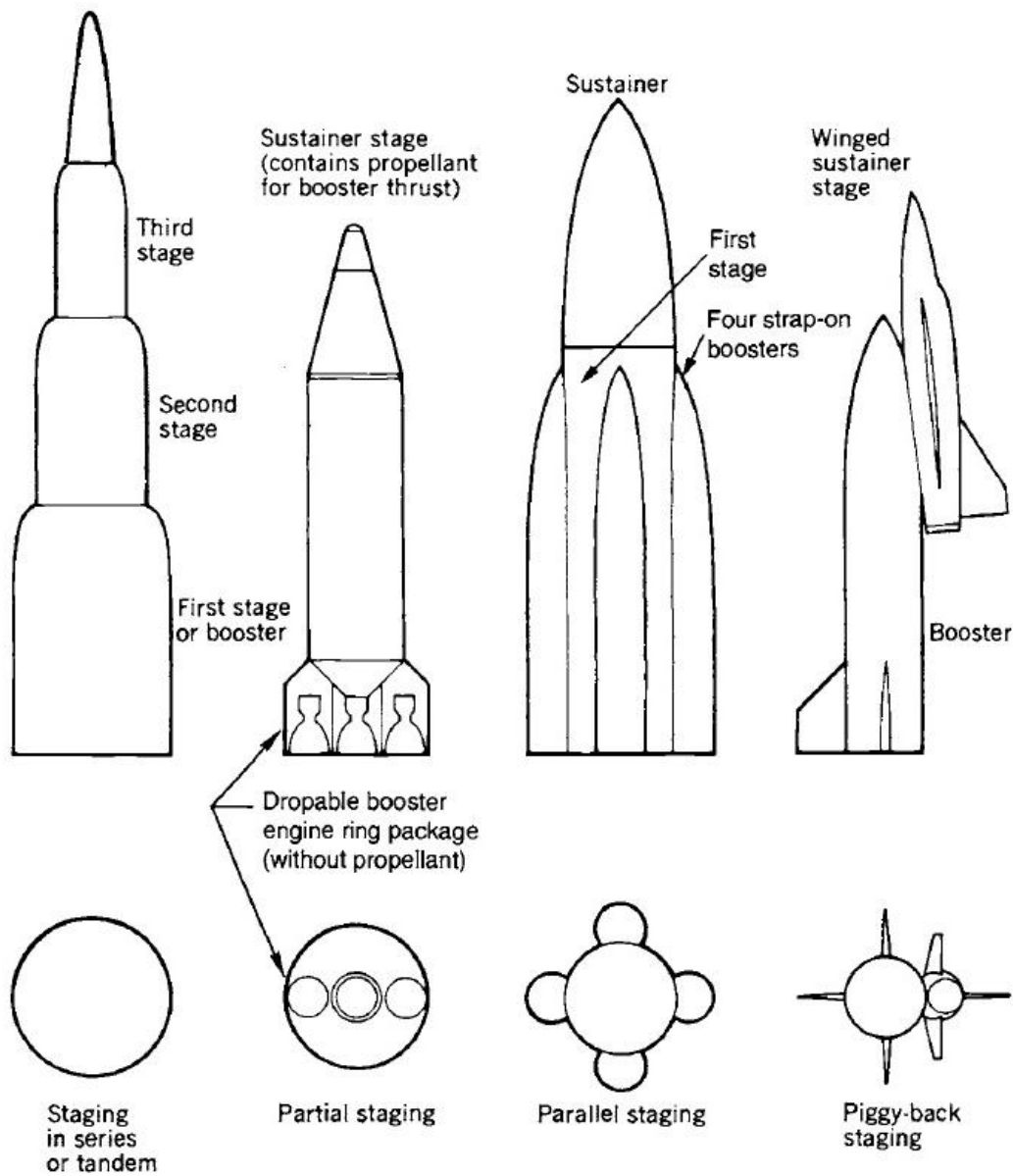
Figure 4.1: Multi-stage configurations (Sutton and Biblarz, 2001).

A two stage vehicle can have a higher velocity than a single stage because the total velocity increment, ΔV, for a multi-stage rocket is the sum of each stage's velocity for n stages:

$$\Delta V = \sum_{1}^{n} \Delta V = \Delta V_1 + \Delta V_2 + \cdots + \Delta V_n \qquad (4.1)$$

Sutton and Biblarz (2001) state that for orbital trajectories a two stage rocket can improve the payload mass by 22% compared to a single stage. An advantage of a two stage vehicle is that each stage can be optimised for its particular operating conditions, but the cost and complexity of the rocket increases with the number of stages. This decreases the reliability because there is a greater risk of failure due to complications such as separation and ignition failure. The minimum number of stages that can meet the given flight mission should be selected to minimise complexity and improve system reliability. A single stage hybrid rocket is feasible for a 100 km apogee and was chosen for Phoenix-2A.

A dart configuration was considered for Phoenix-2A however the payload dimensions restrict the geometry of the dart design. Table 4.1 from the work of Bollermann (1970) gives examples of typical dart dimensions. The dart configuration was not selected because of the increased complexity required, similar to that of a multi-stage vehicle.

Table 4.1: Darted vehicles dimensions (Bollermann 1970).

Vehicle	Length of dart (including nose cone) (m)	Diameter of dart (cm)
Cajun Dart	1.15	4.45
Loki Dart	1.57	3.49
Meteorological Probe	1.42	3.65
Super Loki	1.22	4.13
Viper Dart	1.47	5.08

Hybrid Configuration

The three most common hybrid rocket configurations are classical, reverse, and tribrid systems, as discussed in Chapter 1. The classic configuration was selected due to the simplicity in design and manufacture and because of the expertise gained from other motors in the programme which have had classical configurations. This configuration restricts the propellant survey to liquid oxidisers and solid fuels.

4.2.2   Propellant Selection

There are numerous propellant options for hybrid rockets. Common oxidisers are nitrous oxide
(N_2O), hydrogen peroxide (H_2O_2), and liquid oxygen (LOX). Paraffin-based wax, polyethylene
(PE), and hydroxyl-terminated polybutadiene (HTPB), are examples of solid fuels. The
propellants selected for Phoenix-2A are nitrous oxide and Sasol 0907 paraffin wax, with
motivation as follows:

Fuel Selection

Sasol 0907 paraffin wax ($C_{50}H_{102}$) is a non-carcinogenic, non-toxic, and non-hazardous fuel and
is thus easier and safer to handle in a university environment. Paraffin wax is relatively
inexpensive, commonly available, and has a regression rate approximately three to four times
higher than that of classical hybrid fuels, as shown in Figure 4.2 (Karabeyoglu et al., 2003).
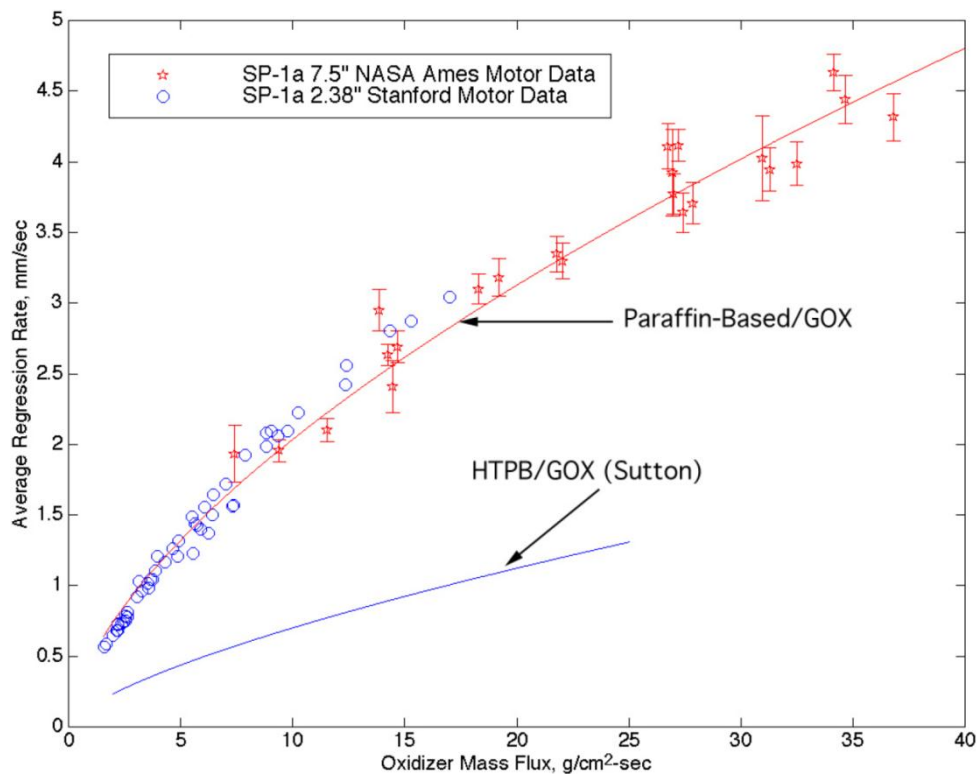
Figure 4.2: Regression rate comparison between paraffin based wax and Hydroxyl-
Terminated Polybutadiene (Karabeyoglu et al., 2003).

The higher regression rate allows for a single port design as a smaller burning surface area is
required. A single port grain configuration was selected because of its advantages over multiport
configurations, mentioned in Chapter 1. These advantages include simplicity in manufacture
and better volumetric efficiency for fuel grains below 700 kg (Humble et al., 1995). The

structural integrity of the large single port configuration is currently being investigated by a PhD candidate at UKZN (Leverone et al., 2013).

Paraffin wax forms water and carbon dioxide as by-products of combustion which are less environmentally damaging than the combustion products generated by high performance composite solid propellants. The Space Propulsion Group have successfully manufactured single grains with outer diameters of up to 0.56 m, demonstrating the feasibility of large fuel grains for Phoenix-2A (Space Propulsion Group, 2012).

An important challenge to be overcome with paraffin wax is that of sloughing. This can result in large pieces of unburned fuel breaking away from the grain and being ejected through the nozzle, causing a reduction in chamber pressure. Opaque dyes such as carbon black will be blended into the fuel grain to reduce radiative heat transfer through the wax towards the combustion chamber wall, minimising this effect (Humble et al., 1995). Approximately 1% dye by mass will be added, which has a minimal effect on the thermochemical properties of the combustion process and thus is not accounted for in modelling the motor's performance in the HRPC.

Oxidiser Selection

Nitrous oxide (N_2O) was chosen as the oxidiser because it is commonly available, has a low toxicity, and has self-pressurising capability. It is relatively inexpensive, non-cryogenic and therefore can be handled, transported, and stored with ease. Nitrous oxide is a subcritical fluid meaning that it can concurrently be in a liquid and gas phase in a closed tank system. The vapour gives it self-pressuring capability. Nitrous oxide supports combustion at high temperatures and is non-corrosive with common materials such as aluminium and stainless steel. Caution is necessary when selecting materials that come into contact with it such as O-rings, as many materials are incompatible with nitrous oxide (for example chlorofluorocarbons and nitrile rubber).

Although other oxidisers may have higher performance and impulse densities, nitrous oxide is a known substance within the Phoenix programme and has been adopted for use with all existing motors. It is also more environmentally friendly than many commercially available solid propellants that use perchlorate-based oxidisers.

Figure 4.3 indicates than an O/F ratio of 8 for nitrous oxide and paraffin wax (N_2O/Paraffin line) produces the highest specific impulse. It also shows that the N_2O/Paraffin combination has a small change in specific impulse over a large range of O/F ratios compared to the

LOX/Paraffin combination. This allows for near optimal performance during the entire burn for blowdown motors that have large O/F shifts. The higher the optimal O/F ratio required the more oxidiser necessary and therefore the bulkier the oxidiser tanks which is a disadvantage of the propellant combination of nitrous oxide and paraffin wax.
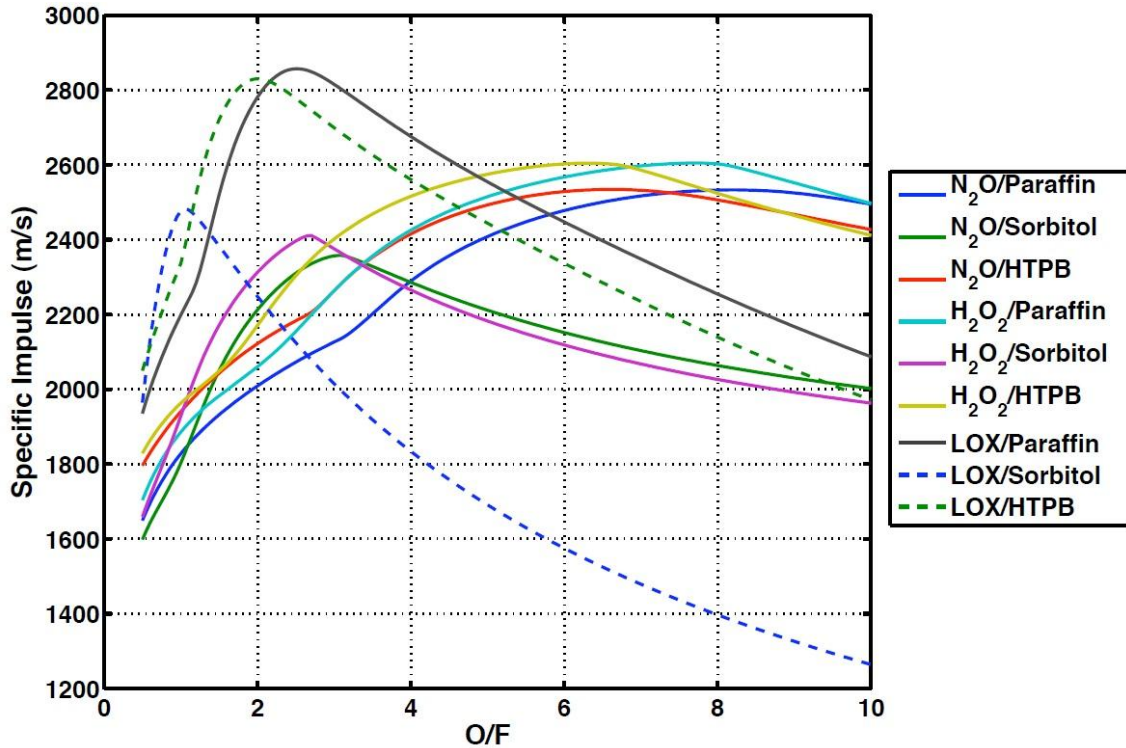
Figure 4.3: Specific impulse propellant trade study (Dyer et al., 2007).

The major safety risk with nitrous oxide is the possibility of decomposition, especially in thin walled oxidiser tanks that contain large amounts of nitrous oxide and are closely coupled to the combustion chamber. When an oxidiser tank is filled mostly with vapour, for example after the depletion of the liquid phase, there is a risk that the hot injector could heat the surrounding nitrous oxide vapour in the tank resulting in a deflagration wave. This could propagate throughout the oxidiser tank leading to over-pressurisation, and catastrophic failure. The increase in pressure is caused by a significant amount of energy being released during the decomposition of nitrous oxide. To reduce the risk of decomposition in the oxidiser tank, it can be designed with a burst disk, or the tank ullage volume can be supercharged with an inert gas (Karabeyoglu et al., 2008). For additional safety a relief valve on the oxidiser tank is recommended, although it is not essential for an unmanned vehicle (Thicksten et al., 2008).

Decomposition is also possible in the feed system. This may be caused by ignition from various heat sources, which include adiabatic compression in dead volumes in the feed system and heat

from the igniter gases that travel into the feed system before the oxidiser valve is opened. Heating of the nitrous oxide may cause a decomposition reaction and result in failure of the feed system. Reducing the dead volumes, opening the oxidiser valve more slowly, and designing the motor to prevent the flow of hot gases from the igniter to the feed system, are ways to minimise the risk.

The combustion chamber is also prone to nitrous oxide decomposition when nitrous oxide collects in the combustion chamber before ignition. When the igniter is fired, decomposition, over-pressurisation and an uncontrolled explosion can result. This occurred during a hot-fire test of the Peregrine motor, as described in Chapter 2. Using the correct ignition sequence prevents this from occurring. Other sources that may result in nitrous decomposition are friction, electrostatic discharge, and overheating of the nitrous oxide pump (Thicksten et al., 2008).

4.2.3 Oxidiser Delivery Method

Section 2.2.1 discussed the different oxidiser flow methods for a hybrid rocket. These are blowdown, pressurant, or pump driven systems. All these systems have the potential to be throttled. A blowdown system was selected due to the self-pressuring properties of nitrous oxide at room temperature, and to reduce the complexity in the design by decreasing the plumbing requirements. A regulated pressurant system that maintains a constant tank pressure was not selected because the performance gain was insignificant compared to the gain in inert mass (Zilliac et al., 2012).

4.3 Initial Conceptual Design

The initial conceptual design of Phoenix-2A is based on the requirements, constraints, and concepts described in section 4.2. The hybrid motor is the essential part in a hybrid rocket and forms the starting point of the design. There are many approaches which can be used to develop a hybrid rocket motor such as scaling, apogee trade studies, or the use of an existing database (Figure 3.10). In this study, existing data related to the Peregrine sounding rocket shown in Table 4.2 (Dunn et al., 2007; Zilliac et al., 2012) is used as a guideline on design inputs. This is due to the lack of available test data of the Phoenix-1A flight motor, at the time of writing, to verify its performance for scaling. Stanford's Peregrine is similar to Phoenix-2A as it uses the same propellants and has the same apogee and payload mass specifications. The paraffin wax used in Peregrine however, has a different chemical formula. Peregrine was found to have an O/F ratio of 4 which is unusually low. This was a design choice by the Peregrine team due to

the specific application required and the possibility of higher combustion efficiencies in this region.

Table 4.2: Design parameters of the Peregrine hybrid sounding rocket (Dunn et al., 2007; Zilliac et al., 2012).

Peregrine Parameter	Description
Oxidiser	Nitrous oxide (N_2O)
Mass of oxidiser	435.0 kg
Fuel	SP1-A paraffin wax ($C_{32}H_{66}$)
Mass of fuel	107.0 kg
Gross mass	782.0 kg
Length	10.6 m
Outer diameter	0.5 m
Average thrust (at sea level)	62.3 kN
Burn time	18.0 s
Tank pressure	58.6 bar
Nominal chamber pressure	48.3 bar
Combustion efficiency	95%

A trade-off between ideal characteristic velocity and combustion efficiency is required to determine the optimised point, as little to no gain is provided if too much characteristic velocity is sacrificed. Testing of larger scale motors, as part of the Phoenix-2A project, should be conducted focusing on combustion efficiency at various O/F ratios. For this study the combustion efficiency was assumed constant for any O/F ratio as no hot-fire testing was conducted.

4.3.1 Hybrid Rocket Performance Code

HRPC-Motor Design Model

The final design inputs for the HRPC-Motor Design Model were established from an iterative process and are shown in Table 4.3. Higher design O/F ratio and thrust values were selected, above the average Peregrine values, due to the shift that occurs during the burn of a blowdown motor. The initial Phoenix-2A concept has a design O/F ratio of 7 as this value provides the highest characteristic velocity, produces lower combustion temperatures, and has a smaller optimum expansion ratio than the optimal ratio of 8 (Figure 4.3). The effect of various O/F ratios on apogee is discussed in Chapter 5.

Table 4.3: HRPC-Motor Design Model input parameters for the initial conceptual design of Phoenix-2A.

Phoenix-2A Parameters	Description
Oxidiser	Nitrous oxide (N_2O)
Oxidiser temperature	291.7 K
Fuel	Sasol 0907 paraffin wax ($C_{50}H_{102}$)
Fuel temperature	298.2 K
Fuel density	924 kg/m^3
Fuel enthalpy	-1438.2 kJ/mol
Design thrust	76 kN
Design O/F ratio	7
Design chamber pressure	40 bar
Tank pressure	60 bar
Nozzle design altitude	Sea level
Theoretical burn time	18 s
Flow composition	Equilibrium
Port diameter	0.252 m
Regression rate coefficient	0.000155
Regression rate exponent	0.5

The design chamber pressure of 40 bar represents a compromise between safety and performance, there is an increase in the pressure difference between the combustion chamber and oxidiser tank when compared to higher chamber pressures. This prevents the possibility of tank over-pressurisation due to the backflow of hot chamber gases, and mitigates feed-system-coupled instabilities. The regression rate coefficient and exponent were taken from experimental data for a paraffin wax and nitrous oxide hybrid rocket (McCormick et al., 2003). The intended launch site for the Phoenix-2A is the Denel Overberg Test Range (OTR) which is at sea level, hence the design nozzle altitude is 0 m. The inert fuel and oxidiser temperatures used in the HRPC-Motor Design Model are 298.2 K and 291.7 K respectively. The oxidiser temperature is equal to the average temperature of the tank during the blowdown of the motor which is conservative compared to when the maximum temperature is used.

The port area of the fuel grain is similar to the chamber area of a liquid rocket. It is the area where combustion occurs. A 4:1 fuel-port-to-throat-area ratio was selected to significantly reduce the throat pressure and thrust reduction losses as shown in Table 4.4 (Sutton and Biblarz, 2001), and so that uniform regression occurs (Casalino et al., 2012).

Table 4.4: Estimated losses for chambers with small diameters (Sutton and Biblarz, 2001).

Chamber-to-Throat-Area Ratio	Throat Pressure (%)	Thrust Reduction (%)	Specific Impulse Reduction (%)
∞	100	0	0
3.5	99	1.5	0.31
2.0	96	5.0	0.55
1.0	81	19.5	1.34
k=1.20; P_c/P_e=1000			

The diagram in Figure 4.4, shows the port diameter, D_p, and throat diameter, D_t, of a hybrid rocket. The throat diameter is proportional to the design thrust and inversely proportional to the design chamber pressure and thrust coefficient. The thrust coefficient is found using NASA CEA. The port diameter is found through a single feedback loop of the HRPC-Motor Design Model because the port diameter has no effect on the throat diameter. The throat diameter was found to be 0.126 m which resulted in a 0.252 m port diameter.
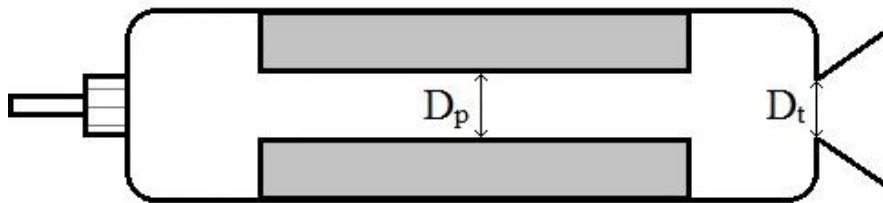
Figure 4.4: Hybrid rocket motor indicating port and throat diameter.

The outputs of the Motor Design Model were used to size the rest of the propulsion system including the nozzle and oxidiser tank. The outputs include a characteristic velocity, c^*, of 1618.60 m/s, thrust coefficient, C_F, of 1.52 and optimal expansion ratio, ε, of 5.77 for the conceptual design. The expansion ratio was used to determine the nozzle exit diameter of 0.303 m. The steady mass flow rates given by the model determine the mass of the propellants required. The fuel and oxidiser mass flow rates are 3.87 kg/s and 27.06 kg/s. The final grain geometry is 1.464 m in length and 0.368 m in diameter. A 4 mm thickness was added to the grain outer diameter to act as a buffer if the burn rate was higher in reality than simulated. This unused fuel increased the inert mass and was accounted for in the flight simulation.

HRPC-Performance Model

The motor performance was found using the HRPC-Performance Model. The inputs for this model are shown in Appendix A.1 and divided into the following sub-sections:

1. Blowdown system and oxidiser parameters
2. Atmospheric parameters
3. Feed system parameters
4. Simulation parameters
5. Performance correction factors
6. Motor, grain and nozzle geometry

The blowdown system parameters include the oxidiser mass, m_{ox}, tank mass, m_T, and tank volume, V_T, which are calculated using Equations (4.2), (4.3), and (4.4). To determine the mass of the tank, the structure is simplified to a cylindrical section with constant thickness and two hemispherical end caps. These can be improved in future designs to torispherical caps to reduce the overall length of the vehicle. The outer diameter of the oxidiser tank is restricted so that an angle of less than an 8° exists between the chamber and tank to prevent external flow separation from occurring (US Army Missile Command, 1990). The mass of the oxidiser tank, m_T, is determined by the material selection, as described below. The final tank volume, V_T, is determined by the mass of nitrous oxide, m_{ox}, required and a mandatory 15% ullage volume, V_{ull}, for safety, which adds significant inert mass. A design ullage volume trade study is discussed in Chapter 5.

$$m_{ox} = t_b \dot{m}_{ox} \qquad (4.2)$$

$$m_T = \rho_T V_{cyl} + \rho_T 2V_{hemi} \qquad (4.3a)$$

or

$$m_T = \rho_T \big[(\pi/4)\big(D_{cyl}^2 - d_{cyl}^2\big)L_{cyl}\big] + \rho_T\big[(4\pi/3)\big(R_{hemi}^3 - r_{hemi}^3\big)\big] \qquad (4.3b)$$

$$V_T = V_{ull}(m_{ox}/\rho_{ox}) \qquad (4.4)$$

Supercharging of the oxidiser tank with 0.05 kg of helium is specified to prevent cavitation in the feed system, to increase motor performance by boosting the chamber pressure, to prevent backflow from the chamber and to extend the liquid phase of the nitrous oxide (Lohner et al., 2006; Dyer et al., 2007). This results in a tank pressure of 60 bar.

Material selection of the major components is essential to ensure availability, manufacturability, and cost-effectiveness. The mass of the oxidiser tank affects the motor's performance due to mass and heat transfer variations of the liquid and vapour nitrous oxide inside, and is detailed in Chapter 5. Aluminium alloys were selected for both the oxidiser tank and combustion chamber casing because aluminium has a higher specific strength ratio than stainless steels and is cheaper than both stainless steel and titanium as illustrated in Figure 4.5 (Granta Design, 2009).
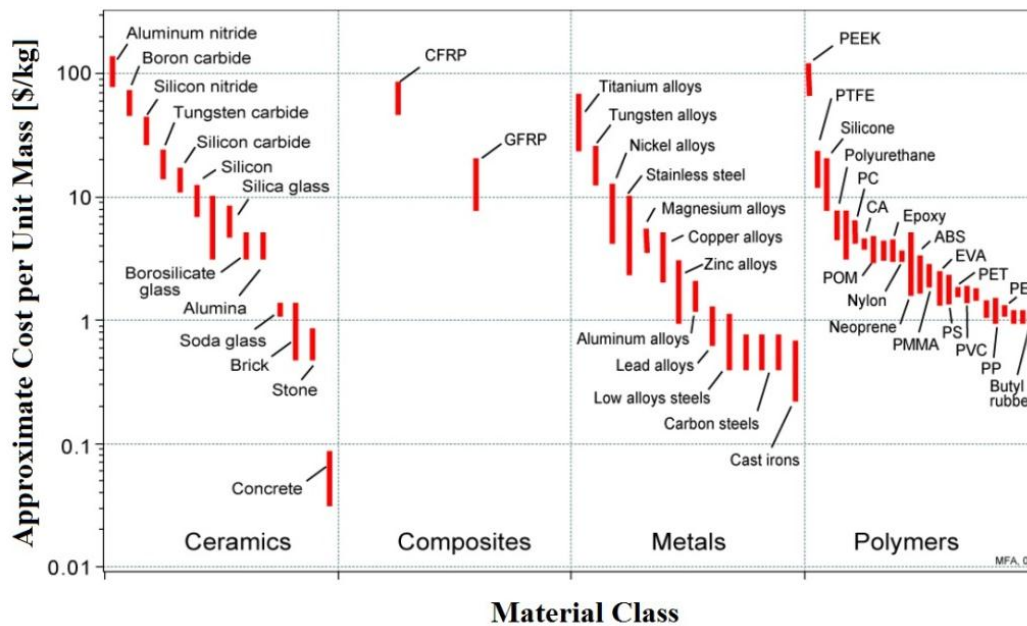
Figure 4.5: Material comparison of yield strength versus cost (Granta Design, 2009).

The oxidiser tank is the largest portion of the rocket and therefore it is important to keep the tank as light as possible. A compromise between specific strength, cost, and availability led to the selection of aluminium 2219-T851 and 6082-T6 alloys for the oxidiser tank and combustion chamber respectively. Aluminium 6082-T6 is the same material that was used for the Phoenix-1A combustion chamber and oxidiser tank. It is commonly available in South Africa and has good weldabilty.

Aluminium 2219-T851 was selected because it is easier to weld and has a better specific strength than common aluminium grades, such as 6082-T6, and is cheaper than aerospace alloys such as 7075-T6. Other favourable qualities include good resistance to corrosion and fatigue (Doran et al., 2009). The material data for these alloys is provided in Tables A.2, A.3, and A.4 in Appendix A.2. Complex filament-wound composite pressure vessels offer high specific strength for the design of the oxidiser tank and combustion chamber but are not feasible in terms of local availability.

The American Society of Mechanical Engineers (ASME) Code for Pressure Vessels Section VIII was used to determine the wall thickness, t, of the oxidiser tank and motor casing. Equation 4.5, based on hoop stress, was used (Megyesy, 2001):

$$t = P_d r / \left(\sigma_y E - 0.6 P_d \right) \qquad (4.5)$$

where σ_y is the yield strength of the material. The design pressure, P_d, includes a safety factor of 1.5 times, the maximum expected operating pressure (MEOP) (Federal Aviation Administration, 2005). The MEOP for the oxidiser tank is 1.1 times the working pressure of 60 bar. A joint efficiency, E, of 0.85 (Megyesy, 2001) is used to account for the welding of the oxidiser tank during fabrication. The MEOP for the combustion chamber is taken as 1.1 times 45 bar, which is 5 bar more than the selected chamber pressure of 40 bar in the Motor Design Model. This provides additional safety as pressure spikes may occur during testing due to combustion instability. The number of injector holes is selected to provide the desired burn time of 18 s.

The internal radius of the combustion chamber is dependent on the fuel grain outer diameter and thermal liner thickness. A 6 mm glass/cotton phenolic composite thermal liner is included to minimise heat transfer to the casing. The thickness is based on experience with Phoenix-1A (Geneivève, 2013) although further investigation should be performed during the testing phase of the project to determine the optimal thickness. Phoenix-2A has a shorter burn time with the same propellants, however caution is required since the combustion temperatures are expected to be higher due to a higher design O/F ratio. The final oxidiser tank and combustion chamber outer diameters are 0.413 m and 0.391 m respectively. This creates a taper angle of 1.7° between them.

The grain and nozzle geometry are Motor Design Model outputs. The motor geometry input is the free volume in the combustion chamber. This was determined based on the pre- and post-combustion chamber insert geometries. The chambers are included to provide time for the oxidiser to vapourise fully before coming into contact with the fuel and for complete mixing to occur. Length-to-diameter ratios of 0.5 and 1 were chosen for the pre- and post-combustion chambers respectively (Humble et al., 1995).

A shortened bell-shaped nozzle was selected because it is more efficient than a conical nozzle with similar parameters (Humble et al., 1995). An 80% bell-shaped nozzle (80% length of a conical nozzle length) was chosen as it provided an optimal performance-to-mass compromise. A 0.985 nozzle correction factor, λ, is included to decrease the performance of the motor and

therefore provided a more conservative design approach. The nozzle correction factor was obtained using Figure 4.6 (Humble et al., 1995).
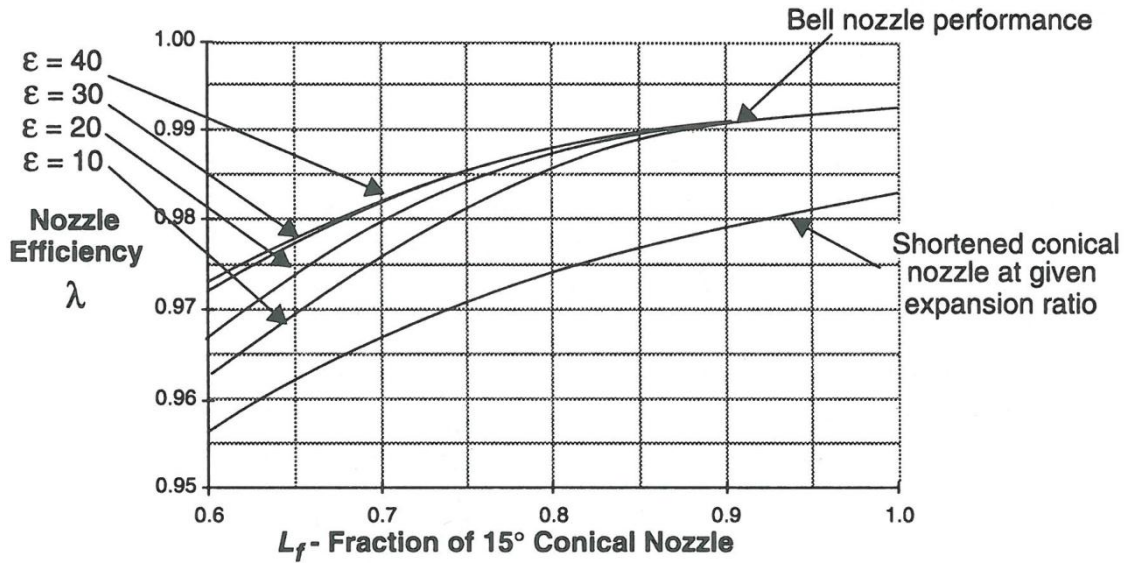
Figure 4.6: Graph representing nozzle efficiency (Humble et al., 1995).

The length of the conical nozzle is determined using Equation 4.6 (Humble et al., 1995), where D_e is the exit diameter of the nozzle, D_t is the nozzle throat diameter and θ_{cn} is the half angle of a conical nozzle. An additional 0.1 m length is added to the casing of the post combustion chamber for the converging section of the nozzle.

$$L_{noz} = (D_e - D_t)/(2 \tan \theta_{cn}) \qquad (4.6)$$

The simulations in this dissertation are modelled using only the liquid phase of nitrous oxide to give a conservative motor performance. A theoretical injector discharge coefficient is used, based on the required diameter for liquid flow (Sutton and Biblarz, 2001). The theoretical value is decreased to incorporate both discharge and viscous losses resulting in a conservative design (Karabeyoglu et al., 2007).

A combustion efficiency of 95% is assumed and equilibrium flow conditions are used in the HRPC-Performance Model (Humble et al., 1995). The combustion efficiency accounts for expected losses and is based on the design efficiency of Peregrine (Table 4.2). The pressure drop in the feed system is assumed to be 5 bar. An axial showerhead injector design is specified for simplicity, to promote hot gas re-circulation in the pre-combustion chamber, and to reduce the combustion instabilities that occur with conical injectors.

The pressure results obtained from the HRPC-Performance Model are shown in Figure 4.7. The tank, chamber, and nozzle exit pressures decrease during the burn due to the blowdown configuration of the rocket. The tank is supercharged to 60 bar with helium. The brown line illustrates the pressure at the inlet of the injector which is equal to the tank pressure minus the assumed 5 bar pressure loss in the feed system.
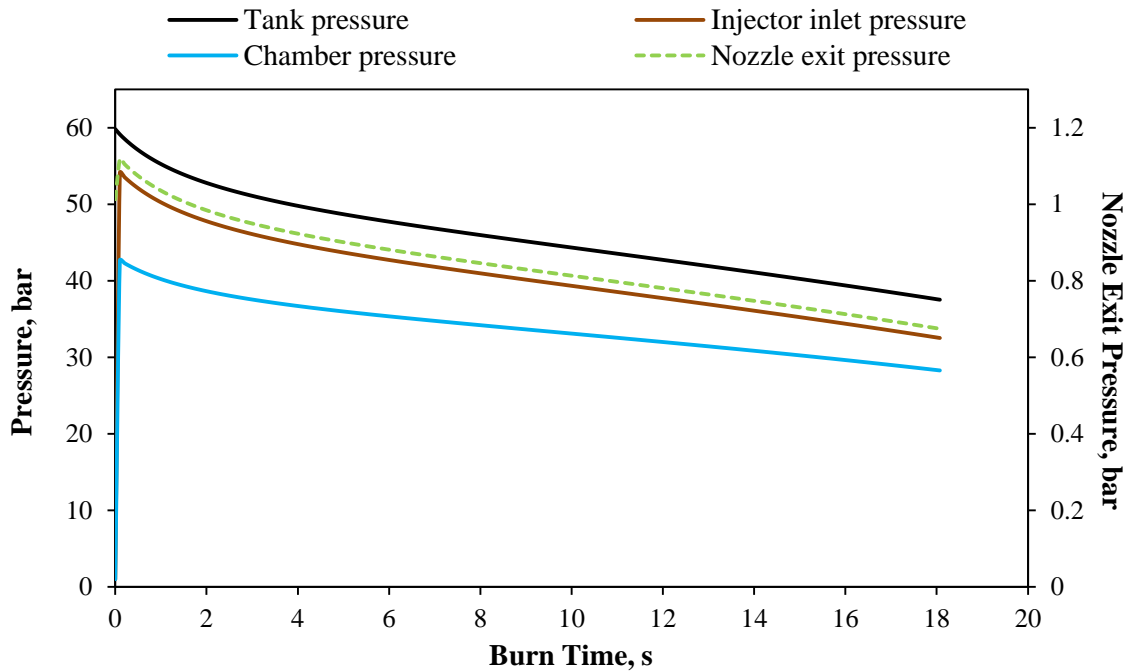
Figure 4.7: Pressure versus burn time for the conceptual Phoenix-2A design.

The wall of the combustion chamber casing is designed with adequate thickness to accommodate the maximum pressure which is 43 bar. This is higher than the design value (40 bar) due to the number of injector holes restricting the burn time and not the maximum chamber presure. The exit pressure shown in Figure 4.7 was calculated using NASA CEA and based on the expansion ratio, O/F ratio, and chamber pressure of the motor. The nozzle is designed for atmospheric pressure at sea level, however due its constant geometry the exit pressure only equals the design atmospheric pressure once during the burn. The exit pressure corresponds to sea level pressure (1 bar) when the chamber pressure equals its design value of 40 bar. This occurs 1.1 s into the burn. The steady state design parameters, found using the HRPC-Motor Design Model, are also only found once during the burn due to the blowdown delivery system used in the HRPC-Performance Model.

The conceptual design of Phoenix-2A is intended to minimise combustion instabilities. The injector ensures that the pressure drop is greater than or equal to 15% relative to the chamber pressure, and the oxidiser mass flux is kept below 650 kg/m^{2}s (Figure 4.8). The oxidiser, fuel,

and nozzle mass flow rates are depicted in Figure 4.9. The oxidiser and nozzle flow rates decrease with time due to the decreasing tank pressure. The fuel mass flow rate decreases at a much lower rate.
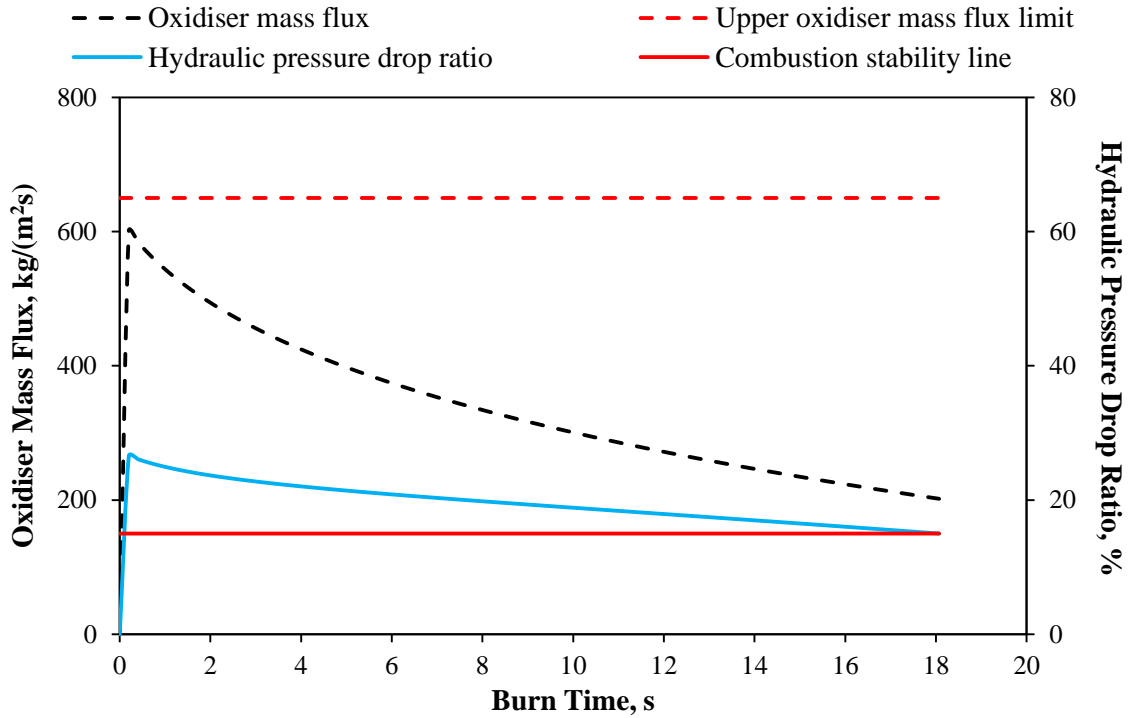
Figure 4.8: Oxidiser mass flux and hydraulic pressure drop ratio of the conceptual Phoenix-2A design.
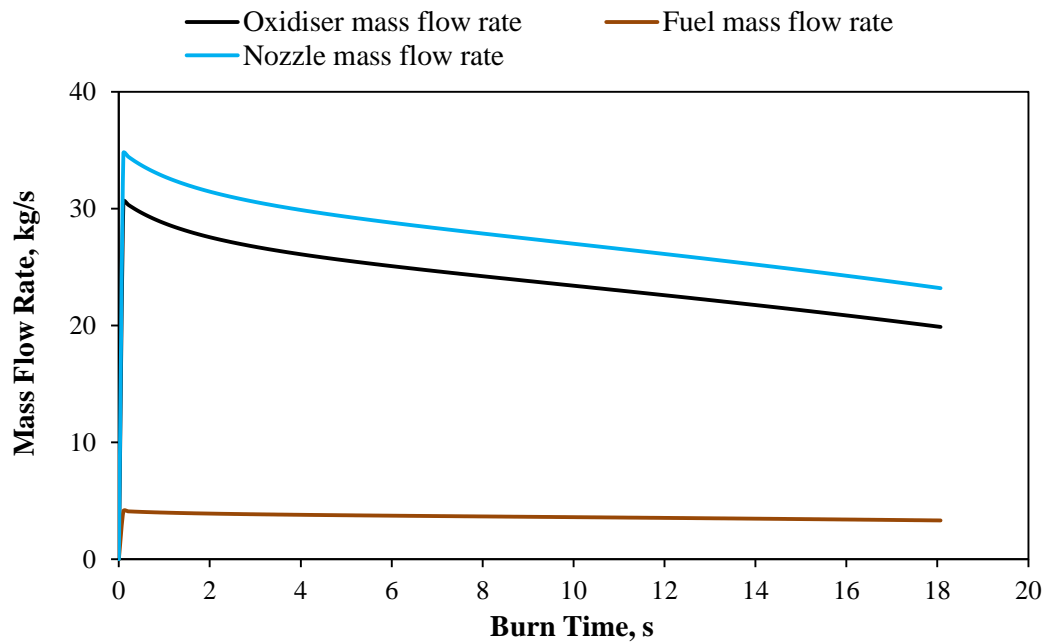
Figure 4.9: Mass flow rate versus burn time for the conceptual Phoenix-2A design.

4.3.2   6 DOF Flight Dynamics Simulator

The vehicle geometry with correct mass distribution is modelled in the flight dynamics software using simplified geometries. The external structure is made up of a nose cone, recovery system bay, oxidiser tank, interstage structure, combustion chamber, fins, and boat-tail. The nose cone selected for the concept design is a Von Kármán ogive which gives better drag characteristics at supersonic Mach numbers relative to most other shapes, as illustrated in Figure 4.10 (Crowell, 1996), where the key is (1) superior, (2) good, (3) fair, and (4) inferior.
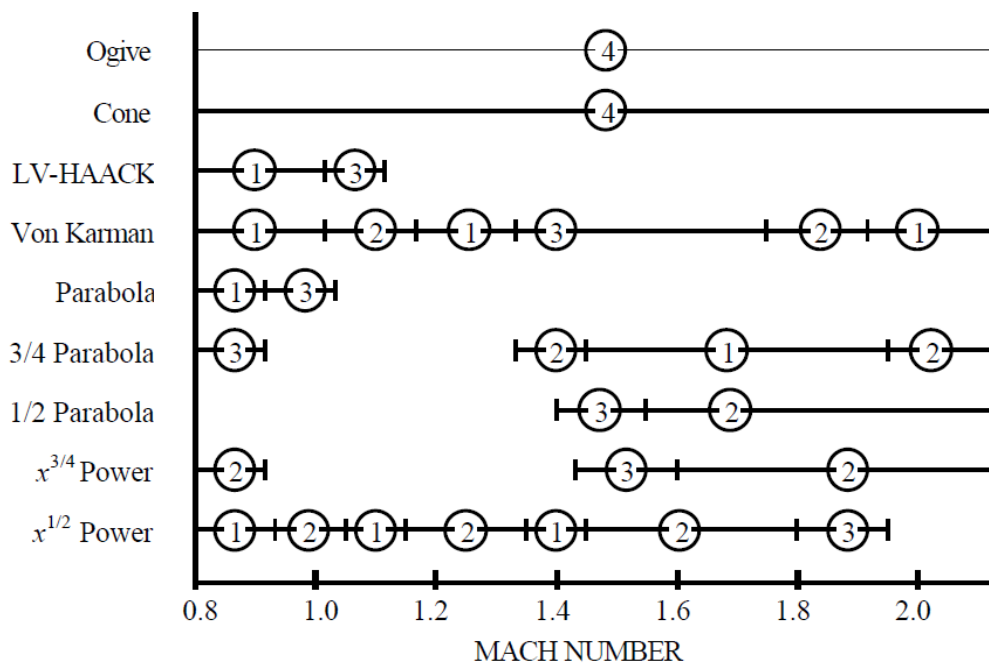
Figure 4.10: Drag characteristic versus Mach number for various nose cone shapes (Crowell, 1996).

The base diameter of the nose cone is equal to the outer diameter of the oxidiser tank. The nose cone length divided by its base diameter is known as the fineness ratio, and was selected to be 3.5 calibre (the maximum diameter of the rocket is equal to one calibre). This was chosen to reduce wave drag and provide adequate payload space compared to lower fineness ratios, and to reduce skin friction compared to higher fineness ratios. A sharp nose cone tip was selected. An investigation into blunting the nose cone tip is conducted in Chapter 5. It is assumed that the airframe sections will be fastened together using joints that limit the formation of surface protrusions, such as V-band joints (Schindwolf et al., 1998) and radax joints (Weydert, 1968).

Four trapezoid fins set up in a cruciform shape were selected for the conceptual design as they offer stability and reliability should a fin shear off the airframe. A trapezoid planform gives the

best control effect, as shown in Figure 4.11 (Fleeman, 2001), and shows no major weakness in design. A hexagonal aerofoil is used for strength and stiffness with maximum thickness occurring at the centre of fin.
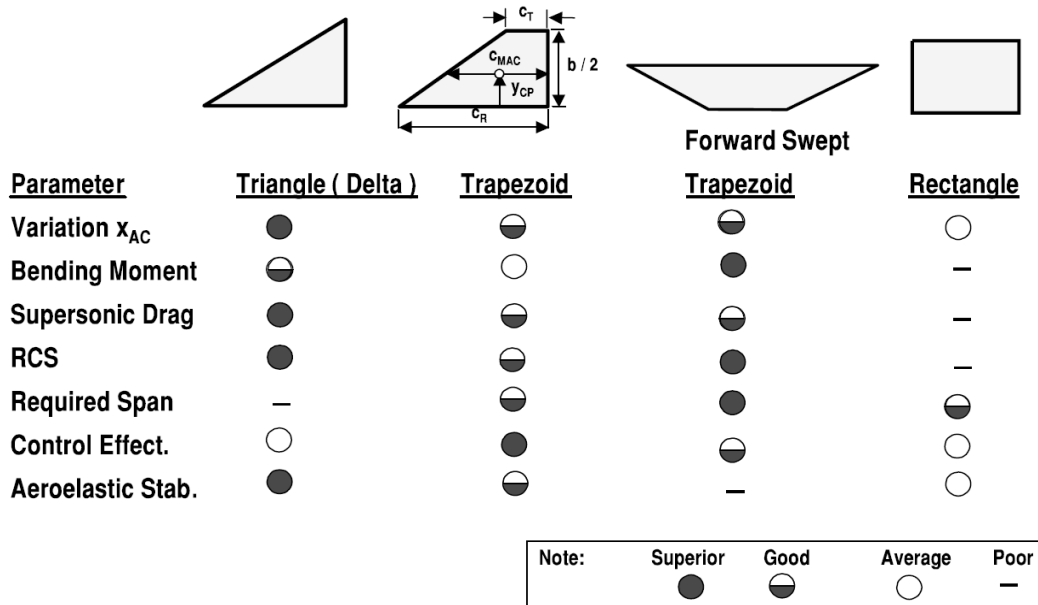
Figure 4.11: Fin planform comparisons (Fleeman, 2001).

The leading and trailing edge length are 10% of the length of the fin at the half span height. The edges are blunted slightly to weaken the shock wave at supersonic speeds. The issue of fin flutter is addressed in Chapter 5. A straight boat-tail equal to the diameter of the combustion chamber casing is included. The boat-tail's outer diameter caters for the thickness of the nozzle, thermal protection liner, and boat-tail housing material. A tapered boat-tail is generally preferred to reduce base drag but has been shown to have less affect at high Mach numbers (Fleeman, 2001). The interstage structure connects the oxidiser tank to the combustion chamber.

The vehicle component masses are compared to those of Peregrine (Dyer et al., 2007) in Figures 4.12 and 4.13, indicating a fair degree of similarity. A significant difference is that there is no pressurant system for Phoenix-2A, which was later excluded from the Peregrine design (Zilliac et al., 2012). The helium used for supercharging the Phoenix-2A oxidiser tank is included in the oxidiser mass.

A 5 kg scientific payload is located in the nose cone as stipulated by the mission statement. A detailed recovery system was not included in the conceptual design however an estimated mass of this system is used in the simulation. The mass of auxiliary components such as the flight

computer and sensors are included and assigned to avionics. The mass of the 0.5 m long feed system is included under the valves/plumbing label of Figure 4.12.
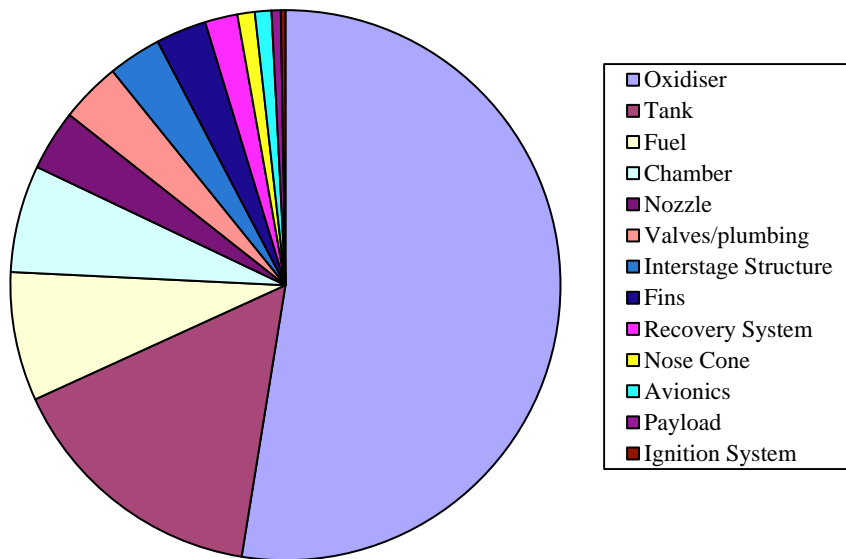
Figure 4.12: Phoenix-2A conceptual design mass distribution.
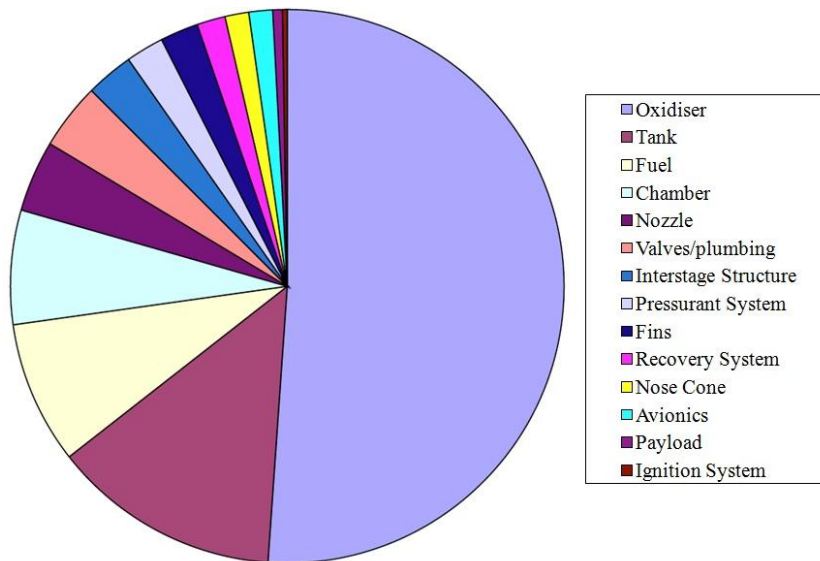
Figure 4.13: Peregrine mass distribution during its preliminary phase (Dyer et al., 2007).

The nozzle mass, m_{noz}, was estimated using Equation 4.7 (Humble et al., 1995) based on propellant mass, m_{prop}, and the nozzle expansion ratio, ε:

$$m_{noz} = 125\left(m_{prop}/5400\right)^{3/4}(\varepsilon/10)^{1/4} \qquad (4.7)$$

A mass equal to 10% of the combustion chamber is included to account for a thrust skirt, as described by Humble et al. (1995) and a 5 kg buffer is included for all the nozzle mass calculations. The overall mass for the conceptual Phoenix-2A design is 145 kg heavier than Stanford's Peregrine.

The flight trajectory of the rocket was modelled using the Flight Dynamics Simulator, which requires the motor's time-dependent exit pressure, P_e, and the momentum term, made up of the nozzle mass flow rate, $\dot{m}_{noz}$, and the exit velocity of the nozzle, v_e, from the HRPC. It calculates the vehicles thrust, F, using Equation 4.8. The simulator uses the rocket's position to determine the corresponding atmospheric pressure, P_{atm}, during the boost phase:

$$F = \dot{m}_{noz}v_e + (P_e - P_{atm})A_e \qquad (4.8)$$

Propellant variations were included to investigate the mass reduction and changes in the centre of mass, due to the regression of the fuel grain and the draining of the oxidiser tank. The variations are modelled as linear in the Flight Dynamics Simulator which deviate from the HRPC values. The slight difference illustrated in Figure 4.14 and the effects they have on the performance was assumed negligible. A future goal of the Phoenix programme is to integrate the HRPC and the Flight Dynamics Simulator, allowing the propellant variations to be modelled based on the HRPC values.
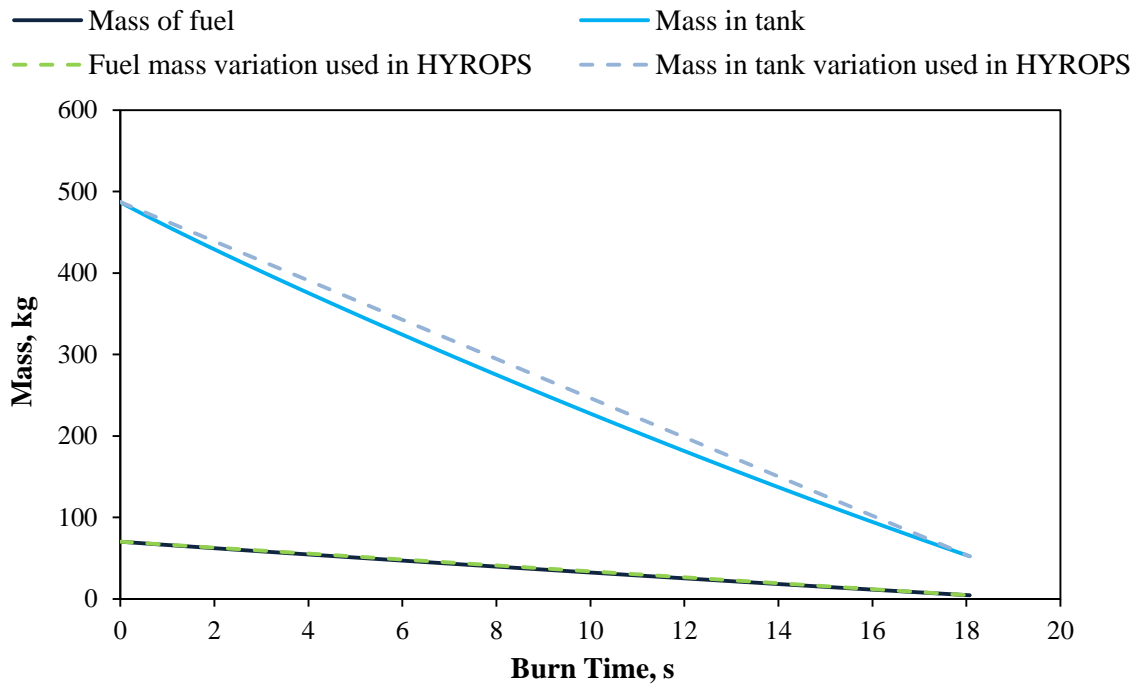
Figure 4.14: Propellant mass variation versus burn time.

The aerodynamic data for the vehicle was obtained using RASAero. The fully turbulent flow and Rogers Modified Barrowman Method options in RASAero were selected for all simulations in this dissertation. The Rogers Modified Barrowman Method provides better accuracy for the subsonic centre of pressure at low angles of attack than the Barrowman Method. The modified method includes the fuselage flow interactions such as fin-fuselage interference and viscous flow across the fuselage which is excluded from the Barrowman Method. A polished surface finish was selected. RASAero limits the aerodynamic characteristics to angle of attacks of up to 15° and Mach number up to 5. The results of the conceptual design of the Phoenix-2A rocket demonstrate that the rocket does not exceed this Mach number limitation. Large angles of attack are expected to occur as Phoenix-2A re-enters the atmosphere on its descent. The simulation can limit the angle of attack so that the RASAero constraint does not affect the trajectory.

The launch of Phoenix-2A was simulated from OTR in the Western Cape of South Africa with a launch angle of 85°. The rocket was launched towards the ocean as a safety precaution. A designed launch rail of 15 m was used to support the entire vehicle and to allow the rocket to reach a large enough velocity when exiting the rail, for stability, if ground winds are present. If a longer rail length is constructed the Phoenix-2A rocket would reach a higher apogee. A longer rail has the ability to launch rockets with a larger dimensional envelope and therefore incorporates launch facility growth in a cost-effective manner.

4.3.3   Results

Figure 4.15 shows the significant effect which varying the propellant mass fraction, ζ, (the propellant mass, m_{prop} divided by the total mass, m_{tot}) by 1% has on the flight performance. The flight trajectory path of the rocket that achieved a 100 km apogee is represented by a blue line.

$$\zeta = {m_{prop}}/{m_{tot}} \qquad (4.9)$$

This flight path corresponds to a propellant fraction of 0.6 and is lower than the Peregrine value of 0.7. Peregrine initially had an aluminium combustion chamber but it has been redesigned to a filament-wound composite to reduce inert mass and therefore improve the propellant mass faction. The results indicate that increasing the propellant mass fraction by reducing the inert mass improves the apogee of the rocket. The Mach number remains below 5 in the supersonic regime. The conceptual design achieves stable flight since the minimum distance between the centre of pressure and centre of mass (static margin) was 1.6 calibre during flight. This is

greater than the recommended value of 1 calibre (Niskanen, 2009). Vehicle spin and wind modelling are discussed in Chapter 5.
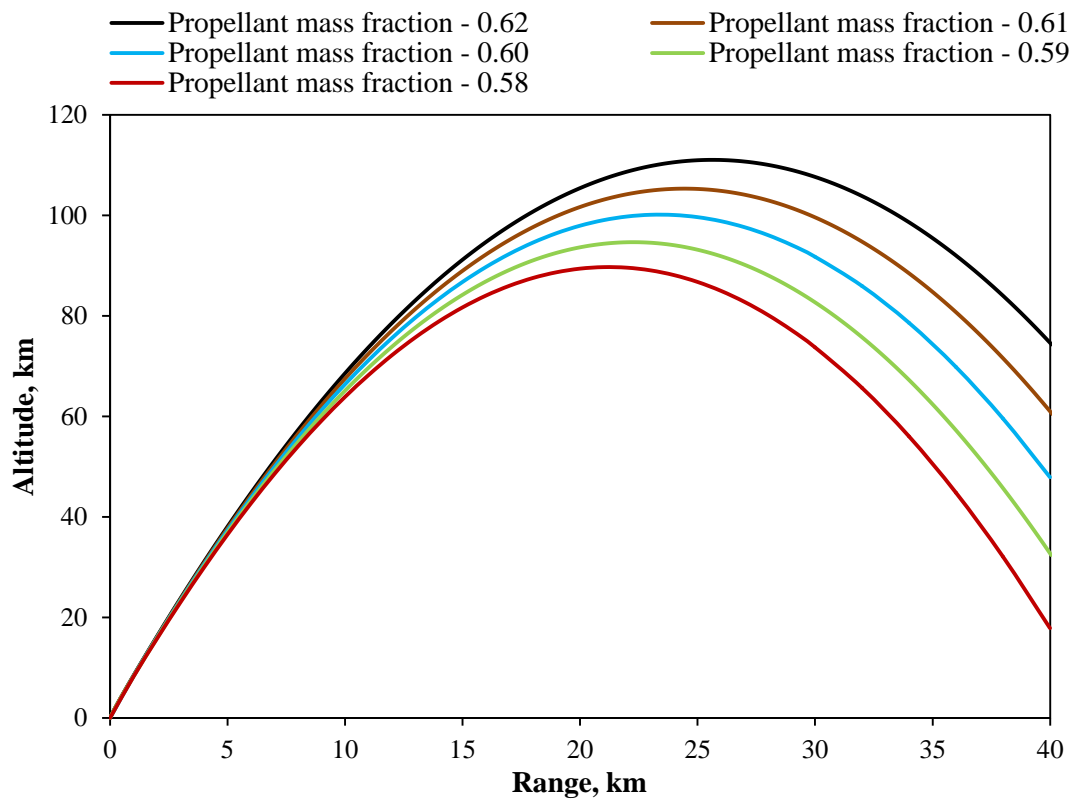
Figure 4.15: Altitude versus range for the Phoenix-2A conceptual design.

Recent hot-fire testing of Peregrine has shown that the highest practical combustion efficiency obtained is 93% and not the desired 95% (Zilliac et al., 2012). The effect of changing the combustion efficiency on the altitude of the conceptual Phoenix-2A design is illustrated in Figure 4.16. The vehicle with 100% combustion efficiency trajectory had the highest burnout altitude, escaping the dense atmosphere the fastest and thus had less resistance retarding it.

The conceptual design was modified so that a 100 km apogee could be achieved with 93% combustion efficiency. The thrust was increased until the rocket met the mission requirements; a 9 kN increase was necessary. Figure 4.17 demonstrates that the new conceptual design follows the same trajectory path as before. Figures A.1 to A.2 in Appendix A.3 illustrate a comparison between the momentum thrust, tank, and chamber pressures of the two designs. The pressures remained similar due to the same design chamber pressure and amount of helium used. The increase in thrust means more propellant is required and thus a longer grain and oxidiser tank are necessary. The external diameter of the tank was kept constant and so the aerodynamic characteristics only varied due to the increased length of the vehicle.
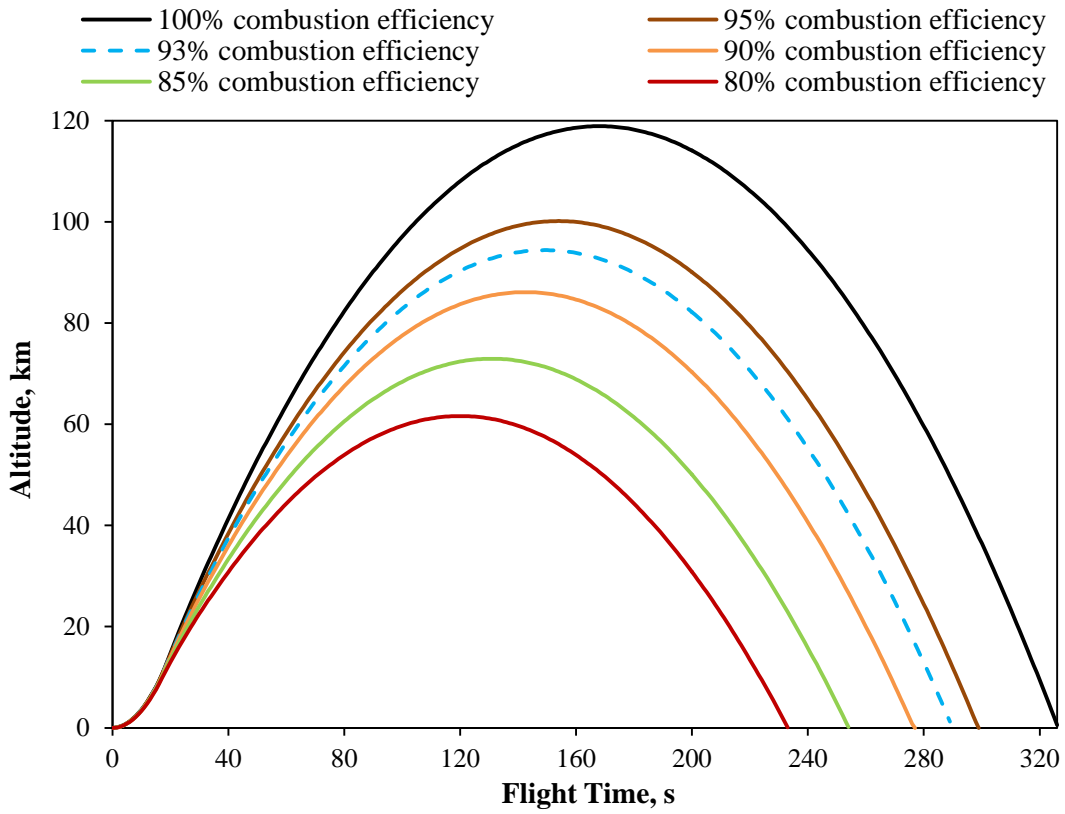
Figure 4.16: Effects of varying the combustion efficiency on altitude for the Phoenix-2A conceptual design.
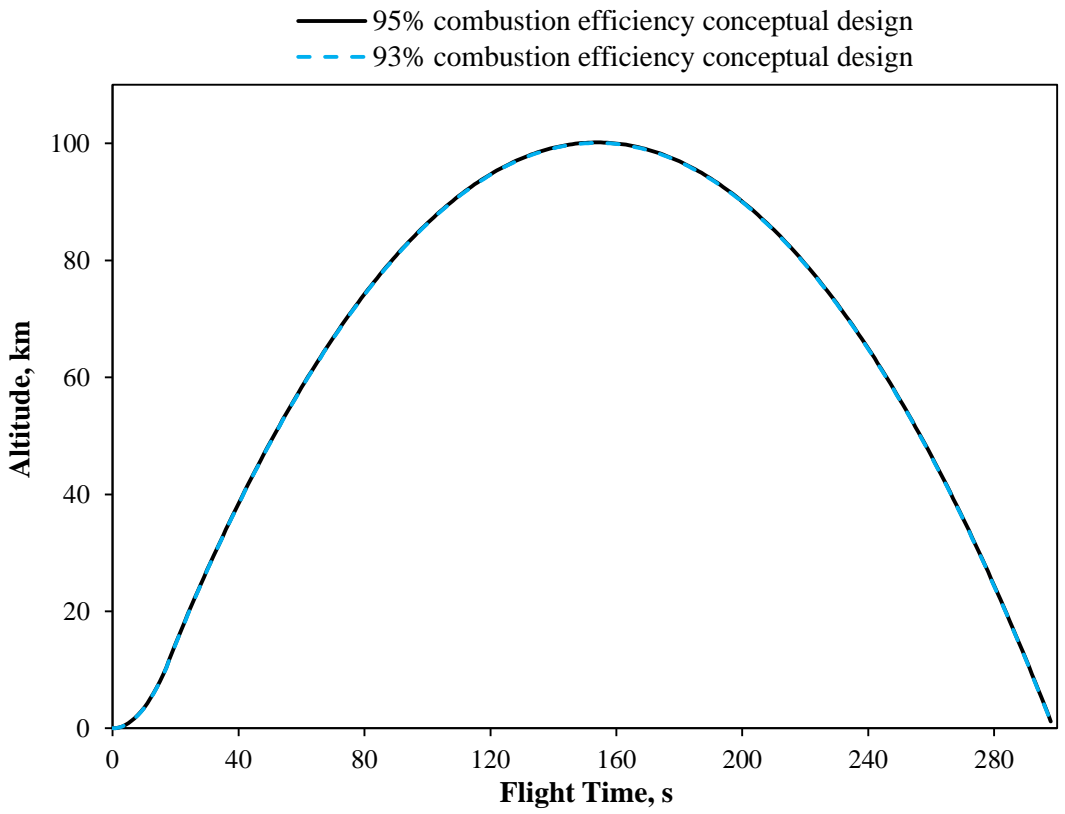
Figure 4.17: Altitude versus flight time for the 95% and 93% combustion efficiency designs.

66

The differences in mass between the 95% and 93% combustion efficiency designs are given in Table 4.5. The total mass increases by 10.6% for the final Phoenix-2A design with 93% combustion efficiency while maintaining the same propellant mass fraction of 0.6.

Table 4.5: Mass differences between the 95% and 93% combustion efficiency designs.

Component	95% efficiency (kg)	93% efficiency (kg)	Difference (%)
Oxidiser	487.1	544.7	11.2
Tank	145.0	162.0	11.1
Fuel	70.2	77.6	10.4
Combustion chamber	58.4	64.9	10.5
Nozzle	33.0	35.0	5.9
Valves/plumbing	33.0	35.0	5.9
Interstage structure	29.0	33.0	12.9
Fins	27.5	27.5	-
Recovery system	17.7	25.1	34.1
Nose cone	9.5	9.5	-
Avionics	9.0	9.0	-
Payload	5.0	5.0	-
Ignition system	2.5	2.5	-
Total	927.0	1031.0	10.6

The parabolic flight trajectory of the selected conceptual design is shown in Google Earth in Figure 4.18. This figure illustrates a vehicle launch from OTR near Cape Agulhas, South Africa, at an angle of 85°.

Figure 4.18: HYROPS flight path of the final conceptual design of Phoenix-2A.

The final conceptual design utilising 93% combustion efficiency is shown in Figure 4.19. This figure also indicates the difference between the two Phoenix programme vehicles; Phoenix-1A and the conceptual Phoenix-2A design.
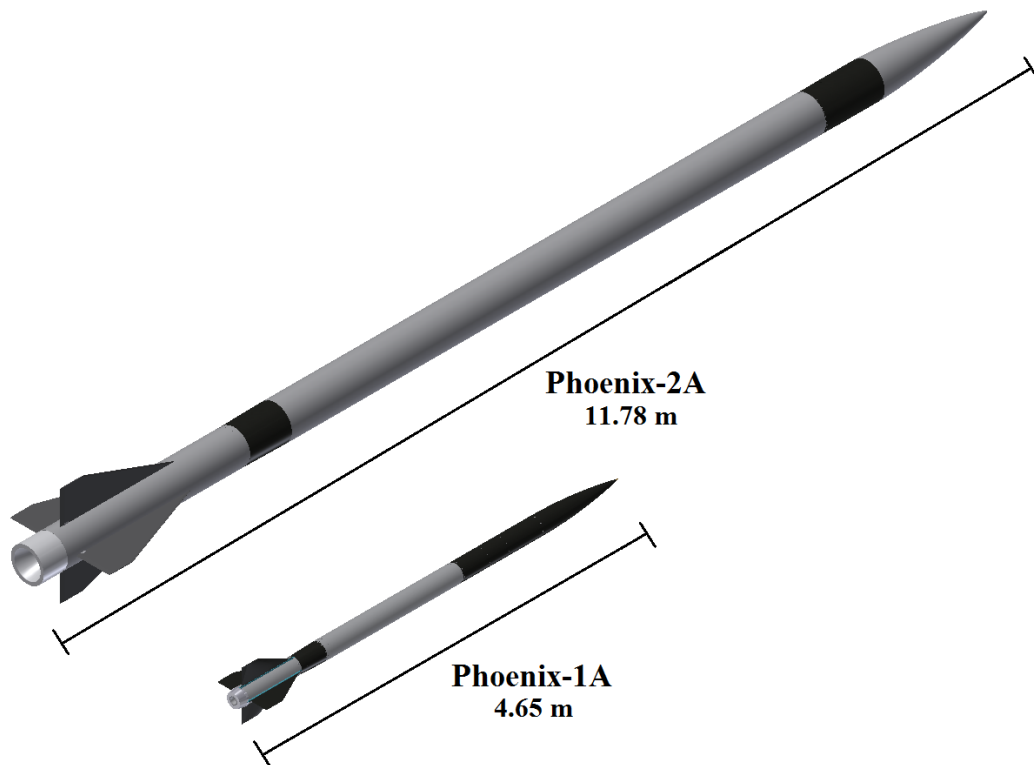
Figure 4.19: Visual comparison between the Phoneix-1A rocket and the Phoenix-2A conceptual design.

4.3.4   Summary

The conceptual design phase was carried out based on the mission statement and pre-existing hybrid rocket vehicle data from the Stanford Peregrine Sounding Rocket Program. The Phoenix-2A mass distribution was compared with Peregrine to ensure design assumptions were reasonable. The aim of this dissertation is to model the performance of a 100 km apogee hybrid rocket and therefore the altitude was restricted to this apogee. Continual performance analysis should be conducted throughout the design procedure to ensure that the rocket achieves its objective. The final conceptual design has a combustion efficiency of 93% to match the highest combustion efficiency achieved in large-scale testing of nitrous oxide and paraffin wax motors in the Peregrine hot fire tests. Designing for lower efficiency increases the conservative nature of the design. The conceptual design forms the foundation for the propulsion parametric trade studies in Chapter 5.

CHAPTER 5

Parametric Trade Study

This chapter investigates the effects which various design parameters of a hybrid rocket have on its performance. The initial concept of Phoenix-2A, discussed previously, is used as the base design for a series of parametric trade studies. These studies are performed, using the HYROPS software, to identify the most appropriate range of each parameter for a 100 km hybrid sounding rocket carrying a 5 kg payload. The results of the trade studies are discussed and used to identify key parameters for minimising cost, length, and mass, so as to reach the desired 100 km apogee. The results are preliminary and further analysis of each component is necessary to determine structural integrity and thermal performance.

5.1 Propulsion Trade Study

The parameters considered as part of the propulsion trade study were chamber pressure, O/F ratio, nozzle design altitude, fuel grain geometry, ullage volume, and thrust. The methodology used for evaluating each parameter is discussed in the sections below, including how variations affect the geometry and performance of each motor.

The combustion stability was also checked for each new motor design. Motor configurations that give a pressure drop across the injector relative to the chamber pressure ($\Delta P_{inj}/P_c$), referred to as the hydraulic pressure drop ratio, below 15% and an oxidiser mass flux above 650 kg/m^{2}s are disregarded because they are assumed to produce unstable combustion. During the trade study, any resultant geometry changes of the propulsion system were modified in the vehicle structure of the Flight Dynamics Simulator and the corresponding aerodynamic characteristics were updated. The Flight Dynamics Simulator modelled the flight performance of the updated design and determined if the objective was achieved. The selection of the design parameters was based on the HYROPS results.

5.1.1   Chamber Pressure

An increase in chamber pressure results in an increase of the specific impulse (Figure 3.7). Specific impulse, I_{sp}, refers to a rocket's efficiency and is a common term used when comparing motor performance (Sutton and Biblarz, 2001). It is defined as the total impulse, I_t per unit weight of propellant, (Equation 5.1), where $I_t = Ft_b$. An increase in chamber pressure

in the motor may cause the combustion to become unstable due to the smaller pressure difference between the oxidiser tank and combustion chamber. The addition of helium into the oxidiser tank was also considered because it raises the initial tank pressure and therefore increases the pressure difference across the injector. Increasing the oxidiser tank and combustion chamber pressure results in larger wall thicknesses required due to larger stresses, affecting the inert mass of the rocket. A trade study on the chamber pressure is necessary to determine the pressure range that provides a balance in performance, combustion stability, geometry, and cost.

$$I_{sp} = F/(\dot{m}_{noz}g) \qquad\qquad (5.1)$$

Methodology

This trade study was performed by constraining the maximum chamber pressure to the design value. The scenarios governing the variation in chamber pressure are shown in Figure 5.1. Scenario 1 includes five vehicles with different maximum chamber pressures and no helium supercharging.
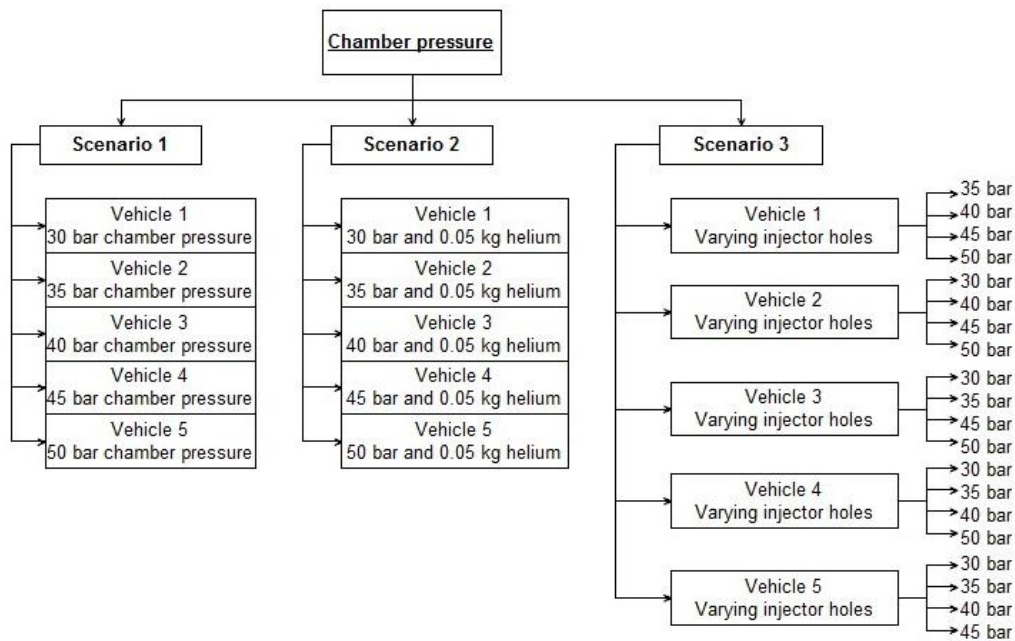
Figure 5.1: Scenarios investigated in the chamber pressure trade study.

Scenario 2 modifies the first five motors by adding 0.05 kg of helium to the oxidiser tank to increase the pressure. The advantages of adding helium are to mitigate cavitation that could occur in the feed system, and to help improve combustion stability by creating a greater pressure difference between the tank and the chamber. Scenario 3 takes the motors from

Scenario 2 and varies the number of injector holes. This constrains the oxidiser mass flow rate and the chamber pressure, shedding light on the variation of the injector area (throttling) of the motors of Scenario 2.

The vehicle geometry and propellant mass fraction are kept constant unless otherwise specified. Table B.1 in Appendix B, gives the design inputs for the HRPC-Motor Design Model. These inputs are the same as the initial conceptual design except for the design chamber pressure which varies from 30 to 50 bar in 5 bar increments. The size of the injector holes remains the same for all the scenarios as the coefficient of discharge is known from literature (Sutton and Biblarz, 2001). Future work should involve comparing different size holes with experimental discharge coefficients.

Results

The design chamber pressures for Scenario 1 and 2 were set to equal the maximum chamber pressure during the burn time of the motor, as depicted in Figure 5.2. This figure only shows the chamber pressures that produced stable combustion, and illustrates that the chamber pressure decreases at a faster rate and has a longer burn time when the oxidiser tank is supercharged with helium.
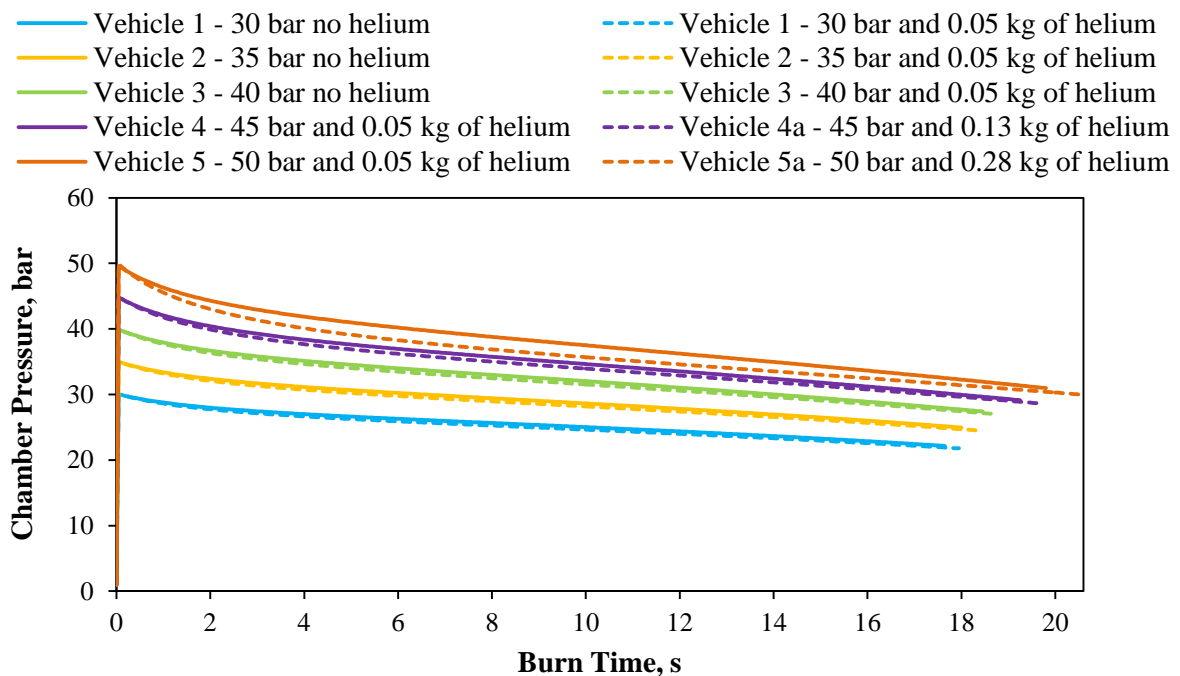
Figure 5.2: HRPC-Performance Model output of chamber pressure versus burn time for Scenario 1 and 2.

The HRPC-Motor Design Model outputs the motor and nozzle geometries. The thrust coefficient obtained from NASA CEA was found to increase with the inverse pressure ratio

input (P_c/P_{atm}), as illustrated in Figure 5.3. This is due to a constant design atmospheric pressure for all the vehicles. The characteristic velocity increases slightly with increasing chamber pressure for a design O/F ratio above 6, as shown in Figure 5.4. The results in Figures 5.3 and 5.4 do not include helium supercharging.
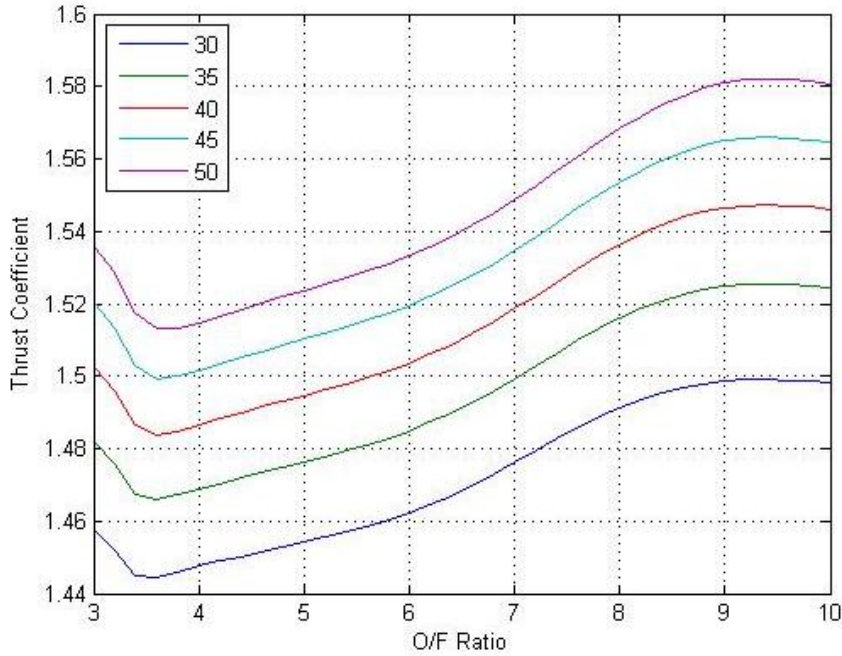
Figure 5.3: HRPC-Motor Design Model output of thrust coefficient versus O/F ratio for varying chamber pressure.
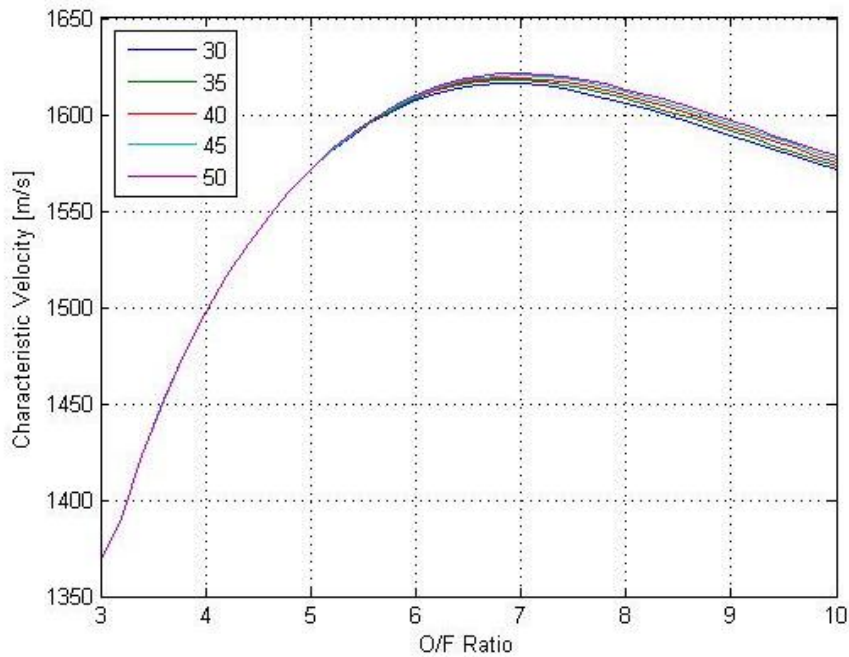
Figure 5.4: HRPC-Motor Design Model output of characteristic velocity versus O/F ratio for varying chamber pressure.

The nozzle mass flow rate, $\dot{m}_{noz}$, is inversely proportional to the thrust coefficient, C_F, combustion efficiency, η, and the characteristic velocity, c^* (Equation 5.2). It decreases with increasing chamber pressure, P_c, because the design thrust, F_d, is kept constant. The fuel and oxidizer mass flow rates are directly proportional to the nozzle mass flow rate (Equations 3.3 and 3.4). This results in a reduction in total mass for the vehicles that have the same propellant mass fraction.

$$\dot{m}_{noz} = (P_c A_t)/(\eta c^*) = [P_c/(\eta c^*)] \, [F_d/(P_c C_F)] = F_d/(\eta c^* C_F) \qquad (5.2)$$

$$A_t/A_e = \left(\frac{k+1}{2}\right)^{1/(k-1)} \left(P_e/P_c\right)^{1/k} \sqrt{\frac{(k+1)}{(k-1)}\left[1 - \left(P_e/P_c\right)^{(k-1)/k}\right]} \qquad (5.3)$$

The variation in motor parameters from the HRPC-Motor Design Model is illustrated in Table 5.1. It clearly indicates the reduction in propellant mass for an increase in design chamber pressure. The oxidiser mass decreases at a greater rate than the fuel because the oxidiser mass is dependent on both the nozzle and fuel mass flow rate. The nozzle expansion ratio is greater for a larger design chamber pressure. Equation 5.3 illustrates that the nozzle expansion ratio, ε, which is equivalent to the exit area divided by the throat area of the nozzle, A_e/A_t, is proportional to the chamber pressure. This equation includes the specific heat ratio, k, and the nozzle exit pressure, P_e.

Table 5.1: HRPC motor output parameters for various design chamber pressures.

Motor parameter		Design Chamber Pressure				
		30 bar	35 bar	40 bar	45 bar	50 bar
Fuel Grain	Length (m)	1.572	1.559	1.548	1.539	1.532
	Port diameter (m)	0.313	0.287	0.267	0.250	0.236
	Outer diameter (m)	0.411	0.390	0.375	0.363	0.353
Nozzle	Expansion ratio	4.74	5.26	5.76	6.25	6.73
	Throat diameter (m)	0.1563	0.1436	0.1335	0.1252	0.1182
	Exit diameter (m)	0.3402	0.3294	0.3205	0.3131	0.3067
Propellant	Fuel mass (kg)	80.2	78.9	77.8	76.9	76.2
	Oxidiser mass (kg)	561.4	552.2	544.7	538.5	533.3

Scenario1

The results in Figures 5.5 and 5.6 from Scenario 1 indicate that vehicles 4 and 5 have a $\Delta P_{inj}/P_c$ less than 15% which may produce unstable combustion. The oxidiser mass flux of vehicle 5 was also greater than the upper mass flux limit.
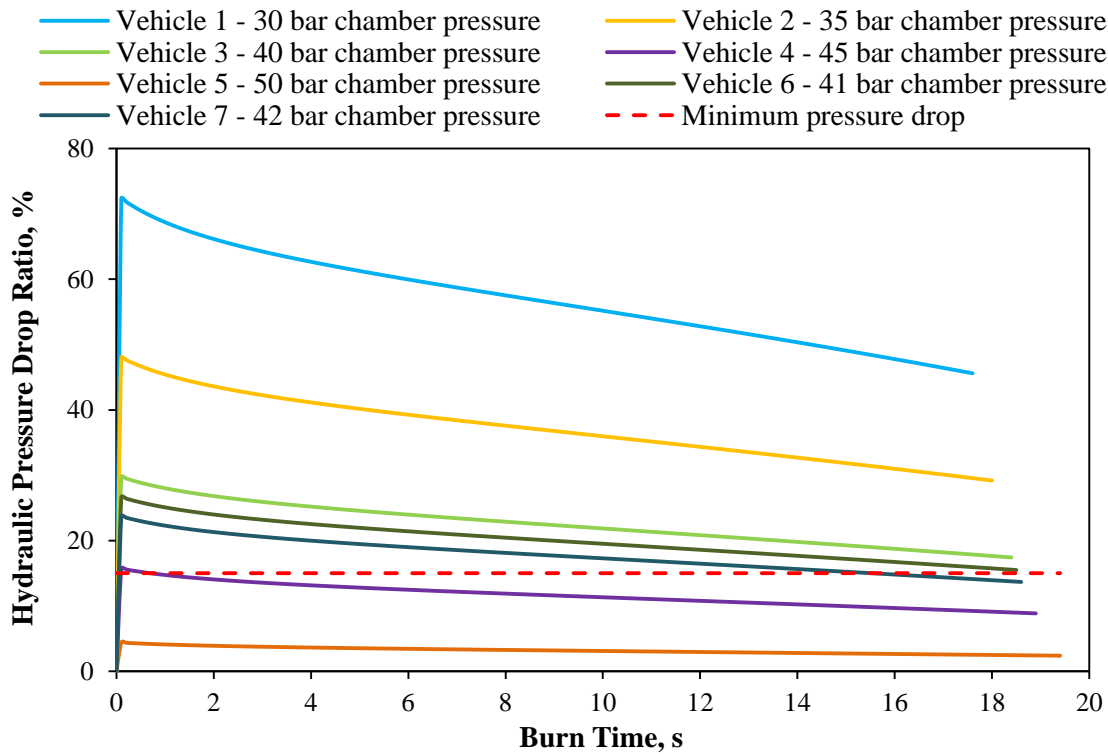
Figure 5.5: Hydraulic pressure drop ratio versus burn time for various design chamber pressures - Scenario 1.

Intermediate pressures were investigated to determine the maximum design chamber pressure that produces stable combustion in this scenario. These pressures were 41 bar, 42 bar, 43 bar, and 44 bar, denoted as vehicle 6 to 9 respectively. The results indicate that a design chamber pressure of 41 bar is the only intermediate pressure that has a $\Delta P_{inj}/P_c$ greater than 15% (Figure 5.6).

Figure 5.7 shows that the apogee improves with an increase in the design chamber pressure. The design thrust (maximum thrust) was kept constant for all the vehicles. The rate at which the thrust decreases is faster for a higher design chamber pressure, as illustrated in Figure 5.8, because of the faster rate of decrease in pressure (Figure 5.2) and thus limits the increase apogee.
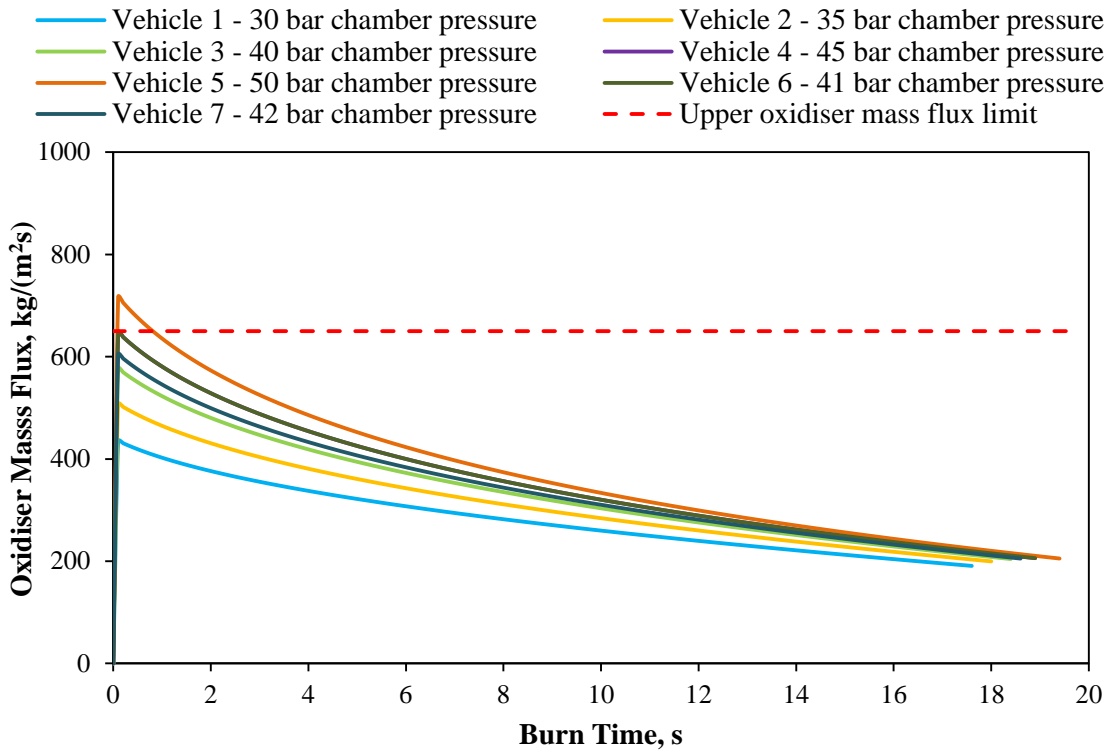
Figure 5.6: Oxidiser mass flux versus burn time for various design chamber pressures - Scenario 1.
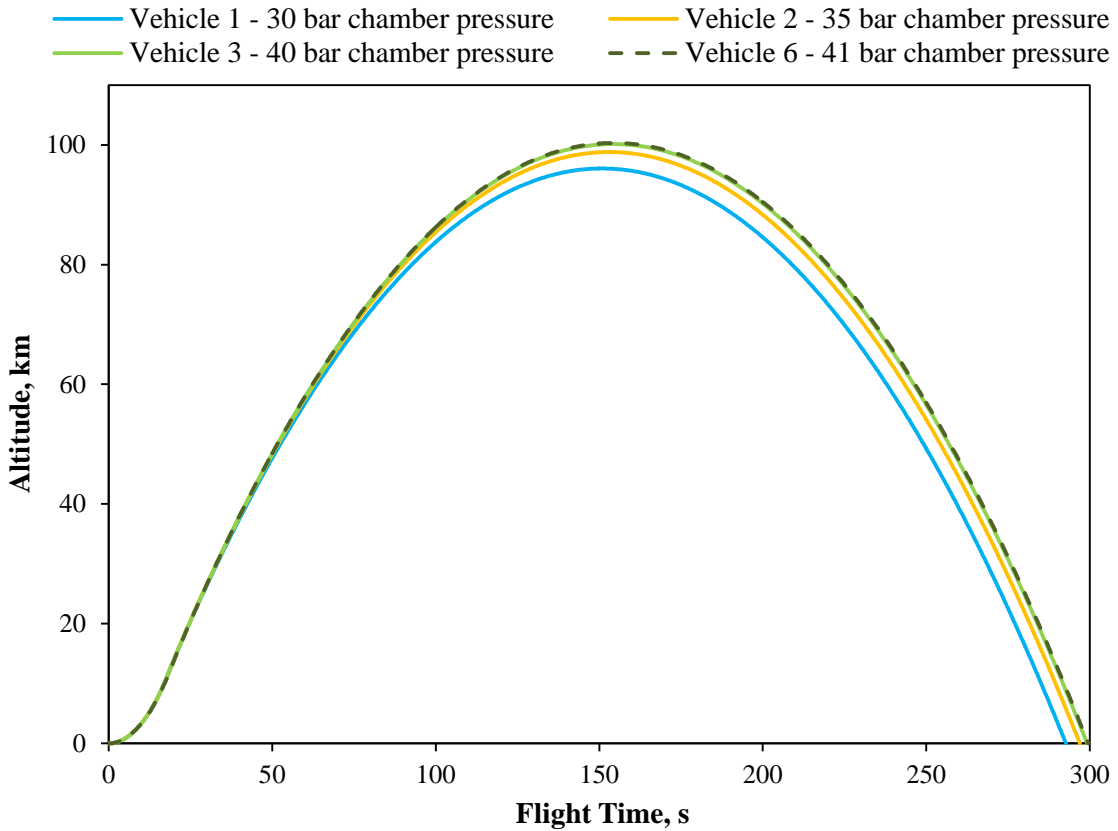
Figure 5.7: Altitude versus flight time for various design chamber pressures - Scenario 1.
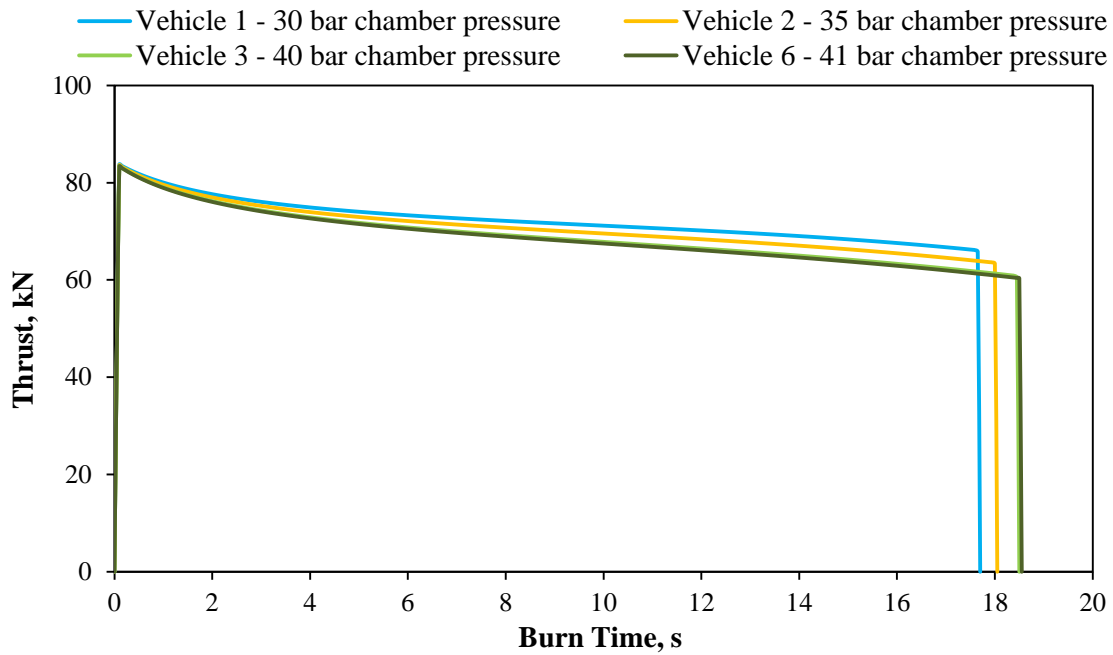
Figure 5.8: Thrust versus burn time for various design chamber pressures - Scenario 1.

Figure 5.9 indicates that the atmospheric pressure is similar for all the simulations because the motors experience comparable altitudes during the boost phase of the flight trajectory. The vehicle's total mass reduces with an increase in design chamber pressure due to less propellant mass required and the fact that the propellant mass fraction remains constant. The nozzle exit pressure is also shown to decrease at a faster rate with an increase in design chamber pressure.
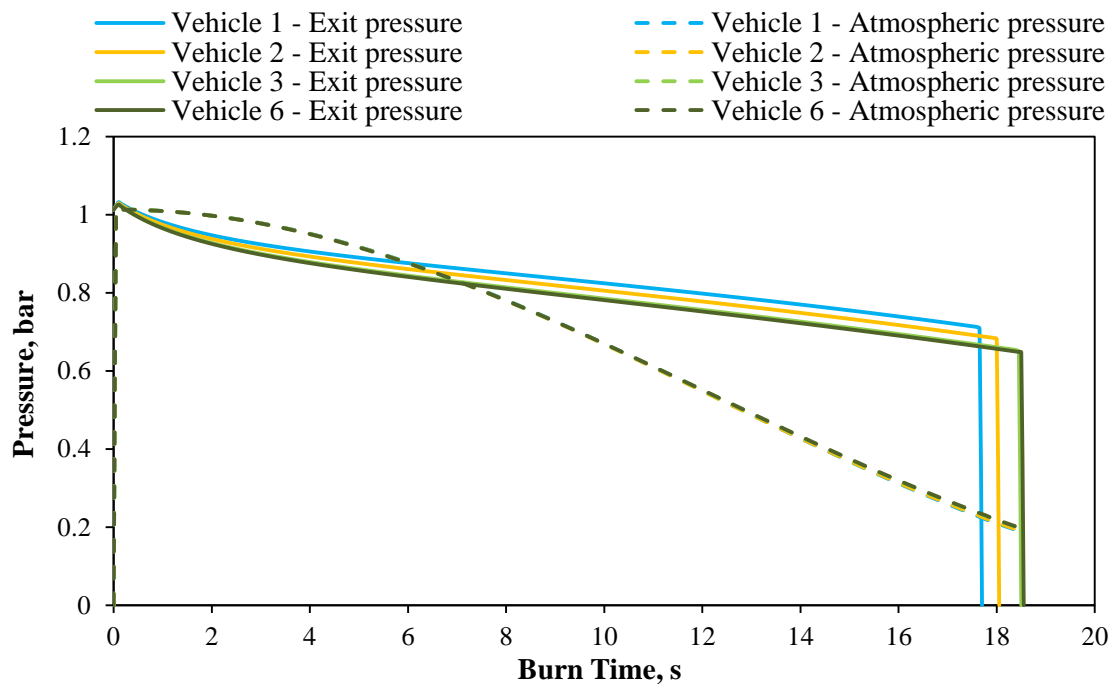
Figure 5.9: Nozzle exit and atmospheric pressure versus burn time for various design chamber

pressures - Scenario 1.

Scenario 2

Scenario 2 investigates the addition of helium into the oxidiser tank while varying the design chamber pressure. The wall thickness of the oxidiser tank needs to be increased to accommodate the higher tank pressure, thereby increasing the inert mass of the tank. This increase in oxidiser tank mass means there is less available inert mass for other components for the same propellant mass fraction. The addition of 0.05 kg of helium into the oxidiser tank of all the Scenario 1 vehicles increased the oxidiser tank pressure to 60 bar.

Unstable combustion is still prominent in vehicles 4 and 5, seen in Figures 5.10 and 5.11, from the oxidiser mass flux and hydraulic pressure drop plots. These vehicles were modified by increasing the added helium until the minimum $\Delta P_{inj}/P_c$ was above 15% and were classed as vehicles 4a and 5a with 0.13 kg and 0.28 kg of helium respectively.
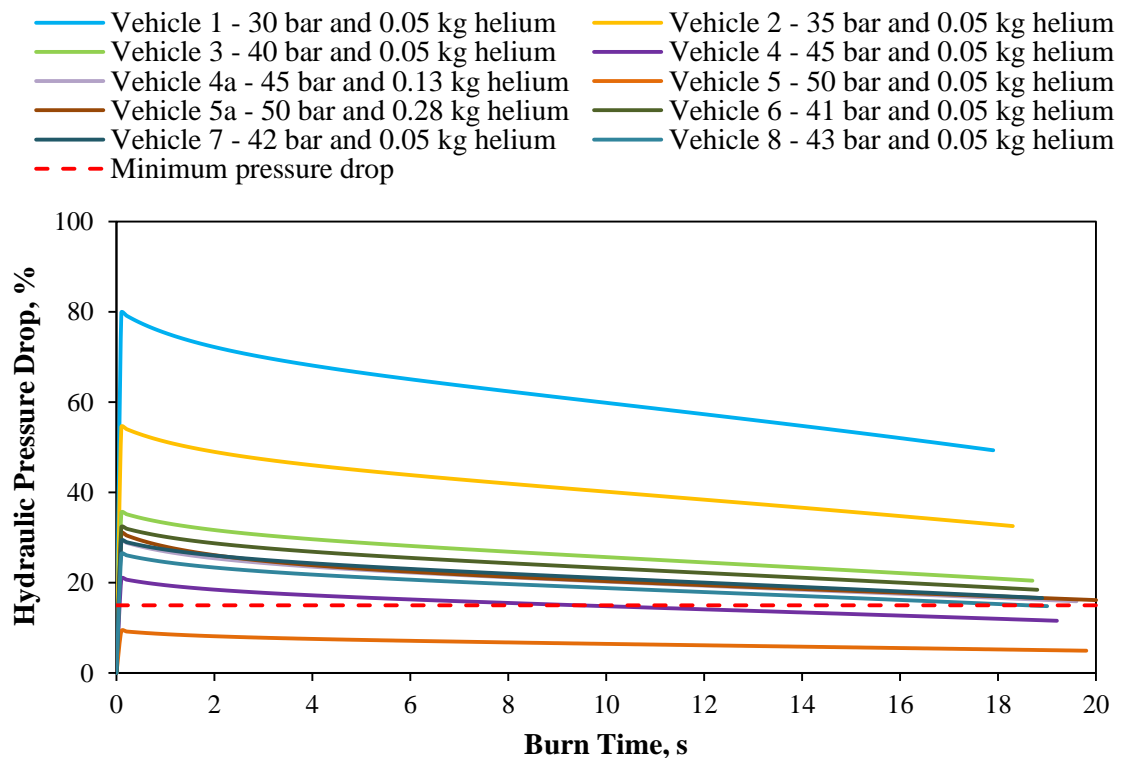
Figure 5.10: Hydraulic pressure drop ratio versus burn time for various design chamber pressures - Scenario 2.

Unfortunately helium only improves the $\Delta P_{inj}/P_c$ and does not reduce the maximum oxidiser mass flux. Thus vehicle 5a, which is included in the flight trajectory simulation for comparison purposes, may still produce unstable combustion. To determine the maximum design chamber pressure for this scenario, intermediate chamber pressures were investigated. Figure 5.10 shows that design chamber pressures above 45 bar would exceed the oxidiser mass flux limit. Figure

5.11 illustrates that a maximum chamber pressure of 42 bar with 0.05 kg of helium gives stable combustion.
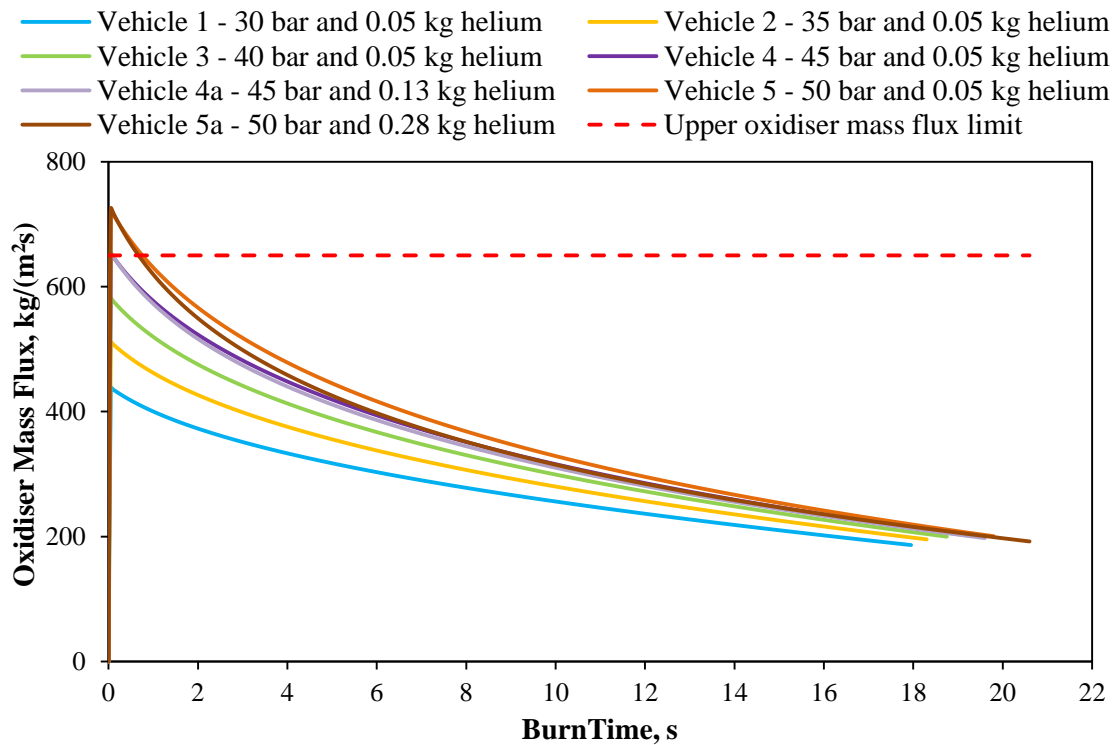
Figure 5.11: Oxidiser mass flux versus burn time for design chamber pressures -
Scenario 2.

The altitude results shown in Figure 5.12 are similar to that of Figure 5.7 of Scenario 1, where the performance improves with an increase in design chamber pressure. Figure 5.12 illustrates that vehicle 5a obtains the lowest apogee and is an outlier in terms of the other flight trajectories. This is due to vehicle 5a having a lower propellant mass fraction. The propellant mass fraction decreased because the initial oxidiser tank pressure was 71 bar which resulted in a larger wall thickness required and therefore a significant mass increase when compared to the other vehicles.

Table 5.2 lists the apogees of Scenario 2 vehicles as Figure 5.12 is unclear for vehicles 3, 6, 7 and 4a. It shows that the performance increases at a decreasing rate when the amount of helium added is kept constant and the design chamber pressure increases. Vehicle 4a achieves the highest apogee and demonstrates the usefulness of adding helium to produce stable combustion. The helium added to vehicle 4a caused the initial oxidiser tank pressure to be 63.5 bar requiring a larger wall thickness and therefore increased the mass of the oxidiser tank. This results in less available inert mass for other components.
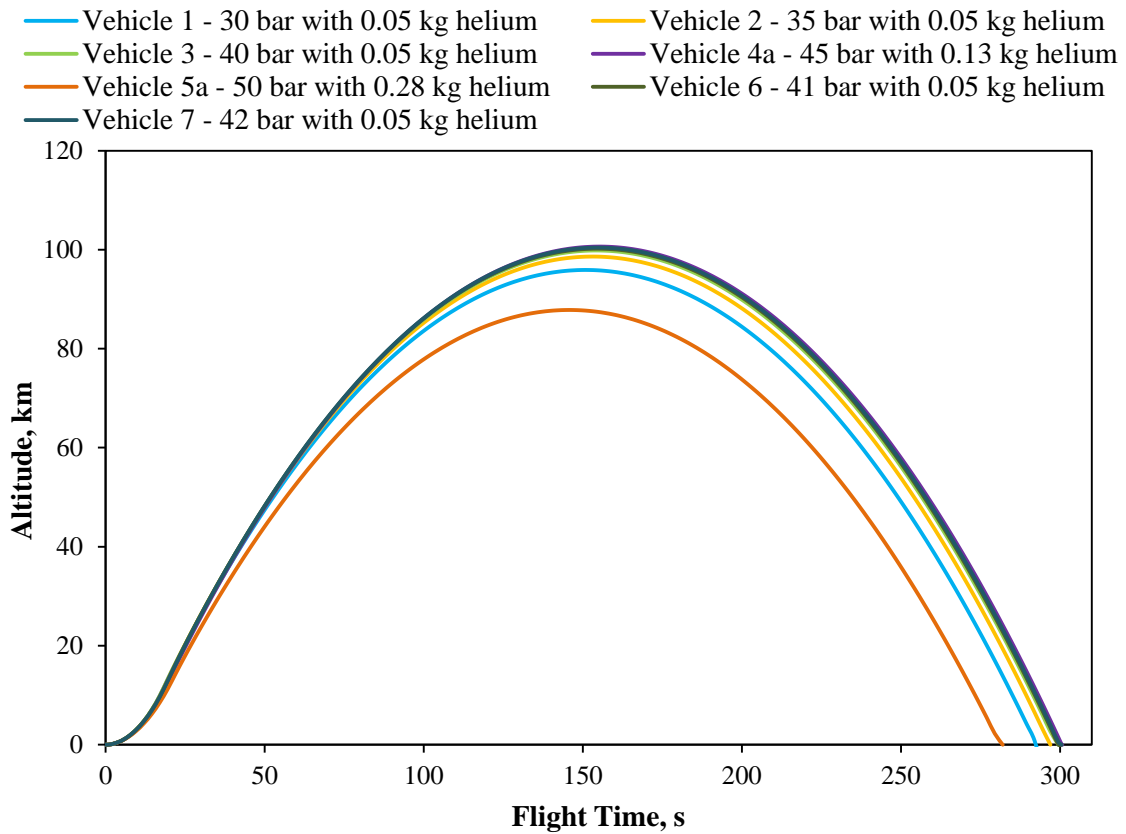
Figure 5.12: Altitude versus flight time for various design chamber pressures - Scenario 2.

Table 5.2: Scenario 2 vehicle parameters for design chamber pressures.

Vehicle	1	2	3	6	7	4a	5a
Design chamber pressure (bar)	30.0	35.0	40.0	41.0	42.0	45.0	50.0
Helium mass (kg)	0.05	0.05	0.05	0.05	0.05	0.13	0.28
Apogee (km)	95.90	98.60	99.84	100.20	100.42	102.11	87.81

The HYROPS simulations are compared to the specific impulse results obtained from NASA CEA to determine similarity. Figure 5.13 illustrates the specific impulse for a nitrous oxide and paraffin wax hybrid rocket motor. Comparing Figure 5.13 to the results in Figure 5.12 it is clear that the rate at which the performance improves, decreases.

The difference between vehicle 3 in this study and the initial conceptual design of Phoenix-2A from Chapter 4 is that vehicle 3 has fewer injector holes restricting the maximum chamber pressure from exceeding the design value. The initial Phoenix-2A concept had a maximum chamber pressure of 41.8 bar. This accounts for the difference in apogee obtained for the 40 bar design chamber pressure in this scenario, compared to the conceptual design.
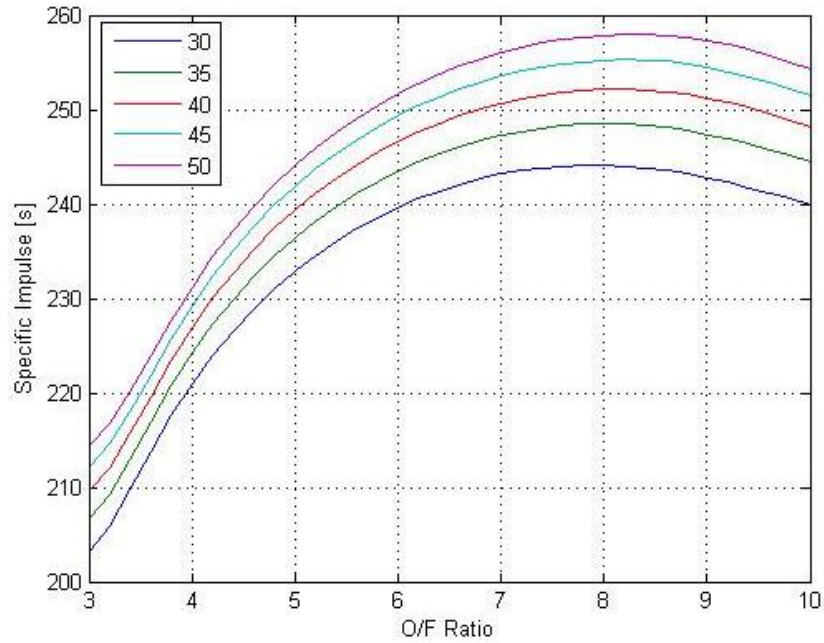
Figure 5.13: Specific impulse versus O/F ratio for various chamber pressures.

Scenario 3

In this scenario the effects of throttling are investigated by keeping the vehicle geometries the same and varying the area of the injector. This is conducted by changing the number of holes which affects the oxidiser flow rate and therefore the chamber pressure. The propellant mass, inert mass, and aerodynamic characteristics of the vehicle are also kept constant. The maximum allowable chamber pressure is limited by possible combustion instability, as the amount of helium remains constant.

The results in Figure 5.14 indicate that there is a loss in performance for reducing the chamber pressure by reducing the injector area. If the injector area increases it increases the maximum chamber pressure. This results in an improvement in apogee up until a certain pressure peak, after which the performance will decrease. This peak occurs at approximately 16% of the original pressure as shown by vehicle 1 and 2 in Figure 5.14. Vehicles 3, 4, and 5 do not exceed 16% of their original chamber pressure because combustion becomes unstable before the pressure peak was reached.

Parameter Selection – Chamber Pressure

Consideration of performance, cost, and manufacturability is important when determining the design chamber pressure of Phoenix-2A. The wall thickness of the combustion chamber and oxidiser tank are affected by the chamber pressure and the amount of helium respectively. A larger wall thickness requires more inert mass and therefore a higher cost is involved.
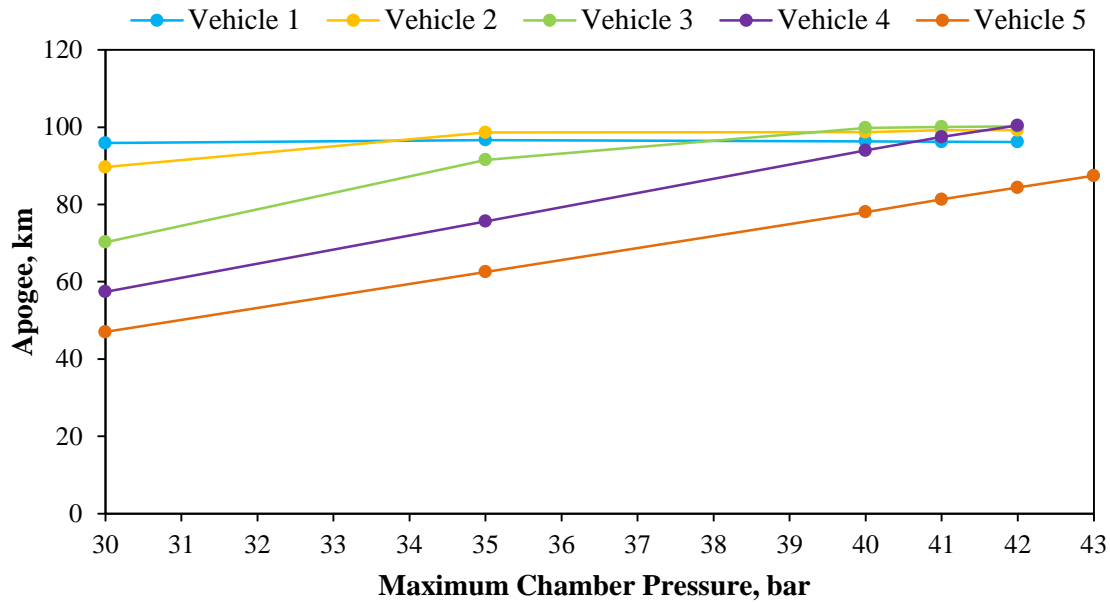
Figure 5.14: Apogee versus maximum chamber pressure - Scenario 3.

A design chamber pressure of 42 bar with 0.05 kg of helium supercharging was selected because this vehicle obtains an apogee of 100 km and incorporates the benefits of supercharging without substantially increasing the oxidiser tank pressure and mass. It requires less propellant mass than a vehicle with a lower design chamber pressure. This reduces the propulsion system geometry making it more cost-effective, and decreases the probability of buckling.

From the work of Waxman et al. (2013) the chamber pressure should be kept below the saturated pressure to create two-phase flow. This should provide isolation to prevent the tank pressure from oscillating in response to the chamber pressure and prevent feed-system-coupled instabilities. It was found that the chamber pressure versus saturation pressure of nitrous oxide was below 0.8 for the full burn duration, therefore reducing the possibility of feed-system-coupled instabilities. Verification of this theory is currently in progress within the Peregrine hot-fire test programme.

5.1.2   Nozzle Design Altitude

A nozzle with a fixed geometry, as used for Phoenix-2A, can only be designed to produce optimum expansion for a specific atmospheric pressure. The design of the nozzle geometry requires selecting a design atmospheric pressure for a specific altitude during the rocket's boost phase, with a view to minimising the losses that occur when the nozzle is under- or over-expanded. The goal of this parameter trade study is to determine the effect of varying the nozzle design altitude on the performance of Phoenix-2A.

Methodology

The motor that emerged from the previous trade study had a burnout altitude of 12.2 km. Nozzles lose efficiency when their exit pressure decreases below 40% of the ambient pressure due to the reduction in thrust coefficient and specific impulse (Sutton and Biblarz, 2001). Phoenix-2A is intended to be launched at sea level, hence the decision to vary the nozzle design altitude between 0 km and 7 km above sea level. The higher the design altitude, the larger the nozzle expansion ratio needed and thus the larger nozzle exit diameter. Within the selected range, altitudes above 4 km were disregarded as they required flared boat-tails which would increase the base drag of the vehicle. The vehicle selected in the previous study had a nozzle design-point of atmospheric pressure for sea level.

The HRPC-Motor Design Model inputs for various nozzle design altitudes are shown in Table B.2, in Appendix B. The Standard Atmosphere Equations 5.4 to 5.6 (Boiffier, 1998), for attitudes from sea level up to 11 km, were used to calculate the design-point atmospheric pressure, P_{atm}, for certain altitudes above sea level, h. The parameters used in these equations are defined in Table 5.3. The five test cases were 0 km, 1 km, 2 km, 3 km, and 4 km above sea level to determine the sensitivity of nozzle design altitude on apogee.

$$P_{atm} = P_0 \left(T / T_0 \right)^{-g_r/[R_{air}(dT/dh)]} \tag{5.4}$$

$$g_r = (Gm_{ear})/(r_{ear} + h)^2 \tag{5.5}$$

$$T = T_0 + [(dT/dh)h] \tag{5.6}$$

Table 5.3: Variable definition of standard atmospheric equations.

Symbol	Value	Definition
dT/dh	-0.0065 K/m	Temperature gradient for up to 11 km altitude
G	$6.67428e^{-11}$	Constant of gravitation
m_{ear}	$5.9736e^{24}$ kg	Mass of the earth
P_0	101325 Pa	Standard sea level pressure
R_{air}	287 J/kg	Ideal gas constant for air
r_{ear}	6370 km	Radius of the earth
T_0	288.2 K	Standard sea level temperature

Results

Figure 5.15 shows the exit pressures obtained from the HRPC-Performance Model. The initial exit pressure experienced by the motor is equal to the design atmospheric pressure. For instance, the exit pressure for the 0 km above sea level simulation corresponds to 1 bar at the start of the burn. The motors have a blowdown configuration which causes the exit pressure to decrease over time. The simulations experience minimal variation in apogee and therefore display similar flight trajectory paths during the boost phase. This results in the atmospheric pressures in Figure 5.15 overlapping. The five test cases all remained within the combustion stability theoretical values and no vehicles were disregarded (Figure 5.16).
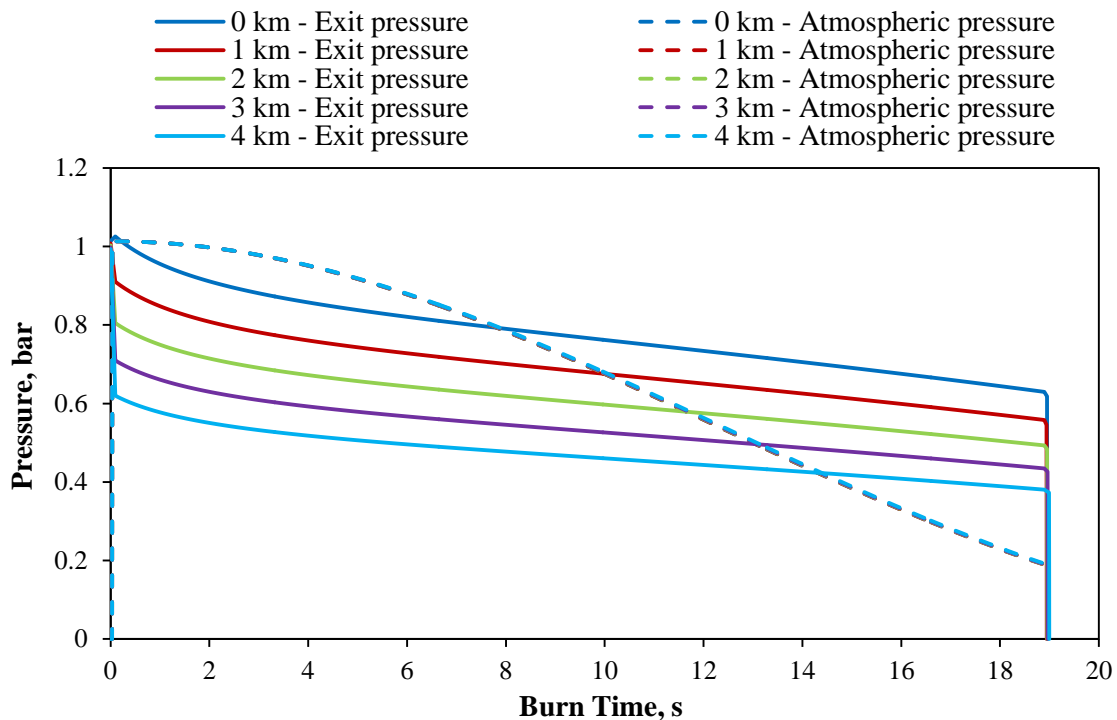
Figure 5.15: Exit and atmospheric pressure versus burn time for various nozzle design altitudes.

This study shows minimal effect on performance, as illustrated by Figure 5.17. A higher nozzle design altitude reduces the required propellant mass which reduces the size of the oxidiser tank and combustion chamber required. This is because the inverse pressure ratio (P_{c_d}/P_{atm_d}) increases. This variable is used in the HRPC-Motor Design Model to determine the NASA CEA theoretical parameters. The thrust coefficient increases causing the nozzle mass flow rate to decrease (Equation 5.2).
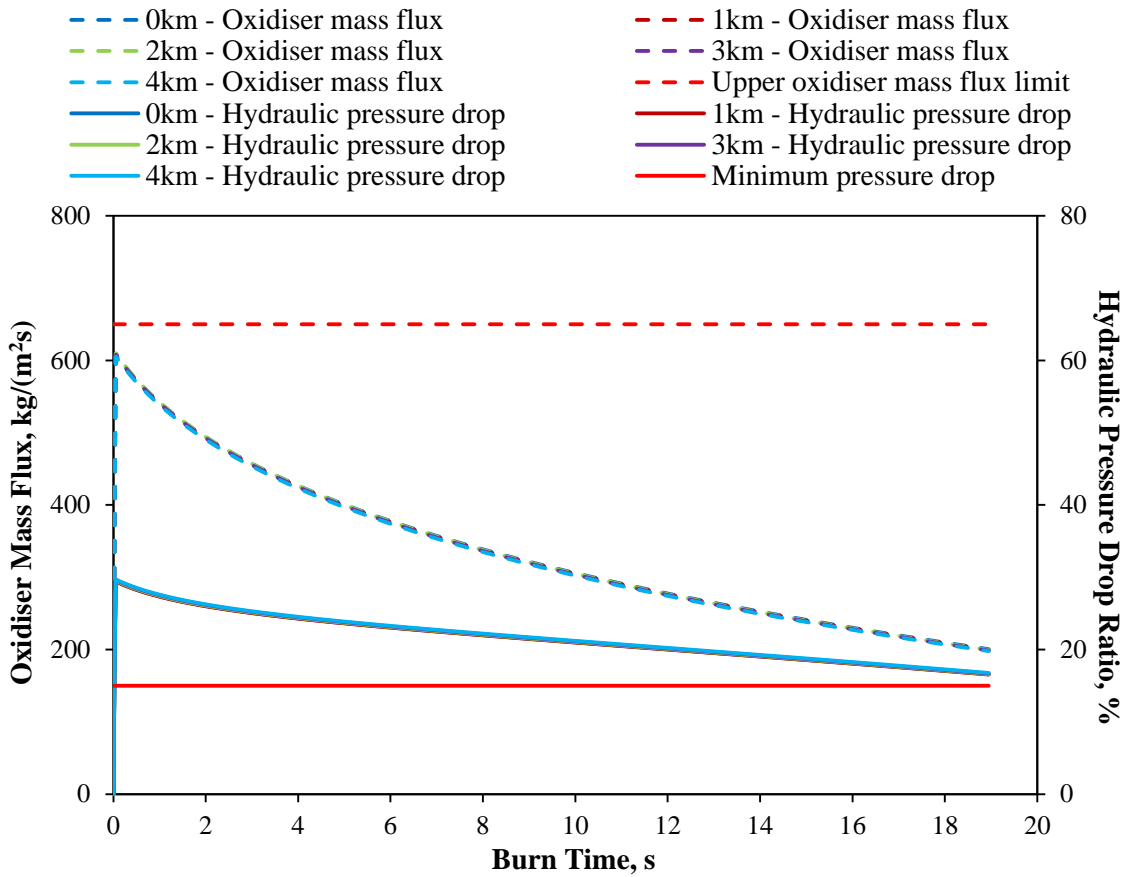
Figure 5.16: Oxidiser mass flux and hydraulic pressure drop ratio versus burn time for various nozzle design altitudes.
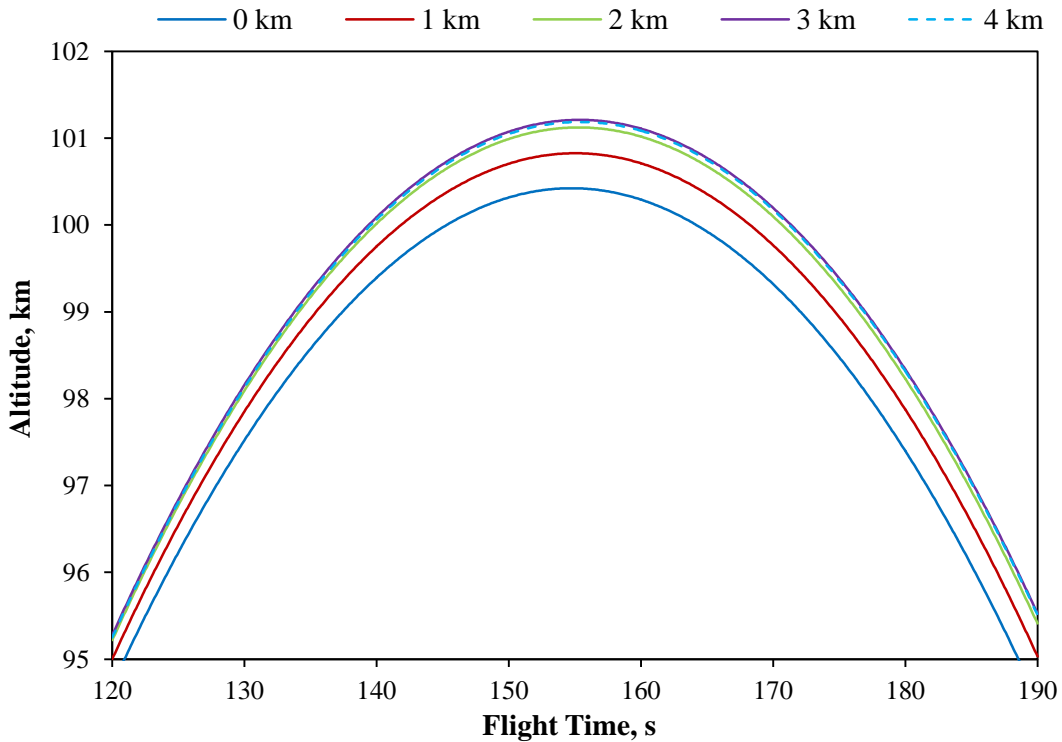
Figure 5.17: Altitude versus flight time for various nozzle design altitudes.

The HRPC-Motor Design Model characteristic velocity for all the simulations in this trade study was found to be the same. This is due to the design thrust, chamber pressure, and combustion efficiency remaining constant.

Parameter Selection – Nozzle Design Altitude

The selection of the design nozzle altitude should be based on nozzle geometry, propellant mass, propulsion system geometry, and total vehicle mass. A design atmospheric pressure of 0.7 bar which corresponds to an altitude of 3 km above sea level, was selected as it results in the highest apogee. This design altitude results in an improved performance of 1 km and a reduction in the oxidiser and fuel mass by 17.3 kg and 2.5 kg respectively when compared with the design altitude at sea level, as shown in Table 5.4. This reduces the size of the combustion chamber and oxidiser tank and therefore the total length by 1.6%, and the overall mass by 3.2%, making it a more cost-effective design. The increase in nozzle geometry results in an approximate 1.1 kg mass increase which is minimal when compared to the reduction of the propellant mass.

Table 5.4: Vehicle specifications for various nozzle design altitudes.

	Design-point Atmospheric Pressure				
	0 km	**1 km**	**2 km**	**3 km**	**4 km**
Oxidiser mass (kg)	542.06	536.12	530.34	524.75	519.38
Fuel mass (kg)	77.44	76.59	75.76	74.96	74.20
Nozzle mass (kg)	34.80	35.14	35.48	35.86	36.28
Tank mass (kg)	160.50	158.80	157.10	155.50	153.90
Overall mass (kg)	1026.16	1014.91	1003.98	993.40	983.23
Overall length (m)	11.74	11.66	11.61	11.55	11.50
Apogee (km)	100.42	100.83	101.12	101.21	101.19

5.1.3   O/F Ratio

Every propellant combination has a specific optimal O/F ratio that produces the best performance. The O/F ratio of a hybrid rocket motor is expected to shift in time due to the fuel grain port opening and/or throttling. In the case of Phoenix-2A, the O/F ratio is independent of the port diameter because the regression rate exponent, n, is equal to 0.5 (Humble et al., 1995). The O/F ratio shifts because the oxidiser is modelled as a blowdown system which acts similarly to throttling, as the oxidiser mass flow rate reduces over time. The performance sensitivity for different design O/F ratios was investigated in this study.

Methodology

The design O/F ratio is determined by selecting an oxidiser and fuel mass accordingly. The blowdown system of the motor makes it difficult to obtain the steady state conditions. Figure 5.13 illustrates that the optimal O/F ratio for a nitrous oxide and paraffin wax (N_2O/Paraffin) propellant combination is approximately 8 for a chamber pressure of 42 bar.

To investigate variation in O/F ratio, the design O/F values were increased from 4 to 10, as shown in Table B.3 (Appendix B). The design chamber pressure and nozzle atmospheric altitude from the previous trade studies were used. The mass of the oxidiser and fuel selected from the HRPC-Motor Design Model are also shown in Table B.3. Equations 3.3 and 3.4 illustrate the dependency of oxidiser and fuel mass flow rates on the design O/F ratio. The vehicle selected in the previous trade study is the same as the vehicle shown in Table B.3 with a design O/F ratio of 7.

Results

The O/F ratio shift obtained from the HRPC-Performance Model (Figure 5.18) is due to the decreasing oxidiser mass flow rate with respect to time. The O/F ratio equals the design O/F ratio at 1.25 s into the burn where all the steady state design conditions are met in the blowdown system.
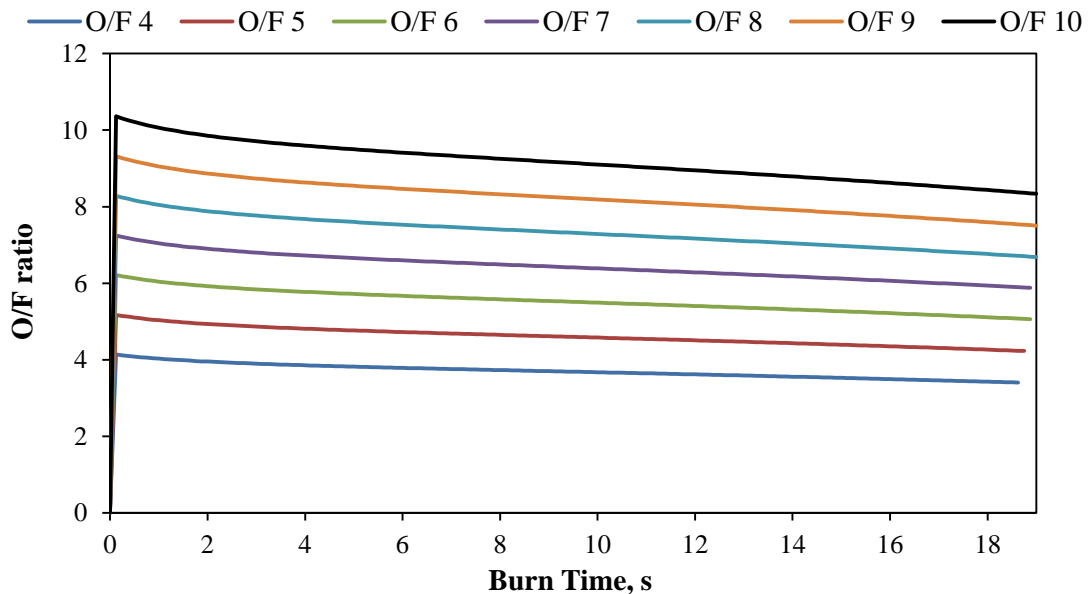
Figure 5.18: HRPC-Performance Model output of O/F ratio versus burn time.

Figure 5.18 illustrates that for a design O/F ratio of 9, the O/F shifts from approximately 9 to 7.5 throughout the duration of the burn. This range corresponds to the best specific impulse values from Figure 5.13 compared to the other O/F shifts in this study.

It can be seen in Figure 5.19 that all the design O/F ratio simulations remained within the combustion stability limits, and therefore all 7 cases were investigated. Figure 5.20 illustrates that, according to the simulations performed, a design O/F ratio of 9 achieves the best apogee.
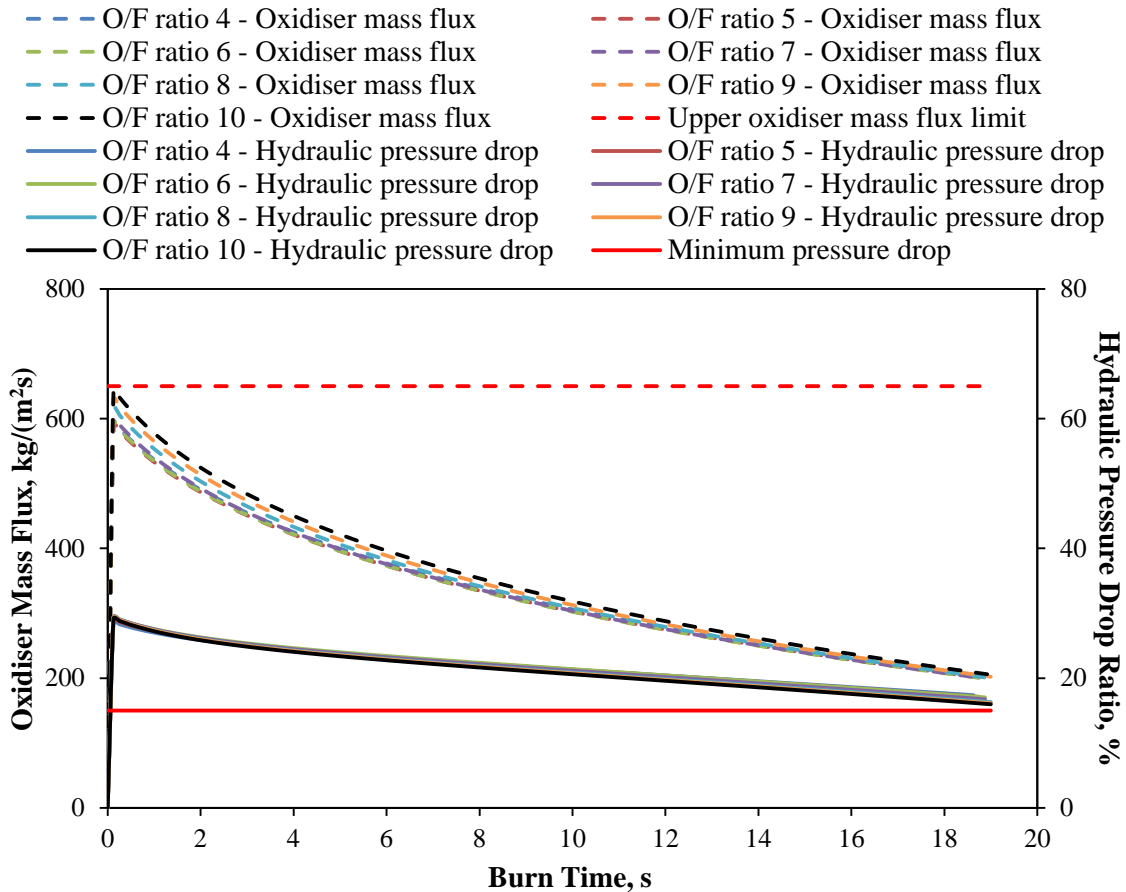
Figure 5.19: Oxidiser mass flux and hydraulic pressure drop ratio versus burn time for various design O/F ratios.

Parameter Selection - O/F Ratio

The overall vehicle length was found to decrease with an increase in design O/F ratio. This is due to a decrease in fuel length as less fuel is required for the motor. This is true up to a design O/F ratio of 10, when the oxidiser mass increases more than the fuel mass decreases. The design O/F ratios 4, 5, and 6 were disregarded as they did not reach the target altitude of 100 km. Figures 5.21 and 5.22 illustrate that a design O/F ratio of 8 or 9 gives the best trade-off between mass, length and performance.
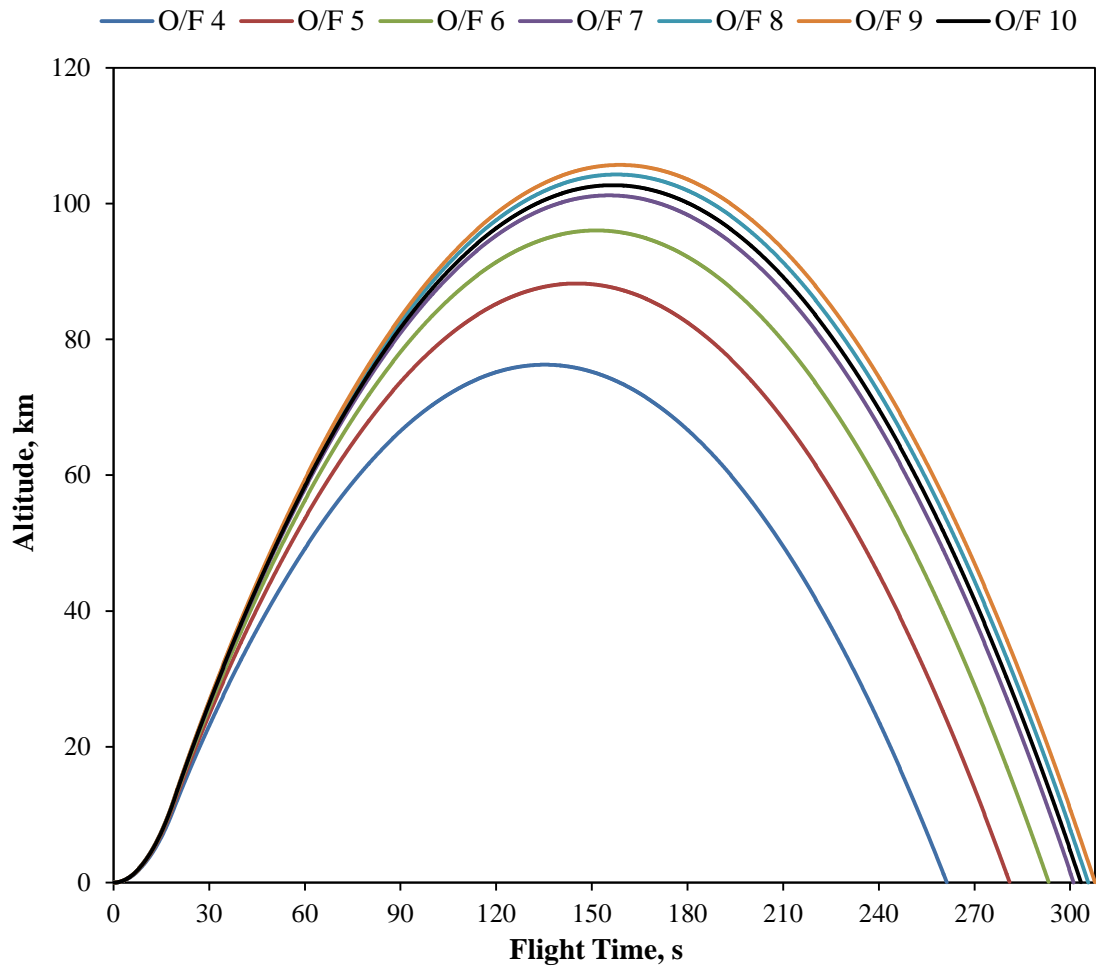
Figure 5.20: Altitude versus flight time for various design O/F ratios.

The design O/F ratio of 9 requires a larger nozzle exit diameter than a design O/F ratio of 8 but both have the same external combustion chamber diameter. This restricts the nozzle thickness if a straight boat-tail section is to be used, as in the simulation, and would most likely require a flared boat-tail after a structural analysis was conducted on the required nozzle thickness. This would then affect the aerodynamic characteristics of the vehicle structure and possibly decrease the performance. The design O/F ratio of 9 was therefore eliminated.

A design O/F ratio of 8 was selected for Phoenix-2A because even though it requires 6.52 kg more paraffin wax than a ratio of 9, it requires 7.45 kg less nitrous oxide which is more expensive. It also requires the least amount of propellant mass when compared to all the design O/F ratios and gives the lowest overall vehicle mass because the propellant mass fraction remains constant for all the simulations (Figure 5.21).
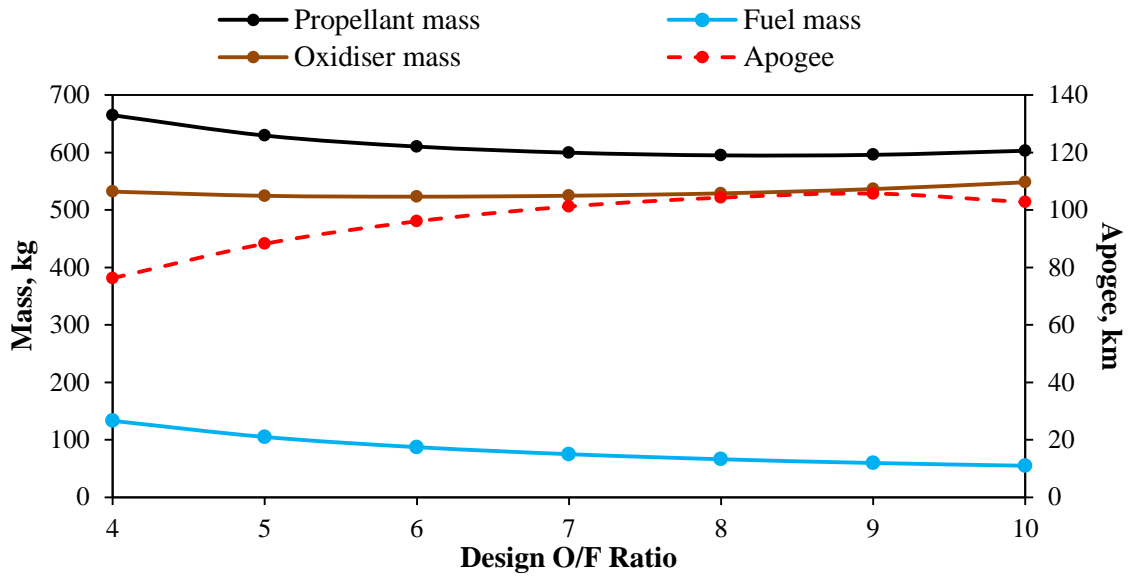
Figure 5.21: Mass and apogee versus design O/F ratio.
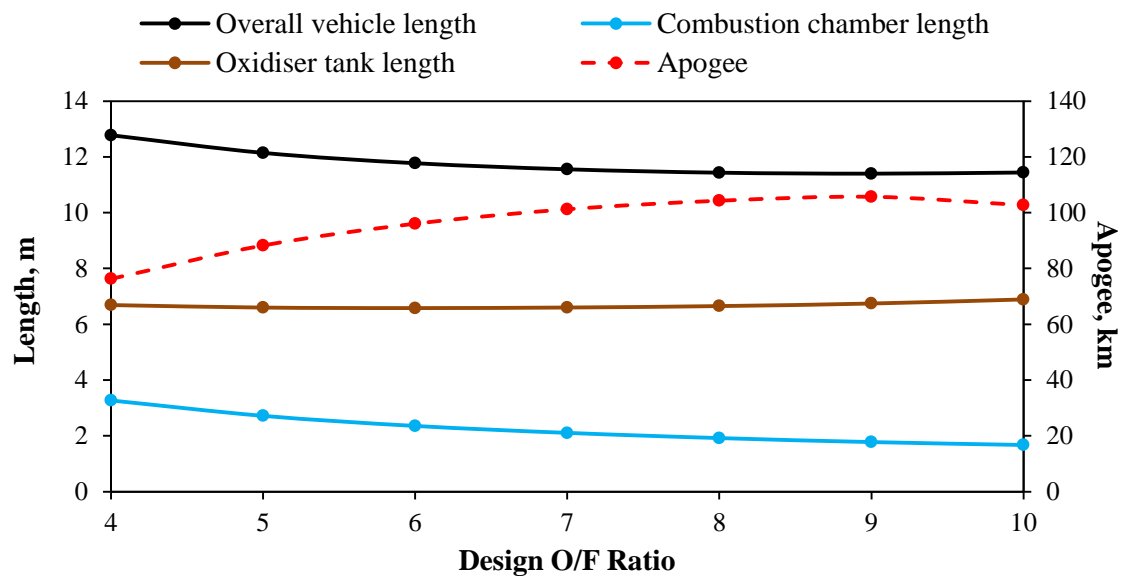
Figure 5.22: Length and apogee versus design O/F ratio.

5.1.4 Ullage Volume

The ullage volume in an oxidiser tank is defined as the open space above the liquid nitrous oxide for maximum oxidiser mass. Ullage volume affects the oxidiser tank length and mass, and thus a varying ullage volume was investigated to determine its effect on the vehicle's performance. The density of nitrous oxide decreases with increasing temperature in a closed system, and therefore increases the pressure of the oxidiser tank, over and above the increase in vapour pressure. Sufficient ullage volume is required to allow for expansion of the nitrous oxide

in the event of an increase in oxidiser tank temperature (Thicksten et al, 2008). This helps to prevent the pressure in the oxidiser tank exceeding the designed value if the oxidiser tank temperature increases unexpectedly before launch.

Methodology

The HRPC-Motor Design Model was not used in this trade study because the oxidiser tank geometry is the only variable, and this affects the HRPC-Performance Model. The tested ullage volume values were 5%, 10%, 15%, and 20% of the nitrous oxide liquid volume. A design ullage volume of 15% was used for all previous vehicles in this dissertation.

Results

Resulting tank dimensions for various design ullage volumes are given in Table 5.5. The HRPC models the oxidiser tank as a closed system assuming that once the oxidiser tank is filled it is heated to an initial temperature. This results in the initial tank pressure increasing exponentially for decreasing design ullage volumes, since there is less volume available for the nitrous oxide to expand in to. The design ullage volume of 5% has the highest oxidiser tank pressure which results in a larger wall thickness required when compared to other design ullage volumes. This increases the mass of the oxidiser tank for the 5% ullage volume vehicle. The length of the oxidiser tank reduces as the design ullage volume decreases because less volume is necessary above the liquid nitrous oxide. The external diameter of the vehicle was kept constant throughout the simulations. To maintain the same propellant mass fraction, the mass of the recovery bay was modified according to the increase or reduction in tank mass.

Table 5.5: Vehicle specifications for various design ullage volumes.

Parameters	Design Ullage Volume			
	5%	10%	15%	20%
Tank pressure (bar)	64.65	60.97	59.60	58.99
Tank length (m)	6.516	6.769	7.052	7.335
Tank outer diameter (m)	0.413	0.413	0.413	0.413
Tank wall thickness (mm)	7 .0	6.5	6.5	6.5
Tank mass (kg)	154.923	149.995	156.663	163.331
Total vehicle mass (kg)	985.61	985.61	985.61	985.61
Burnout mass (kg)	452.20	444.60	449.30	454.60

The burnout mass of the vehicles includes the unused oxidiser and fuel at the end of the burn time. The motor performance simulations for design ullage volumes of 10%, 15%, and 20% end with the depletion of the liquid nitrous oxide, whereas the simulation for a design ullage volume of 5% ends due to the depletion of the paraffin wax fuel. The vehicle's mass after burnout for the 5% design ullage volume therefore includes both liquid and vapour oxidiser mass and helium vapour mass in the tank. In terms of safety the depletion of the fuel first is worse than that of the liquid nitrous oxide as it will expose the liner directly to the combustion temperature which could result in failure of the combustion chamber casing. Finishing the liquid nitrous oxide first reduces the pressure in the oxidiser tank which affects buckling strength, but as long as the gaseous nitrous oxide remains in the tank the internal pressure is high enough to withstand the compressive forces (discussed in section 5.3).

All simulations were within the combustion stability limits. Figure 5.23 depicts the apogee results for this trade study. A design ullage volume of 10% gives the best apogee.
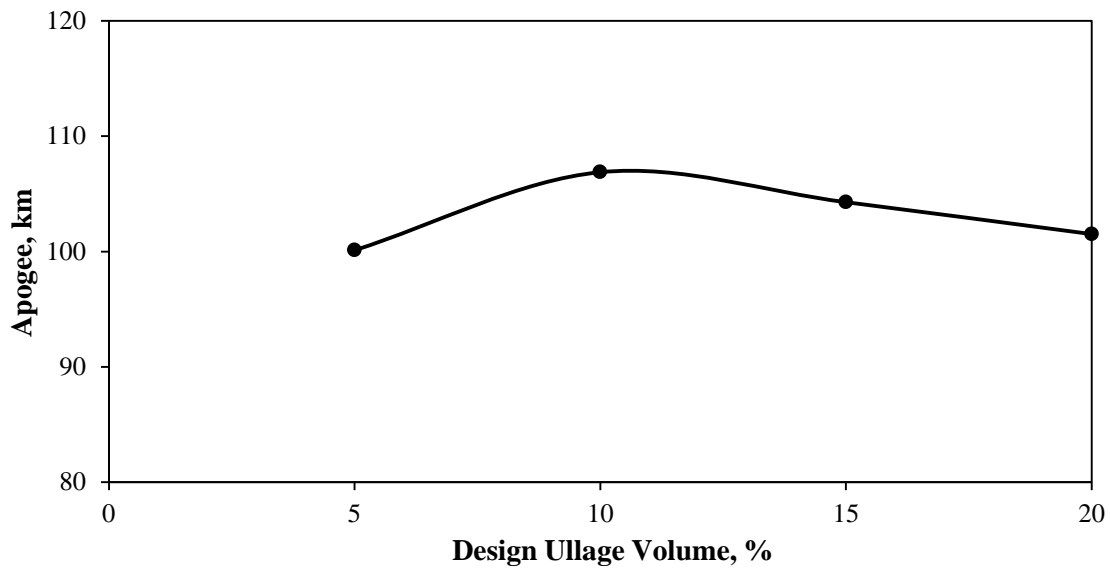
Figure 5.23: Apogee versus design ullage volume.

The reference (cross-sectional) area remained constant for each vehicle simulated in the trade study and therefore the total length shortens with a decrease in design ullage volume. This decreases the skin friction which reduces the drag coefficient of the vehicle (Figure 5.24).

The thrust (Equation 4.8) of the vehicle is made up of a momentum term, which is proportional to chamber pressure, and a pressure term, which is dependent on the nozzle exit and atmospheric pressures since the nozzle geometry remains fixed. These parameters are affected by the oxidiser tank pressure. The maximum thrust is similar for all test cases as the combustion

chamber pressure was limited to a maximum of 42 bar by varying the number of injector holes and they had the same design thrust. The rate at which the thrust decreases is faster near the start of the burn for a lower design ullage volume and slower at the end of the burn as it follows the same profile as the oxidiser tank pressure, as shown in Figure 5.25. A decrease in design ullage volume results in a lower average thrust and longer burn time.
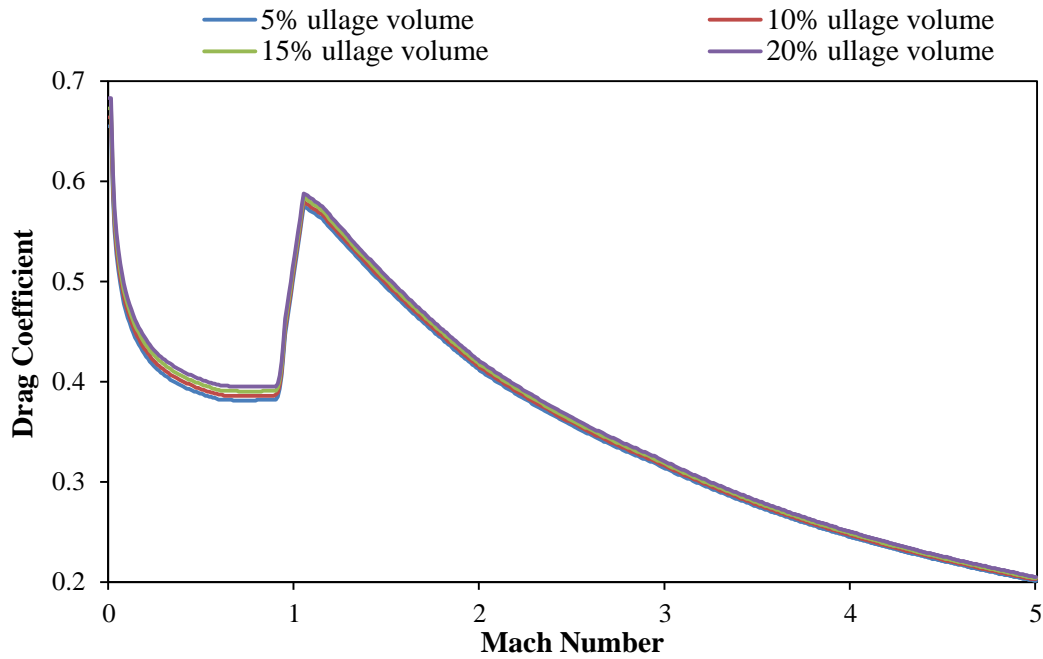
Figure 5.24: Drag coefficient versus Mach number for various design ullage volumes.
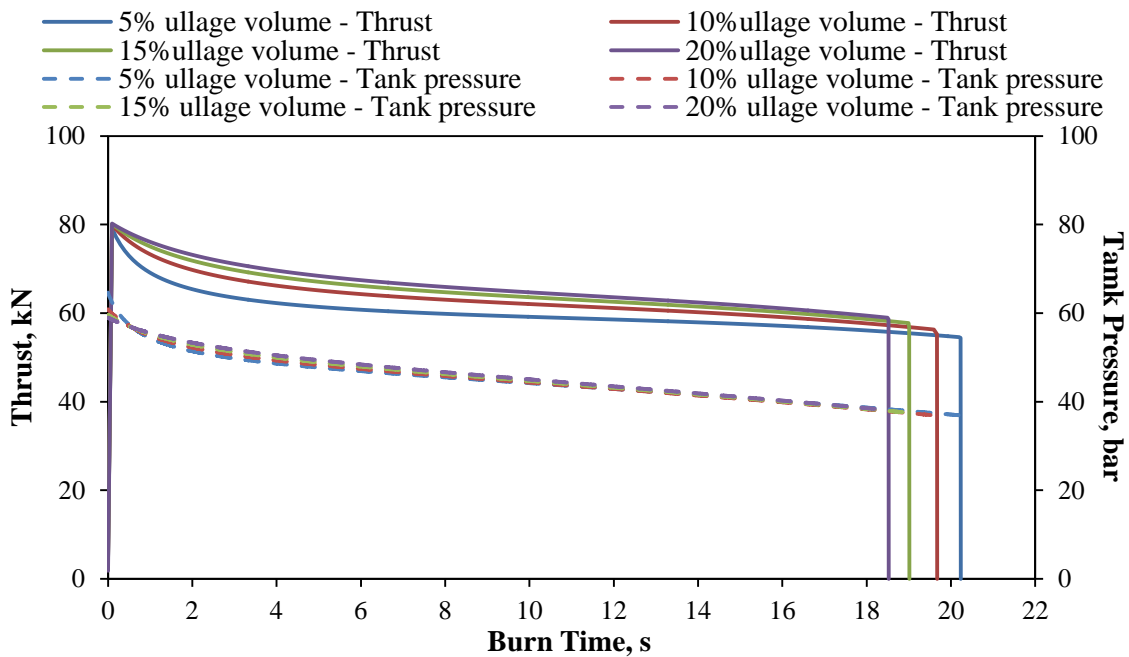
Figure 5.25: Thrust and tank pressure versus burn time for various design ullage volumes.

The burnout velocity affects the kinetic energy of the vehicle which in turn affects the apogee. Figure 5.26 shows the velocity profiles for the various design ullage volumes. This indicates that the vehicle with a design ullage volume of 10% has the highest burnout velocity. The drag force, F_D, (Equation 5.7) decreases with decreasing ullage volume due to the reduction in drag coefficient, C_D, and the lower velocity, v, during the boost phase, shown in Figure 5.26. The reference area, A_{ref}, is constant and the density of the air, ρ, depends on the altitude of the rocket. The burnout velocity in combination with the low drag force resulted in this vehicle reaching the highest apogee.

$$F_D = \frac{1}{2}\rho v^2 C_D A_{ref} \tag{5.7}$$
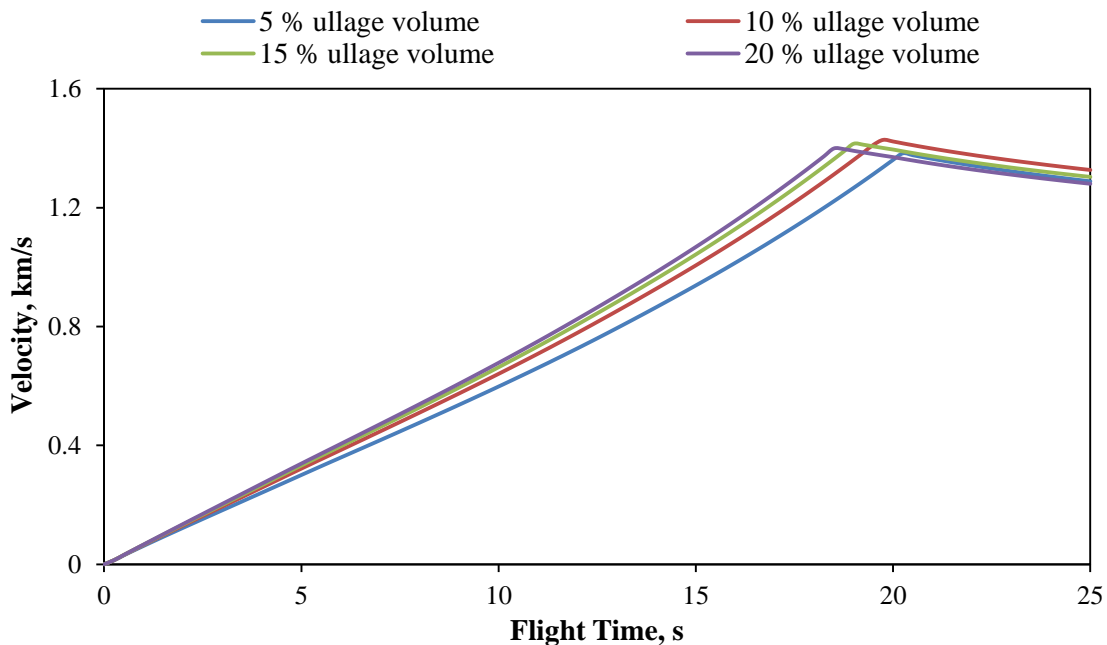
Figure 5.26: Velocity versus flight time for various design ullage volumes.

Parameter Selection – Ullage volume

The ullage volume was retained at 15% because this is the minimum considered safe, as stipulated by the UKZN safety regulations. It gives a lower drag force and a higher apogee than the 20% ullage volume. Since the vapour pressure builds with temperature, having a larger ullage volume increases the area the vapour can fill and provides a level of safety to accommodate slight temperature changes before launch.

5.1.5 Thrust

This trade study considers the minimum design thrust required to obtain an apogee of 100 km. A reduction in thrust lowers the inertial loading and stress that act on components of the vehicle.

Methodology

The design thrust values modelled in the HRPC-Motor Design Model are shown in Table B.4 (Appendix B). A design thrust value of 85 kN corresponds to the same inputs as used for the O/F ratio trade study (O/F of 8). Design thrust values from 0 kN to 80 kN were investigated in 20 kN increments. Smaller increments were analysed around a design thrust of 85 kN, which yielded an apogee above 100 km in the previous trade study.

Results

All the hybrid rocket motors in this trade study remained within the combustion stability limits. The expansion ratio, characteristic velocity and thrust coefficient are independent of the design thrust value. Increasing the design thrust of a vehicle increases the throat area of the nozzle and therefore the exit area due to a constant expansion ratio. The increase in throat area increases the nozzle mass flow rate substantially (Equation 5.2). This then gradually increases the fuel mass flow rate as the design O/F ratio is kept constant (Equation 3.3). This results in an increase in oxidiser mass flow rate. The steady state mass flows obtained from the HRPC-Motor Design Model are depicted in Figure 5.27. The increase in mass flow rates result in an increase in oxidiser and fuel mass.
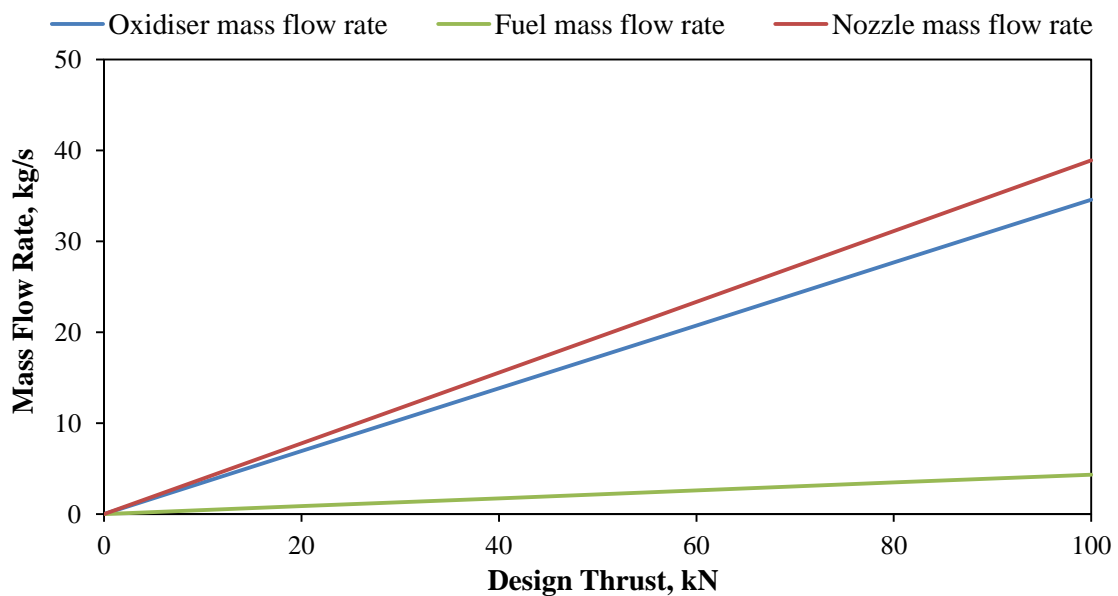
Figure 5.27: Mass flow rate versus design thrust.

For a linear increase in design thrust the velocity of the vehicle increases, but with a decreasing rate as shown in Figure 5.28. Figure 5.29 indicates that the apogee improves for an increase in design thrust, but the improvement begins to level off at the upper thrust range of the graph. This is due to the increase in energy loss caused by the increased velocity, which results in a higher drag force. The drag coefficient is also raised for an increase in design thrust due to the longer vehicle length and therefore larger skin friction.
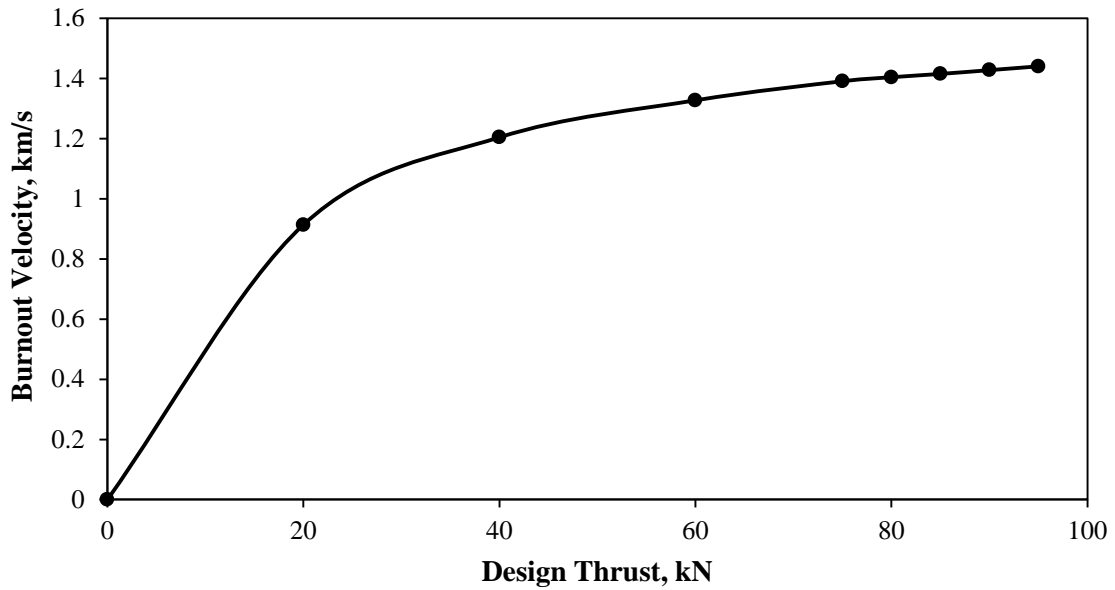
Figure 5.28: Burnout velocity versus design thrust.
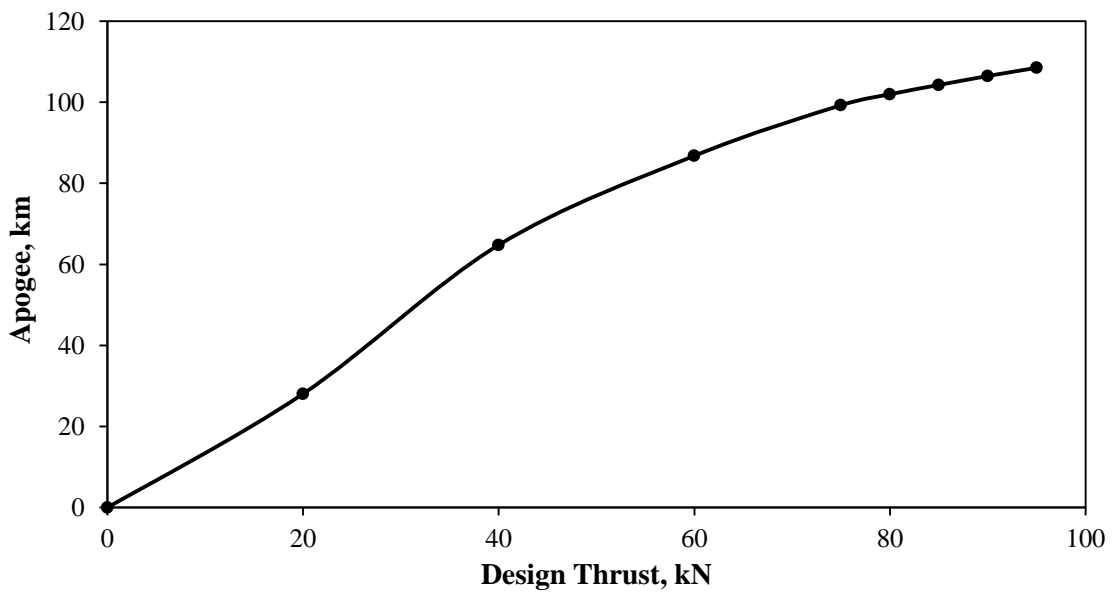
Figure 5.29: Apogee versus design thrust.

Parameter Selection – Thrust

A design thrust value of 80 kN was selected. The vehicle reaches an apogee of 101.98 km, however the minimum apogee of 100 km falls between 75 kN and 80 kN. The chosen value adds a 2% buffer and reduces the stress on the vehicle from the previous 85 kN design thrust.

5.1.6   Fuel Grain Geometry

The fuel grain geometry consists of its length, port diameter, and final diameter. In this trade study the fuel grain port diameter was left constant because the nozzle geometry and port-to-throat ratio were fixed. The fuel grain length and thickness were varied and a selection was then based on minimising the mass of fuel and reducing the stresses acting on the grain.

Methodology

The length was investigated by simulating various fuel grain length-to-diameter (L/D) ratios. The L/D ratios analysed were 4, 4.5, 5, 5.5, 6, and 6.5, together with several thicknesses. The HRPC-Performance Model was modified for each simulation to determine the performance of the hybrid rocket motor for various fuel grain geometries.

Results

Grain length-to-diameter ratio

An increase of the length of the fuel grain results in an increase in length of the combustion chamber and thermal liner. This increases the total length of the vehicle while adding more inert mass. The fuel mass flow rate found using the HRPC-Performance Model is proportional to the length of the fuel grain (Equation 3.6). The regression rate and port diameter change with respect to time during the burn while the fuel grain length and density remain constant. The O/F ratio of each motor is affected because of the change in mass flow rates. The increase in fuel mass flow rate reduces the overall O/F ratio as depicted in Figure 5.30 below.

The number of holes in the injector was modified to ensure that the maximum chamber pressure was 42 bar and the propellant mass fraction remained constant for each simulation. The results, shown in Figure 5.31, indicate that the best apogee is obtained for an L/D ratio of 5. This produces an O/F shift that gives the best specific impulse. The apogee illustrated with a red marker in Figure 5.31 represents the apogee obtained from the selected design thrust parameter in the previous thrust trade study.
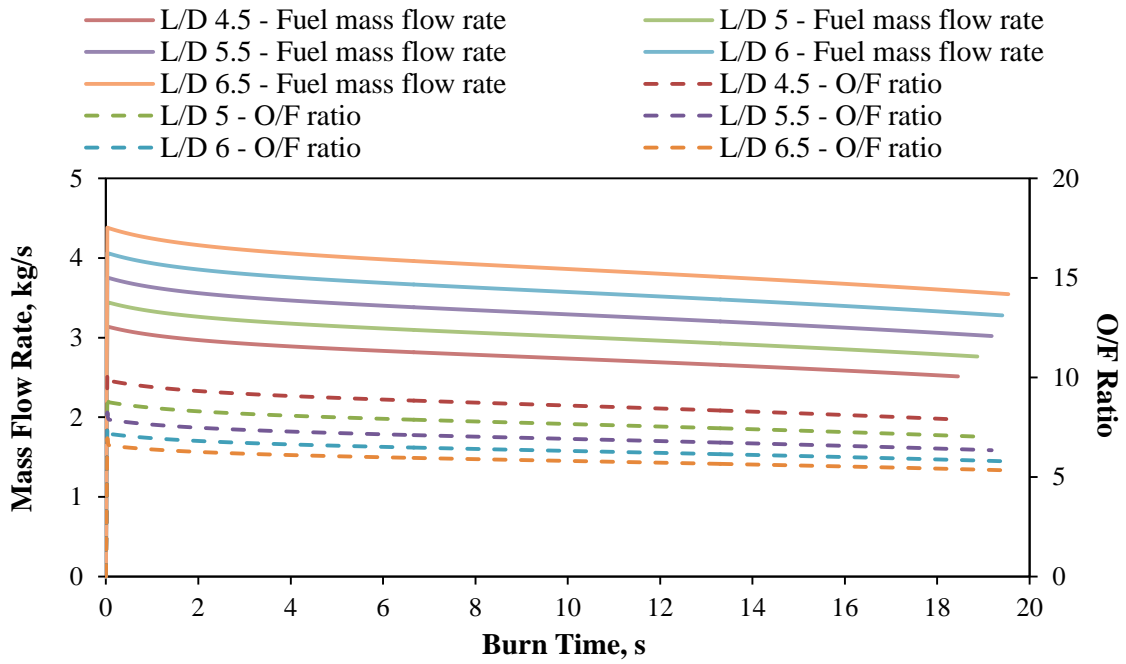
Figure 5.30: Fuel mass flow rate and O/F ratio versus burn time for various fuel grain length-to-diameter ratios.
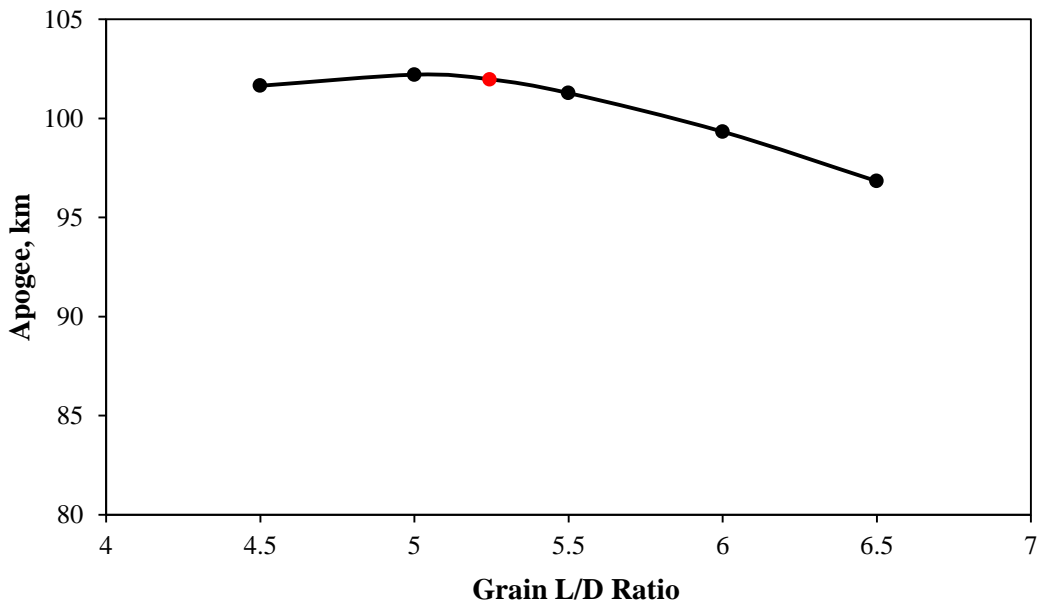
Figure 5.31: Apogee versus length-to-diameter ratio of a fuel grain.

Grain thickness

Karabeyoglu (2011) found that an increase in thickness results in higher hoop stresses in the fuel grain (Figure 5.32). It also increases the sliver fraction remaining at the end of the burn. A variation in thickness does not affect the fuel mass flow rate, it only affects the amount of fuel there is and the sizing of the combustion chamber. In this study it was found that a reduction of

5 mm in thickness caused the fuel to be depleted before the liquid oxidiser in the simulation, resulting in 30 kg of unused liquid nitrous oxide remaining in the oxidiser tank.
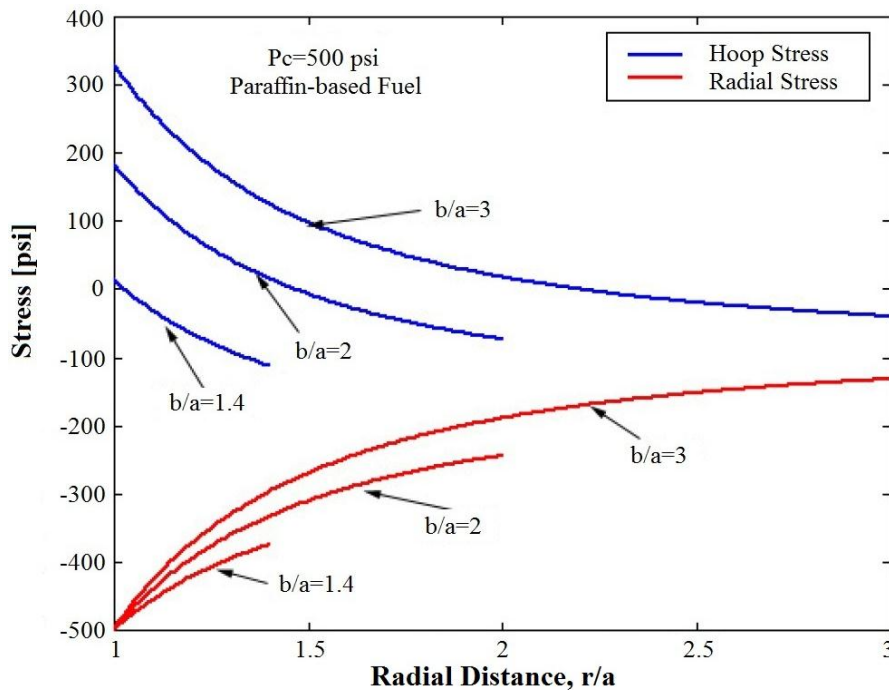
Figure 5.32: Stress versus radial distance for a single circular fuel grain port (Karabeyoglu, 2011).

Parameter Selection – Grain Geometry

Grain length-to-diameter ratio

A L/D ratio of 5 was selected as it results in the best apogee, improving performance over the previous trade study. It also reduces the length of grain therefore reducing the length of the combustion chamber and thermal liner. This leaves more inert mass for other components, since the propellant mass fraction is kept constant for all the vehicles in this study.

Grain thickness

A fuel grain thickness of 55 mm was selected because it yields a minimal sliver fraction of 3.74% at the end of the liquid nitrous oxide burn. This acts as additional thermal protection in front of the liner in case the regression rate is higher than expected. It also gives an outer radius to initial port radius (b/a) of 1.45 therefore minimising the hoop stresses acting on the paraffin wax, while ensuring that a small amount of wax remains after burnout.

5.2 Aerodynamic Trade Study

Design parameters investigated in the aerodynamic trade study are the nose cone, fuselage, and fin geometry. The effects of varying these parameters on the performance of the vehicle were conducted using the Flight Dynamics Simulator of the HYROPS software and RASAero. The methodological approach and results are discussed in the following sections. The propulsion system remained constant for all the simulations performed in this trade study as the focus was on improving the vehicle performance through aerodynamic characteristic adjustment, except for the fuselage trade study.

5.2.1 Nose Cone Geometry

The design of the nose cone requires consideration of the scientific payload's dimensional envelope and its effect on performance. The three nose cone geometries analysed were limited by RASAero's capabilities and comprised conical, ogive, and Von Kàrmàn ogive. The effect of varying the fineness and bluffness ratios on performance was studied. The fineness ratio is defined as the nose cone length, L_n, divided by its base diameter, D_n, and the bluffness ratio is the tip diameter, D_{tip}, divided by the base diameter, D_n, as shown in Figure 5.33.
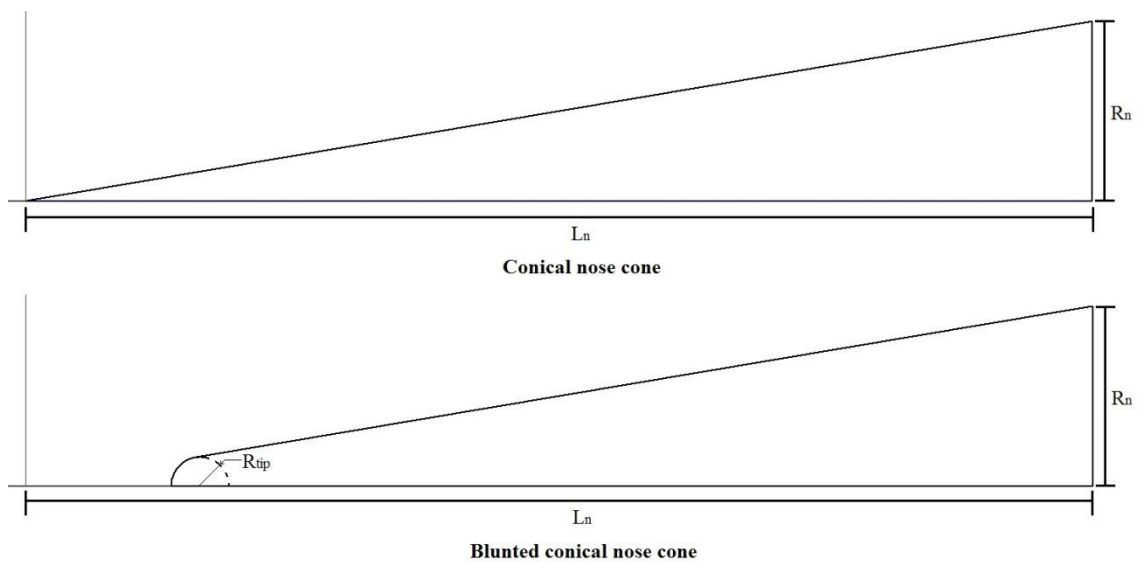
Figure 5.33: Conical nose cone representation of fineness and bluffness ratio dimensions.

Methodology

The fineness ratio was varied by modifying the vehicle's nose cone length, since the base diameter is restricted by the outer diameter of the oxidiser tank. A graphic representation of the nose cone geometries for the same length and base diameter is given in Figure 5.34.

99
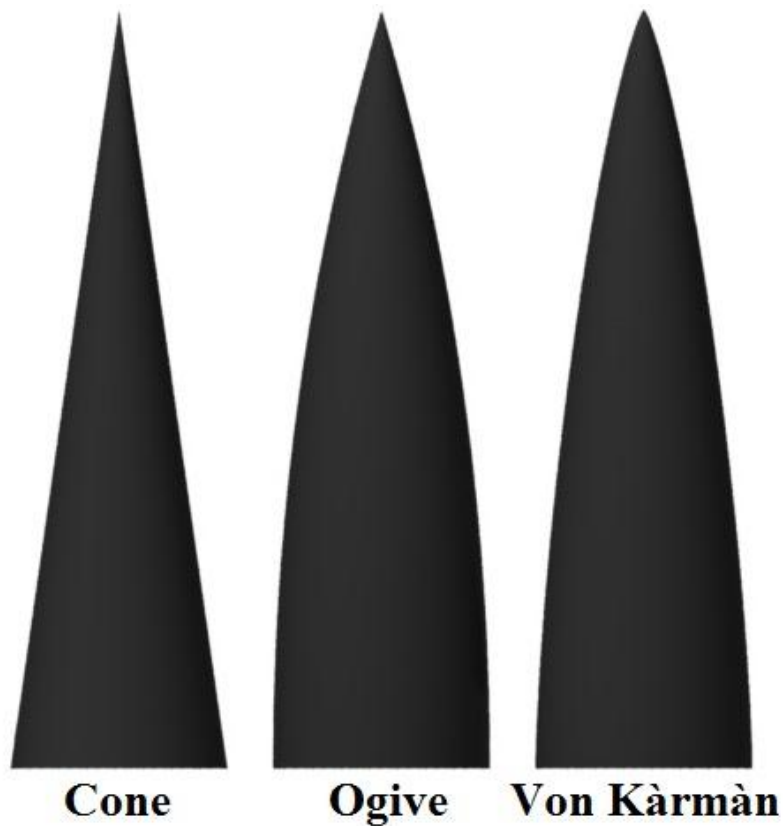
Figure 5.34: Comparison of the nose cone geometries investigated.

The fineness ratios investigated were 1, 3, 5, and 7 and the bluffness ratios were 0, 0.01, 0.05, 0.1, and 0.2. Phoenix-2A is a supersonic sounding rocket which experiences Mach numbers between 1 and 5, with a predominant Mach number of 3.

Two scenarios were used to investigate the variation in nose cone fineness ratio. Scenario 1 involves the nose cone mass varying with changes in length, and scenario 2 involves no change in nose cone mass due to an assumed constant propellant mass fraction.

Results

Fineness ratio

The drag coefficients found from RASAero for different fineness ratios and nose cone geometries are given in Figures 5.35 to 5.37. The results indicate that an increase in fineness ratio, that is an increase in nose cone length, reduces the drag coefficient at supersonic speeds. This is caused by a reduction in the wave drag acting on the nose cone due to shock waves. At high fineness ratios the increase in skin friction from the larger nose cone, results in the drag advantage becoming significantly less as shown in the figures below.
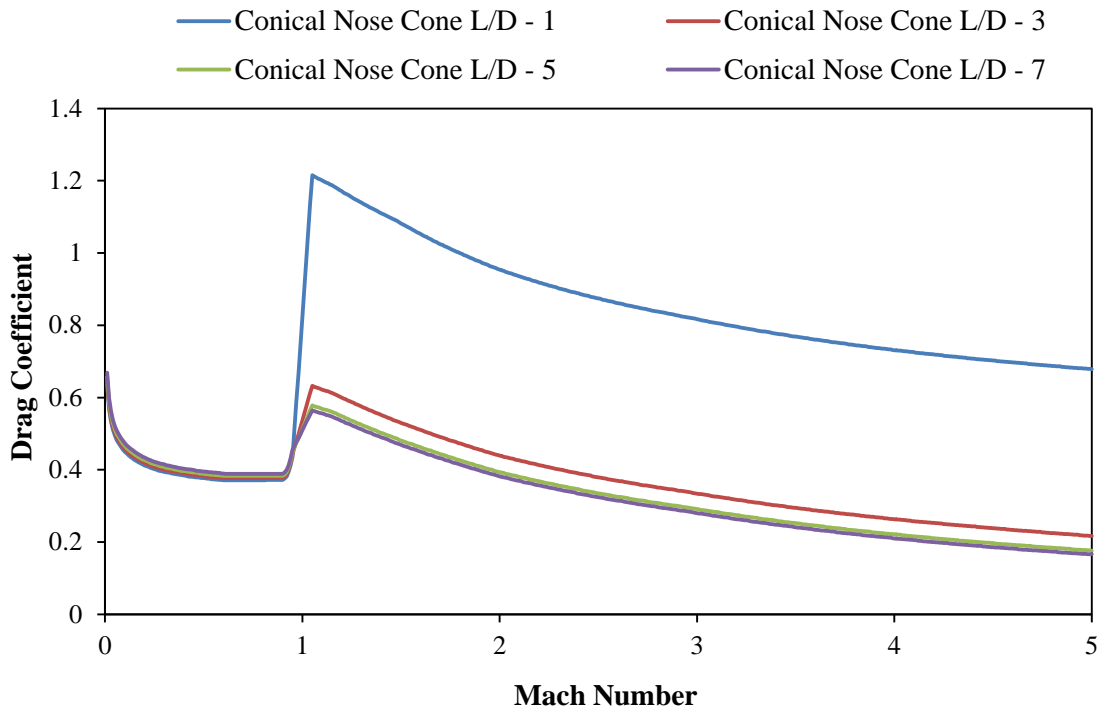
Figure 5.35: Drag coefficient versus Mach number for conical nose cone.
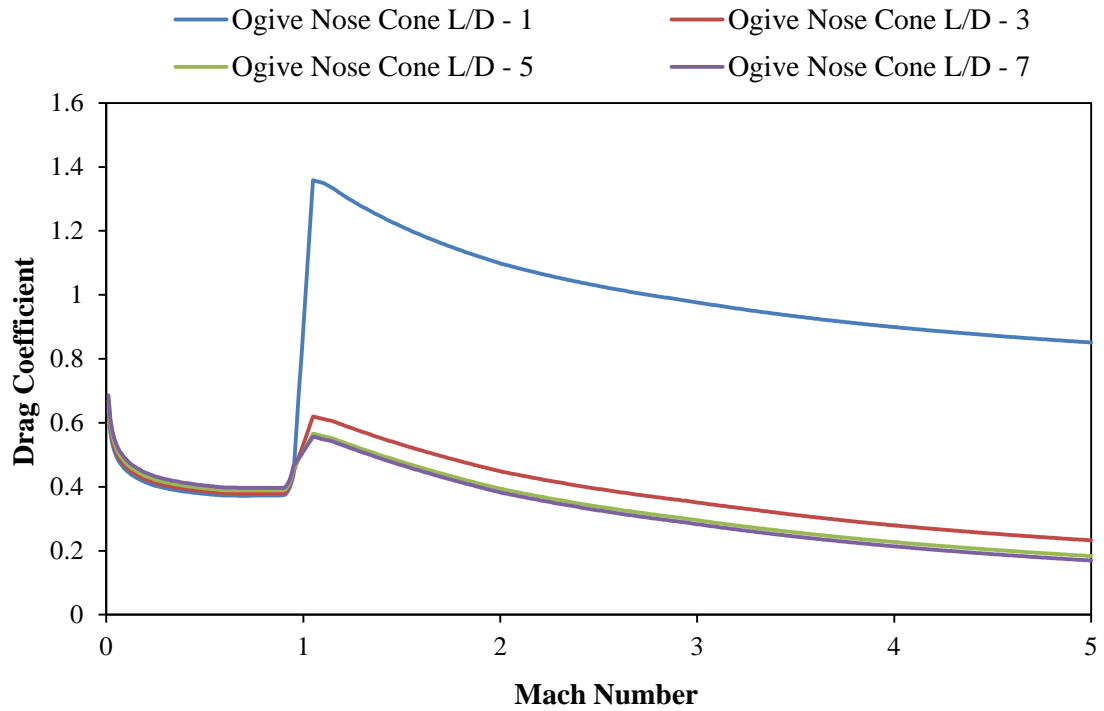
Figure 5.36: Drag coefficient versus Mach number for ogive nose cone.
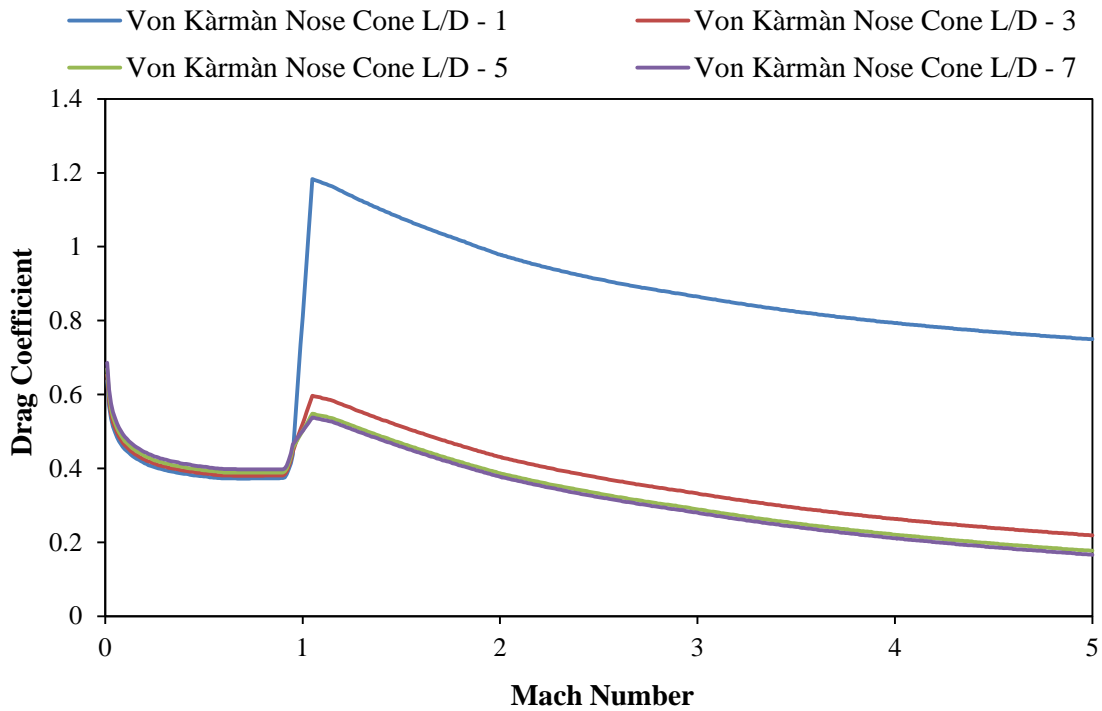
Figure 5.37: Drag coefficient versus Mach number for Von Kàrmàn nose cone.

The results indicate that above a fineness ratio of 5 there is no significant improvement in drag. Figure 5.38 compares the drag coefficient for the different nose cone geometries with a fineness ratio of 5.
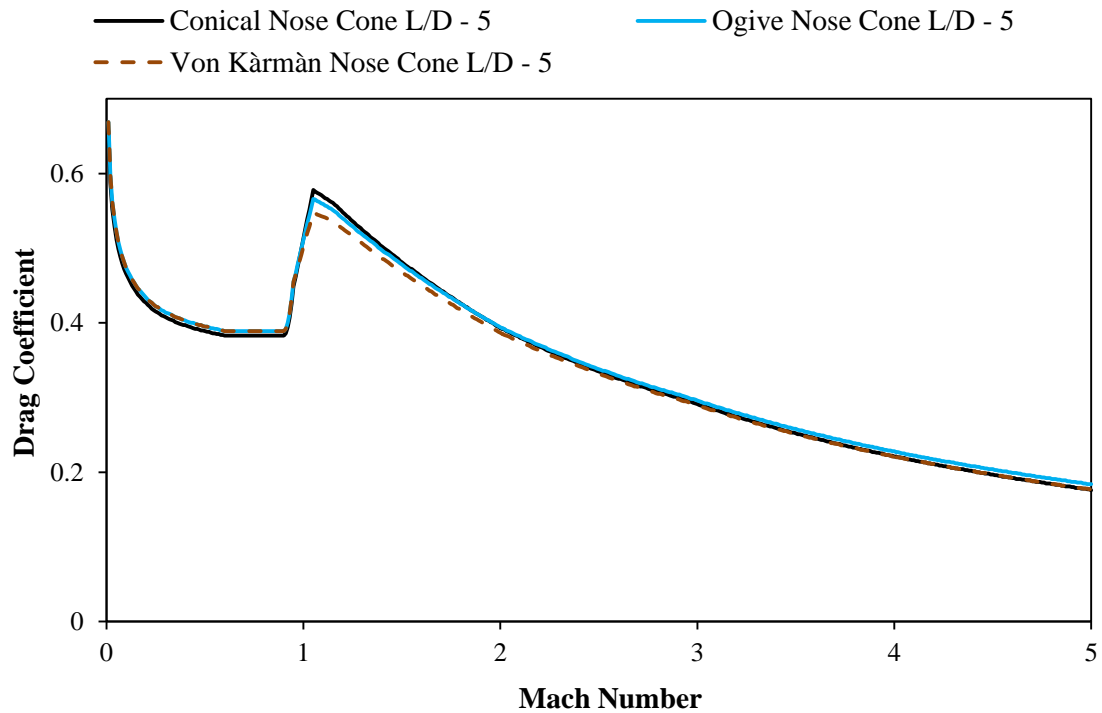
Figure 5.38: Drag coefficient versus Mach number for various nose cone geometries with a fineness ratio of 5.

It was found that the geometry itself had a minimal effect on the drag coefficient. The conical nose shape has the lowest subsonic drag coefficient and the Von Kàrmàn ogive has the lowest coefficient up to a Mach number of approximately 4.

The conical nose cone has the lowest mass because it requires the least material for a constant thickness (see Figure 5.34 to view geometrical comparison). This results in the conical nose cone achieving the best apogee for all fineness ratios under the first scenario (Figure 3.39).
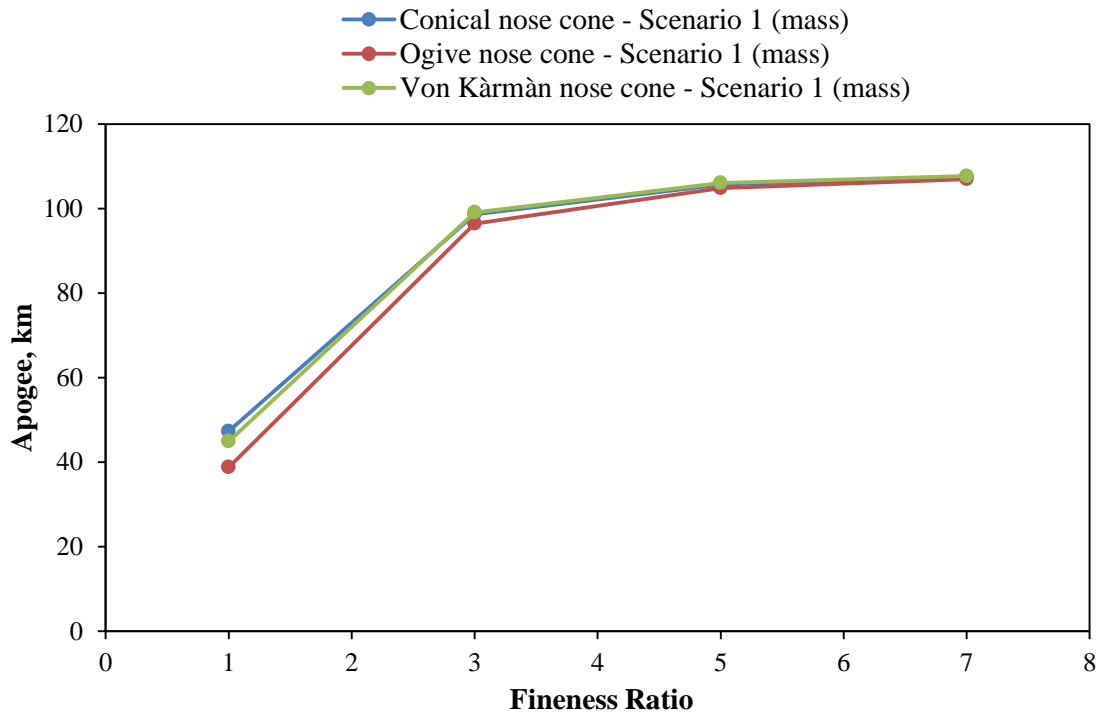
Figure 5.39: Apogee versus fineness ratio for nose cone – Scenario 1.

For Scenario 2, the mass of the nose cones remains constant for the various fineness ratios. For a fineness ratio of 1 the conical geometry produces the lowest drag coefficient for supersonic Mach numbers.

The results for Scenario 2 are shown in Figure 5.40. This figure illustrates that for fineness ratios 3 and above, the Von Kàrmàn ogive yields the highest apogee. The higher the fineness ratio, the less the apogee differs for each geometry. This indicates that geometry has an almost negligible effect at high fineness ratios.
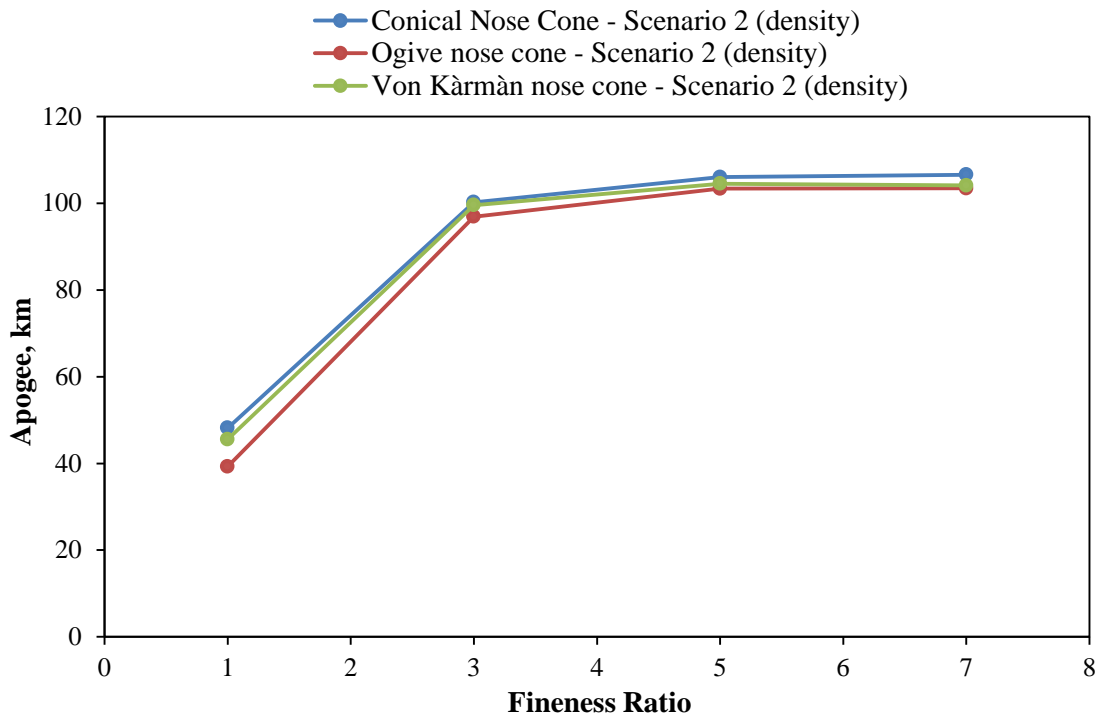
Figure 5.40: Apogee versus fineness ratio for nose cone – Scenario 2.

Bluffness ratio

An investigation of the bluffness ratio, or nose tip blunting, indicates that for ratios above 0.2 the vehicles do not achieve the target apogee and therefore are disregarded. An increase in bluffness ratio increases the wave drag acting on the vehicle and therefore increases the drag coefficient. This causes a decrease in apogee as depicted in Figure 5.41. Low bluffness ratios have a minimal effect on apogee as shown.
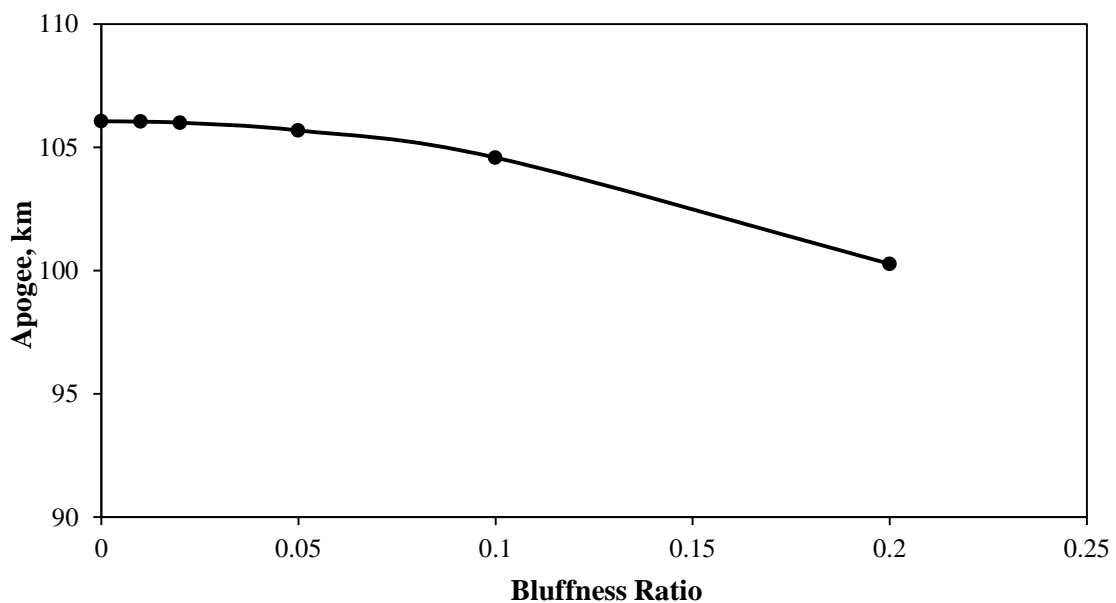
Figure 5.41: Apogee versus bluffness ratios.

Parameter Selection – Nose Cone

Fineness ratio

A trade-off between the reduction in wave drag, and increase in skin friction, performance, and volume capacity for the payload is required to determine the fineness ratio of the nose cone. A Von Kàrmàn nose cone with a fineness ratio of 5 was selected for Phoenix-2A because minimal performance improvement was found for higher ratios. A fineness ratio of 5 has a larger payload capacity available than if lower ratios are used or compared to a conical nose cone. The Von Kàrmàn geometry with a fineness ratio of 5 achieves an apogee of 104.5 km for Scenario 1 and 106.1 km for Scenario 2. The Scenario 2 vehicle was selected, for the following trade study, to maintain a 0.6 propellant mass fraction as the increase of inert mass in nose cone length is minimal compared to the gross mass of the vehicle.

Bluffness ratio

A bluffness ratio of 0 was chosen as this gave the highest apogee. For thermal protection against stagnation temperatures, a material that has high yield and creep properties should be used for the tip of the nose cone. Examples include Inconel alloy or a carbon-carbon composite. Blunting of the nose cone tip reduces the heat transfer rate from the air stream to the surface and thus results in lower surface temperatures. Future work should investigate the thermal implications of blunting the nose cone tip.

5.2.2 Fuselage Diameter

This study considers variation in the maximum diameter of the vehicle fuselage to determine the effect on the rocket's drag and apogee. A change in fuselage diameter affects the oxidiser tank geometry requiring the propulsion system of each design to be analysed using the HRPC-Performance Model.

Methodology

The maximum external fuselage diameters were analysed as ratios of the diameter used in the previous trade study ($D_T = 0.413\ m$). These ratios were 0.8, 0.9, 1.0, 1.1 and 1.2. To reduce the effect of form drag the nose cone fineness ratio was kept constant for all the vehicles.

The HRPC-Performance Model was run to determine the thrust curve based on the change in oxidiser tank mass. The aerodynamic characteristics of the vehicle were then reassessed using RASAero due to the change in outer diameter and length. The overall mass was kept constant as the same propellant mass fraction and mass of propellants were used.

Results

The vehicle geometries simulated in this trade study are given in Table 5.6. An increase in fuselage diameter causes the vehicle length and the L/D ratio to reduce, and the reference area (cross-sectional area) to increase.

The mass of the oxidiser tank was the only parameter which varied in the HRPC-Performance Model. Increasing the external diameter of the oxidiser tank increases the hoop stress for the same working pressure and therefore increases the required wall thickness. The wall thicknesses in this trade study were restricted to vary in increments of 0.5 mm in order to obtain the required outer diameters. This led to various oxidiser tank masses, as shown in Table 5.6. An increase in oxidiser tank mass results in less inert mass being available for other components.

Table 5.6: Vehicle specifications for various design fuselage diameters.

Parameters	Design Fuselage Diameter				
	0.8 x D	0.9 x D	1.0 x D	1.1 x D	1.2 x D
Fuselage diameter (m)	0.330	0.372	0.413	0.455	0.496
Oxidiser tank thickness (mm)	5.5	6.0	6.5	7.5	8.0
Oxidiser tank mass (kg)	155.1	150.6	147.6	156.1	154.0
Oxidiser tank length (m)	9.745	7.691	6.269	5.222	4.428
Overall rocket length (m)	14.6	12.8	11.6	10.7	10.1
L/D ratio	44.2	34.4	28.1	23.5	20.4
Reference area (m)	0.0855	0.1087	0.1340	0.1626	0.1932

The HRPC-Performance Model, based from the work of Fernandez (2009), uses the conservation of mass and energy, and Raoult's Law to numerically solve for the change in the number of moles of nitrous oxide in the oxidiser tank, both in liquid and gas phase, and for the change in temperature of the oxidiser tank. The HRPC-Performance Model assumes that the oxidiser and tank wall are in thermal equilibrium and the heat transfer to and from the environment is neglected. The oxidiser and oxidiser tank are considered as the control volume for this analysis.

A change in the oxidiser tank's temperature, ${dT_T}/{dt}$, is inversely proportional to the mass of the tank. During the burn time of the motor, this increase in tank mass results in a reduced change in temperature within the control volume. This causes a smaller change in oxidiser tank pressure

when compared to a vehicle with the same propulsion specifications but with a lighter oxidiser tank mass, such as the 1.0 x D vehicle. This reduced change in oxidiser tank pressure results in a higher average thrust.

The maximum design thrust was the same for each vehicle in this study, however the rate at which it decreases is slower for the vehicles with a higher oxidiser tank mass. The change in oxidiser tank mass is shown (Table 5.6) to be minimal and the effect it has on the thrust and therefore the apogee of the vehicles, is negligible.

Figure 5.42 illustrates that the drag coefficient decreases with an increase in fuselage diameter at 0° angle of attack. This can be primarily attributed to the decrease in skin friction because of the reduction in L/D ratio of the rocket.
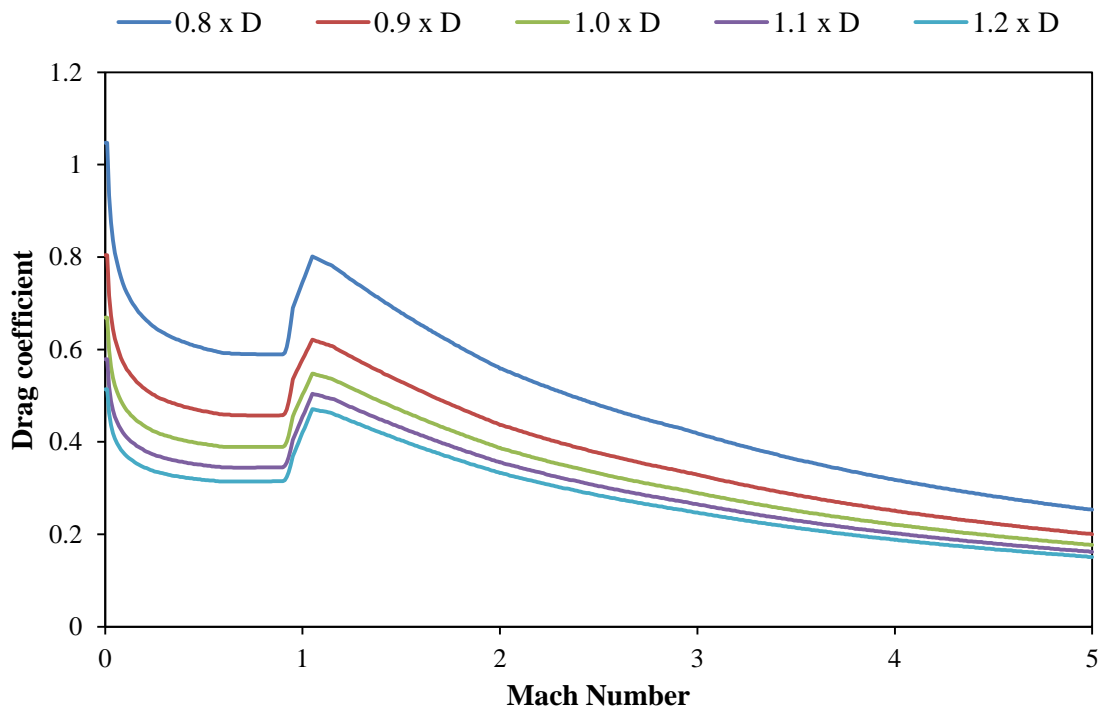
Figure 5.42: Drag coefficient versus Mach number for various fuselage diameters.

The drag coefficient has less effect on the drag force (Equation 5.7) than the reference area of the vehicle, for vehicles 1.2 x D to 0.9 x D. This is indicated by the apogee increasing for a reduction in reference area for these vehicles (Figure 5.44). The benefit of the reduced reference area for the 0.8 x D vehicle is outweighed by the substantial increase in the drag coefficient (Figure 5.42). Vehicle 0.9 x D has the lowest drag force, shown in Figure 5.43, and thus the highest apogee.
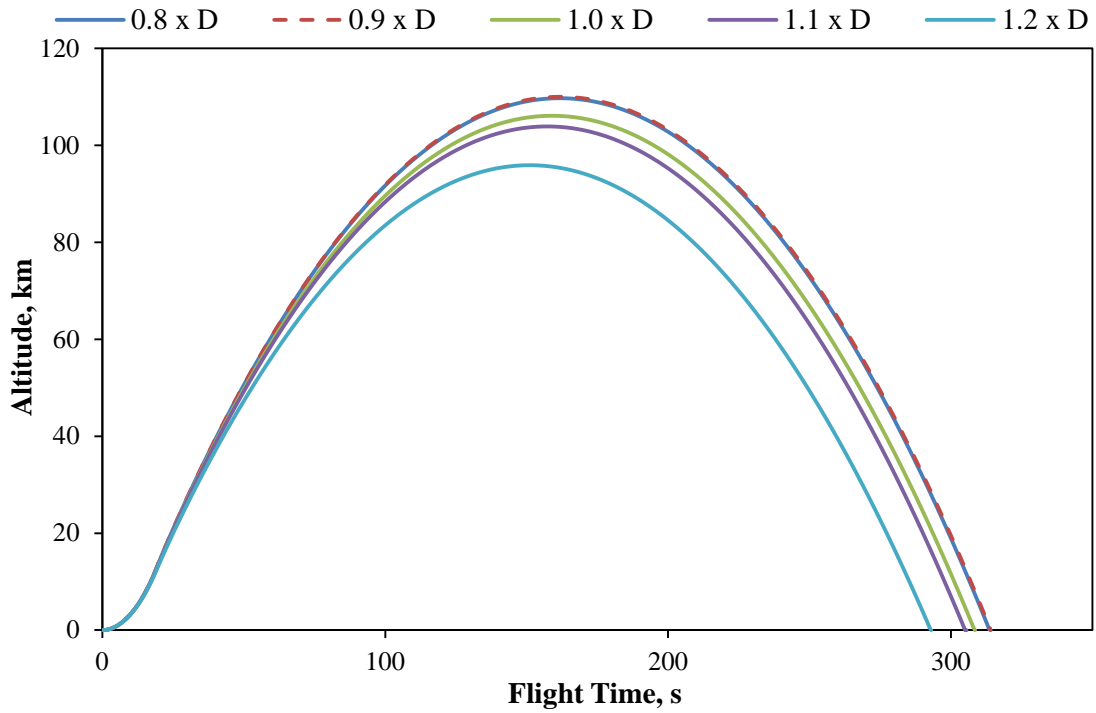
Figure 5.43: Altitude versus flight time for various design fuselage diameters.
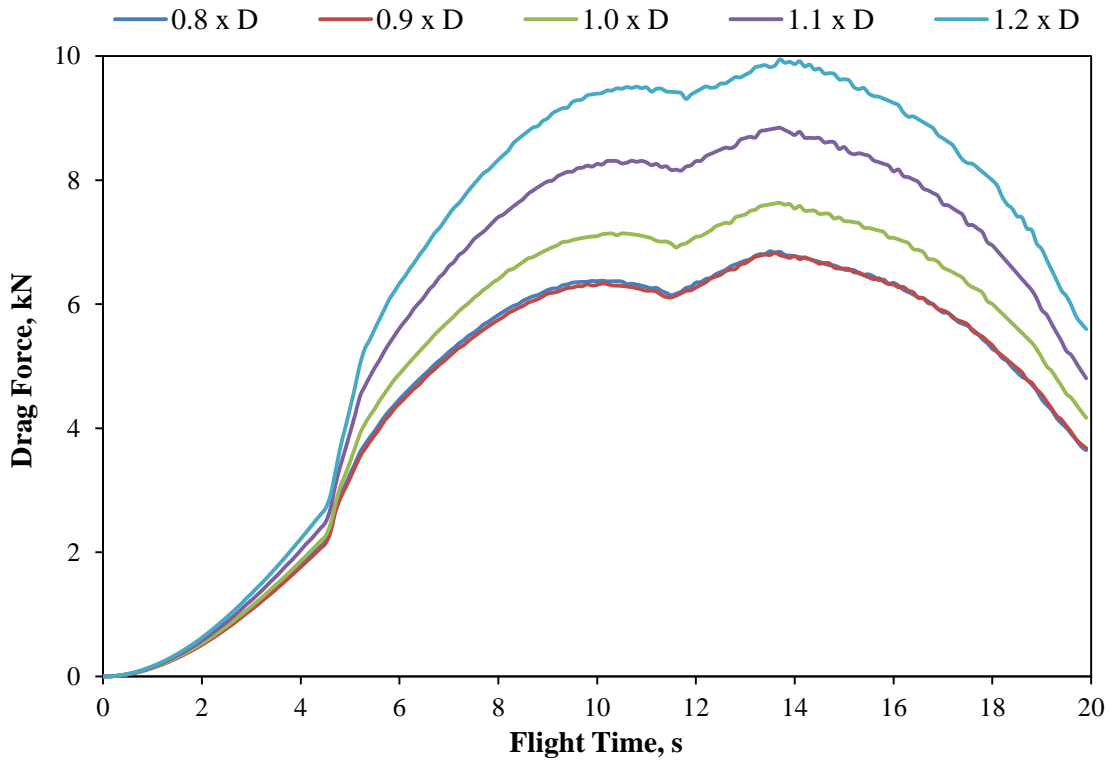
Figure 5.44: Drag force versus flight time for various fuselage diameters.

The steep rise in the drag force plot, at approximately 5 s into the burn, is due to the increase in the drag coefficient as the vehicle reaches transonic Mach numbers (Figure C.1 in Appendix C).

The discontinuous behaviour in the drag force plot at approximately 12 s and 14 s of the flight time can be attributed to associated discontinuities in the prediction of drag coefficients at these times (Figure C.2). It is presumed that the drag coefficient discontinuities were synthetically generated during the numerical solution process in which drag coefficient values are interpolated from the RASAero lookup tables.

Parameter Selection – Fuselage Diameter

Low L/D ratios are desired to reduce the occurrence of buckling. The 1.2 x D vehicle has the next lowest L/D ratio but does not reach the target apogee of 100 km due to the increase in drag force. The 1.1 x D vehicle has the lowest L/D ratio for an apogee above 100 km, however it was not selected because it has the heaviest oxidiser tank. This led to the selection of the 1.0 x D vehicle and therefore a fuselage diameter of 0.413 m.

5.2.3   Fin Geometry

A rocket's fins are designed to ensure that stability is maintained during flight. For stability to be achieved the fins should have a static margin of above 1. The static margin (*SM*) of a rocket is defined by Equation 5.8 which is the centre of gravity (*CG*) minus the centre of pressure (*CP*) of the rocket divided by the maximum diameter, which in this case is the tank diameter (D_T).

$$SM = (CG - CP)/D_T \tag{5.8}$$

The fin geometry was investigated to improve the fin planform for performance while ensuring it is resistant to oscillations and mitigates fin flutter. The most common fin flutter, namely bending-torsion flutter (Martin, 1958), was examined in this trade study. The fin design is required to be lightweight, cost-effective, and easily machined. The fin planforms examined were rectangular, delta, clipped delta, and swept clipped delta. The aerofoil, which is the cross-sectional area of the fin, was also briefly examined.

Methodology

The effect of varying the root chord, tip chord, sweep, span, and thickness of the fin geometry was considered in this study. The root span, not indicated in Figure 5.45, remained constant as the distance from the centre line of the combustion chamber to the fin is the same. This is because the hybrid motor is the same for all fin simulations. All simulations have a cruciform configuration of four fins located 100 mm forward of the boat-tail.

The study proceeds with a flutter analysis of the fins used in the previous trade studies. This is followed by the effects that various planforms have on the vehicle's performance. The fin planforms are illustrated in Figure 5.45 and include:

1. Rectangular fin planform - Various root/tip chord and span dimensions
2. Delta fin planform - Various root chord and span dimensions
3. Clipped delta fin planform - Various taper ratios
4. Swept clipped delta fin planform - Various angles and fin dimensions
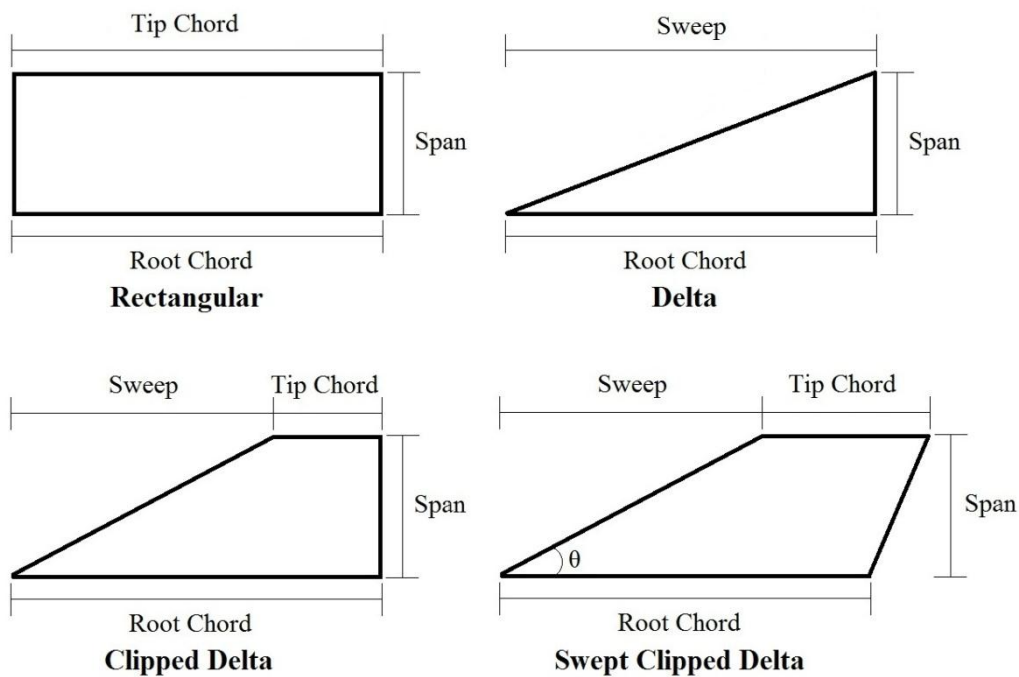
Figure 5.45: Geometrical parameters of various fin planforms.

The aerofoil was varied to improve the performance of the selected fin planform. The fin masses were allowed to vary, meaning that the propellant mass fraction was variable. The objective of this study was to reduce fin mass and aerodynamic forces, while designing against fin flutter. The analytical approach used to determine the fin thickness based on bending-torsion flutter is given in Appendix C.2. The maximum velocity of the rocket used in the study was 1400 m/s unless the flight simulation design exceeded this value, in which case it was increased accordingly. The fin designs incorporate a safety factor of 1.25 based on the shear modulus of the material. For simplicity the fins are assumed to be made out of aluminium for the fin flutter investigation. For all the simulations the mass of the fin is calculated by assuming a constant thickness throughout its cross-section thus ignoring the shape of the aerofoil. This is to account for mass required for fin attachment and other miscellaneous mass.

Future work may investigate different fin materials, especially composite lay-ups for mass reduction. The static margins illustrated in this trade study are equivalent to the minimum static margin that the vehicle experiences during its flight.

Results

The analysis demonstrated that the fin geometry used in previous trade studies was unacceptable for flight in terms of flutter. An increase in thickness to 15.2 mm is required as shown in Appendix C.2. This increases the drag due to an increase in frontal area of the fins, and increases the inert mass of the fins by 28 kg. The propellant mass fraction decreases to 0.585 and results in a significant reduction in flight performance. The vehicle achieves an apogee of 93.5 km, which is below the target apogee. This illustrates the importance of considering fin flutter in preliminary design analyses.

Aerofoil

The aerofoil was improved from the existing hexagonal planform used in the original fin design. The tabulated wave drag coefficients of various aerofoils used in missile design are given in Table C.5 in Appendix C.2. The aerofoils that have the lowest wave drag coefficient are the single wedge and double symmetrical wedge aerofoils (Figure 5.46). The minimum drag coefficient at a Mach number of 3 was obtained with the double symmetrical wedge profile and was used in all further simulations. A sharp leading edge was selected over the previous smoothed edge to improve the aerodynamic characteristics.
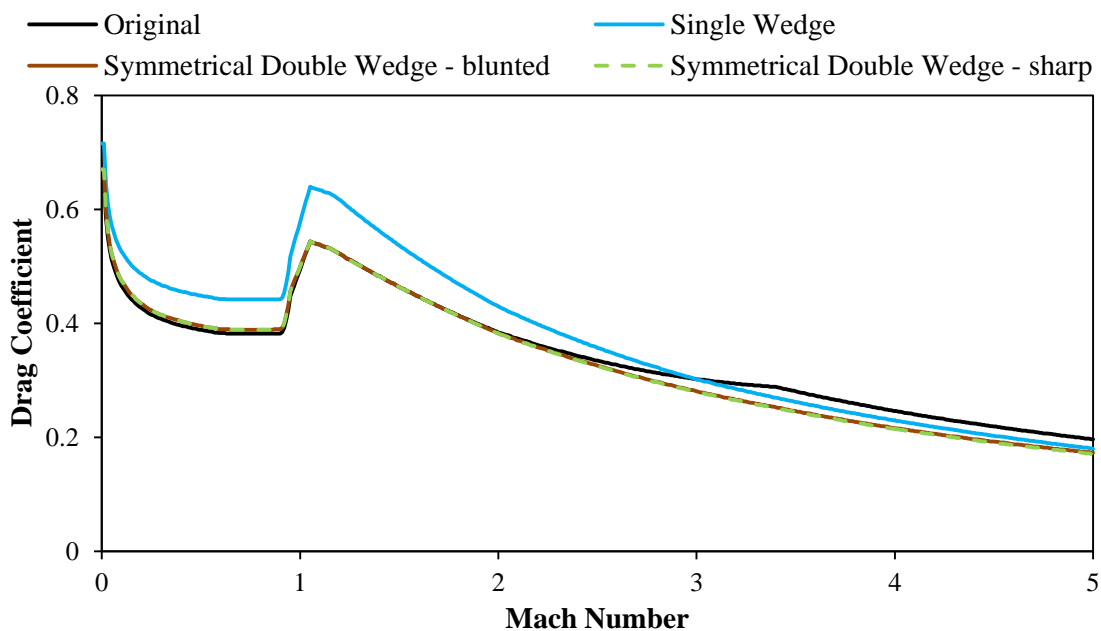
Figure 5.46: Drag coefficient versus Mach number for various aerofoils.

Rectangular planform

The results of the rectangular planform are shown in Figures 5.47 and 5.48. The analysis on the rectangular fin planform illustrates that as the root chord and tip chord decrease the apogee increases and the static margin decreases. The static margin is directly proportional to the change in root and tip chord. The decrease in root and tip chord reduces the surface area of the fin and the effective lift it can provide. Figure 5.47 shows that a 100 km apogee cannot be obtained with a static margin above 1 by decreasing the fins root and tip chord.
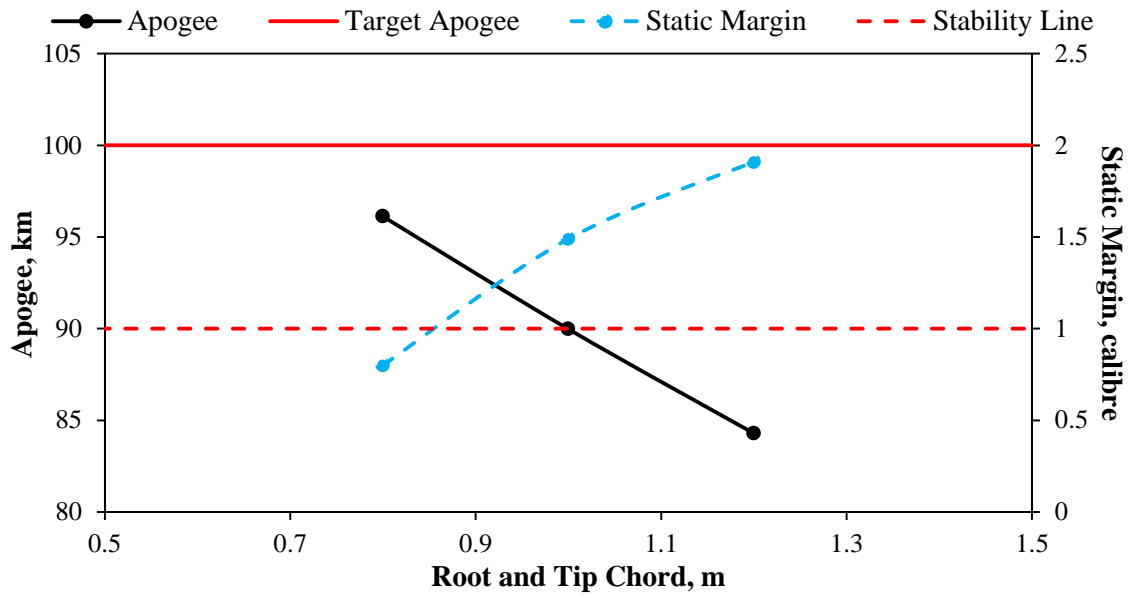
Figure 5.47: Apogee and static margin for various root chords of rectangular fins.
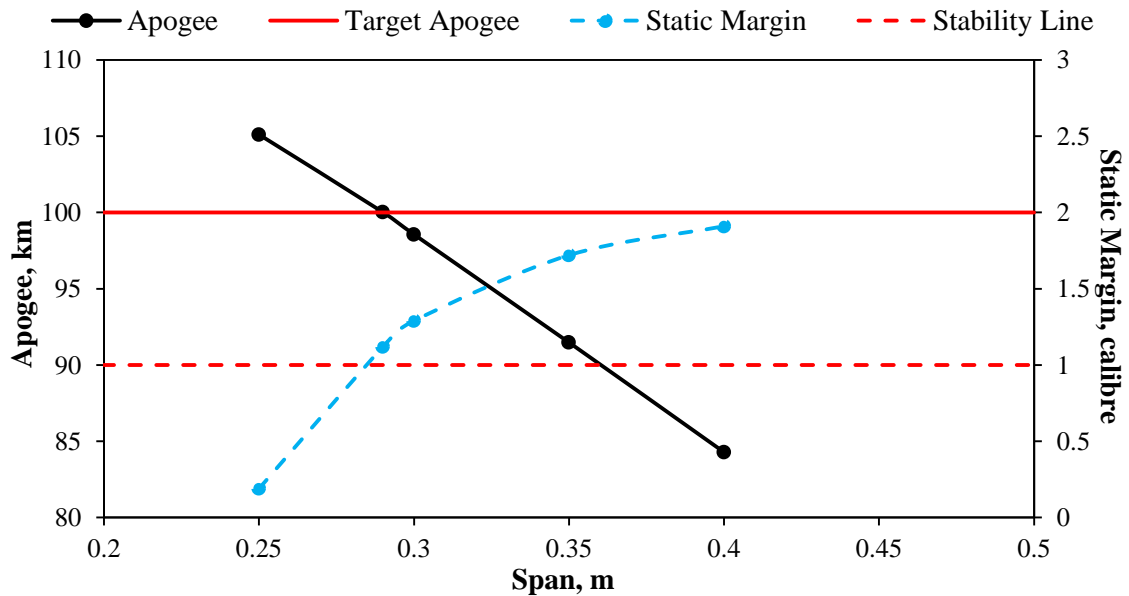
Figure 5.48: Apogee and static margin for various span lengths of rectangular fins.

The variation of the fin's span has the same proportional trends as the variation of the fin's root chord, however the decrease in span leads to designs that reach the target altitude with static margins greater than 1, as illustrated in Figure 5.48. The decrease in the root and tip chord or span results in a smaller thickness required for the fin due to fin flutter. The fin flutter analysis results on the rectangular planform are given in Appendix C.2.

Delta planform

The investigation into the delta fin designs shows that the simulations all give static margins below 1 and are therefore disregarded (Figures 5.49 and 5.50).
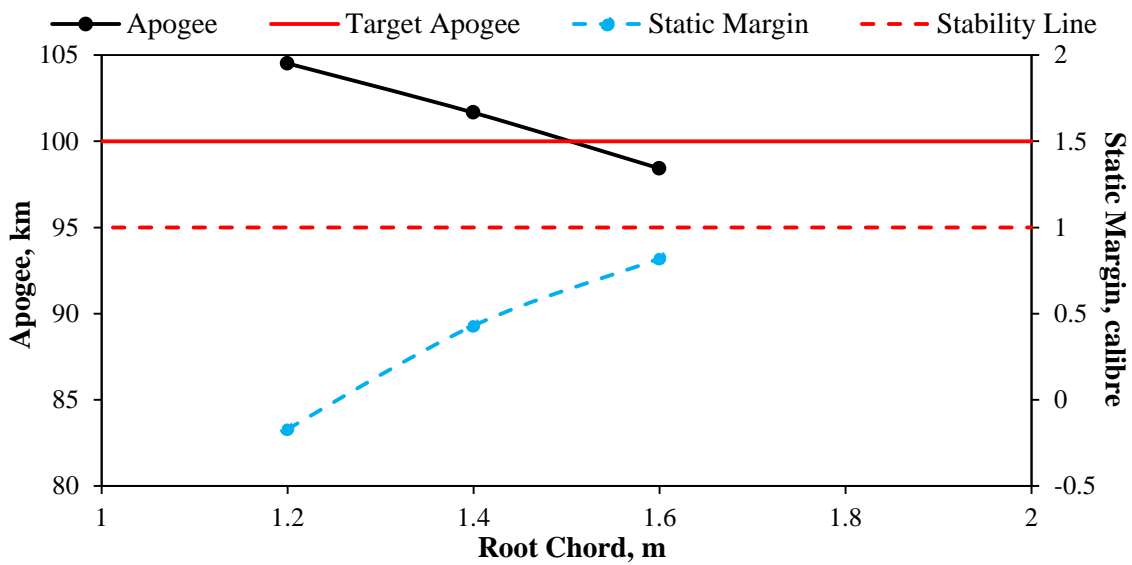
Figure 5.49: Apogee and static margin for various root chords of delta fins.
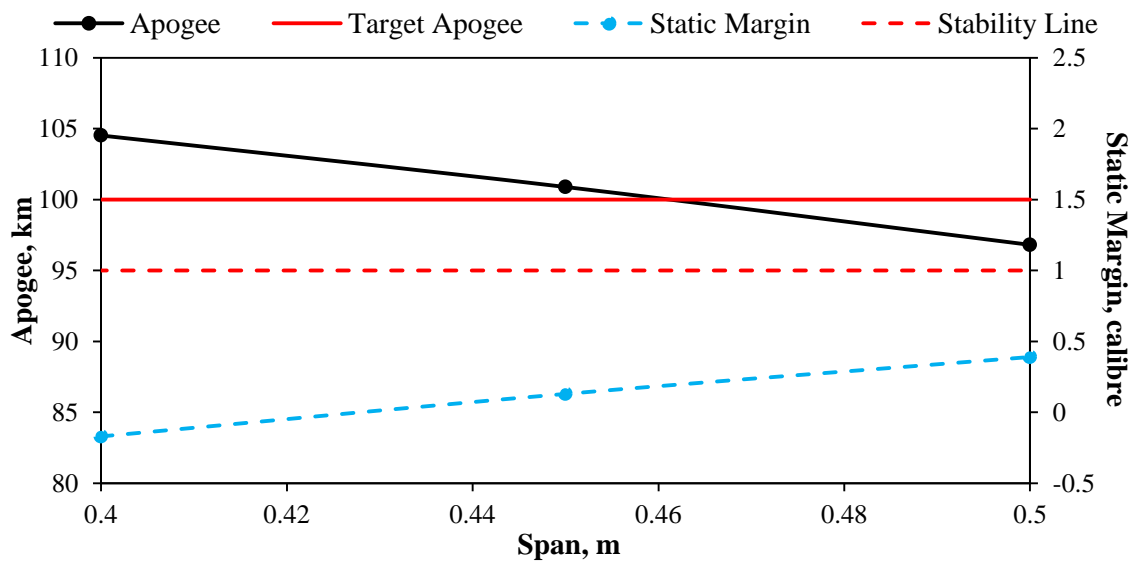
Figure 5.50: Apogee and static margin for various span lengths of delta fins.

The delta configuration does not have a large enough root chord and span to offer the required surface area for lift. The increase in dimensions causes the thickness to increase, which increases the inert mass of the vehicle and thus lowers performance.

Clipped delta planform

The taper ratio was varied from the initial delta configuration of 0 up to a ratio 0.5 to analyse fins with clipped delta planforms. Figure 5.51 shows that increasing the fin's taper ratio improves the static margin by increasing the surface area of the fins (refer to Table C.3 in Appendix C). Increasing the taper ratio also increases the required fin thickness and this mass penalty causes a loss in apogee. The designs are unable to achieve the target apogee with a static margin above 1.
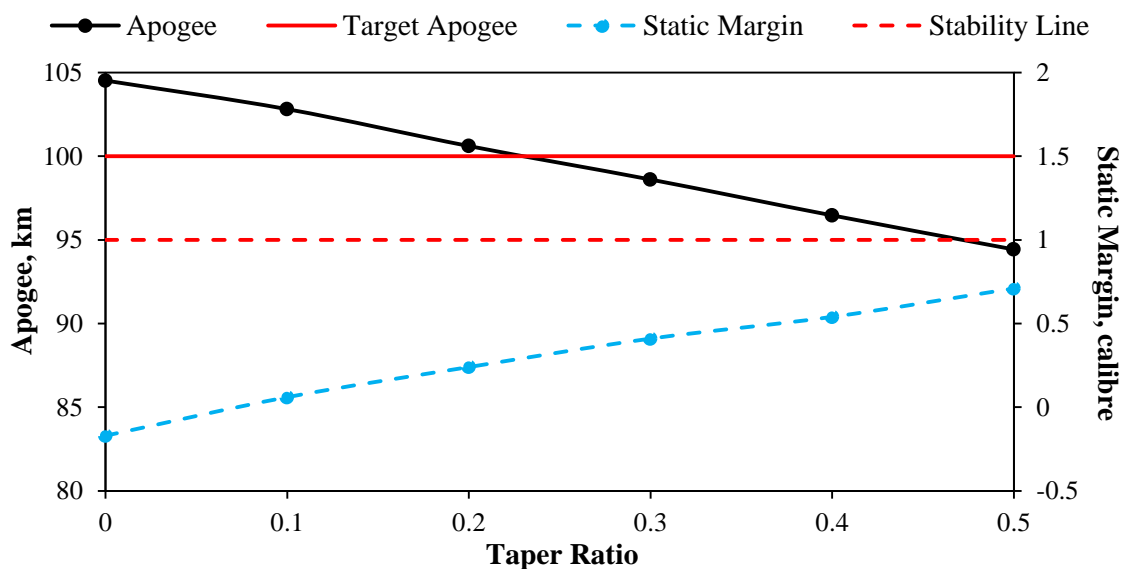
Figure 5.51: Apogee and static margin for various taper ratios for clipped delta fins.

Swept clipped delta planform

The rectangular fin that was stable and gave an apogee of 100 km (Rect 7, in Table C.1) was used to determine the effect of changing the leading edge angle by increasing the sweep distance. The leading edge angle for the rectangular planform is 90°, while the other angles examined were 60°, 30°, 20°, and 15°. Smaller angles were not investigated as they lead to fins that are difficult to fabricate with unrealistic profiles. The root length, tip chord, span, and thickness remained constant for all simulations.

The results illustrate that the rectangle has the best static margin. It is noted that the static margin improves again as the leading edge angle reduces past 60°. The simulation results in Table 5.7 indicate that the swept fins do not have static margins above 1 so further analysis was

required by varying the fin geometry to obtain enough surface area for stability. Figure 5.52 demonstrates a major improvement in the drag coefficient in the subsonic region and a slight improvement at low supersonic Mach numbers.

Table 5.7: Flight performance for various leading edge angles of swept clipped delta fins.

Varying Fin Geometry		Flight Performance	
Angle (°)	Sweep (m)	Apogee (km)	Static Margin (calibre)
90	0.000	100.010	1.12
60	0.167	100.016	0.20
30	0.502	100.154	0.58
20	0.797	100.244	0.67
15	1.082	100.304	0.83
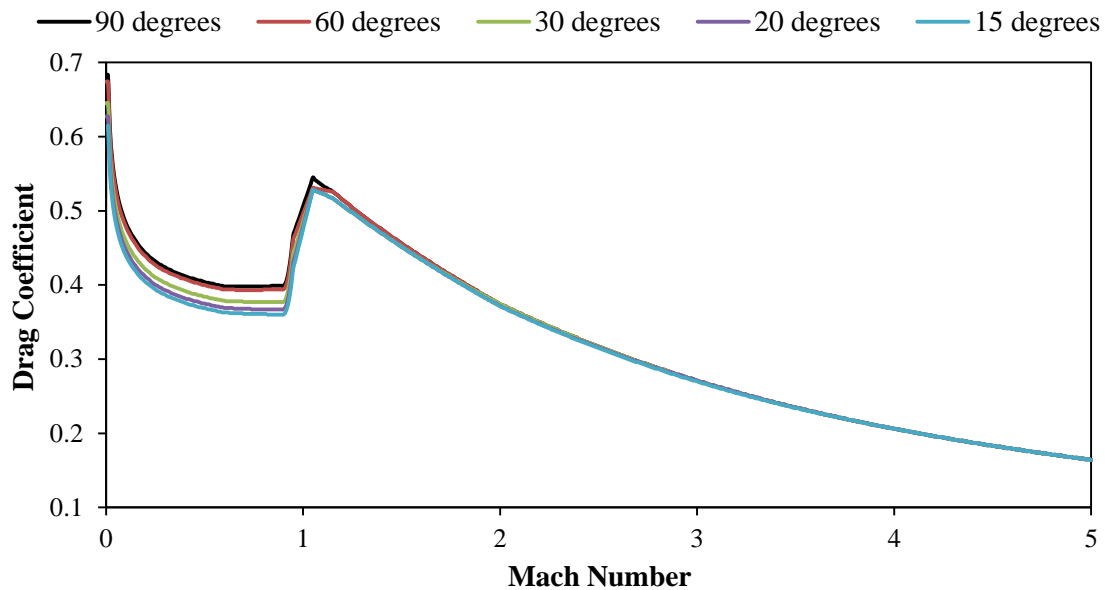
Figure 5.52: Drag coefficient versus Mach number for various leading edge fin angles.

Generally, smaller leading edge angles improve stability and aerodynamic characteristics by moving the centre of pressure further back, from the nose tip. An angle of 20° and various span and root chord lengths were used in the following fin designs (Table 5.8). The sweep length and tip chord were changed with increasing span to obtain the same surface area as the Rect 7 design. Table 5.8 shows that Fin Design C has the best stability but the static margin is not above the required value of 1. The design was therefore modified to have an angle of 19° to achieve the correct minimum static margin. This resulted in a stable vehicle that achieves an apogee of 96.3 km. The average flight static margin of this design is 2.6. Figure 4.53 illustrates

that all the designs have similar drag coefficients with Fin Design C1 having the best drag coefficient up to a Mach number of 3.

Table 5.8: Fin geometry and flight performance for various swept clipped delta fins.

Fin Design	Varying Fin Geometry					Flight Performance	
	Root Chord (m)	Span (m)	Sweep (m)	Tip Chord (m)	Thickness (mm)	Apogee (km)	Static Margin (calibre)
A	1.4	0.3	0.824	0.90	13.0	100.001	0.49
B	1.3	0.35	0.962	0.65	14.5	98.101	0.78
C	1.2	0.40	1.099	0.50	16.0	96.283	0.94
C1	1.2	0.40	1.162	0.50	16.0	96.312	1.00
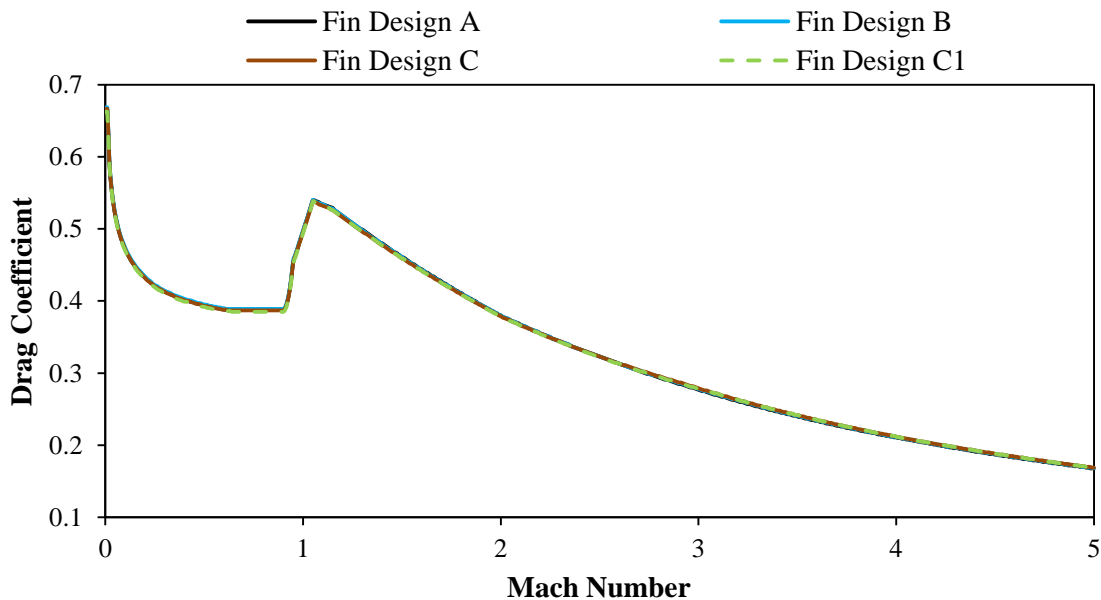
Figure 5.53: Drag coefficient versus Mach number for various fin designs.

Parameter Selection – Fin Geometry

Rectangular fins were not selected due to their high bending moments and higher drag coefficient in the low supersonic drag regions. Rectangular fins provide large surface areas and are advantageous if the launch platform geometry constrains the dimensions of the fin design. The launch platform for Phoenix-2A still has to be manufactured and therefore is not a constraint on the design. The delta and clipped delta fin designs had insufficient area for stable flight and were disregarded. The fin design C1 was selected even though it did not obtain the target altitude because it has a minimum static margin of 1. Fin design C1 is a swept clipped

delta fin planform that has lower bending moments and drag coefficients, better control, and more resistance to aeroelastic instability than the rectangular planform (Fleeman, 2001). For protection against aerodynamic heating on the fins' leading edges Inconel, titanium, ceramics, carbon, reinforced carbon composites, or steel can be used as well as a heat resistant coating. Another propulsion iteration was required to improve the thrust of the vehicle to reach the desired apogee and is discussed in the next section.

5.3 Final Phoenix-2A Design

A trade study incorporating fin flutter determined that an increased thrust of 85 kN is necessary to reach the target apogee of 100 km. With this in mind, and considering the previous parametric trade studies, the inputs for the final Phoenix-2A design are given in Table 5.9.

Table 5.9: HRPC-Motor Design Model inputs for the final Phoenix-2A design.

Final Parameters	Description	
Oxidiser	Nitrous oxide	
Oxidiser temperature	283.1 K	
Fuel	Sasol 0907 paraffin wax	
Fuel temperature	298.2 K	
Fuel density	924 kg/m^3	
Fuel enthalpy	-1438,2 kJ/mol	
Thrust	85 kN	
O/F ratio	8	
Chamber pressure	42 bar	
Nozzle design altitude	70079.00 Pa	3 km above sea level
Burn time	18 s	
Flow composition	Equilibrium	
Regression rate coefficient	0.000155	
Regression rate exponent	0.5	

A design O/F ratio of 8 was used in the HRPC-Motor Design Model. The O/F ratio was increased in the HRPC-Performance Model due to a reduction of the L/D ratio of the fuel grain from 5.2 to 5. This reduction in L/D ratio reduces the mass of the fuel and thus increases the O/F ratio from the original design value of 8. A design atmospheric pressure of 3 km above sea

level was used. The design burn time remains at 18 s and the port diameter is constrained to twice the nozzle throat diameter.

The oxidiser tank and combustion chamber were designed based on the ASME Pressure Vessel Design Code. The mass of these components increases from the previous fin trade study due to an increase in dimensions because more propellant is needed to obtain a higher design thrust. The nozzle mass (Equation 4.7) increases because of the increase in propellant mass. The mass allocated for the recovery system is increased as the inert mass is greater than the previous design and thus may require slightly larger parachutes.

The oxidiser tank is the largest component of the vehicle and was analysed to determine if buckling would occur using the work of Bruhn (1965), which treats the part as a monocoque cylinder. The minimum tank pressure of 37 bar and the maximum axial loading obtained from the HYROPS software were applied to the oxidiser tank. It was found that the oxidiser tank would not fail due to buckling with the presence of internal pressure, but would fail if there was no internal pressure (see Appendix D.1). Modelling of aeroelastic behaviour and dynamic instabilities of a rocket can be found in the work of Hodges (2004), Chae (2004), Pradhan and Datta (2006), and Datta and Biswas (2011) which can be incorporated into the Flight Dynamics Simulator. It is advised that a complete buckling analysis of the entire vehicle is conducted in future phases of the design.

The initial conceptual design obtained in Chapter 4 had the incorrect fin thickness to withstand fin flutter. This vehicle was modified by increasing the fin thickness to 15.2 mm (as determined by section 5.23). The larger thickness results in an increase in inert mass and drag and therefore reduces the apogee. Table 5.10 compares the three vehicles below:

1. Initial conceptual design (Chapter 4)
2. Modified vehicle (the initial conceptual design - fin thickness increased to 15.2 mm)
3. Final design

The gross mass of the final vehicle is 1006 kg which is 25.0 kg and 53.3 kg lighter than the initial conceptual design and modified vehicle respectively. The oxidiser mass was reduced by 15.8 kg and the fuel mass required by 16.5 kg. The overall length of the final Phoenix-2A vehicle increases by 0.21 m. This is mainly due to the substantial increase in the fineness ratio of the nose cone. The initial fineness ratio of 3.5 did not provide the best trade-off between wave and skin friction drag and larger fineness ratios offers more volume capacity for the scientific payload.

Table 5.10 includes the major components of the final design of Phoenix-2A and their dimensions. These are preliminary designs that require in-depth structural and thermal FEA analysis as part of the future work of the Phoenix-2A project.

Table 5.10: Design comparison between the initial conceptual and final Phoenix-2A vehicles.

		Initial Conceptual Design	Modified Vehicle	Final Design
Oxidiser Tank	Mass (kg)	162.0	162.0	157.7
	Length (m)	6.843	6.843	6.651
	External diameter (m)	0.413	0.413	0.413
	Wall thickness (m)	6.5	6.5	6.5
Combustion Chamber	Length (m)	2.151	2.151	1.856
	External diameter (m)	0.398	0.398	0.388
	Wall thickness (mm)	5.5	5.5	5.5
Propellant	Oxidiser mass (kg)	544.7	544.7	529.0
	Fuel mass (kg)	77.6	77.6	61.1
Nozzle	Throat diameter (m)	0.133	0.133	0.127
	Exit diameter (m)	0.320	0.320	0.364
Fin	Mass (kg)	27.5	55.8	58.8
	Thickness (mm)	7.5	15.2	16.0
Overall	Mass (kg)	1031.0	1059.3	1006.0
	Propellant mass fraction	0.60	0.59	0.59
	Length (m)	11.78	11.78	11.99
	Apogee (km)	100.1	89.6	100.9

Figure 5.54 illustrates the apogee versus range of the final Phoenix-2A design and modified vehicle. The figure shows that the final design reaches an apogee of 100.9 km at 155.2 s, which is 11.3 km higher than the modified vehicle. The final design has a minimum static margin of 1.09 at motor burnout and can therefore achieve stable flight condition. Additional graphs on the flight and motor performance of the final design are given in Appendix D, such as the acceleration and thrust curves of Phoenix-2A.
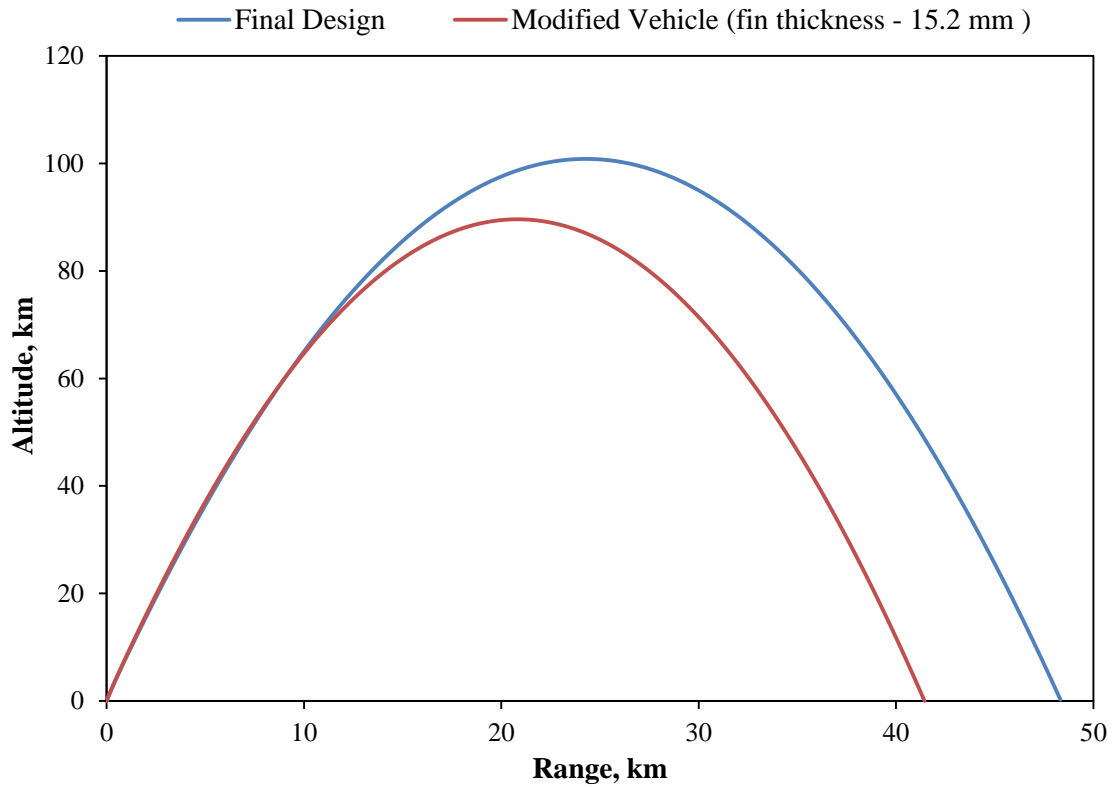
Figure 5.54: Altitude versus flight time and range for the final Phoenix-2A design.

A 0.2° fin cant angle was included in the final design to induce spin on the vehicle to maintain stability should thrust misalignment occur and reduces the impact dispersion. A maximum induced spin of 1.24 rev/s was found with no wind and the apogee reduced slightly. The Phoenix-2A vehicle with a 0.2° fin cant angle was simulated in HYROPS with various wind gradients, specified in Table 5.11. The altitude gradient (change in velocity versus altitude) and ground speed were based on the work of Entico Corporation (2003).

Table 5.11: Wind profile used in the wind modelling of Phoenix-2A.

	Altitude Gradient (/s)	Direction (°)	Cut-off Altitude (km)	Ground Speed (m/s)	Turbulence	Jet Stream
Case A	0.00055	0	110	5	Yes	No
Case B	0.00055	90	110	5	Yes	No
Case C	0.00055	180	110	5	Yes	No
Case D	0.00055	270	110	5	Yes	No
Case E	0.00055	0	110	5	Yes	Yes

Figure 5.55 illustrates the effect these wind gradients have on the apogee and range of the final design. Case E includes a jet stream between 10 km and 15 km above sea level that has a 50 m/s speed in an Easterly direction. Flight trajectory simulations of the final design with various OTR monthly wind data, which are pre-programmed in the HYROPS Flight Dynamics Simulator, are given in Figure D.9 in Appendix D. These results demonstrate the importance of wind modelling. All vehicles were launched in a South Easterly direction from OTR.
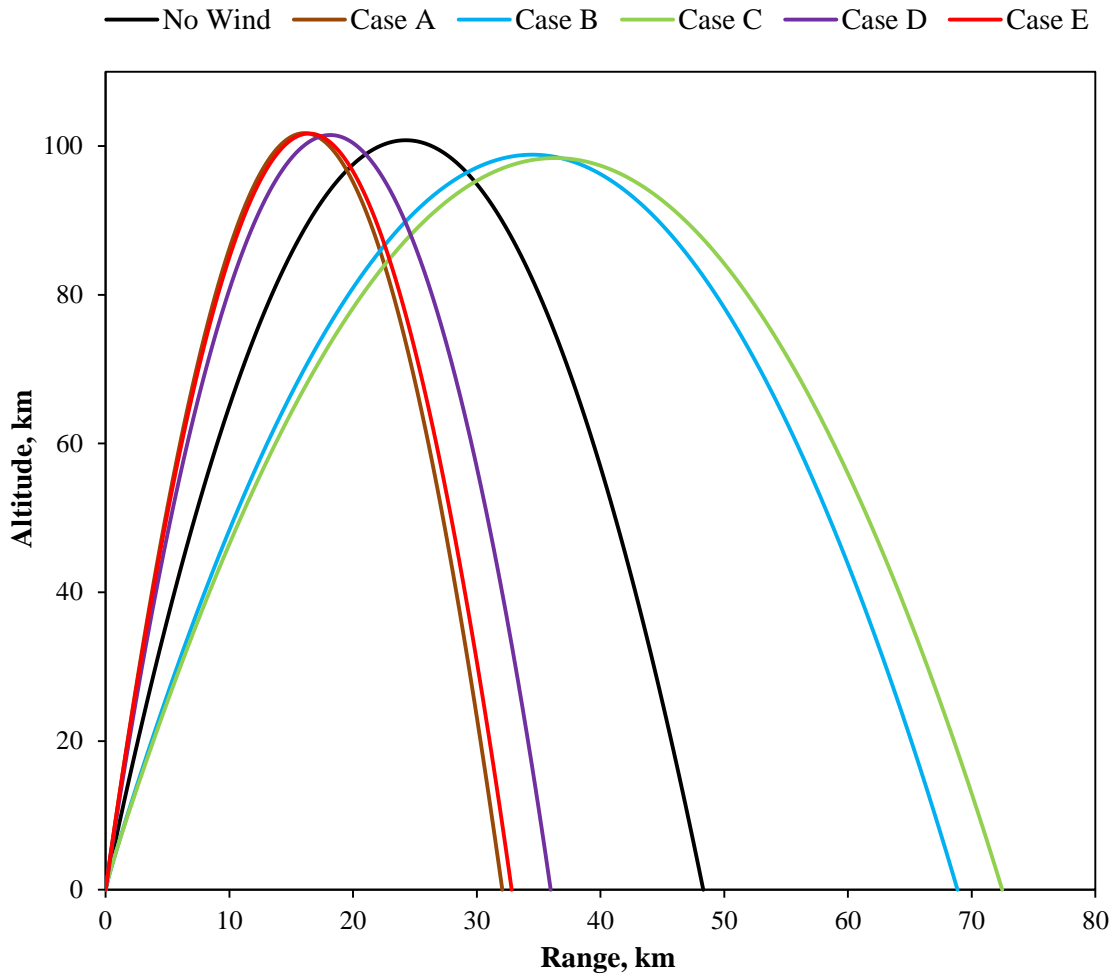
Figure 5.55: The effects gradient winds have on the final Phoenix-2A design.

Figure 5.56 is an exploded view of the final design of the Phoenix-2A rocket illustrating key components. A simplified cross-sectional view of the combustion chamber is shown in Figure 5.57 that includes the fuel grain, the pre- and post- combustion chamber inserts, the thermal liner, the nozzle and the bulkhead.
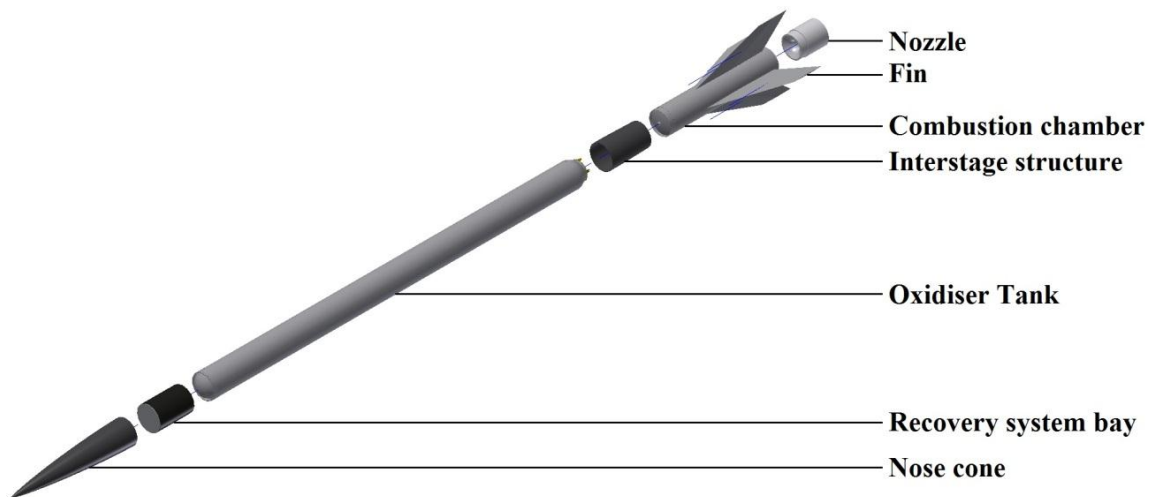
Figure 5.56: Exploded view of the final Phoenix-2A design.
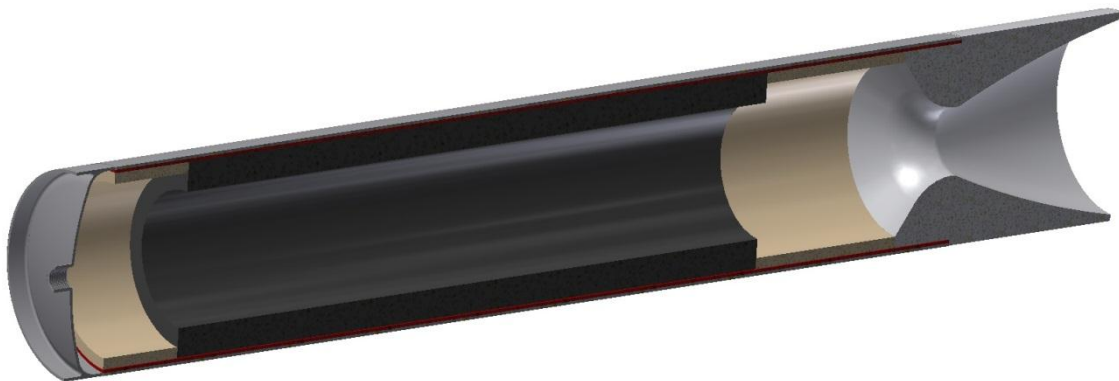
Figure 5.57: Cross-section view of the combustion chamber.

The propellant mass fraction could be improved substantially if lightweight materials such as filament-wound composite pressure vessels are used for the oxidiser tank and combustion chamber. Composite pressure vessels carry a risk of nitrous oxide decomposition if not lined correctly (Karabeyoglu et al., 2008). Given the lack of manufacturing capability in South Africa of composite pressure vessels for nitrous oxide, simulations utilising them were not conducted.

Improvement of the motor performance can be achieved by mixing aluminised particles into the paraffin wax fuel grain. To manufacture an aluminised fuel grain in South Africa is feasible and is investigated briefly in the next section.

5.4 Aluminised Propellant Trade Study

The benefits of adding aluminium particles to pure paraffin wax are an increased specific impulse and fuel density, and a decreased optimal O/F ratio. The disadvantages of aluminised

fuels are increased nozzle erosion and decreased combustion efficiency. Research at Stanford University indicates that the regression rate coefficient, a, improves by 10%, and the regression rate is approximately the same or higher than that of pure paraffin (McCormick et al., 2005; Doran et al., 2007). More work is required to validate the Stanford University findings, including experimentation.

Methodology

This study assumes that the regression rate coefficient, a, equals 0.000175 and the regression rate exponent, n, remains the same as for pure paraffin. The objective is to demonstrate the possible benefit of adding aluminium particles to the paraffin wax fuel grain. Figure 5.58 indicates that increasing the percentage of aluminium in the fuel grain results in a lower O/F ratio and a higher specific impulse.
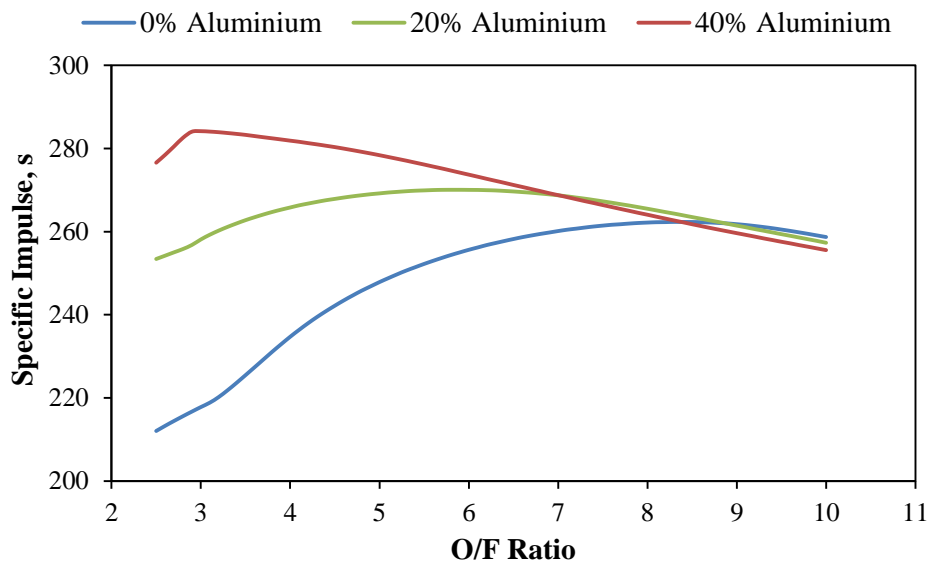
Figure 5.58: Specific impulse versus O/F ratio for various additions of aluminium particles in the fuel gran.

The final Phoenix-2A design was then compared to a vehicle with a paraffin wax grain consisting of 40% aluminium. The inputs that were varied were the design O/F ratio, fuel density, and regression rate coefficient. A design O/F ratio of 4 was selected because the O/F decreases during the burn and thus results in a better specific impulse, as shown in Figure 5.58. The density of 40% aluminised paraffin wax is 1250 kg/m^3.

Results

An apogee of 101.6 km can be achieved with 40% aluminium paraffin fuel. The total vehicle mass is equal to that of the non-aluminised version (1006 kg), however the total propellant mass

is 36.7 kg less than the pure paraffin design, as shown in Table 5.12. This means that the inert mass available for the vehicle increases by 6.5%. The required oxidiser mass is reduced by 86.3 kg which results in a smaller tank that is 25 kg lighter than the pure paraffin design. The mass of the fuel increases for the aluminised propellant vehicle due to the lower selected O/F ratio but is shorter than the final design because it has a much higher density. The reduction in the combustion chamber and oxidiser tank results in reducing the overall length by 5.1%. These results powerfully demonstrate the advantages of using aluminised propellant fuel grains. The Phoenix programme intends initiating studies into the addition of aluminium to the motors of the 1A and 2A vehicles.

Table 5.12: Design comparison between pure and 40% aluminised paraffin wax vehicles.

		Final Design	Aluminised Propellant Design
Fuel	Mass (kg)	61.1	110.7
	Length (m)	1.64	1.33
	Outer diameter (m)	0.365	0.365
	Port diameter (m)	0.254	0.254
Oxidiser	Mass (kg)	529.0	442.7
Overall	Mass (kg)	1006.0	1006.0
	Length (m)	11.99	11.31
	Apogee (km)	100.9	101.6

CHAPTER 6

Conclusion

An extensive review of hybrid rockets indicates that in the past they were unsuccessful in large-scale applications due to inefficient and complex classical fuel grain configurations, low fuel regression rates, and freezing of the oxidiser valves. The development of liquefying fuels however shows promise in large-scale hybrid applications because these fuels have higher regression rates than classical fuels and thus require simpler single port configurations.

A preliminary design of the Phoenix-2A hybrid sounding rocket, that is capable of reaching an apogee of 100 km with a 5 kg payload, was generated in this study. The propulsion and aerodynamic design parameters were investigated to determine their effect on the motor and flight performance.

A methodological design procedure was developed that integrates the use of the UKZN HYROPS software with a formal design process for hybrid rockets. The procedure can be implemented for any future vehicles in the Phoenix programme.

The performance of existing sub-orbital rockets similar to Phoenix-2A was modelled in the HYROPS Flight Dynamics Simulator as a validation exercise. The HYROPS simulator was compared to a 2 DOF model, a 6 DOF model, and flight test data. The largest discrepancy found between HYROPS and the 2 DOF model was 25% due to techniques used to model the gravity turn, aerodynamic characteristics and thrust assumptions. The use of constant average thrust curves was necessitated by a lack of actual motor thrust data. A HYROPS simulated trajectory was compared to the Malemute rocket flight data and shown to underestimate the apogee by 8.1% when thrust data were provided. This was considered as verification that the Flight Dynamics Simulator may be used for sub-orbital sounding rocket analyses. The lack of unclassified large-scale thrust data requires that the HRPC be further validated with hot-fire tests conducted within the Phoenix programme.

The methodology developed in this dissertation was used to design the initial concept for the Phoenix-2A rocket. The mission statement of Phoenix-2A provided requirements and constraints that were used to aid in concept selection. A single stage configuration was chosen because it was found to be simpler, cheaper, and more reliable than a multi-stage rocket or dart configuration. The propellant survey resulted in the combination of SASOL 0907 paraffin wax

and nitrous oxide being selected as the fuel and oxidiser respectively. The selection of nitrous oxide, which has self-pressurising properties, allows for the use of a blowdown oxidiser delivery method. The N_2O/Paraffin wax Peregrine sounding rocket was used as guideline to reduce the design lead time. An original design thrust input of 76 kN was used in the HRPC-Motor Design Model but was amended to 85 kN due to a reduction in combustion efficiency from 95% to 93%. This was indicated by results from the 2012 hot-fire testing of the Peregrine motor. The propellant mass fraction of the initial Phoenix-2A conceptual design was 0.6.

The initial conceptual design was used as the foundation for a chamber pressure parametric trade study. Motors with an oxidiser mass flux above 650 kg/m^{2}s or a hydraulic pressure drop ratio of less than 15% were disregarded to avoid the risk of combustion instabilities. The trade study showed that an increase in design chamber pressure results in an increase in performance. The performance increase is limited due to feed-system-coupled instability occurring at higher design chamber pressures and an increase of inert mass due to the larger wall thicknesses required. The addition of helium increases the oxidiser tank's initial pressure and the hydraulic pressure drop ratio. Helium also has beneficial attributes such as mitigating cavitation in the feed lines.

The effect of throttling the oxidiser mass flow rate by varying the number of injector holes, and therefore varying the chamber pressure from the design value, was considered. Results indicate that reducing the number of holes decreases the performance of the hybrid rocket motor. An increase in holes improves performance by up to approximately 16% of the original chamber pressure. A design chamber pressure of 42 bar enables Phoenix-2A to reach its target apogee and creates two-phase flow in the injector. This can provide possible isolation between the tank and combustion chamber and prevent feed system coupled instabilities.

The effect of nozzle geometry was investigated by varying the altitude for which the nozzle is designed. A design altitude of 3 km gives a 1 km improvement in apogee over the sea level alternative, as well as a 19.8 kg mass reduction of propellant, a 1.6% reduction in overall length, and a 3.2% reduction in overall mass. It was found that the nozzle design altitude has the least effect on performance in the trade studies.

An O/F ratio shift was noticed for all motor simulations due to the use of a blowdown oxidiser delivery method. The directly proportional relationship between performance of the rocket and specific impulse was demonstrated and a design O/F ratio of 8 was selected as an optimal trade-off between apogee, propellant mass, overall mass and length.

An increase in design ullage volume decreases apogee primarily due to the decrease in burnout velocity. The ullage volume is restricted to 15% based on the UKZN oxidiser tank regulations. This allows space for the liquid nitrous oxide to expand so that the oxidiser tank pressure does not exceed its design pressure in case of a temperature increase.

The fuel grain port diameter is fixed to equal twice the throat diameter, lowering throat pressure and thrust losses. A reduction in the grain length-to-diameter ratio to 5 reduces the fuel needed, yields a higher O/F ratio and produces a better specific impulse. The grain thickness was chosen to reduce the sliver fraction and hoop stresses acting on the wax.

The aerodynamic parameter trade study was focused on the nose cone, fuselage, and fin geometries. An increase in fineness ratio reduces the wave drag, and increases the skin friction and the payload volume capacity. A fineness ratio of 5 provides the best trade-off between these attributes. A sharp nose cone is used in the final design along with a tip made out of an Inconel alloy or carbon-carbon composite for thermal protection. Reducing the fineness ratio to 1 significantly decreases the apogee the vehicle can obtain. The fuselage diameter of 0.413 m was selected as a trade-off between lowering the length-to-diameter ratio of the vehicle to reduce the possibility of buckling and reducing the diameter to reduce the drag force acting on the vehicle.

A fin trade study demonstrated that fin flutter must be considered in the preliminary design. The original fins were found to be susceptible to fin flutter and when increased to a sufficient thickness, the vehicle did not achieve the target apogee. The trade study showed the optimal aerofoil for Phoenix-2A to be the symmetrical double wedge profile due to its low wave drag coefficient. It was found that delta and clipped delta fin planforms provide insufficient area for stable flight for apogees equal to or above 100 km. The final fin design is a swept clipped delta fin. It has lower bending moments and drag coefficients, and better aeroelastic stability than the rectangular planform. The fin design gives a stable vehicle however the apogee decreases to 96.3 km. This requires another propulsion iteration to increase the thrust of the motor and enable the vehicle to reach the target apogee. The fin leading edges will be fabricated from temperature resistant material, such as Inconel or carbon reinforced carbon composites, to protect against aerodynamic heating.

The final Phoenix-2A design was established using the methodology developed in Chapter 3 and is based on the results of parametric trade studies. The vehicle requires an 85 kN design thrust to achieve an apogee of 100 km. The final overall dimensions of the rocket are 12 m in length with an outer diameter of 0.413 m. The gross launch mass is 1006 kg. The poor

propellant mass fraction is due to low motor performance resulting from a 93% combustion efficiency.

An aluminised propellant trade study indicates the feasibility and benefits of using metal additives. The addition of 40% by mass of aluminised particles into the paraffin wax enables the vehicle to increase its inert mass by 6.5% while achieving an apogee of 101.6 km.

A reduction in overall mass and an improvement in propellant mass fraction are possible during the testing phase of the Phoenix-2A motor through improved combustion efficiency. This would reduce the thrust and propellant required to obtain an apogee of 100 km. Future work on composite pressure vessels and fins is required to reduce the inert mass of Phoenix-2A. Future work should also seek to integrate dynamic stability and slosh dynamic analyses as functional tools in the HYROPS software. This would enable the modelling of aeroelastic effects. The HYROPS wind modelling should be extended to include more than one jet stream and various gradient winds.

The Phoenix-2A vehicle that emerged from this research can be used as the basis for continued development of high-altitude hybrid rockets in the UKZN Phoenix programme. Greater in-depth structural analyses are required on most components to assess structural integrity and reduce mass. Before the Phoenix-2A design can be considered complete, system integration must be addressed for components such as the avionics, sensors, and payload systems. This work highlights the need for a test facility where experimental testing of large-scale motors can be conducted in a safe environment to determine actual performance and analyse combustion instability. Such testing could lead to the development of large-scale hybrid sounding rockets for the South African scientific community.

REFERENCES

Aerospace Specification Metals, 2013. Metal Distributor, [online]. Available at: http://www.aerospacemetals.com/ [accessed 10 February 2013].

Altman, D., 1991. Hybrid Rocket Development History. *27th AIAA/SAE/ASME/ASEE Joint Propulsion Conference*. Sacramento, CA, United States of America, 24-26 June.

Apogee Rockets, 2013. *RockSim Pro v1 – CD*, [online]. Available at: http://www.apogeerockets.com/Rocket_Software/RockSim_Pro/RockSim_Pro_v1_CD [accessed 26 August 2013].

Arves, J., Gnau, M., Kearney, D., McNeal, C. and Murbach, M., 2003. Overview of the Hybrid Sounding Rocket (HYSR) Project. *39th AIAA/ASME/SAE/ASEE Joint Propulsion Conference and Exhibit*. Huntsville, AL, United States of America, 20-23 July.

Benson, T., 2010. *NASA Brief History of Rockets*, [online]. Available at: http://www.grc.nasa.gov/WWW/k-12/TRC/Rockets/history_of_rockets.html [accessed 5 July 2012].

Blake, W. B., 2011. *Missile DATCOM User's Manual: 2011 Revision*, [online]. Available at: http://www.dtic.mil/dtic/tr/fulltext/u2/a548461.pdf [accessed 3 August 2013].

Boardman, T. A., Brinton, D. H., Carpenter, R. L. and Zoladz, T. F., 1995. An Experimental Investigation of Pressure Oscillations and their Suppression in Subscale Hybrid Rocket Motors. *31st AIAA/ASME/SAE/ASEE Joint Propulsion Conference & Exhibit*. San Diego, CA, United States of America, 10-12 July.

Bollermann, B., 1970. *A Study of 30 km to 200 km Meteorological Rocket Sounding Systems: Literature and Data Review*. Vol. 1, NASA Technical Report, United States of America.

Brooks, M. J., Pitot de la Beaujardiere, J. F., Genevieve, B., Chowdhury, S. M. and Roberts, L. W., 2010. Introduction to the University of KwaZulu-Natal Hybrid Sounding Rocket Program. *46th AIAA/ASME/SAE/ASEE Joint Propulsion Conference & Exhibit*. Nashville, TN, United States of America, 25-28 July.

Brown, C. D., 2002. *Elements of Spacecraft Design*. Reston, VA, United States of America: AIAA Education Series.

Brown, R. C., Brulle, R. V., Combs, A. E. and Griffin, G. D., 1964. *Six Degree-of-Freedom Flight-Path Generalized Computer Program: Part I Volume 1 – Basic Problem Formulation*, FDL-TDR-64-1, under USAF Contract No. AF33(657)-8829, Air Force Flight Dynamics Laboratory, Research and Technology Division, United States of America.

Bruhn, E. F., 1965. *Analysis and Design of Flight Vehicle Structures*. Cincinnati, OH, United States of America: Tri-State Offset Company.

Busse, J. R., Leffler, M. T., Kraft, G. E. and Bushnell, P. S., 1967. *A Compendium of NASA Aerobee Sounding Rocket Launchings for 1964*. NASA Technical Report, United States of America.

Calabro, M., 2011. Overview on Hybrid Propulsion. *Progress in Propulsion Physics*, 2, p.353-374.

Casiano, M. J., Hulka, J. R. and Yang, V., 2010. Liquid-Propellant Rocket Engine Throttling: A Comprehensive Review. *Journal of Propulsion and Power*, 26(5), p.897-923.

Casalino, L., Letizia, F. and Pastrone, D., 2012. Design Trade-offs for Hybrid Rocket Motors. *48th AIAA/ASME/SAE/ASEE Joint Propulsion Conference & Exhibit*. Atlanta, GA, United States of America, 30 July - 01 August.

Chae, S., 2004. *Effect of Follower Forces on Aeroelastic Stability of Flexible Structures*. PhD Thesis, School of Aerospace Engineering, Georgia Institute of Technology, United States of America.

Chiaverini, M. J. and Kuo, K. K., 2007. *Fundamentals of Hybrid Rocket Combustion and Propulsion*. Reston, VA, United States of America: AIAA.

Chowdhury, S. M., 2012. *Design and Performance Simulation of a Hybrid Rocket*. MSc Eng Dissertation, College of Agriculture, Engineering and Science, University of KwaZulu-Natal, South Africa.

Copenhagen Suborbitals, 2013. *Copenhagen Suborbitals: Mission*, [online]. Available at: http://www.copenhagensuborbitals.com/mission.php [accessed 26 August 2013].

Corliss, W. R., 1971. *NASA Sounding Rockets, 1958-1968: A Historical Summary,* [Online]. Available at: http://ntrs.nasa.gov/archive/nasa/casi.ntrs.nasa.gov/19720005224_1972005224.pdf [accessed 29 August 2013].

Crowell, G. A. Sr., 1996. *The Descriptive Geometry of Nose Cones*. Miscellaneous Paper.

Datta, P. K. and Biswas, S., 2011. Aeroelastic Behaviour of Aerospace Structural Elements with Follower Force: Review. *International Journal of Aeronautical & Space Science*, 12(2), p.134-148.

Doran, E., Dyer, J., Marzona, M., Karabeyoglu, A., Zilliac, G., Mosher, R. and Cantwell, B., 2009. Status Update Report for the Peregrine Sounding Rocket Project: Part III. *45th AIAA/ASME/SAE/ASEE Joint Propulsion Conference & Exhibit*. Denver, CO, United States of America, 2-5 August.

Dunn, Z., Dyer, J., Lohner, K., Doran, E., Bayart, C., Sadhwani, A. and Zilliac, G., 2007. Test Facility Development for the 15,000 lb Thrust Peregrine Hybrid Sounding Rocket. *43rd AIAA/ASME/SAE/ASEE Joint Propulsion Conference & Exhibit*. Cincinnati, OH, United States of America, 8-11 July.

Dyer, J., Doran, E., Dunn, Z., Lohner, K., Bayart, C., Sadhwani, A., Zilliac, G., Cantwell, B. and Karabeyoglu, A., 2007. Design and Development of a 100 km Nitrous Oxide/Paraffin Hybrid Rocket Vehicle. *43rd AIAA/ASME/SAE/ASEE Joint Propulsion Conference & Exhibit*. Cincinnati, OH, United States of America, 8-11 July.

Entico Corporation, 2003. International Communications Project – Mobile telecommunication via stratosphere, [online]. Available at: http://www.intercomms.net/AUG03/content/struzak1.php [accessed 28 November 2013].

Federal Aviation Administration, 2005. *Guide to Verifying Safety-Critical Structures for Reusable Launch and Reentry Vehicles.* Version 1.0, Commercial Space Transportation, Washington, DC, United States of America.

Fernandez, M. M., 2009. *Propellant Tank Pressurization Modelling for a Hybrid Rocket*. MSc Eng Dissertation, Kate Gleason College of Engineering, Rochester Institute of Technology, Rochester, New York, United States of America.

Fleeman, E. L., 2001. *Tactical Missile Design*. Reston, VA, United States of America: AIAA Education Series.

Geneviève, B., 2013. *Development of a Hybrid Sounding Rocket Motor*. MSc Eng Dissertation, College of Agriculture, Engineering and Science, University of KwaZulu-Natal, South Africa.

Gordon, S. and McBride, B. J., 1994. *Computer Program for Calculation of Complex Chemical Equilibrium Compositions and Applications*. NASA Technical Report, RP-1311, United States of America.

Granta Design, 2009. *The CES EduPack Resource Booklet 2: Material and Process Charts*, [online]. Available at:
http://www.me.uprm.edu/vgoyal/inme4011/Online_inme4011/Topic2_MaterialSelection/Ashby Charts.pdf [accessed 22 September 2013].

Hodges, D. H., 2004. *A New Approach to Aeroelastic Response, Stability and Loads of Missiles and Projectiles*. Final Report, Grant DAAD19-00-1-0408, US Army Research Office, United States of America, 18 June.

Humble, R. W., Henry, G. N. and Larson, W. J., 1995. *Space Propulsion Analysis and Design*. United States of America: McGraw-Hill.

Johns Hopkins University, 2004. *The Johns Hopkins University Sounding Rocket Program*, [online]. Available at: http://www.pha.jhu.edu/groups/rocket/papers.html [accessed 20 August 2013].

Kanner, L., Ortmann, O., Raine, E., McWilliams, K., Madsen, C., Reiber, R., Krauss, O., Lewis B. and Owen, D., 2007. MaCH-SR1: Development and Characterization of Hybrid Rocket Technologies through Undergraduate R&D. *54th JANNAF Propulsion Meeting*. Denver, CO, United States of America, 14-18 May.

Karabeyoglu, M. A., 1998. *Transient Combustion in Hybrid Rockets*. PhD Thesis, Department of Aeronautics and Astronautics, Stanford University, United States of America.

Karabeyoglu, M. A., Cantwell, B. J. and Altman, D., 2001. Development and Testing of Paraffin-Based Hybrid Rocket. *37th AIAA/ASME/SAE/ASEE Joint Propulsion Conference and Exhibit*. Salt Lake City, UT, United States of America, 8-11 July.

Karabeyoglu, M. A., Altman, D. and Cantwell, B. J., 2002. Combustion of Liquefying Hybrid Propellants: Part 1, General Theory. *Journal of Propulsion and Power*, 18(3), p.610-620.

Karabeyoglu, M. A., Zilliac, G. G., Cantwell, B. J., De Zilwa, S. and Castelluci, P., 2003. Scale-Up Tests of High Regression Rate Liquefying Hybrid Rocket Fuels. *41st AIAA/ASME/SAE/ASEE Joint Propulsion Conference & Exhibit*. Reno, NV, United States of America, 6-9 July.

Karabeyoglu, M. A., Cantwell, B. J. and Stevens, J., 2005. Evaluation of Homologous Series of Normal-Alkanes as Hybrid Rocket Fuels. *41st AIAA/ASME/ASEE Joint Propulsion Conference & Exhibit*. Tucson, AZ, United States of America, 10-13 July.

Karabeyoglu, A., Stevens, J. and Cantwell, B., 2007. Investigation of Feed System Coupled Low Frequency Instabilities in Hybrid Rockets. *43rd AIAA/ASME/SAE/ASEE Joint Propulsion Conference & Exhibit*. Cincinnati, OH, United States of America, 8-11 July.

Karabeyoglu, A., Dyer, J., Stevens, J. and Cantwell, B., 2008. Modeling of N2O Decomposition Events. *44th AIAA/ASME/SAE/ASEE Joint Propulsion Conference & Exhibit*, Hartford, CT, United States of America, 21-23 July.

Karabeyoglu, A., 2011. *Chapter X2.1: Hybrid Rockets Propulsion Design Issues*. Lecture notes distributed in AIAA Hybrid Rocket Propulsion Course at the 47th AIAA/ASME/SAE/ASEE Joint Propulsion Conference & Exhibit, San Diego, CA, United States of America, 4-5 August.

Knop, T., Huijsman, R., Powell, S., Werner, R., Ehlen, J., Lindermann, F., Wink, J., Becker, C., Samarawickrama, K., Zandbergen, B. and Vervone, A., 2013. Sorbitol-Based Hybrid Fuel Studies with Nitrous Oxide for the Stratos II Sounding Rocket. *49th AIAA/ASME/SAE/ASEE Joint Propulsion Conference & Exhibit*. San Jose, CA, United States of America, 14-17 July.

Leverone, F. K., Veale, K. L., Brooks, B. J., Pitot de la Beaujardiere, J. P. and Roberts, L. W., 2013. Performance Modeling of the Phoenix-2A Hybrid Sounding Rocket using HYROPS Software. *49th AIAA/ASME/SAE/ASEE Joint Propulsion Conference & Exhibit*, San Jose, CA, United States of America, 14-17 July.

Lohner, K., Dyer, J., Doran, E., Dunn, Z. and Zilliac, G, 2006. Fuel Regression Rate Characterization Using a Laboratory Scale Nitrous Oxide Hybrid Propulsion System. *42nd AIAA/ASME/SAE/ASEE Joint Propulsion Conference & Exhibit*. Sacramento, CA, United States of America, 9-12 July.

Marcom, 2012, *Chatspace: Launch Simulation*, [online]. Available at: http://www.marcom-as.com/sa-lv-chat-space/page/2 [accessed 10 September 2013].

Martin, D. J., 1958. *Summary of Flutter Experiences as a Guide to the Preliminary Design of Lifting Surfaces on Missiles*. NACA Technical Note, 4197, Langley Aeronautical Laboratory Langley Field, VA, United States of America.

MatWeb, 2013. Online Materials Information Resource, [online]. Available at: http://www.matweb.com/ [accessed 10 February 2013].

Marxman, G. A., Woolridge, C. E. and Muzzy R. J., 1964. Fundamentals of Hybrid Boundary-Layer Combustion. *Progress in Aeronautics and Astronautics*, 15, p.485-522.

McCormick, A., Hultgren, E., Lichtman, M., Smith, J., Sneed, R. and Azimi, S., 2005. Design, Optimization, and Launch of a 3" Diameter N2O/Aluminized Paraffin Rocket. *41st AIAA/ASME/SAE/ASEE Joint Propulsion Conference & Exhibit*, Tucson, AZ, United States of America, 10-13 July.

Megyesy, E. F., 2001. *Pressure Vessel Handbook*. 12th ed. Tulsa, OK, United States of America: Pressure Vessel Publishing, Inc.

Miles, D., Mann, I., Knudsen, D., McWilliams, K., Dahle, K., Grande, J., Moen, J., Thrane, E., Hansen, A. and Burchill, J., 2012. The Canadian/Norwegian Student Sounding Rocket Program (CaNoRock) Updates and Graduate Training. *63rd International Astronautical Congress*. Naples, Italy, 1-5 October.

Millard, W. A., Barton, W. R. and Steinkraus, E. J., 1977. *Development, Flight Performance, and Test Results for Two Single-Stage Malemute Rocket Vehicles Launched at the Tonopah Test Range*. Technical Report, SAND-77-0061, Sandia Laboratories, United States of America.

NASA, 1999. *Sounding Rocket Program Handbook (SRPH)*. Suborbital Program and Projects Directorate, Sounding Rocket Program Office, Wallops Island, VA, United States of America.

Niskanen, S., 2009. *Development of an Open Source Model Rocket Simulation Software*. MSc Eng Dissertation, Department of Computational Science and Engineering, Helsinki University of Technology, Finland.

Pitot de la Beaujardiere, J. F., Brooks, M. J., Genevieve, B., Chowdhury, S. M. and Roberts, L. W., 2010. Sounding Rockets for Africa. *1st South African Space Association Congress*. Cape Town, South Africa, September.

Pradhan, S. and Datta, P. K., 2006. Dynamic Instability Characteristics of a Free-Free Missile Structure under a Controlled Follower Force. *Aircraft Engineering and Aerospace Technology*, 78(6) p.509-514.

Rogers, C. E. and Cooper, D., 2008. *Rogers Aeroscience RASAero Aerodynamic Analysis and Flight Simulation Program: User's Manual*. Version 1.0.0, Rogers Aeroscience, Lancaster, CA, United States of America.

Russ, K. and Randall, F., 1961. *Performance Summary for the Aerobee 150A Sounding Rocket Vehicle*. Technical Report, AST/EIR-13319, Vought Astronautics, United States of America, April.

Schindwolf, E. J., Swanson, B. E. and Millard, W. A., 1998. Launch of "Smallsats" Using Low-Cost Sounding Rocket Technologies, Methods, and Practices. *Proceedings of the 12th AIAA/USU Conference on Small Satellites, New Approaches to Space Launch, SSC98-III-2*. United States of America [online] Available at: http://digitalcommons.usu.edu/smallsat/1998/all1998/15/ [accessed 10 November 2013].

Seibert, G., 2006. *The History of Sounding Rockets and their Contribution to European Space Research.* Netherland: ESA Publications Division.

Sierra Nevada Corporation, 2013. *Space Exploration Systems*, [online]. Available at: http://www.sncspace.com/ss_space_exploration.php [accessed 25 August 2013].

Space Propulsion Group, 2012. *Fuel Grain Production*, [online]. Available at: http://www.spg-corp.com/fuel-grain-production.html [accessed 20 September 2013].

Sutton, G. and Biblarz, O., 2001. *Rocket Propulsion Elements*. 7th ed. New York: John Wiley & Sons.

The Hindu, 2010. *Sounding Rocket Developed at VITU*, [online]/ Available at: http://www.thehindu.com/features/education/research/sounding-rocket-developed-at-vitu/article497143.ece [accessed 29 August 2013].

Thicksten, Z., Macklin, F. and Campbell, J., 2008. Handling Considerations of Nitrous Oxide in Hybrid Rocket Motor Testing. *44th AIAA/ASME/SAE/ASEE Joint Propulsion Conference & Exhibit*. Hartford, CT, United States of America, 21-23 July.

Tsohas, J., Appel, B., Rettenmaier, A., Walker, M. and Heister, S. D., 2009. Development and Launch of the Purdue Hybrid Rocket Technology Demonstrator. *45th AIAA/ASME/SAE/ASEE Joint Propulsion Conference & Exhibit*. Denver, CO, United States of America, 2-5 August

US Army Missile Command, 1990. *Design of Aerodynamically Stabilized Free Rockets*. Military Handbook MIL-HDBK-762(MI), Department of Defense, United States of America, 17 July.

Van Pelt, D., Hopkins, J., Skinner, M., Buchanan, A., Gulman, R., Chan, H., Karabeyoglu, A. and Cantwell, B., 2004. Overview of a 4-inch OD Paraffin-based Hybrid Sounding Rocket Program. *40th AIAA/ASME/SAE/ASEE Joint Propulsion Conference & Exhibit*. Fort Lauderdale, FL, United States of America, 11-14 July.

Virgin Galactic, 2013. *SpaceShipTwo: An Introductory Guide for Payload Users*, [online]. Available at: http://www.virgingalactic.com/uploads/VG_Web_PayloadUsersGuide_20130103.pdf [accessed 20 August 2013].

Wade, M., n.d. *EncyclopediaAstronautica*, [online]. Available at: http://www.astronautix.com [accessed 20 August 2011].

Waxman, B. S., Zimmerman, J. E., Cantwell, B. J. and Zilliac, G. G., 2013. Mass Flow Rate and Isolation Characteristics of Injectors for Use with Self-Pressurizing Oxidizers in Hybrid Rockets. *49th AIAA/ASME/SAE/ASEE Joint Propulsion Conference & Exhibit*. San Jose, CA, United States of America, 14-17 July.

Weydert, J. C., 1968. *A discussion of Rocket Vehicle Joint Characteristics*. Technical Report, Sandia National Laboratories, United States of America.

Wilsons, 2013. Datasheets: Aluminium Alloys, [online]. Available at: http://www.wilsonsmetals.com/datasheets/?gId=1 [accessed 12 February 2013].

Zilliac, G. G., Waxman, B. S., Dyer, J., Karabeyoglu, A. M. and Cantwell, B. J., 2012. Peregrine Hybrid Rocket Motor Ground Test Results. *48th AIAA/ASME/SAE/ASEE Joint Propulsion Conference & Exhibit*. Atlanta, GA, United States of America, 30 July - 1 August.

APPENDIX A

Initial Conceptual Design

A.1 Initial Conceptual Design HRPC inputs

Table A.1: Phoenix-2A preliminary design HRPC-Performance Model inputs

Input Parameter		95%	93%
Blowdown	Mass of nitrous oxide	487 kg	545 kg
	Mass of helium	0.05 kg	0.05 kg
	Initial tank temperature	298 K	298 K
	Mass of tank	145 kg	162 kg
	Volume of tank	0.753 m^2	0.842 m^2
Atmospheric properties	Pressure	Sea level	Sea level
	Temperature	298 K	298 K
	Molecular mass	28.97 Kg/kmol	28.97 Kg/kmol
	Density	1.184 kg/m^3	1.184 kg/m^3
	Specific heat at constant pressure	1005 J/(kg.K)	1005 J/(kg.K)
	Specific heat ratio	1.401	1.401
Run time	Time step	30000	30000
	Delta time	0.001	0.001
Grain specifications	Number of ports	1	1
	Initial port diameter	0.252 m	0.267 m
	Final port diameter	0.360 m	0.375 m
	Length	1.464 m	1.548 m
	Density	924 kg/m^3	924 kg/m^3
	Regression rate coefficient	0.000155	0.000155
	Regression rate exponent	0.5	0.5
Feed system	Injector discharge coefficient (Liquid nitrous oxide)	0.5	0.5
	Injector diameter	2.0 mm	2.0 mm
	Number of injector holes	479	486
	Estimated pressure drop in feed system	5 bar	5 bar
Motor and nozzle geometry	Free volume in chamber* (excluding port volume)	0.0386 m^2	0.0443 m^2
	Nozzle throat diameter	0.126 m	0.133 m
	Nozzle exit diameter	0.303 m	0.320 m
Performance correction factors	Combustion efficiency	95%	93%
	Bell-shaped nozzle correction factor	0.985	0.985
Critical pressure ratios	1st	0.9938	0.9938
	2nd	0.2315	0.232
	3rd	0.0253	0.0253

*Note: Combustion chamber inserts L/D ratios and thicknesses remained constant therefore varying free volume in the chamber.

A.2 Material Comparison Tables

Table A.2: Aluminium alloy material comparison (Aerospace Specifications Metals, 2013; MatWeb, 2013; Wilsons, 2013)

Material	UTS (MPa)	Yield Strength (MPa)	Melting Temperature (°C)	Density (kg/m^3)	Young's Modulus (GPa)	Specific Strength	Thermal Conductivity (W/mK)	Manufacturability
6063-T6	241	214	616-654	2700	68.9	0.079	200	Good weldability. Good corrosion resistance. Good brazability.
6061-T6/ T651	310	276	582-652	2700	68.9	0.102	167	Good corrosion resistance. Good workability. Good weldability in annealed condition.
6082-T6	340/310	310/250	555	2700	70	0.115	180/170	Good weldability. Good machinability. Good brazability. Good solderability.
2219-T851	455	352	543-643	2840	73.1	0.124	120	Good weldability. Good machinability.
2024-T6	427	345	502-638	2780	72.4	0.124	151	Good machinability. Welding not recommended.
2024-T361	496	393	502-638	2780	73.1	0.141	121	Good machinability. Good surface finish capabilities.
2024-T851	455	400	502-638	2780	72.4	0.144	151	Average weldability. Good stress corrosion resistance. Good machinability. Good surface finish capabilities.

Material	UTS (MPa)	Yield Strength (MPa)	Melting Temperature (°C)	Density (kg/m^3)	Young's Modulus (GPa)	Specific Strength	Thermal Conductivity (W/mK)	Manufacturability
7050-T73511	496	434	524-635	2830	71.7	0.153	155	Avoid welding.
2124-T851	483	441	502-638	2780	73.1	0.159	151	Crack sensitive during welding. Good resistance welding.
7475-T61	565	490	477-635	2810	70.3	0.174	138	Good machinability. Avoid welding.
7075-T6	572/524	503/462	477-635	2810	71.7	0.179	130	Poor weldability. Average machinability. Excellent hardness. Poor corrosion resistance.
2090-T83	550	520	560-650	2590	76	0.201	88	Corrosion resistant. Good weldability.

Table A.3: Stainless steel material comparison (MatWeb, 2013)

Material	UTS (MPa)	Yield Strength (MPa)	Density (kg/m^3)	Young's Modulus (GPa)	Specific Strength	Manufacturability
S32205	655/ 760	450/ 515	7820/ 7880	190	0.058	Good weldability.
S32507	802	530	7800	-	0.068	Good weldability.

Table A.4: Titanium alloy material comparison (Aerospace Specifications Metals, 2013)

Material	UTS (MPa)	Yield Strength (MPa)	Melting Temperature (°C)	Density (kg/m^3)	Young's Modulus (GPa)	Specific Strength	Thermal Conductivity (W/mK)	Manufacturability
Ti-5Al-2.5 Sn	861	827	Max 1590	4480	110-125	0.185	7.8	Good weldability. Oxidation resistant. Creep resistant.
Ti-6Al-4V (Grade 5), Annealed	950	880	1604-1660	4430	113.8	0.199	6.7	Corrosion resistant. Good weldability. Good fabrication.
Ti-6Al-6V-2 Sn	1050	980	1627-1649	4540	110.3	0.216	6.6	Limited weldability. Less ductile and tough than Ti-6Al-4V.
Ti-6Al-4V (Grade 5), STA	1170	1100	1604-1660	4430	114	0.248	6.7	Corrosion resistant. Good weldability. Good fabrication.

## A.3 Combustion Efficiency Designs
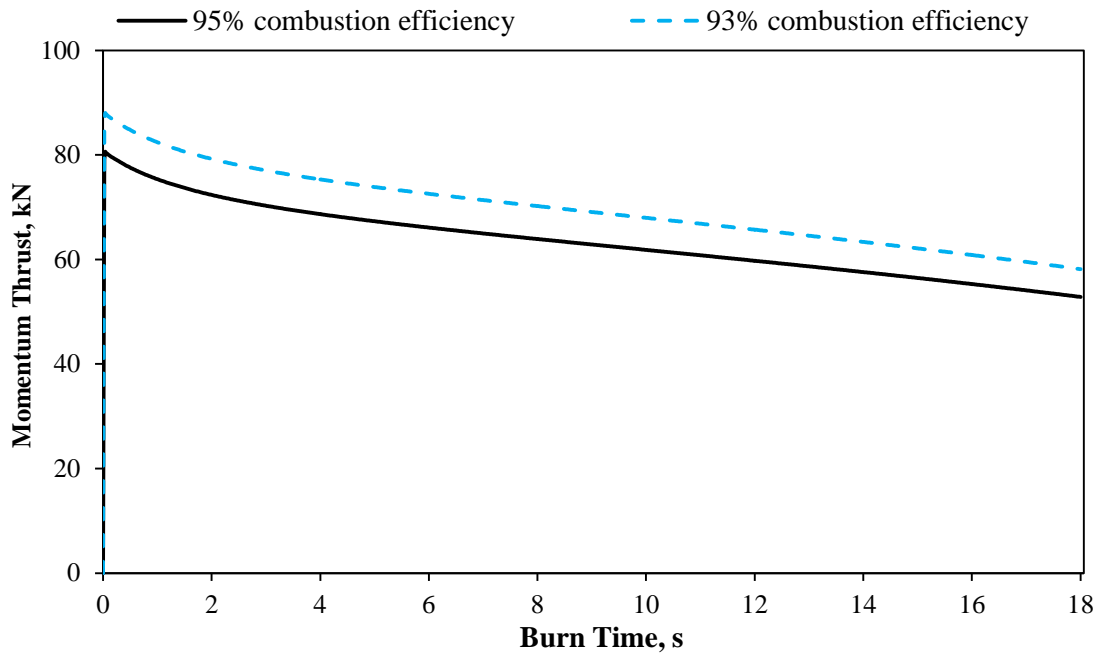
Figure A.1: Momentum thrust versus burn time for 95% and 93% combustion efficiency.
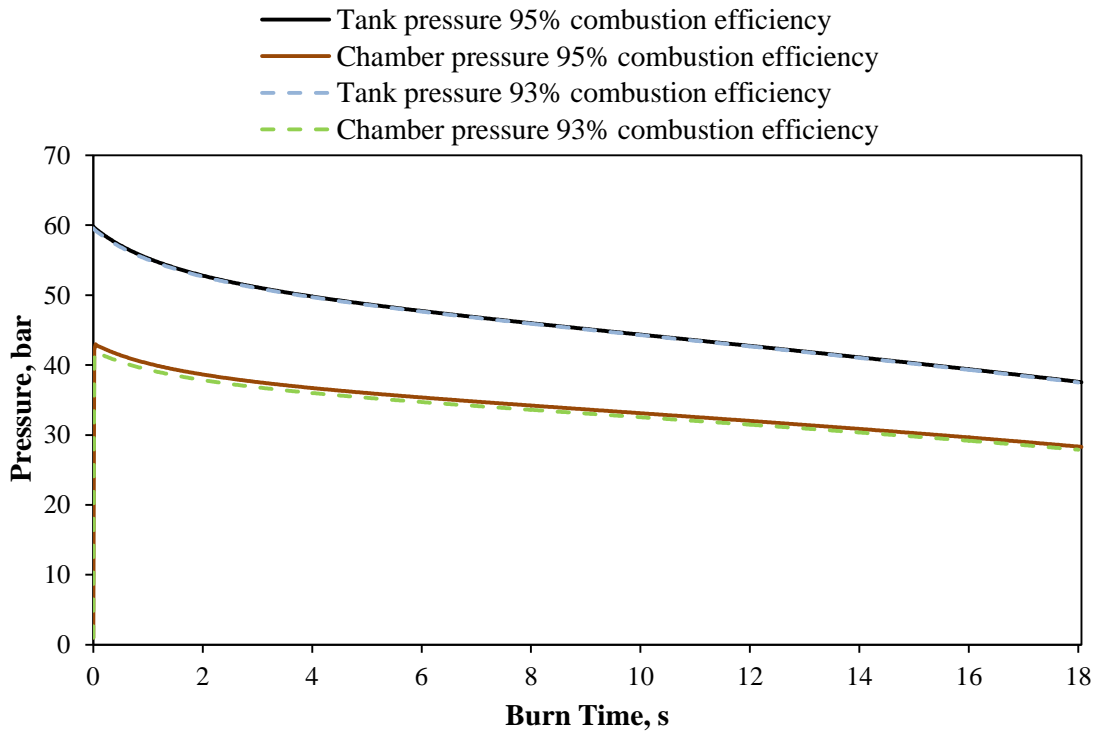
Figure A.2: Tank and chamber pressure versus burn time for 95% and 93% combustion efficiency.

143

APPENDIX B

Propulsion Trade Study

B.1 HRPC-Motor Design Inputs

Table B.1: HRPC-Motor Design Model inputs for various chamber pressures.

Parameters	Description
Oxidiser	Nitrous oxide
Oxidiser temperature	292 K
Fuel	Sasol 0907 paraffin wax
Fuel temperature	298 K
Fuel density	924 kg/m^3
Fuel enthalpy	-1438.2 kJ/mol
Thrust	85 kN
Nozzle design altitude	Sea level
O/F ratio	7
Burn time	18 s
Flow composition	Equilibrium
Regression rate coefficient	0.000155
Regression rate exponent	0.5
Chamber pressure	30 bar
	35 bar
	40 bar
	45 bar
	50 bar

Table B.2: HRPC-Motor Design Model inputs for various nozzle design altitudes.

Parameters	Description	
Oxidiser	Nitrous oxide	
Oxidiser temperature	292 K	
Fuel	Sasol 0907 paraffin wax	
Fuel temperature	298 K	
Fuel density	924 kg/m^3	
Fuel enthalpy	-1438.2 kJ/mol	
Thrust	85 kN	
Chamber pressure	42 bar	
O/F ratio	7	
Burn time	18 s	
Flow composition	Equilibrium	
Regression rate coefficient	0.000155	
Regression rate exponent	0.5	
Nozzle design altitude	101325.00 Pa	0 km above sea level
	89855.45 Pa	1 km above sea level
	79467.08 Pa	2 km above sea level
	70079.00 Pa	3 km above sea level
	61614.82 Pa	4 km above sea level

Table B.3: HRPC-Motor Design Model inputs for various O/F ratios.

Parameters	Description		
Oxidiser	Nitrous oxide		
Oxidiser temperature	292 K		
Fuel	Sasol 0907 paraffin wax		
Fuel temperature	298 K		
Fuel density	924 kg/m^3		
Fuel enthalpy	-1438.2 kJ/mol		
Thrust	85 kN		
Chamber pressure	42 bar		
Nozzle design altitude	70079.00 Pa	3 km above sea level	
Burn time	18 s		
Flow composition	Equilibrium		
Regression rate coefficient	0.000155		
Regression rate exponent	0.5		
O/F ratio	4	M_{ox} = 531.88 kg	M_f = 132.97 kg
	5	M_{ox} = 525.60 kg	M_f = 104.92 kg
	6	M_{ox} = 523.14 kg	M_f = 87.19 kg
	7	M_{ox} = 524.75 kg	M_f = 74.96 kg
	8	M_{ox} = 528.90 kg	M_f = 66.11 kg
	9	M_{ox} = 536.35 kg	M_f = 59.59 kg
	10	M_{ox} = 548.22 kg	M_f = 54.82 kg

Table B.4: HRPC-Motor Design Model inputs for various thrust values.

Parameters	Description	
Oxidiser	Nitrous oxide	
Oxidiser temperature	292 K	
Fuel	Sasol 0907 paraffin wax	
Fuel temperature	298 K	
Fuel density	924 kg/m^3	
Fuel enthalpy	-1438.2 kJ/mol	
O/F ratio	8	
Chamber pressure	42 bar	
Nozzle design altitude	70079.00 Pa	3 km above sea level
Burn time	18 s	
Flow composition	Equilibrium	
Regression rate coefficient	0.000155	
Regression rate exponent	0.5	
Thrust	0 kN	
	20 kN	
	40 kN	
	60 kN	
	75 kN	
	80 kN	
	85 kN	
	90 kN	

APPENDIX C

Aerodynamic Trade Study

C.1 Fuselage Trade Study
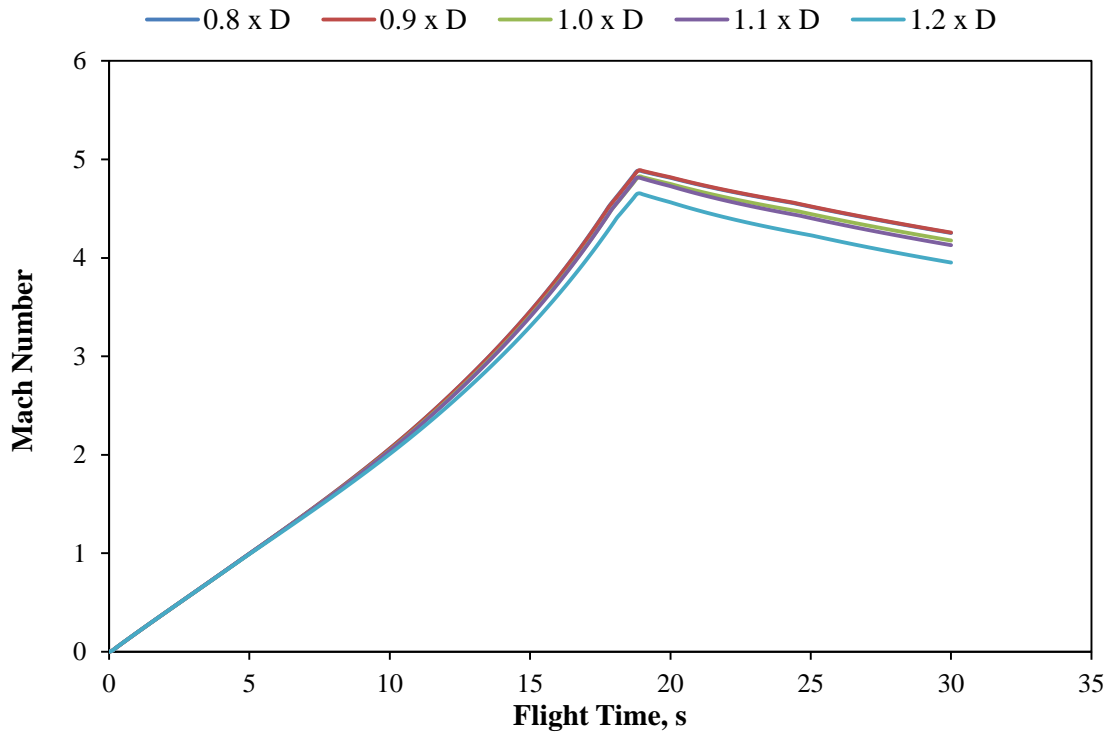
Figure C.1: Mach number versus flight time for various fuselage diameters.
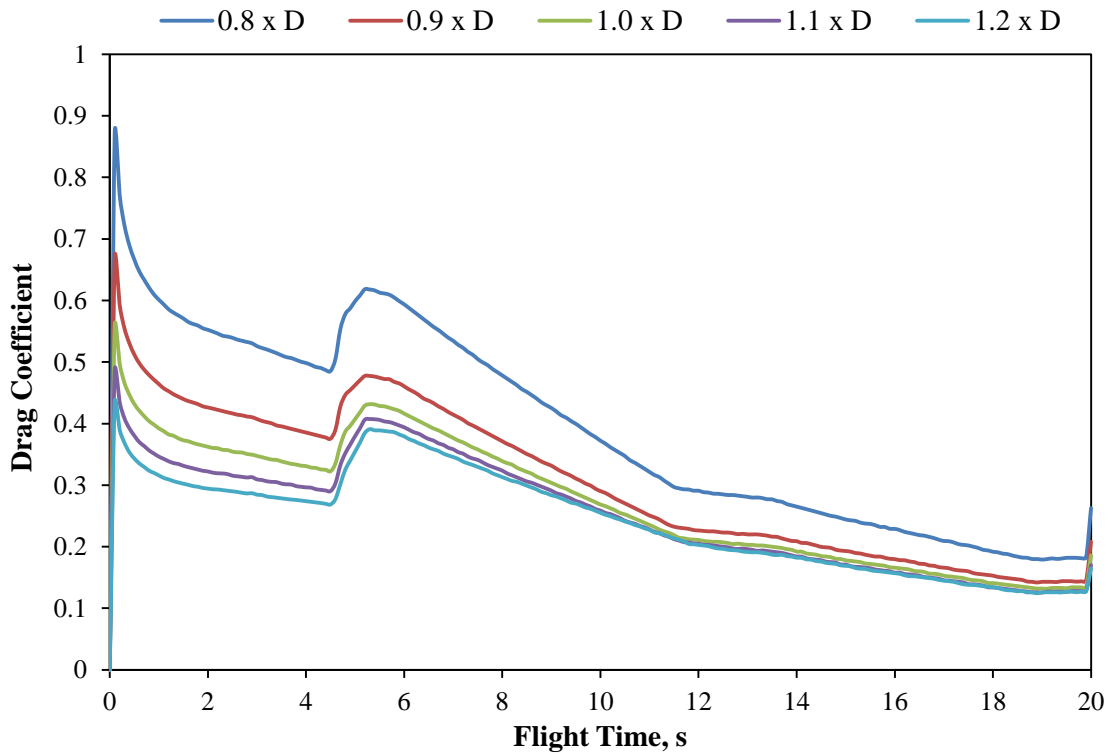

Figure C.2: Drag coefficient versus flight time for various fuselage diameters.

C.2 Fin Trade Study

Fin Flutter Analysis

The thickness of an aluminium fin was determined based on flutter using Equations C1 to C.4 (Martin, 1958). The shear modulus, G_E, for aluminium is 3770981 Psi. It is important to note that these equations require using imperial units:

$$\lambda = C_t/C_r \tag{C.1}$$

$$AR = b^2/S \tag{C.2}$$

$$\left(v_{fl}/a\right)^2 = G_E/\left[X\left(\lambda + \frac{1}{2}\right)\left(P/P_0\right)\right] \tag{C.3}$$

$$X = [39.3AR^3]/\left[\left(t/c\right)^3(AR + 2)\right] \tag{C.4}$$

where λ is the fin taper ratio, AR is the fin aspect ratio, X is a nondimensional parameter used to determine the required thickness, t and c is the fin chord. The flutter velocity, v_{fl}, which is equal to the maximum velocity of the rocket was 1400 m/s, unless the vehicle exceeded this velocity and then this value was increased. The atmospheric pressure is denoted as, P, and the pressure at sea level is P_0. Phoenix-2A is assumed to be launched at sea level therefore the pressure ratio was assumed to be 1 as this provided the worst case situation.

Table C.1: Rectangular planform fins.

	Root (m)	Tip (m)	Sweep (m)	Span (m)	λ	Angle (°)	AR	c (m)	Area (m)	t (mm)
Rectangular Planform										
Rect 1	1.2	1.2	0	0.40	1	90	0.33	1.2	0.48	18.3
Rect 2	1.0	1.0	0	0.40	1	90	0.40	1.0	0.40	18.1
Rect 3	0.8	0.8	0	0.40	1	90	0.50	0.8	0.32	17.9
Rect 4	1.2	1.2	0	0.35	1	90	0.29	1.2	0.42	16.1
Rect 5	1.2	1.2	0	0.30	1	90	0.25	1.2	0.36	13.9
Rect 6	1.2	1.2	0	0.25	1	90	0.21	1.2	0.30	11.6
Rect 7	1.2	1.2	0	0.29	1	90	0.24	1.2	0.35	13.4

Table C.2: Delta planform fins.

Delta Planform									
	Root (m)	Tip (m)	Sweep (m)	Span (m)	λ	Angle (°)	AR	c (m)	Area (m)	t (mm)
Delta 1	1.2	0	1.2	0.4	0	18.4	0.67	0.6	0.24	13.9
Delta 2	1.4	0	1.4	0.4	0	15.9	0.57	0.7	0.28	14.0
Delta 3	1.6	0	1.6	0.4	0	14.0	0.50	0.8	0.32	14.2
Delta 4	1.2	0	1.2	0.45	0	20.6	0.75	0.6	0.27	15.5
Delta 5	1.2	0	1.2	0.5	0	22.6	0.83	0.6	0.30	17.0

Table C.3: Clipped delta planform fins.

Clipped Delta Planform									
	Root (m)	Tip (m)	Sweep (m)	Span (m)	λ	Angle (°)	AR	c (m)	Area (m)	t (mm)
Clipped 1	1.2	0.12	1.08	0.4	0.1	20.3	0.61	0.66	0.26	14.4
Clipped 2	1.2	0.24	0.96	0.4	0.2	22.6	0.56	0.72	0.29	15.0
Clipped 3	1.2	0.36	0.84	0.4	0.3	25.5	0.51	0.78	0.31	14.4
Clipped 4	1.2	0.48	0.72	0.4	0.4	29.1	0.48	0.84	0.34	15.9
Clipped 5	1.2	0.60	0.60	0.4	0.5	33.7	0.44	0.90	0.36	16.3

Table C.4: Swept clipped delta planform fins.

Swept Clipped Delta Planform									
	Root (m)	Tip (m)	Sweep (m)	Span (m)	λ	Angle (°)	AR	c (m)	Area (m)	t (mm)
Swept 1 (90°)	1.2	1.20	0.000	0.29	1.0	90	0.24	1.2	0.48	13.4
Swept 2 (60°)	1.2	1.20	0.167	0.29	1.0	60	0.33	1.2	0.48	13.4
Swept 3 (30°)	1.2	1.20	0.502	0.29	1.0	31	0.33	1.2	0.48	13.4
Swept 4 (20°)	1.2	1.20	0.797	0.29	1.0	20	0.33	1.2	0.48	13.4
Swept 5 (15°)	1.2	1.20	1.082	0.29	1.0	15	0.33	1.2	0.48	13.4
Design A	1.3	0.90	0.824	0.30	0.7	20	0.27	1.1	0.33	13.0
Design B	1.3	0.65	0.962	0.35	0.5	20	0.36	0.98	0.34	14.5
Deign C	1.2	0.50	1.099	0.40	0.4	20	0.47	0.85	0.34	16.0
Design C1	1.2	0.50	1.162	0.40	0.4	19	0.47	0.85	0.34	16.0
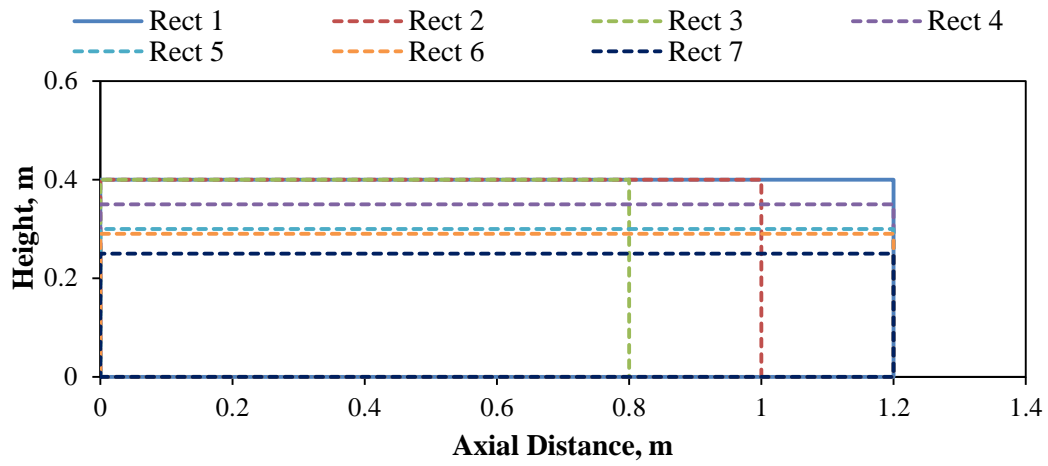
Figure C.3: Rectangular fin planforms investigated.
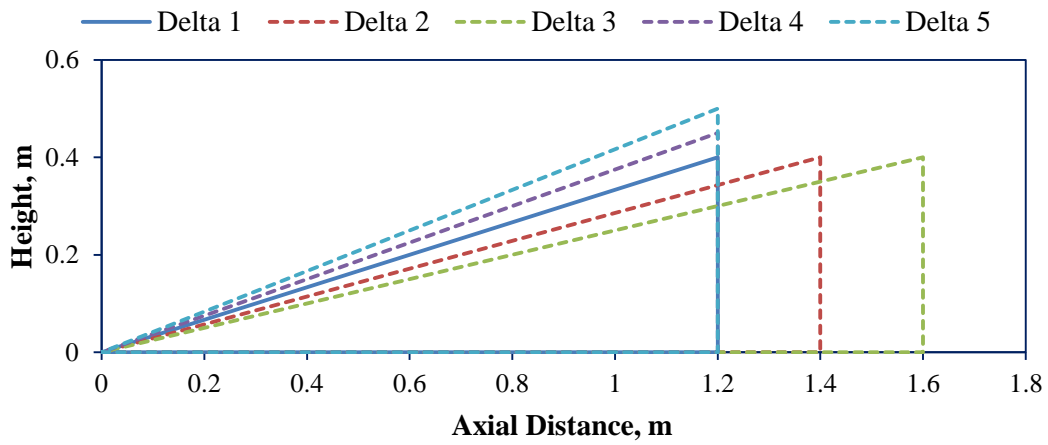
Figure C.4: Delta fin planforms investigated.
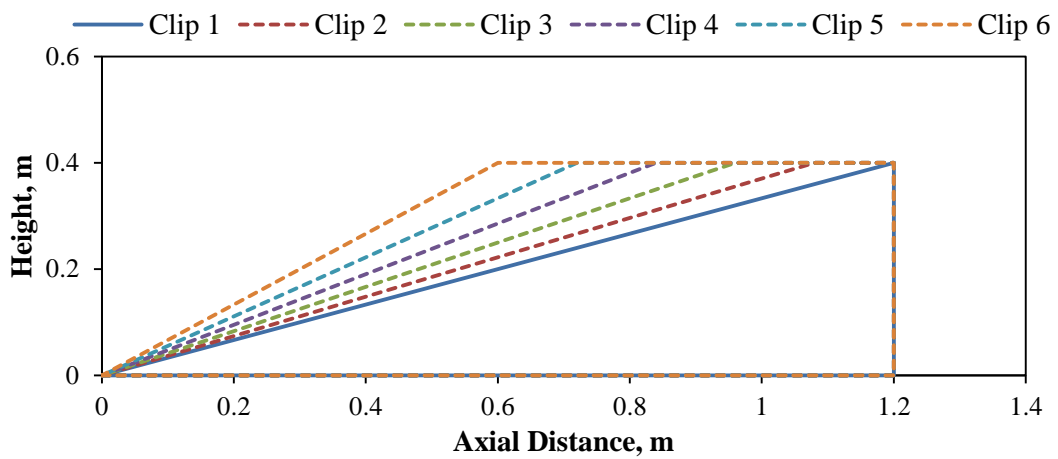
Figure C.5: Clipped delta fin planforms investigated.
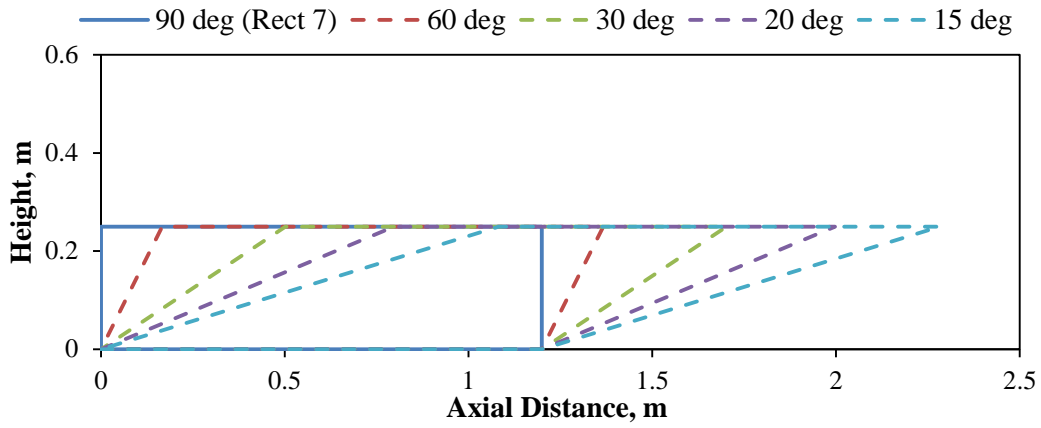
Figure C.6: Swept clipped delta fin planforms investigated.
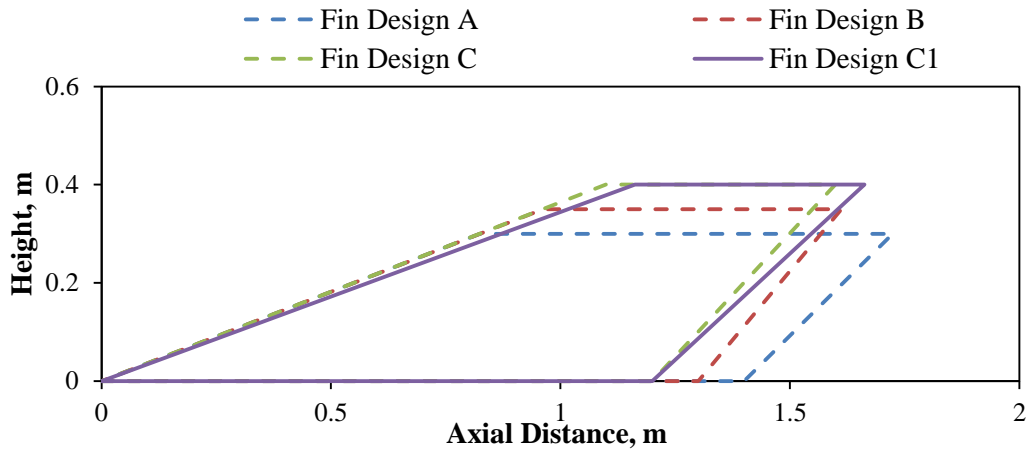
Figure C.7: Additional swept clipped delta fin planforms investigated.

Aerofoils

Table C.5: Wave drag coefficient of fins of various sectional shapes (US Army Missile Command, 1990).

Type	Profile	Two-Dimensional Drag Coefficient Based on Planform Area	Factor
Symmetrical Double Wedge		$\dfrac{4}{\beta}\left(\dfrac{t}{c}\right)^2$	1
Double Wedge		$\dfrac{1}{\beta}\cdot\left(\dfrac{t}{c}\right)^2\cdot\dfrac{1}{m(1-m)}$	$\dfrac{1}{4m(1-m)}$
Single Wedge		$\dfrac{1}{\beta}\cdot\left(\dfrac{t}{c}\right)^2$	$\dfrac{1}{4}$
Cropped Double Wedge		$\dfrac{1}{\beta}\left[\left(\dfrac{t}{c}\right)^2\cdot\dfrac{1}{m}+\dfrac{(t-h)^2}{c^2(1-m)}\right]$	$\dfrac{1}{4}\left[\dfrac{1}{m}+\dfrac{\left(1-\dfrac{h}{t}\right)^2}{1-m}\right]$
Symmetrical Parallel Double Wedge		$\dfrac{2}{\beta}\left(\dfrac{t}{c}\right)^2\cdot\dfrac{1}{m}$	$\dfrac{1}{2m}$
Parallel Double Wedge		$\dfrac{1}{\beta}\cdot\left(\dfrac{t}{c}\right)^2\left[\dfrac{1}{m_1}+\dfrac{1}{m_2}\right]$	$\dfrac{1}{4}\left[\dfrac{1}{m_1}+\dfrac{1}{m_2}\right]$
Symmetrical Biconvex (Circular or Parabolic Arcs)		$\dfrac{4}{\beta}\cdot\dfrac{4}{3}\cdot\left(\dfrac{t}{c}\right)^2$	$\dfrac{4}{3}$
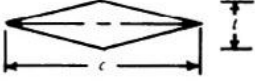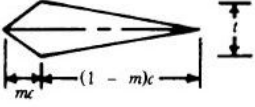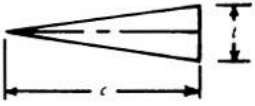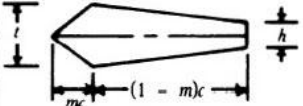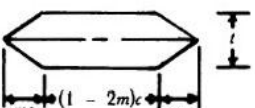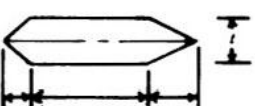
$$\beta=\sqrt{M_\infty^2-1}$$

153
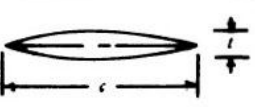
APPENDIX D

Final Design

D.1 Buckling

A simple buckling analysis on the oxidiser tank was conducted based on the work of Bruhn (1965). Figure D.1 and D.2 are valid for steel and aluminium structures however caution is necessary as the oxidiser tank dimensions used exceed the test data boundaries, therefore this study is a preliminary estimation. Axial compression and internal pressure were applied to the tank. The internal pressure of the tank increases the compressive and bending strength substantially (Bruhn, 1965).

The oxidiser tank was analysed as a monocoque structure made out of aluminium with an initial pressure of 60 bar. The burn time for Phoenix-2A ended with the depletion of the liquid nitrous oxide. This results in a minimum tank pressure of 37 bar at the end of the burn due to gaseous nitrous oxide and helium still in the oxidiser tank. The maximum thrust and axial aerodynamic force were applied with the minimum internal oxidiser tank pressure. This simulates the worst case scenario as the maximum forces occur near the start of the burn where the tank pressure is near maximum. A 99% probability was used where possible as it analyses the oxidiser tank as a critical component and is therefore more conservative. The total length of the oxidiser tank included the bulkhead ends to provide a worst case length. The known variables used in the following calculations are given in Table D.1. This analysis was performed using imperial units.

Table D.1: Know variables for the buckling analysis.

	SI Units	Imperial Units
Tank thickness, t_T	0.0065 m	0.256 in
Tank internal radius, r_T	0.2 m	7.9 in
Length of oxidiser tank, L_T	6.24 m	245.63 in
Young's Modulus, E	73.1 GPa	10.6×10^6 psi
Minimum tank pressure, P_T	37 bar	537 psi

Axial compressive loading

$$r_T/t_T = 7.874/0.256 = 30.76$$

$$L_T/r_T = 245.63/7.874 = 31.2$$

Using Figure D.1 (Bruhn, 1965)
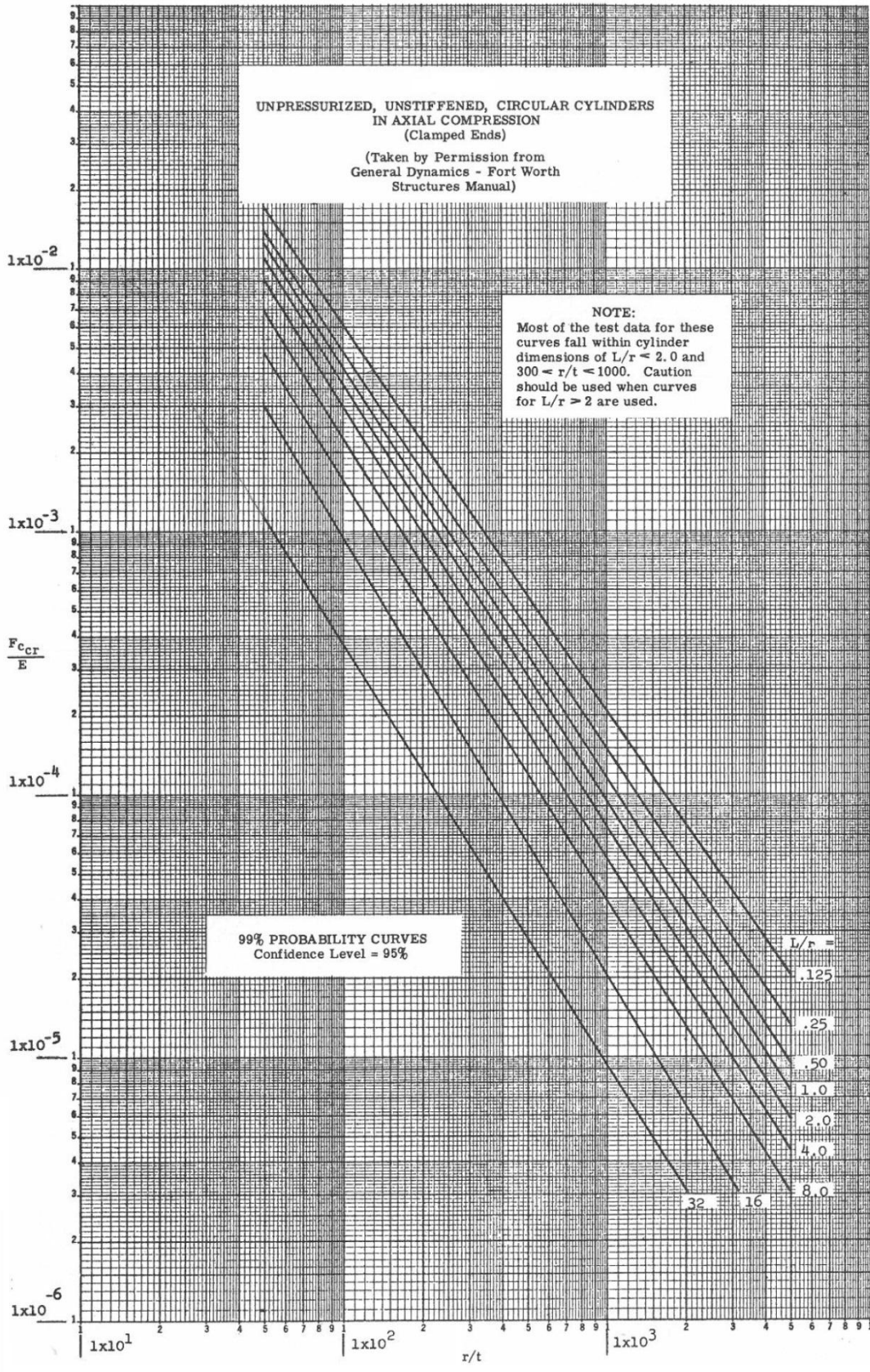
Figure D.1: Axial compression on unpressurised and unstiffened circular cylinders (Bruhn, 1965).

156

Critical compressive stress, $\sigma_{c_{cr}}$ of oxidiser tank

$$\sigma_{c_{cr}}/E = 6.5 \times 10^{-5}$$

$$\sigma_{c_{cr}} = (6.5 \times 10^{-5})(10.6 \text{ x } 10^6)$$

$$\sigma_{c_{cr}} = 689 \, psi$$

The change in critical compressive stress, $\Delta\sigma_{c_{cr}}$, due to internal pressure using Figure D.2 (Bruhn, 1965)

$$P_T/_E \left(^{r_T}/_{t_T}\right)^2 = (536.64)\Big/_{(10.6 \text{ x } 10^6)} (30.76)^2 = 0.048$$
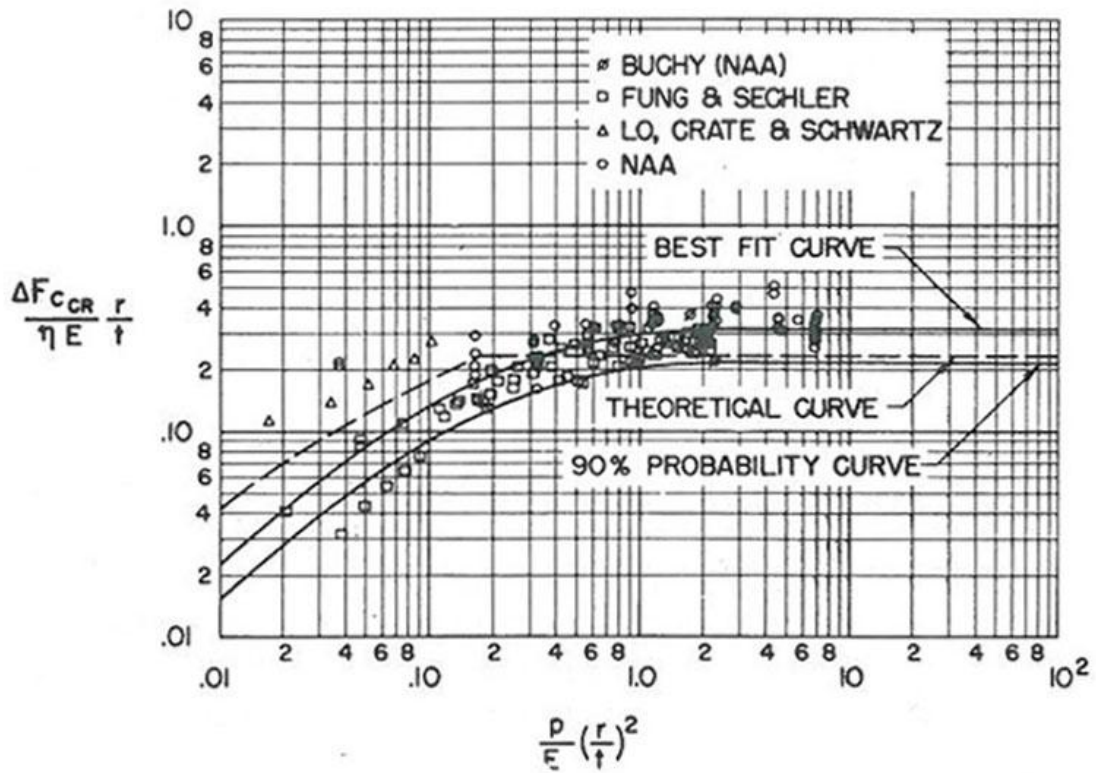
Figure D.2: The effect of internal pressure on compressive buckling stress (Bruhn, 1965).

The plasticity correction factor, η_p, is 1 due to the stress blow the proportional limit

$$\left[\Delta\sigma_{c_{cr}}/(\eta_p E)\right]\left[^{r_T}/_{t_T}\right] = 0.055$$

$$\Delta\sigma_{c_{cr}} = (0.055)(1)(10.6 \text{ x } 10^6)/30.76$$

$$\Delta\sigma_{c_{cr}} = 18953.2 \, psi$$

Longitudinal tensile stress, σ_t caused by the internal pressure of the tank

$$\sigma_t = (P_T r_T)/2t$$

$$\sigma_t = 8253.5 \; psi$$

Allowable axial compressive load, F_{all}

$$\sigma_{tot} = \sigma_{c_{cr}} + \Delta\sigma_{c_{cr}} + \sigma_t$$

$$F_{all} = 2\pi r_T t_T (\sigma_{tot})$$

$$F_{all} = 2\pi (7.874)(0.256)(689 + 18953.2 + 8253.5)$$

$$F_{all} = 353307.2 \; lb_f$$

$$\therefore F_{all} = 1571.59 \; kN$$

Safety factor (axial thrust and aerodynamic loading found using HYROPS)

$$SF = {F_{all}}/{F_{axial}}$$

$$SF = {1571590}/{(80449 + 7077)}$$

$$SF = 17.96$$

$$\therefore Will \; not \; fail \; due \; to \; buckling$$

The high safety factor demonstrates the importance of internal pressure in buckling scenarios. Buckling should be considered when allowing the gaseous phase to exit the oxidiser tank. The calculation below indicates the oxidiser tank would buckle if the tank has no internal pressure at the maximum loading condition.

Allowable axial compressive load, F_{all}, with no internal oxidiser tank pressure

$$F_{all} = 2\pi r_T t_T (\sigma_{tot})$$

$$F_{all} = 2\pi (7.874)(0.256)(689)$$

$$F_{all} = 8726.39 \; lb_f$$

$$\therefore F_{all} = 38.82 \; kN$$

Safety factor

$$SF = {F_{all}}/{F_{axial}}$$

$$SF = {38820}/{(80449 + 7077)}$$

$$SF = 0.44$$

$$\therefore Fail \; due \; to \; buckling$$

D.2 Performance Graphs
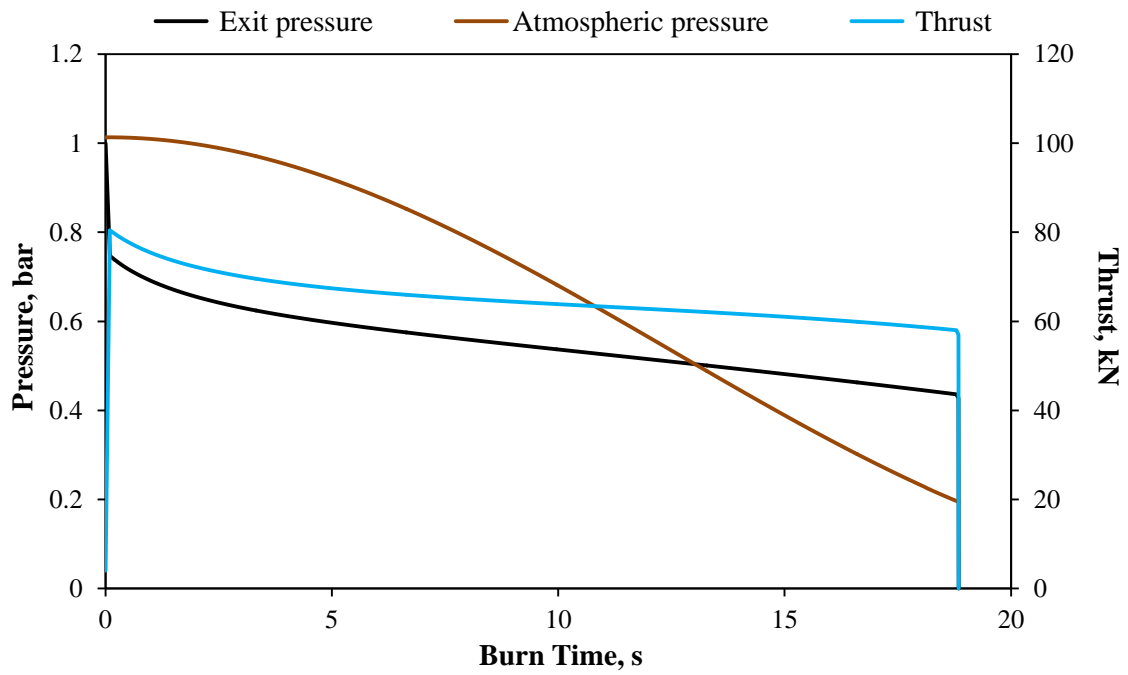
Figure D.3: Exit pressure, atmospheric pressure and thrust versus burn time of the final
Phoenix-2A design.
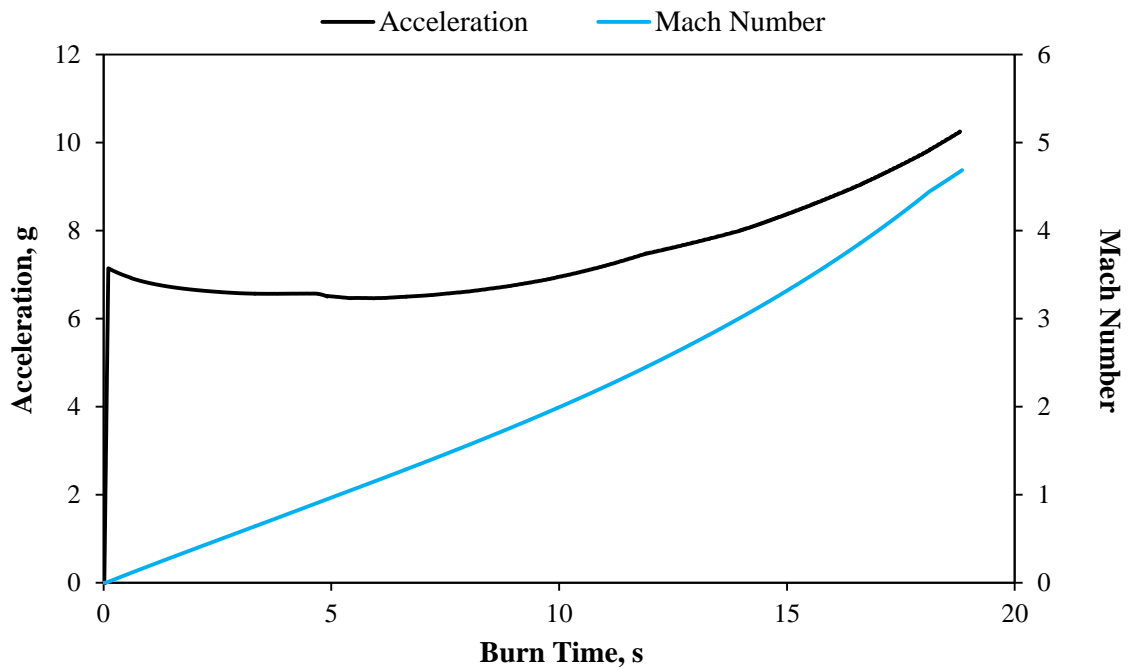
Figure D.4: Acceleration and Mach number versus burn time of the final Phoenix-2A
design.
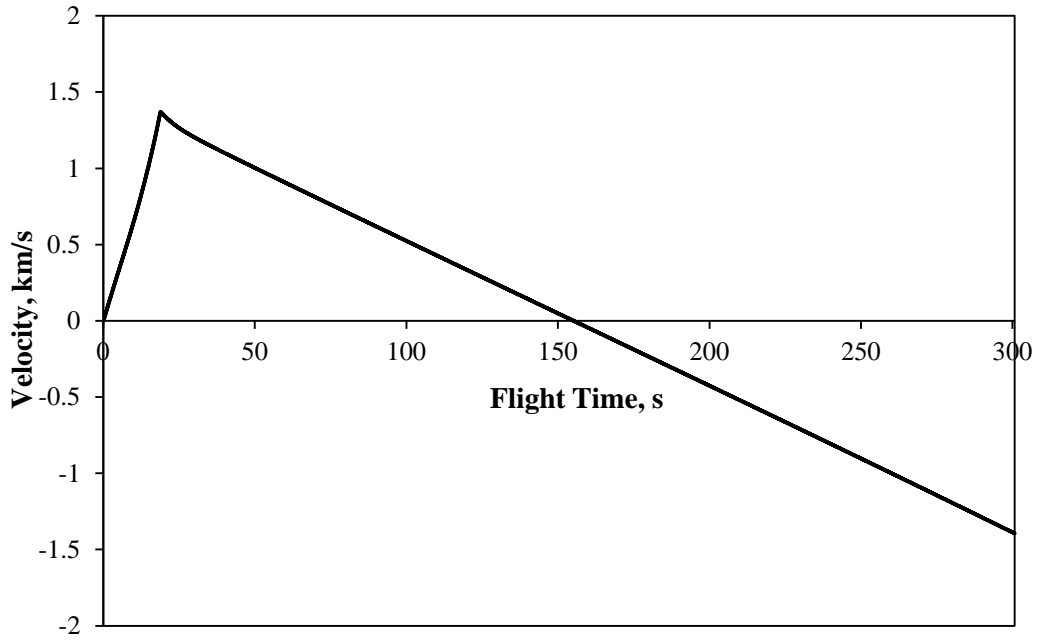
Figure D.5: Velocity versus flight time of the final Phoenix-2A design.
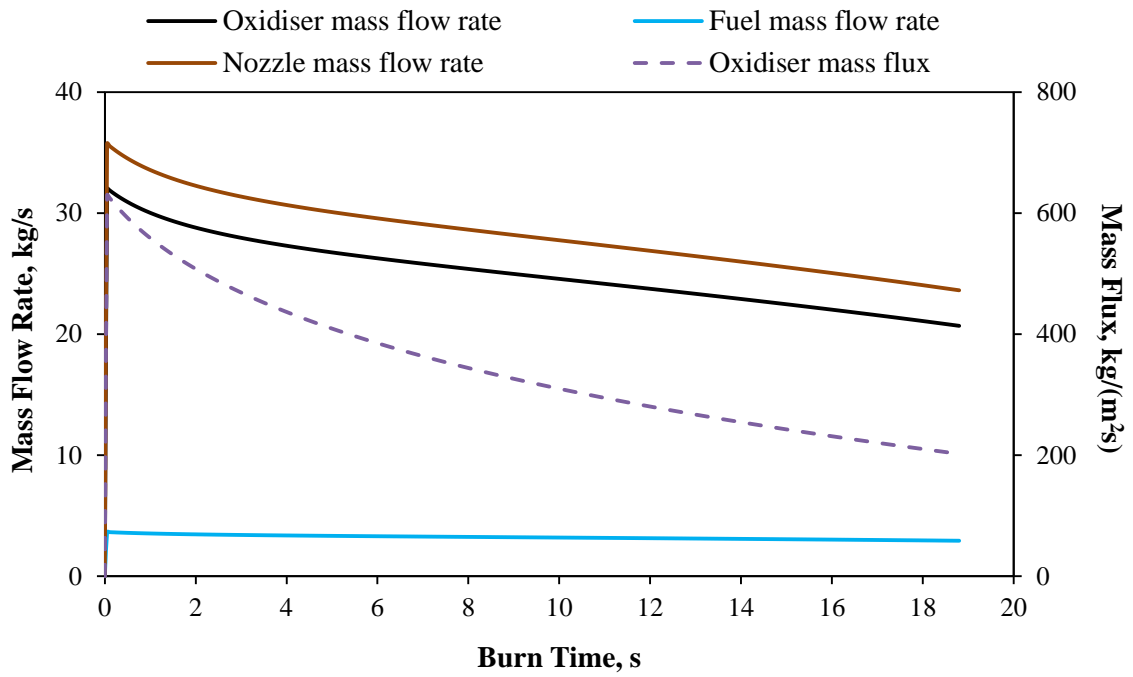
Figure D.6: Mass flow rate and flux versus burn time of the final Phoenix-2A design.
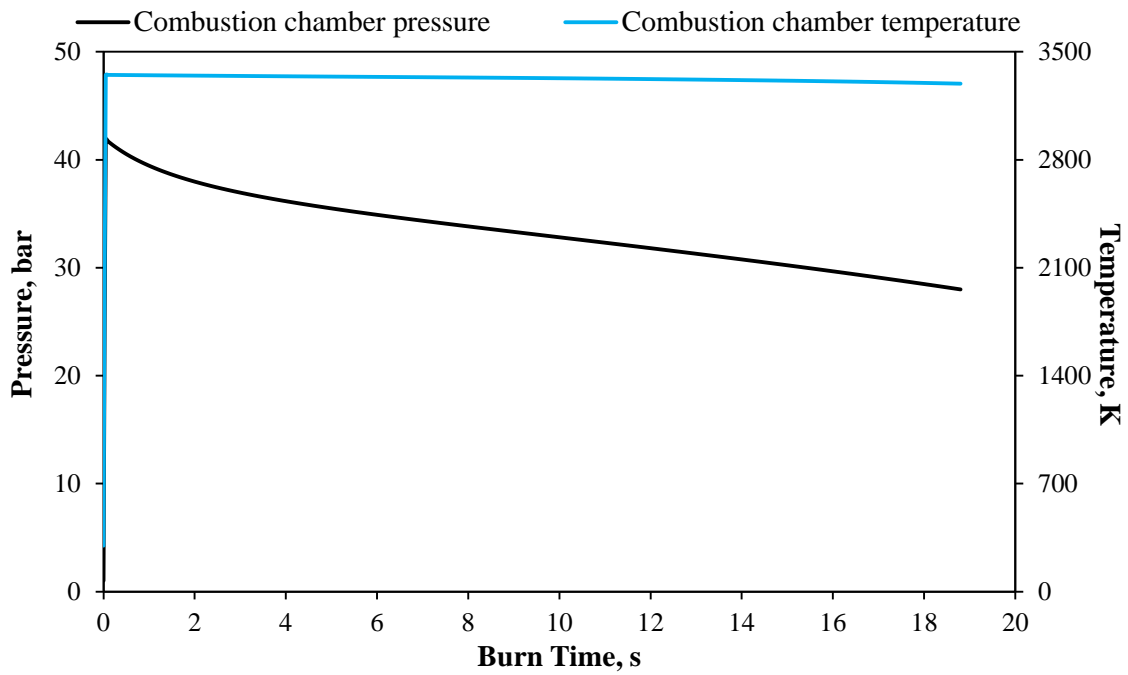
Figure D.7: Combustion chamber pressure and temperature versus burn time of the final Phoenix-2A design.
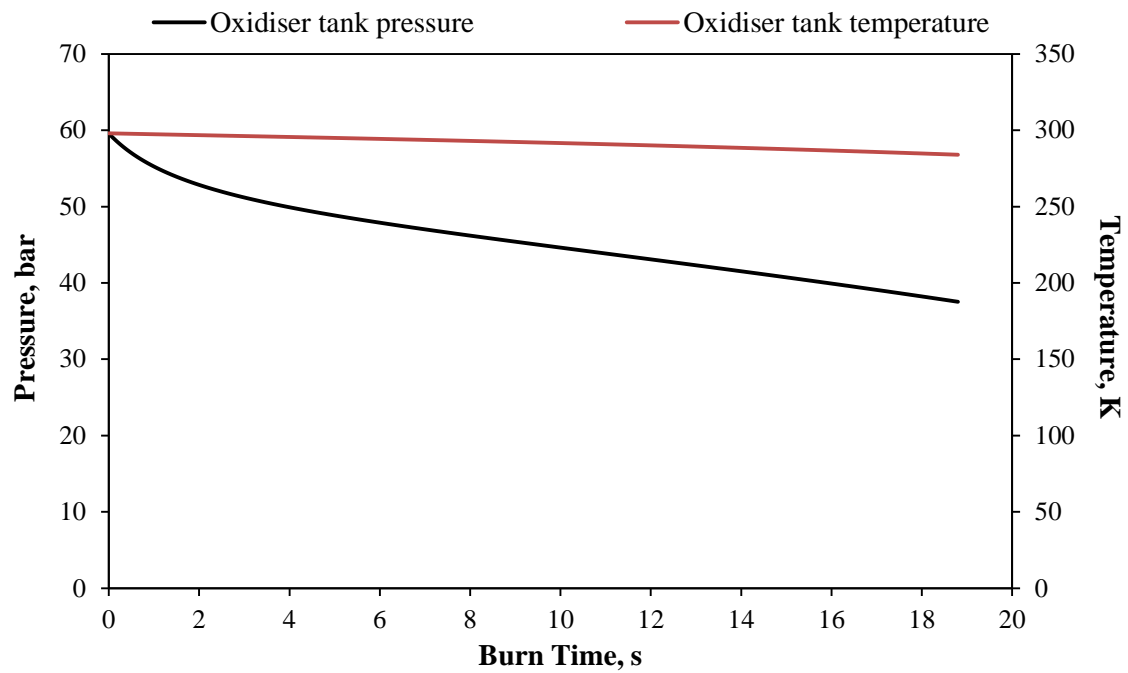
Figure D.8: Oxidiser tank pressure and temperature versus burn time of the final Phoenix-2A design.
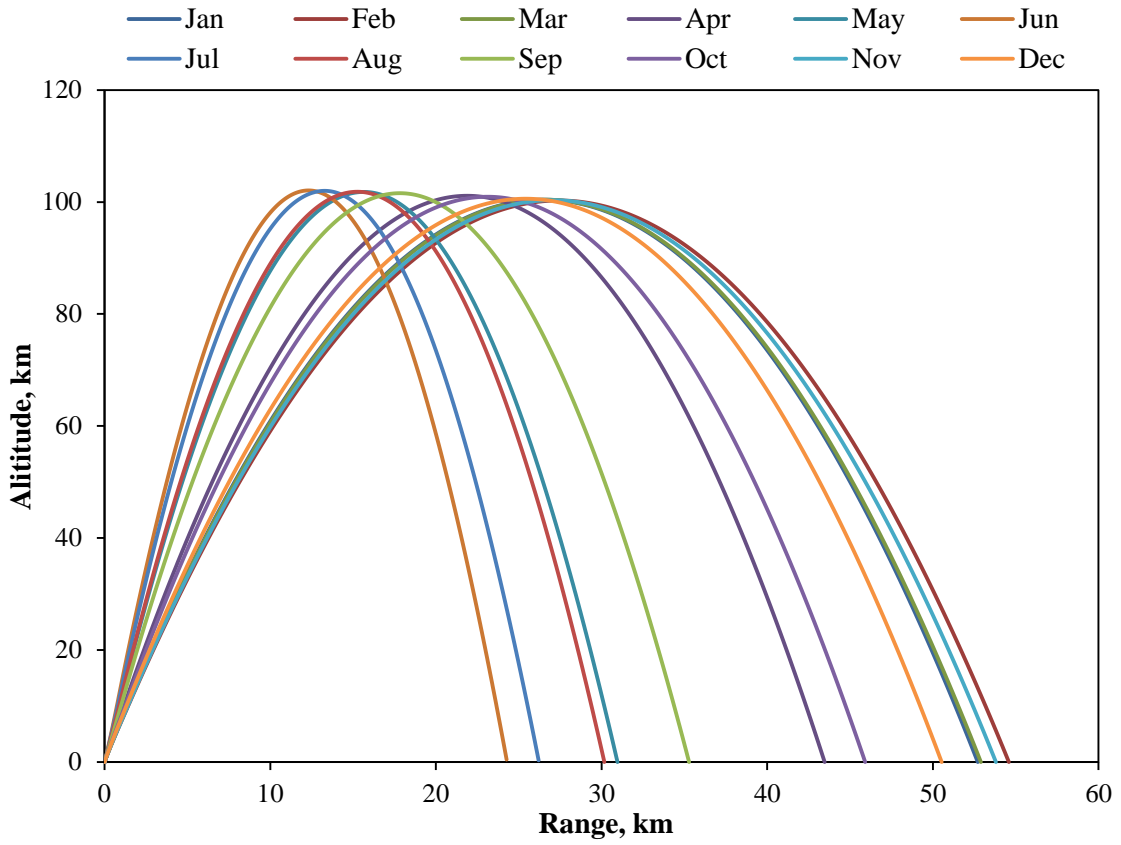
Figure D.9: The effects of monthly winds from OTR on the altitude and range of Phoenix-2A.